FRANK J. SEILER RESEARCH LABORATORY
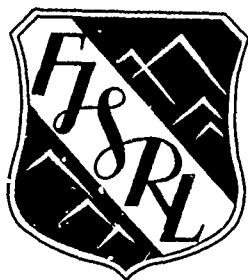
SRL-TR-76-0013   AUGUST 1976

AN EXPERIMENTAL INVESTIGATION OF WING TRAILING VORTEX FORMATION

FINAL REPORT FOR PERIOD JUN 74 - AUG 76

PROJECT 2307

AIR FORCE SYSTEMS COMMAND

UNITED STATES AIR FORCE

REPORT DOCUMENTATION PAGE		READ INSTRUCTIONS BEFORE COMPLETING FORM
1. REPORT NUMBER FJSRL-TR-76-0013 AD-A	2. GOVT ACCESSION NO.	3. RECIPIENT'S CATALOG NUMBER
4. TITLE (and Subtitle) AN EXPERIMENTAL INVESTIGATION OF WING TRAILING VORTEX FORMATION.		5. TYPE OF REPORT & PERIOD COVERED Final Report. June 74 — August 76.
		6. PERFORMING ORG. REPORT NUMBER
7. AUTHOR(s) Captain Michael S. Francis		8. CONTRACT OR GRANT NUMBER(s)
9. PERFORMING ORGANIZATION NAME AND ADDRESS Frank J. Seiler Research Laboratory (AFSC) USAF Academy, Colorado 80840		10. PROGRAM ELEMENT, PROJECT, TASK AREA & WORK UNIT NUMBERS DRS 61102F AF-2307-F1-33
11. CONTROLLING OFFICE NAME AND ADDRESS Frank J. Seiler Research Laboratory (AFSC) USAF Academy, Colorado 80840		12. REPORT DATE August 1976
		13. NUMBER OF PAGES 207
14. MONITORING AGENCY NAME & ADDRESS(If different from Controlling Office)		15. SECURITY CLASS. (of this report) UNCLASSIFIED
		15a. DECLASSIFICATION/DOWNGRADING SCHEDULE

16. DISTRIBUTION STATEMENT (of this Report)

Approved for public release; distribution unlimited.

17. DISTRIBUTION STATEMENT (of the abstract entered in Block 20, if different from Report)

18. SUPPLEMENTARY NOTES

19. KEY WORDS (Continue on reverse side if necessary and identify by block number)

Vortices, Vortex Formation, Trailing Vortex, Wind Tunnel, Hot-Wire Anemometry, Bound Vorticity, Near Wake, Vorticity, Streamlines, Flow Visualization

20. ABSTRACT (Continue on reverse side if necessary and identify by block number)

The incompressible flowfield in the vicinity of a lifting rectangular finite wing is investigated experimentally to ascertain the nature and detailed characteristics of the formation and early development of a trailing vortex. The apparatus was designed and fabricated to facilitate a direct comparison of real flow data with existing theories and flow models.

The mean velocity field was mapped directly using a linearized constant temperature hot-wire anemometry probe in conjunction with a precision wind

(over)

DD FORM 1473   EDITION OF 1 NOV 65 IS OBSOLETE
1 JAN 73

Abstract (cont'd)

tunnel traversing mechanism. The associated vorticity field was inferred from these measurements through a spatial contour integration procedure.

The existence of several identifiable "flow regions" exhibiting similar characteristics was established and verified with both hot-wire and flow visualization data. Among the regions examined extensively are the three-dimensional wing boundary layer, the inboard potential flow region and the region of vortex shedding and roll-up adjacent to the wing tip.

Measurements of the three-dimensional boundary layer were employed to determine the accuracy of the measurement technique close to the solid surface boundary and to insure that the boundary layers over the wing remained thin and attached.

The inboard potential flow region was observed to exhibit the simplifying characteristic of a spanwise cross-flow velocity component which is independent of the surface normal coordinate. As a result, a possible ambiguity in the determination of the stream-wise vorticity component was removed. Graphs of the near-surface (bound) vorticity distribution are presented along with a map of "Prandtl bound vortex filaments." The associated bound circulation function could be expressed approximately as the product of two separable functions of the planform spatial coordinates. Measurements at the wing trailing edge are employed to show that the properly non-dimensionalized characteristic vorticity distribution in this region is independent of angle of attack.

Shed vorticity emanating from the lower aerodynamic surface near the wing tip was observed to roll-up adjacent to the tip and roll over onto the upper wing surface at a predictable chordwise location. The presence and behavior f this structure which possesses an identifiable "core" is seen as an explana-n to the modified pressure distribution (lift increment) normally observed in this region.

A comparison of the flowfield in the near wake region with this data reveals that roll-up occurs much more violently near the solid surface than in the boundary free zone downstream of the wing. The normalized description of the roll-up process in the near wake region is observed to be nearly independent of both aspect ratio and angle-of-attack.

TABLE OF CONTENTS

CHAPTER

NOMENCLATURE

A — Area, usually referring to that enclosed by a contour

$A(x)$ — Function expressing chordwise variation of circulation

AR — Aspect ratio

B — A constant in the hot-wire response equation

$B(y)$ — Function expressing spanwise variation of circulation

C_D — Wing drag coefficient

C_L — Wing lift coefficient

D — Drag, usually out of the wing

E — Output voltage of hot-wire bridge

E_O — Output voltage of hot-wire bridge at zero velocity

$\bar{E}$ — Average output voltage of hot-wire bridge (Note: overbar denotes "average"; usually with respect to time. If the averaged quantity appears with an adjacent variable in parentheses, the average is taken with respect to that variable, e.g., $\overline{\Gamma(x)}$ is an average with respect to the x coordinate.)

I_{stag} — Contribution to "A" type contour integrals by flow field in the vicinity of the leading edge stagnation line

I_{vis} — Contribution to "A" type contour integrals by flow field over that portion of the contour intercepting the boundary (or viscous) layer

K — A constant, sometimes subscripted if necessary

L — Lift, usually of the wing

M — Slope of the lift curve, $C_L = M\alpha$

N — A dimensionless parameter relating the ratio of crossflow velocity to mainflow velocity

P(x) — Integral of the pressure differential over the local span,

$$\int_0^b \Delta p(x,y)\,dy$$

Q — Dynamic pressure of the free stream, $1/2\ \rho U_o^2$

S — Surface area, usually of the wing

U — General symbol for velocity, subscripted to denote specific spatial components (U_x, U_y, U_z). Also used as velocity component along hot-wire probe direction

U_o — Free stream tunnel velocity

$U_{\parallel}$ — Component of velocity in mainflow direction parallel (locally) to the wing surface

U_θ — Azimuthal component of velocity in cylindrical coordinate system

V — Velocity component perpendicular to hot-wire prove direction

W — Velocity component perpendicular to plane of X-probe

b — Wing semispan, geometric

b* — Effective wing semispan, with respect to the spacing of trailing vortices

c — Wing chord length, geometric; or symbol for "contour"

c_l — Wing section lift coefficient

e' — Fluctuating component of hot-wire bridge output voltage, $E = \bar{E} + e'$, prime <u>denotes a fluctuating quantity</u>

h — A thickness, or thickness parameter--used as slab thickness or that of body plus displacement regions

l — path distance along a contour, c.

l* — Distance from wing trailing edge to a point downstream where vortex has rolled up

o — Symbol meaning "of the order"

p   - Pressure

p_l - Pressure on lower (aerodynamically) wing surface

p_u - Pressure on upper (aerodynamically) wing surface

r   - Radial co-ordinate in cylindrical coordinate system; also radius of curvature

t   - Wing thickness, usually a function of x, t(x)

u'   - Fluctuating component of velocity in x-direction, along probe direction of hot-wire probe

v'   - Fluctuating component of velocity perpendicular to hot-wire probe direction

x   - Flow direction parallel to free stream

y   - Flow direction perpendicular to free stream extending spanwise along the wing

z   - Flow direction perpendicular to free stream extending normal to x-y plane; also the axial component in cylindrical coordinates

α - Wing angle of attack; also hot-wire crossflow angle

Γ - Circulation

Γ_o - Circulation of a contour enveloping the wing plus boundary layer at the centerline spanwise location

Γ_A - Circulation around a contour oriented in the xz-plane which surrounds all or part of the wing

Γ_B - Circulation around a contour oriented in the yz-plane which surrounds all or part of the wing

Δ - "The change in"--when used as a prefix to another symbol it implies the difference in two values of that quantity. In this paper used exclusively to reflect the difference between values on the upper and lower surfaces for the same chordwise and spanwise locations

δ - Boundary layer thickness, sometimes subscripted to denote the reference surface

ξ - Vorticity

$\vec{\xi}$ - Vorticity vector, $\vec{\xi} = \xi_x \,\hat{i} + \xi_y \,\hat{j} + \xi_z \,\hat{k}$

Λ - Wing tip sweep angle

ρ - Density of fluid, usually air

$\dot{\sigma}$ - Sensitivity coefficient of hot-wire anemometer

ϕ - X-meter wire inclination angle

θ - Complement of X-meter wire inclination angle, $\phi = \pi/2 - \theta$; also used as azimuthal coordinate when referring to a cylindrical coordinate system

τ - A reference time, or time constant

CHAPTER I

INTRODUCTION

This investigation is concerned with the formation and early development of a trailing vortex resulting from lift generation on a finite wing. The process is examined experimentally employing measurements of the velocity and vorticity fields adjacent to and immediately downstream of a rectangular wing immersed in a uniform stream. The experiments were conducted in a low speed wind tunnel and involve nominally unseparated flow conditions over the lifting face.

The significance of the problem can clearly understood by considering the entire flow field which results from the passage of fluid over a lifting surface (Figure 1). The disturbances resulting from the wing's presence lead to the appearance of a wake which persists for a long time period (far downstream of the wing) and which evolves through several identifiable stages.

The flow near the solid surface is classically termed the "boundary layer"--that region which is the source of all vorticity generated in the flow field. The behavior of the flow in this region together with

the neighboring "external" flow is directly related to the surface load distribution and is the primary arena of interest in this study. This region is more fully discussed below.

The sector immediately downstream of the wing, referred to as the "near wake" or rollup region, is usually strongly three dimensional. Vortex filaments shed into this area are free to influence each other which results in the ultimate development of two discrete vortices. This region is one of considerable importance in aircraft applications since a good portion of an aircraft structure (tail surface and controls) is usually immersed in it. The behavior of this flow can also influence the behavior of other aircraft flying in this region, e.g., formation flying, aerial refueling. The mechanics of rollup is the subject of a number of recent investigations most of which are numerical in nature.[1-5] It is examined to a limited extent in the present work.

Further downstream the wake is observed to be composed of two separate vortical structures having opposite directions of rotation. Each of these highly stable forms is characterized by a cylindrically symmetric shape and composed of a viscous core and an outer flow which behaves like that induced by a potential line vortex. Frequently, an axial deficit or excess is

detected in the core region which prohibits its being analyzed as a two dimensional field. The behavior of this part of the flow field has drawn increased attention recently due to the hazard it poses to encountering aircraft. Its persistence in high density airport traffic areas has been the cause for much concern especially when generated by heavy "jumbo-jet" type aircraft.

A host of investigators have studied the motion of these vortices,[6-9] including their stability,[10-12] their interaction with various environmental conditions,[12,13] and their decay.[14,15] Prediction methods for their interaction with encountering aircraft have also been developed.[16] They have been studied theoretically,[17,18] numerically[19-21] and experimentally in both laboratory experiments[22-26] and in flight tests.[27,28] In short, many aspects of the flow in the wake region are reasonably well documented.

This is not the case, however, with the flow in the immediate vicinity of the wing. Though the problem of lift generation was one of the first addressed by fluid mechanists at the beginning of this century, the primary objective was and continues to be the determination of airloads on the wing motivated primarily by structural and design considerations. The qualitative

nature of the flow was sketched by Lanchester,[29] and
visualized by Hoerner,[30] but little has since been done
to ascertain its detailed character in the immediate
vicinity of the wing.

Early experimental efforts concentrated largely
on the measurements of integral effects (e.g., lift
coefficient) and the surface pressure distribution.
Direct information regarding the flow field was obtained
primarily through simple flow visualization techniques.

Analytical studies were confined to invisid
models since the pressure distribution was found to vary
only slightly through the boundary layer over a large
portion of the wing surface. In fact, the qualitative
aspects of the flow field were usually prescribed
a priori, reference Prandtl's lifting line theory.
Recent numerical efforts[31,32] which have attempted to
predict the structure of the vorticity field are ham-
pered by the necessity for user supplied "initial
conditions" for the flow. An iteration scheme is usually
employed in which the flow field is allowed to deform
slightly which in turn leads to a new set of interaction
conditions. The procedure is repeated until a "stable"
situation is attained depending on the operating limits
of the computer employed.

Another shortcoming of most finite wing analyses
is the calculated behavior of the flow near the wing

tip. A mathematical singularity in the vorticity distribution corresponding to an infinite velocity is usually found there which is physically impossible. Difficulties encountered in further calculations are usually resolved via mathematical methods which remove or ignore the singularity.[33]

The actual physical situation is related to the analytical model through the concept of bound vorticity. In potential theory this entity is usually ascribed to the "body" in contrast with free vorticity which remains with the fluid particles (or elements). In reality, the bound vorticity is actually that which is continually generated by shear in the wing boundary layer and which appears "attached" to the wing in the appropriate Eulerian reference frame. In two-dimensional flow or at the symmetry plane of a finite wing, the vorticity vector is perpendicular to the free stream direction.

Of equal significance is the apparent redirection of vorticity toward the free stream direction, i.e., the horseshoe vortex concept. The actual re-orientation of vorticity is caused by the spanwise variation of the pressure gradient over the surface. If one considers the effects on a fluid element which lies near the surface as shown in Figure 2, it is

observed to deform and rotate due to the influence of the crossflow velocity gradient as well as that in the mainflow direction. As it moves within the boundary layer it continues to be effected by this rotational tendency depending, of course, on the strength and character of the crossflow shear. Eventually the element enters the free field at some point of boundary layer separation (trailing edge, wing tip or other location where the layer separates) where it becomes part of a free vortex filament in the wake. The above description is not strictly accurate since the hypo-thetical element is, of course, distorted and diffused as it moves over even a small distance, but the discus-sion serves a pedagogical purpose in describing the origins of mainstream directed vorticity.

In addition, this simplistic view is compli-cated by the presence of free vorticity near the sur-face which is not accounted for in the "sheet" models employed to describe most wings. This vorticity, like that shed at the wing tip, can alter the predicted pressure gradient which can, in turn, reinfluence the flow geometry. Hence a simple cause-effect relation-ship can never be established.

These difficulties are discussed in the ensuing pages in an attempt to provide insight into the physical

mechanisms operating on this type of flow field. Hopefully, the experimental evidence uncovered in this investigation will serve to aid in describing flows over other wing configurations.

CHAPTER II

THE EXPERIMENT--APPARATUS AND PROCEDURE

II.1 The Experimental Facilities

Most experiments were conducted in the 2 foot
x 2 foot cross-section low speed wind tunnel at the
University of Colorado (see Figure 3). This open return,
suction type tunnel is driven by a single stage axial
flow impeller powered by a variable speed, direct cur-
rent motor. The useful velocity range of this facility
extended from 5 to 110 feet per second.

Air drawn into the settling chamber was initially
filtered through a furnace filter type dust trap at the
inlet. After passing through a hexagonal-honeycomb
structure and several screens it was accelerated into
the test section through a 16:1 area ratio contraction.
The resulting free stream turbulence level
$((\sum_i \overline{u_i'^2})^{1/2}/U_o)$ was measured at 0.06% for U_o=60 feet per
second. The air was then exhausted back into the room
through a conical diffuser.

The 14 foot long test section is composed of
two separate units. The first unit (nearest the inlet)
is 4 feet in length and constructed of transite
insulating material on all sides. A small quartz window

is located on one wall as a provision for optical heating of immersed bodies. The remaining 10 foot section is constructed of plywood with a formica finish on three sides. The fourth wall is a solid, 1/2 inch thick plexiglas sheet. This latter section was the one utilized during the course of this experiment primarily due to the need for optical viewing, which will be discussed below. Variation of the static pressure gradient was less than 1% over the entire test section length. Cross-sectional variation of mean velocity was less than 0.4% outside the boundary layer in the empty tunnel.

The tunnel environment was a large air-conditioned room nominally maintained at 70°F. Thermal equilibrium with the tunnel operating (60 ft. per sec.) was reached in approximately two hours. All data were obtained with the system in total thermal equilibrium.

A precision traversing mechanism was constructed to provide accurate positioning of the measuring probes (see Figure 4 for a photograph of this mechanism). The center body could be moved either vertically or horizontally with a drive provided by miniature d.c. motors. Movement was accomplished through a screw drive for vertical movement and a rack-and-pinion system for horizontal movement. Geared potentiometers were utilized to monitor distances in both these directions. The

resultant system spatial resolution was ±0.005 inches
in horizontal movement and ±0.002 inches in vertical
movement. Axial movement of the entire traversing
system was accomplished manually by adjustment of a
connecting cable which runs the length of the usable
test section.

A Gaertner optical cathotometer was used to
establish reference distances between the model and
the probes in various configurations. Utilizing this
device, probes could be positioned to within .005 inches
of the model surface without establishing physical
contact. In addition, the instrument was used to
monitor the calibration of the vertical positioning
system of the traversing mechanism.

Flow visualization photographs were obtained in
the 2 foot x 3 foot cross-section subsonic wind tunnel
at the USAF Academy. This closed circuit facility,
powered by a motor-generator driven single stage fan has
a useful test speed range of 50 to 400 feet per second.
A Sage Action, Inc., soap bubble generator was located
in the stilling chamber just upstream of the test
section. Helium filled, neutrally buoyant soap bubbles
were created and injected into the free stream at
approximately the free stream velocity. These bubbles
were then convected into the test section and utilized

as the medium for observing flow field behavior. The plexiglass test section side walls provided a window for photographic purposes.

II.2. The Test Wing

The selection of a suitable lifting shape for the experiment was predicated on both aerodynamic considerations and facility limitations. A simple geometry having a thin cross-section seemed desirable in order to simplify the theoretical aspects of the problem. An airfoil shape which reasonably satisfied the conditions of thin airfoil theory while yielding minimal wake and boundary layer displacement characteristics was required to physically emulate the simple, potential flow theoretical models. Since the detailed flow field about the wing was to be investigated, considerations of the position resolution capabilities of the apparatus and the minimum effective probe size demanded a reasonable wing chord. The relatively small tunnel cross-section, however, imposed a severe restriction on the span parameter thus limiting the maximum effective aspect ratio. (Initial measurements behind a wall-mounted rectangular wing, NACA 2412 cross-section, with half-aspect ratio 3 indicated that almost all vorticity production occurred within a 1 chord length distance of the tip in the spanwise direction.)

On these bases a rectangular, untwisted wing having an NACA 64009 laminar flow airfoil cross-section was constructed from solid wood with a sharp, aluminum trailing edge. The surface was finely polished in an attempt to preserve the laminar flow characteristics. Maximum surface ripple was less than 0.02 inches over the entire span of the model. The surface roughness was minimal except for two small irregularities on the inboard portion of the leading edge. To provide an accurate geometric reference for the measurements, dark black spanwise lines were drawn over the white finish on both upper and lower surfaces and extended around the exposed tip side at 5% chord increments from the leading to the trailing edge. A final coat of plastic sealer was applied to insure a minimal effect of line ink "thickness" on the uniform surface roughness.

With an 8 inch chord and 12 inch semispan (half aspect-ratio of 1.5), the wing was attached to the tunnel wall with a large endplate and protruded to the center of the test section. The angle-of-attack was varied to within ±1/4 degree by a rotation mechanism outside the tunnel.

II.3. Measurement of Fluid Velocities

A constant temperature hot-wire anemometer was employed for the measurement of both mean and turbulent

fluid velocities. Turbulence properties were measured
with an anemometer based on a design by Freymuth[34] which
is detailed in Figure 5. Utilizing only three active
elements in the sensing circuit, this instrument exhibits
low noise characteristics (0.02 microvolts/°C RMS mea-
sured at the input). An anemometer designed by Bank[35]
utilizing an operational amplifier as the error sensing
element was employed for the majority of measurements
of the mean flow field (see Figure 6). Though somewhat
noisier than the transistor version, this circuit's
d.c. stability over long time periods (less than 2 mV
per hour at constant speed equilibrium) rendered it
extremely advantageous for the measurement of the poten-
tial flow field.

The frequency response of these instruments was
obtained with a standard square wave response test.
The response was never below 17 kHz (±3 db) for the
hot-wires employed in this experiment.

King[36] investigated the heat transfer relation
for heated cylinders in a uniform stream. The applica-
tion of his results to hot-wire anemometry gives rise
to a functional relation between the wire output voltage
and the free stream flow velocity--

$$E^2 - E_o^2 = B \, U^n \qquad \qquad (II-1)$$

where B is a constant depending on the fluid and wire properties.

For the speed range employed in this experiment the exponent "n" was found to be very close to 0.5 in value (Figure 7). As a result, an analog circuit utilizing Motorola MC1594 multipliers in a squaring mode was employed to linearize the anemometer output. The basic schematic is shown in Figure 8. Squaring element number 2 multiplies the anemometer output by itself giving E^2. The constant E_o^2 is subtracted electronically by lowering the tunnel speed to zero and adjusting potentiometer, P1. The linearized output is then obtained by squaring $(E^2 - E_o^2)$ with element number 4. Amplifiers 1 and 3 are employed for gain control making it useful over a wide velocity range. The linearizer frequency response was measured flat (± 3 db) to 29 kHz.

The hot-wire probes utilized silver coated Pt. - 10% Rh. Wollaston wire which was soft-soldered between the ends of the needle supports. A weak nitric acid solution was used in electro-chemically etching the silver jacket thus exposing the effective sensing element. The wire core was 0.0001 inches in diameter, and wires were etched to a length/diameter ratio of approximately 300.

Since X-meters were the primary probe types employed, adder and subtractor circuits were constructed utilizing Fairchild Type 741 operational amplifiers. An X-meter circuit constructed by McMichael[37] was utilized for filtering, averaging and integrating the turbulent (a.c.) component of the hot-wire signals. The circuitry for these elements is detailed in Figures 9 and 10.

Turbulence intensities were also measured with a Bruel and Kjaer Random Noise Voltmeter (Type 2417). Variable time constants from 0.3 seconds to 100 seconds were available through this instrument with a d.c. output proportional to the RMS value of the input signal. The instrument bandwidth was 2-20,000 Hz.

Data was recorded from digital voltmeters and a Moseley type 2D-2A X-Y plotter. A Tektronix type 502A oscilloscope was used for constant signal monitoring.

The nature of the investigation demanded that the velocity field be resolved into components. A tri-axial 3-wire system was considered but discarded due to its limited spatial resolution, complicated analog circuitry, and complex calibration procedures. Since an unseparated, surface bounded flow was to be studied, an X-meter type probe was constructed having a variable

head angle (see Figure 11). Alignment of the probe so that the plane of the "X" was locally parallel to the wing surface effectively provided the total velocity vector in most measurement regions. Several standard fixed angle X-meters were also employed for other flow field measurements. The wire angle was maintained nominally at 45° inclined to the tunnel free stream. For a two-dimensional flow, or a locally two-dimensional situation, the X-meter equations are given below. Refer to Figure 12 for a graphical illustration of the variables:

<u>Mean Flow</u>--

$$\tan \alpha = \frac{\bar{E}_1 - \bar{E}_2}{\bar{E}_1 + \bar{E}_2} \cdot \frac{1}{\tan \phi} \qquad (II-2)$$

$$U = \frac{\sigma(\bar{E}_1 + \bar{E}_2)}{2 \cos \phi} \qquad (II-3)$$

$$V = \frac{\sigma(\bar{E}_2 - \bar{E}_1)}{2 \sin \phi} \qquad (II-4)$$

<u>Turbulence Properties</u>--

$$\overline{u^2} = \frac{\sigma^2 \overline{(e_1 + e_2)^2}}{4 \cos^2 \phi} \qquad (II-5)$$

$$\overline{v^2} = \frac{\sigma^2 \overline{(e_2 - e_1)^2}}{4 \sin^2 \phi} \qquad (II-6)$$

$$\overline{uv} = \frac{\sigma^2 (\overline{e_2^2} - \overline{e_1^2})}{4 \sin \phi \cos \phi} \qquad (II-7)$$

where the angles between the free stream and inclined wires, ϕ_i, are equal and the two anemometer system sensitivities have been adjusted to the same value, σ.

The effective sensing region of the X-probes was a rectangular box of dimension 0.02 inches x 0.02 inches x 0.005 inches (volume = 2.0 x 10^{-6} inches).

II.4. Probe Calibration

Rather than rely on derived relationships between the velocity components and linearized anemometer voltages, a direct calibration of probe properties was performed in the tunnel free stream. Employing the proportionality relationships (equation (II-3), (II-4)) for the X-probe, the instrument was first aligned so that its symmetry axis coincided with the free stream direction and the tunnel speed varied to give the linearized output for "U," a typical value shown in Figure 13. The probe was then rotated through known angles in the free stream at constant speed. A typical calibration curve is shown in Figure 14. This curve is found to be independent of the free stream velocity. The validity of this static calibration technique was verified by Singh[38] who compared it with a dynamic cali-bration procedure. Agreement was found to be within 1%. Figure 14 shows that the crossflow component, $\bar{V}$, is linear up to a value of 0.5 $\bar{U}$ allowing for the

measurement of large crossflow components. Periodic probe calibrations revealed that virtually constant characteristics were maintained over the life of the probe.

Since the wire angle with respect to the free stream is never exact (the design angle), two calibrations were made for each probe. First, the probe angle was found for which the inclined wires made equal angles with the undisturbed free stream. This reference angle was then used as the basis of the first calibration. Secondly, the probe was aligned so that its geometric axis coincided with that of the free stream velocity vector. A second calibration utilizing this "zero angle" was obtained. The effect of this "forced calibration" is to shift the curve to one side or another and create an asymmetric characteristic. All measurements taken for this experiment, however, were well inside the linear bounds for all the probes used.

II.5. Measurement Procedure

Measurements of the velocity field were taken in both the wake region downstream of the wing and in close proximity to the surface. For data obtained in the former region either a geometric or an aerodynamic (e.g., vortex core center) reference could be utilized. Measurements near the wing surface were based

on a geometric reference, usually the wingtip, estab-
lished with the traverse positioning system in conjunc-
tion with the optical cathotometer.

In all cases, the probe was first positioned in
the undisturbed free stream with the wing at the zero
lift angle. The linearizers were then adjusted to give
the desirable output. The probe was repositioned at a
point convenient to establishing the required reference.
For situations involving measurements close to the wing,
the distance between the probe and the surface was
established at the position nearest contact by comparing
the cathotometer readings for the surface line reference
and sensing element locations. Traverses were then made
in horizontal or vertical directions either parallel to
or away from the wing. Graphs relating velocity to
position were obtained with the X-Y recorder. In places
where the turbulence level was significant, the data
were taken pointwise by time averaging the signal.

In addition to direct measurements of the
velocity field, information regarding the vorticity
content of various spatial regions was essential.
Three techniques were employed to obtain the rotational
properties of the flow field:

1) In the far wake region, the isolated trail-
ing vortex becomes axisymmetric, its circulation being
given by--

$$\Gamma(r) = 2\pi r \, u_\theta \qquad\qquad\qquad\qquad (II-8)$$

A probe traversal through the vortex center with the X-plane perpendicular to the traverse direction allows for the measurement of $u_\theta(r)$. Hence, Γ can be calculated using equation (II-8). If the vortex is completely rolled up, a constant value Γ_o will be reached. Symmetry was never completely achieved in this experiment due to the limitation on maximum downstream measurement location (x/c = 7.5 chord lengths downstream of the trailing edge). Singh[38] indicates complete rollup (i.e., cylindrical symmetry of the crossflow velocity field) for his higher aspect ratio wing for x/c>10.

2) In regions of concentrated vorticity, a mechanical probe similar to a "paddle wheel" was utilized to obtain the local value of the vorticity. The device is described by Grow.[26] Difficulties in using this device in a quantitative manner stem from its rather large effective volume (i.e., it must average the vorticity over a relatively large region in space) and its inherent mechanical friction which limited its use in weakly rotational regions. It provided, however, a qualitative description of the centers of concentrated vorticity (e.g., vortex cores) and their location around and downstream of the wing.

3) A third technique employs the definition of
circulation as follows:

$$\Gamma_c = \oint_C \vec{U} \cdot d\vec{l} = \iint_A \vec{\xi} \cdot d\vec{A} \qquad (II-9)$$

Contour integral paths were traced out in physical space
by the probe traversing mechanism. The restriction to
independent horizontal or vertical movement restricted
these curves to being rectangles in the Trefftz plane--
sometimes referred to as the "crossflow plane" when the
contour envelops the wing. By orienting the probe
such that the X-plane is parallel to the traversal
direction, the quantities appearing in equations (II-4)
and (II-9) were evaluated. The restrictions and limi-
tations of this technique will be discussed below.

In all cases, the probes were returned to the
zero reference location upon completion of the measure-
ment to examine the electronic drift of the instru-
mentation. In situations where this characteristic
exceeded one third of 1% based on full-scale values,
the data were discarded and remeasured.

II.6.   Restrictions and Limitations
of the Measurements

The techniques described in the foregoing
sections are not, in general, valid for all flow situ-
ations. Certain restrictions on the nature of the

flow field are required to insure compatibility with the experimental apparatus.

The measurements taken near the wing surface rely heavily on the assumptions of locally parallel and unseparated flow near the surface. The first assumption is invalid in the vicinity of the wing tip due to the surface discontinuity that exists there and to the presence of large rotational gradients which result from the rollup of accumulated tip-shed vorticity. As a result, direct velocity field measurements in this region are limited and are presented only when they can be corrected for these effects (e.g., Qualitative nature of the streamlines).

Though not a problem in this experiment, the effect of separated flow can induce large errors into the experimental results. Large reverse flow velocities with respect to the probe body are not readily detected due to the presence of the interfering probe afterbody. Measurements upstream of the separation point suffer errors due to the non-linear probe characteristics which are significant for low values of $\bar{U}$ due to resulting large values of $\bar{V}/\bar{U}$ (see Figure 14).

An additional difficulty encountered in measurements near a solid boundary with a hot-wire anemometer is that of probe-wall heat transfer. This phenomenon was investigated by Wills[39] for a laminar boundary

layer with an extension to turbulent boundary layers and by Repik and Ponomareva[40] for a turbulent boundary layer. The closest point of approach with the probes used in this experiment was 0.05 inches from the wing surface, giving a ratio of probe-wall distance to wire diameter of 500. Wills showed that the required velocity correction at this distance is negligible ($\ll 1\%$). Data from the other reference yield a similar result.

A major problem with the use of an X-meter in three dimensional flow fields is the error due to an out-of-plane velocity component. This error is calculated to be dependent on the inplane crossflow velocity component, the out-of plane component, the wire inclination angle and the local convective or mainflow speed.[41] For small values of the out-of-plane component, W, the linearized relative error to $\bar{V}$ is computed as--

$$\text{Error} \sim \frac{1}{2}\left(\frac{\bar{W}}{\bar{U}}\right)\frac{1}{\sin^2\theta - \cos^2\theta\left(\frac{\bar{V}}{\bar{U}}\right)^2} \qquad \text{(II-10)}$$

For the standard 45 degree inclination employed in these experiments, this expression reduces further to--

$$\text{Error} \sim \frac{(\bar{W}/\bar{U})^2}{1 - (\bar{V}/\bar{U})^2} \qquad \text{(II-11)}$$

It is apparent that the boundaries of the contours employed to determine circulation can greatly affect

measurement accuracy if they pass through a region where large out-of-plane component exists, e.g., regions of concentrated vorticity. These regions may, of course, be enclosed by the contour. All experimental results have been corrected for the out-of-planeness error.

CHAPTER III

VELOCITY FIELD SURROUNDING THE

LIFTING WING

III.1. Optimum Test Configuration

In addition to obtaining the parametric varia-
tion of certain integral wing properties, a primary
objective of this study was to ascertain the detailed
structure of the flow field surrounding the lift
generator for some representative orientation. The
selection of an optimum operating condition was based
largely on two considerations:

1) High lift was desired to accentuate the
crossflow velocities and therefore improve the accuracy
of lift related flow field measurements and,

2) A minimal boundary layer displacement
region was sought in an attempt to simulate the "flat
plate" or idealized thin wing geometry. This condi-
tion is usually optimized through drag minimization.
The angle of attack employed was therefore that corres-
ponding to a maximum lift to drag ratio.

Rather than relying on available high Reynolds
number test data,[42] the gross wing properties were
estimated through preliminary measurements taken in the

wake. The lift coefficient was calculated by determining the circulation about the isolated free tip vortex downstream of the wing and applying the approximate relation from two-dimensional potential airfoil theory:

$$C_L = \frac{2\Gamma_o}{U_o c} \qquad\qquad (III\text{-}1)$$

Circulation measurements were made at 7.5 chord lengths downstream of the trailing edge using the method outlined by Singh,[38] Chapter II. The resultant lift curve is given in Figure 15.

The drag was approximated by evaluating the axial velocity defect in the wake. Through the measurement of this distribution across the wake (z-direction), the drag coefficient per unit span is given approximately as--

$$C_D = \frac{2\int_{-\infty}^{+\infty}(U_o - \bar{U}_x)\, dz}{U_o c} \qquad\qquad (III\text{-}2)$$

The drag variation with angle of attack is shown in Figure 16. This data is based on an average of four spanwise locations. A comparison of data obtained at several chordwise locations indicated an error of less than 5%.

The resultant expression for the approximate lift-to-drag ratio is then--

$$\frac{L}{D} = \frac{\Gamma_O}{\int_{-\infty}^{+\infty}(U_O - \bar{U}_x)\,dz} \qquad\qquad (III-3)$$

The measured characteristic curve is given in Figure 17. This result served as the basis for the selection of a primary test angle of attack of 4 degrees. This low value allows one to apply the small angle approximations $(\sin \alpha \approx \alpha, \cos \alpha \approx 1)$ in relating the wing-fixed (or "body-fixed") and wind axis coordinate systems. The main flow axis here approximately coincides with the airfoil symmetry axis.

The technique used for obtaining the lift characteristic suffers from several deficiencies in this experimental situation. (These discrepancies will be discussed at length in Chapter V.) The method was, however, sufficiently accurate to reveal the shape of the L/D characteristic and provide an adequate choice in the selection of the test orientation.

A free stream tunnel velocity of 60 feet per second was selected as the maximum useable speed for which probe vibration effects were negligible. The corresponding Reynolds number based on wing chord was 247,000.

III.2. Flow Regions in the Crossflow Plane

An examination of the behavior of the flow field in any crossflow (Treffl.:) plane intersecting the wing

surface reveals a general structure which is qualita-
tively independent of the chordwise location. A sketch
detailing this structure is given in Figure 18. The
flow is subdivided into various sections which exhibit
similar properties. The relative physical sizes of
these regions will vary with chord location and other
aerodynamic parameters. For example, the thickness of
the inboard boundary layer (Region 2 and inboard por-
tions of Region 3) will vary with chordwise location
due to the pressure gradient ($\partial p/\partial x$) which is, in turn,
a function of wing orientation. The wavy lines which
depict the interface between regions are not neces-
sarily rigidly defined but can be a function of wing
construction uniformity and subject to some interpre-
tation as, for example, is the thickness of a turbulent
boundary layer. The advantage of this subdivision
concept is that it facilitates the description and
analysis within any given region. While this particu-
lar structure has resulted from an investigation of a
specific rectangular wing shape, the result can be
generalized to a broader class of planforms, aspect
ratios and angles-of-attack providing the flow is
unseparated in the inboard regions. A detailed explan-
ation of this structure follows in the ensuing sections.

The simplest region from an analytical stand-
point is that of two-dimensional ("airfoil") potential

flow inboard of the wing tip and outside the boundary
layers on both surfaces (Region 1). It can be located
about most constant chord, unswept wings of high aspect
ratio but more frequently is realized only in the wing
symmetry plane as is the case in this experiment. An
adjacent two-dimensional boundary layer (Region 2) can
also be present. This airfoil-like flow field coincides
with the flattening of the spanwise lift distribution
near the wing centerline.

Observations nearer the tip indicate that a
spanwise velocity component is introduced resulting
from the spanwise pressure gradient. This component
becomes increasingly more significant as the tip is
approached.

III.3. Characteristics of the Three-Dimensional Boundary Layer

The three-dimensional wing boundary layer
(Region 3 in Figure 18) is a complex structure whose
velocity field is a function of all spatial variables.
It is this region that is solely responsible for the
generation of vorticity in the main flow direction.

Measurements of the mean velocity components
and turbulent intensities were made at various locations
adjacent to the wing to establish the extent of the
displacement region. The results of several represen-
tative measurements are graphically depicted in

Figures 19-27. In these Figures the coordinate
reference for the surface normal direction (z/c = o)
is the local surface location. The data contained in
these illustrations refer to upper surface conditions
only. The lower wing surface exhibited an extremely
thin boundary layer (less than 0.03 inches) preventing
any detailed measurements in its interior.

Figure 19 shows the variation of mainflow
velocity $(\bar{U}_x)$ profiles with spanwise location. Figure
23 shows the variation of the same parameter with chord-
wise position. The local upper surface boundary layer
thickness is seen to be a strong function of chordwise
location but almost independent of spanwise position
except in the immediate vicinity of the tip. The weak
spanwise variation is probably due to irregularities
in wing thickness and surface roughness related to
construction tolerances. An examination of the span-
wise variation of turbulence intensity (Figure 27)
indicates that this may be the case.

The layer thickness varied from immeasurably
thin (less than .03 inches, z/c = .0083) upstream of
the midwing point to over 0.30 inches near the trailing
edge. Measurements of U_z/U_x near the surface verify that
the measured value of the downwash coincides well with
the calculated value of the local surface slope. A

representative example of these data are given in
Figure 28 at a chordwise location near the trailing
edge. This provides some evidence as to the integrity
of the mainflow measurements near the surface and
therefore, the absence of separation. The absence
of separation was confirmed by measurements over the
angle of attack range of 0-8 degrees. Further discus-
sion of this evidence will be found in Chapter V.

The boundary layer characteristics are observed
to be almost independent of span location over a large
portion of the inboard region, as noted in Figures 22
and 27. The tip region, however, is characterized by
gross spatial non-uniformity in all variables. The
crossflow profiles detailed in Figures 20, 21 and 24
dramatically illustrate this variation. These charac-
teristics will be discussed fully in the next section.

The presence of a highly frequency selective
waveform in the fluctuating velocity trace was observed
at the outer edges of the boundary layer over the inboard
region near the aft portion of the wing $(x/c>0.70)$.
These "Tollmien-Schlicting"* waves are associated with
the process of transition to a fully turbulent flow.

---

*These waves were first suggested by Rayleigh,[43]
examined extensively analytically by Tollmien[44] and
Schlicting[45] and verified experimentally by Schubauer
and Skramstad[46] for the case of flow over a flat plate.

Experimental evidence of this phenomenon is displayed
in the correlation function, Figure 26. These waves
were observed through the entire angle of attack range
of unseparated conditions (0-8 degrees), though the
amplitude of the waveform was greatest at the lower
angles.

As indicated above, the lower wing surface
exhibited a much thinner displacement region than upper
surface. Only in the immediate vicinity o." the cusped
trailing edge did a suddenly high turbulence level and
shallow mainflow velocity gradient indicate possible
local separation (or, incipient transition). The char-
acteristics of the outer flow did not seem to be
affected by this situation.

A diagram depicting the growth of the displace-
ment region over the inboard portion of the wing is
given in Figure 25. This scale illustration shows the
chordwise variation of boundary layer parameters for
$\alpha = 4°$.

III.4. Inboard Potential Flow Region

A region of considerable interest is that of
three-dimensional potential flow just outside the
boundary layer inboard of the tip (Region 4 in Figure
18). It is this sector that will be involved in the
computation of wing bound vorticity in Chapter IV.

Continuous spanwise traverses were made at various distances from the upper and lower surfaces to provide a complete quantitative description of this portion of the flow field. Both the mainflow (x) and crossflow (y) components were measured. Data were obtained in 5% chord intervals from the leading edge to the 30% chord point and in 10% chord increments from there aft to the trailing edge. Figures 20, 21, 24 and 29-35 contain a series of various crossflow velocity profiles adjacent to both wing surfaces.

Examination of the crossflow variation reveals that it is apparently not dependent on the normal (z) coordinate in this region. This important simplification is more readily understood by examining the equation for the x-vorticity component:

$$\xi_x = \frac{\partial U_z}{\partial y} - \frac{\partial U_y}{\partial z} \qquad (III-4)$$

The left side of this expression is zero since only potential flow is considered. Since, for the untwisted, non-porous wing with a thin uniform boundary layer the streamlines approximately follow the surface contour, then

$$\frac{\partial U_z}{\partial y} \approx 0$$

and the above equation reduces to--

$$\frac{\partial U_y}{\partial z} = 0, U_y = U_y(x,y) \text{ only} \qquad (III-5)$$

This equation is verified by the existing experimental evidence. The approximation breaks down several inches away from the surface due to the influence of other elements of the flow field. This simplification does, however, allow a wide margin for error in the measurement location employed for calculating the bound vorticity, as will be noted in the next chapter.

The spanwise crossflow velocity profiles, Figures 29-35, represent a complete survey of the velocity field in the potential region adjacent to the inboard upper and lower surfaces of the wing. Each data point has resulted from a spatial average (in the z-direction) in velocity for the region for which equation (III-5) is valid. Error bars have been added for those locations where the range of values exceeds that represented by the symbols.

One disturbing feature that stands out in these data is the reversal of crossflow near the trailing edge on the upper surface and the leading edge on the lower surface. Though it occurs well inboard of the tip and is small in magnitude, this reversed secondary flow seems to oppose the expected spanwise pressure gradient. Two explanations for the existence of this phenomenon seem possible:

(a) Local separation within the boundary layer
is affecting the outer flow in the cross-
flow component, and

(b) The tunnel wall boundary layer is imposing
some effect on the outer flow near the wing-
wall attachment point.

Explanation (a) does not seem reasonable in light of
the results of downwash and mainflow measurements in
this region (see, for example, Figure 28). Additional
measurements (Chapter V) which relate the crossflow
distribution with angle-of-attack also invalidate this
explanation. The effect of the tunnel wall boundary
layer, however, is significant and may well be respon-
sible for this situation. Significant turbulence (well
above the free stream level) was detected as far as
two inches distant from the wall surface. This is
not surprising when it is realized that the test wing
is mounted some 5 feet downstream of the test section
inlet. The net effect of this "thick" tunnel boundary
layer is to reduce the effective aspect ratio of the
wing. This is done, however, in a rather non-uniform
way as will be seen in illustrations presented later.

III.5. Flow Field Near the
        Wing Tip

The flow immediately adjacent to the wing tip
is characterized by the presence of steep velocity

gradients over a small spatial region in addition to an irregular geometric structure. Unlike its regular behavior in the inboard region, the crossflow near the tip is observed to be highly dependent on all spatial coordinates as can be seen in Figure 36. This area, represented by Region 5 of Figure 18, is one character- ized by concentrated vorticity which has accumulated due to shedding upstream in the tip region. The helical flow pattern so commonly associated with the far-field isolated vortices is observed to develop well upstream of the trailing edge as can be seen in the streak photograph in Figure 37. Further examination of qualitative data shows this "lump" of vorticity to adhere to both the sides and upper surface of the tip region.

The actual identity of this region is doubt- lessly related to the wing tip shape in addition to other wing parameters. The measurements described here concern only a flat tip whose plane is perpendicular to the y-coordinate. Since the tip is usually the source of a singularity in theoretical or numerical analyses, the physical characteristics of this portion of the flow field are significant.

The approximate shape of this rollup region in various Trefftz-plane stations along the wing has been reconstructed using detailed X-wire data. Horizontal

and vertical traverses at finely spaced intervals were
used to construct crossflow plane velocity vectors,
local maxima and minima, and crossflow stagnation points,
lines and regions. These reconstructions are shown in
Figures 38-43.

The swirling secondary flow is seen to orig-
inate close to the leading edge (first observed at
$x/c = 0.05$) and progress aft along the side of the
wing. The small scale and radius of curvature are
evident from the sketches. Its growth is restricted to
the side portion of the tip until the 60% chord point
where it apparently begins to "roll over" onto the
upper surface. This repositioning movement is probably
caused by the general influence of the pressure gradient
around the tip. By the time the structure has reached
the vicinity of the trailing edge it is positioned
almost entirely above the upper surface. The complex
structure of the secondary flow at various intermediate
chordwise locations is caused by the local wing tip
geometry.

Figure 44 illustrates more effectively the
regions where "reversed" crossflow exists, i.e., regions
where the local crossflow direction opposes that of the
nominal outer flow pressure gradient. A line repre-
senting locations of zero upwash (i.e., z-velocity

component) is observed to lie almost parallel with the
free stream extending rearward from the leading edge
stagnation point. Measurements of its location are
shown more accurately in Figure 45 which is a picto-
gram showing the locations of significant upwash
parameters adjacent to the side of the tip. As noted
in these Figures, this "stagnation line" interesects
the upper surface location at the approximate point
of rollover.

It would seem useful to be able to ascertain
whether vorticity shed from the lower wing surface could
roll-over onto the upper surface. To estimate this
possibility consider a hypothetical slab, thickness
h, as shown in Figure 46. Assume the pressure to be
uniform adjacent to both surfaces having values P_u on
the upper surface and P_l on the lower surface. A
comparison of the characteristic times associated with
the lateral pressure gradient and the main convective
flow should provide an appropriate parameter for the
estimate. That is, consider--

$$N \equiv \frac{\tau_{lateral}}{\tau_{convective}} \qquad \text{(III-6)}$$

where

$\tau_{lateral}$--time required for a fluid "packet" to traverse
laterally from the lower to the upper surface (see
Figure 46)

$\tau_{convective}$—time associated with flow in the main-stream direction.

The latter quantity can be estimated immediately as—

$$\tau_{convective} = \frac{x}{U_o} \qquad (III-7)$$

To calculate the former term one requires that the flow proceed around the "tip" in a regular fashion. In fact, assume that it follows a semi-circular trajectory as viewed in the Trefftz plane (or in the absence of any main convective stream). With the radial pressure gradient balancing centripetal acceleration to allow this situation to occur, the momentum equation in the θ-direction can be written—

$$\frac{\partial p}{\partial r} = \rho \, \frac{U_\theta^2}{r} \qquad (III-8)$$

The average value of the lateral flow velocity over the assumed trajectory can be expressed as—

$$\bar{U}_\theta = \frac{\pi r}{\tau_{lateral}} = \frac{\pi h}{2\tau_{lateral}} \qquad (III-9)$$

The radial pressure gradient can be estimated—

$$\frac{\partial p}{\partial r} \cong \frac{\Delta p}{h} = \frac{P_l - P_u}{h} \qquad (III-10)$$

Then—

$$\tau_{lateral} \cong \pi h \sqrt{\frac{\rho}{2\Delta p}} \qquad (III-11)$$

and, further—

$$N = \frac{\pi h \, U_o}{x} \sqrt{\frac{\rho}{2\Delta p}} \qquad (III-12)$$

The presssure differential can be expressed in terms of a lift coefficient as follows:

$$\Delta p = \frac{L}{S} = \frac{1}{2} \rho U_o^2 C_L \qquad \text{(III-13)}$$

Hence,

$$N = \frac{\pi h}{x} \sqrt{\frac{1}{C_L}} \qquad \text{(III-14)}$$

The value for x must be selected and in this case should correspond to the length of the slab, c. If the resulting value of the parameter is much greater than unity rollover will not occur onto the upper surface. If the value is less than one it will occur upstream of the "trailing edge." If the value is near unity it should occur in the vicinity of the trailing edge.

The case of an actual wing is more complex, however, and is complicated by a spatially variable surface pressure distribution and an airfoil shape quite different from that of the hypothetical slab. The geometrical wing orientation also becomes an important factor. Nonetheless, if known experimental parameters are substituted into the above equation for the experimental configuration (data at $\alpha = 4°$, h/x = maximum thickness ratio) it is found that

$$N = 0.57,$$

a value that might be expected in view of the experi-
mental observations.

To account for airfoil geometry one would have
to determine the appropriate values for h, x and Δp.

As might be expected the flow surrounding this
region of concentrated vorticity is dominated by its
presence (induced velocity via Biot-Savart Law). The
streamlines in the outer region exhibit a much more
well-organized spiral character approaching a cylin-
drical geometry as viewed in the crossflow plane
(Region 6 of Figure 18).

The area denoted by Region 7 in that Figure is
one dominated equally by the concentrated tip vortex
structure and the influence of the inboard surface
boundary.

III.6. Streamline Pattern

Employing the crossflow and mainflow data
described above, the streamline pattern adjacent to both
the upper and lower wing surfaces was reconstructed.
These diagrams, assembled from planform velocity
vectors are shown in Figures 47 and 48.

Both diagrams appear to indicate shear in
certain locations. These are most obvious near the
tip on both surfaces and near the trailing edge on the
upper surface. No actual streamlines are drawn in the

immediate vicinity of the tip in Figure 47 due to the
swirling non-planar flow pattern which exists there.

In places where the streamlines actually enter
the displacement region the apparent "slippage" actually
represents shear, or vorticity production. In regions
where the streamlines lie wholly outside the boundary
layer, however, the apparent shearing is accompanied
by a variation of mainflow and downwash in the normal
coordinate direction yielding an irrotational gradient.

In contrast to the violent variations observed
in the tip region, the inboard flow exhibits very small
values for the crossflow angle. Streak photographs
taken of this flow sector (Figure 49) indicate almost
undetectably small angles. The sensitive quantitative
nature of the hot-wire anemometer does, however, detect
the distribution accurately even at these small angles.
Measurements at one inch in from the tip ($y/b = .083$)
reveal a maximum crossflow angle of only 6.4 degrees
(at $x/c = 0.80$) with the value dropping below one degree
at $y/b = 0.41$ for the same chordwise station.

CHAPTER IV

VORTICITY FIELD SURROUNDING

THE LIFTING WING

IV.1. The Concept of .ound
       Vorticity

The subject of bound vorticity was discussed
briefly in the introductory chapter (pp. 5-6). The
viability of this concept is not as unphysical as it
might first appear. If one regards the vorticity in
the wing boundary layer as being attached or "bound"
to the surface, the direct physical connection is
apparent. The points at which the bound vorticity and
free vorticity from the trailing sheet meet must then
be a region of vortex shedding. In lifting line theory
this occurs everywhere immediately downstream of and
perpendicular to the lifting line itself. In actual
flows the shedding will occur at any point where the
boundary layer separates, e.g., the trailing edge, the
wing tip, and any location on the wing where a separa-
ation line might exist.

The replacement of a complex wing having a
thick airfoil cross-section with a lifting line or
thin vortex sheet is found to yield integral results
(overall wing characteristics) in good agreement with

experiment. Only recently have complex numerical techniques provided suitable results with regard to the flow field details with discrepancies, however, still existing depending on the mathematical formulation employed. In this chapter, the detailed vorticity field around the lifting wing will be examined to ascertain the significance of various portions of the flow field.

IV.2. Measurements of Spatial Vorticity Content

Chapter II (pp. 20-24) alluded to the use of a hot-wire anemometry probe to measure circulation via the definition of circulation. A more complete discussion of this technique is found in Reference 41. While this reference discusses measurements in unbounded flows, the technique can be employed in the vicinity of solid boundaries as well.

Consider a contour, c, in close proximity to the cross-section of a lifting wing as shown in Figure 50. Furthermore, let the y-direction segments of the contour lie completely outside the upper and lower surface boundary layers. The circulation about region A can be expressed--

$$\Gamma_A = \oint \vec{U} \cdot d\vec{l} = \int_{-h/2}^{h/2} [U_z(y+\Delta y, z') - U_z(y, z')] \, dz'$$

$$+ \int_y^{y+\Delta y} [U_y(y', -h/2) - U_y(y', h/2)] \, dy' \qquad \text{(IV-1)}$$

From Stoke's theorem this integral is also related to the vorticity as follows:

$$\Gamma_A = \iint_A \vec{\xi} \cdot d\vec{A} = \int_{-h/2}^{h/2} \int_y^{y+\Delta y} \xi_x \, dy' \, dz' \qquad \text{(IV-2)}$$

By equating these expressions and taking the limit as Δy approaches zero, the following expression is obtained--

$$\int_{-h/2}^{h/2} \xi_x \, dz' = \Delta U_y(y) \qquad \text{(IV-3)}$$

where

$$\Delta U_y(y) = U_y(y, -h/2) - U_y(y, h/2)$$

Expressed in terms of an average in the z-direction--

$$\bar{\xi}_x(y; n) = \frac{1}{h} \Delta U_y(y) \qquad \text{(IV-4)}$$

Hence, a direct relationship between the boundary layer (or "bound") vorticity and the surface crossflow differential has been established. If the wing and boundary layer thicknesses are negligibly thin ($h \to o$, a vortex sheet), the crossflow differential defines the strength of the sheet. A more complex derivation can be found in Karamcheti,[47] pp. 530-531. The reasons for the

selection of a thin wing with a small displacement region are thus apparent. A graph of ΔU_y as a function will then give the shape of the vorticity distribution when $\Delta z = h$ is kept constant along the span.

The utilization of this technique to measure vorticity close to the surface should then give accurate results over the inboard portions of the wing. In this region the streamlines closely follow the surface curvature and the downwash distribution, W, is found to be independent of the y-coordinate. The outer flow which exhibits a crossflow component independent of z (see Chapter III) provides a suitable range of adjustment for the value of h. The applicability of this analysis is, so far as the vorticity distribution is concerned, predicated on the assumption that the wing plus boundary layer regions exhibit a sheet-like structure of vorticity with finite thickness, h = $o(t + \delta_u + \delta_l)$.

As noted in Chapter III and in later sections, the flow in the vicinity of the tip does not behave in this manner and in fact precludes the applicability of the traditional concept of a vortex sheet. The steep swirling gradients in velocity greatly enlarge the error in X-wire data due to out-of-planeness of the flow. A more extensive examination of the flow field in this region is therefore required.

If one considers a contour extending from $y = -\infty$ to some value of y inboard of the tip and to the left of the wing centerline (as shown in Figure 51, contour B), the circulation about this closed curve can be expressed through an extension of equation (IV-1) as follows:

$$\Gamma(y) = \Gamma_{tip} + \int_{y_o}^{y} \Delta U_y (c,y') \, dy' \tag{IV-5}$$

then

$$\frac{\partial \Gamma(y)}{\partial y} = \Delta U_y (c,y) \tag{IV-6}$$

where c denotes the chordwise location of the contour, in this case at the trailing edge. These equations are applicable over the inboard region of the wing surface. Γ_{tip} represents the overall tip circulation in that region where high rotational gradients are present.

An additional relationship can be established by considering both contours in Figure 51. The one labelled "A" is taken to completely encompass all of the bound vorticity in a direction parallel to the local section. The resultant circulation about this contour will be labeled Γ_A. Similarly, contour "B" as explained above possesses circulation Γ_B. Conservation of vorticity requires that all of the bound vortex lines passing through the capping surface of "A" also pass through "B" if it extends far enough in the

outboard spanwise direction (-y). Separation is assumed to occur only at the wing trailing edge or adjacent to the side of the wing tip. Then--

$$\Gamma_A = \Gamma_B \qquad (IV-7)$$

If it is further assumed that the wing is uniformly thin and at a small angle of attack, the following approximation can be written--

$$\Gamma_A(y) \cong \int_0^c \Delta U_x(x',y)dx' + I_{stag}(y) + I_{vis}(y) \qquad (IV-8)$$

where I_{stag} represents the contribution to the overall contour integral in the vicinity of the leading edge (stagnation line) and I_{vis} relates the contribution due to the viscous wake near the trailing edge. The validity of this expression as it relates to lift will be considered in a later section. Comparing equations (IV-5), (IV-7) and (IV-8), the following is noted--

$$\Gamma_{tip} + \int_{y_0}^y \Delta U_y(c,y')dy' = \int_0^c \Delta U_x(x',y)dx'$$
$$+ I_{stag}(y) + I_{vis}(y) \qquad (IV-9)$$

This establishes a relationship between the crossflow differential and mainflow differential velocity fields. The equivalence of the Γ_A (at wing centerline) and Γ_B (for the entire semi-span) contours was first experimentally verified by Fage and Simmons[48] in 1925.

IV.3. Velocity, Vorticity, Circulation and Pressure Fields

A relationship between the crossflow velocity differential, "bound" vorticity, and circulation was established in the preceding section. These quantities are, in turn, related to the pressure field and, hence, the section and overall lift coefficients.

If the Kutta-Joukowski condition is imposed on the velocity at the sharp trailing edge, the lift per unit span is known to be $\rho U_o \Gamma$, where Γ is the circulation around a circuit encompassing the wing chord and boundary layer and parallel to the free stream. The selection of this contour in an actual viscous flow is sensitive to a number of parameters, most importantly the selection of the region of intersection of the contour with the wake. Thwaites,[49] pp. 192-194, indicates that the error in the selection of this location is negligible providing the wing lift-drag ratio is large. This connection between contour integrals in fully potential flow and actual viscous flow was actually first discussed by G. I. Taylor in a note to Reference 50.

If this is the case, the section lift coefficient can be computed as--

$$c_1(y) = \frac{2 \, \Gamma_A(y)}{U_o c} \qquad\qquad (IV-10)$$

The above is essentially the same expression employed for estimating the lift of the entire wing as outlined in Chapter III. In that case $\Gamma(y)$ was replaced by Γ_o. The wing lift coefficient, however, is not given by the above expression but is obviously dependent on the nature of the Γ-distribution. Figure 52 depicts more accurately the actual physical situation. As bound vorticity is shed at the trailing edge the section lift coefficient decreases toward the wing tip.

The resulting value for the parameter can then be expressed as--

$$C_L = \bar{c}_l = \frac{1}{b} \int_0^b c_l \, dy \qquad \text{(IV-11)}$$

then--

$$C_L = \frac{2}{U_o c} \cdot \frac{1}{b} \int_0^b \Gamma_A(y) \, dy = \frac{2}{U_o c} \, \overline{\Gamma_A(y)} \qquad \text{(IV-12)}$$

The error involved in assuming a flat-rectangular distribution and say, an elliptic lift distribution is $(1 - \pi/4)$ or about 21%. The error involved in the selection of the optimum lift-drag ratio angle of attack using the incorrect lift estimate is discussed in the Appendix.

The expression for the lift coefficient can then be written--

$$C_L = \frac{2}{U_o b c} \left\{ \int_0^b \int_0^c \Delta U_x(x',y')dx'dy' + \int_0^b I_{stag}(y')dy' \right.$$

$$\left. + \int_0^b I_{vis}(y')dy' \right\} \tag{IV-13}$$

The corresponding expression substituting Γ_B as given by equation (IV-9) is not properly posed since the distribution of vorticity near the tip is expressed as a single integral term, Γ_{tip}.

A general expression involving the "B"-type contours can, however, be developed by considering a more general form of these contours. Consider the two general circuits shown in Figure 53. These contours do not intersect at the trailing edge but at some point (x,y). Again, they are assumed to encompass the entire displacement region. Again, the net vorticity passing through capping surface "A" is equivalent to that of "B". This is true at least for the case where the lift distribution is decreasing monotonically toward the tip (see Figure 52). Then, employing previous results--

$$\Gamma(x,y) = \int_0^x \Delta U_x(x',y)dx' + I_{stag}(x,y) + I_{AB}(x,y)$$

$$= \Gamma_{tip}(x,y_o) + \int_{y_o}^y \Delta U_y(x,y')dy' + I_{AB}(x,y) \tag{IV-14}$$

which holds for points over the inboard region on the wing. The term, I_{AB}, represents a contribution to the

contour integral from the downwash at point (x,y) where the contours intersect.

The lift coefficient can be established by considering that group of "B"-contours which extend all the way to the wing centerline, $y = b$. Realizing that equation (IV-12) merely expresses the lift coefficient as an average value of the circulation over the wing surface, an equivalent expression can be written--

$$C_L = \frac{2}{U_o b\,c} \int_o^c \Gamma_B\,(x')\,dx' \qquad \text{(IV-15)}$$

Then--

$$C_L = \frac{2}{U_o b\,c} \left\{ \int_o^c \int_{y_o}^y \Delta U_y (x',y')\,dy'\,dx' + \int_o^c \Gamma_{tip}(x',y_o)\,dx' \right.$$

$$\left. + \int_o^c I_{AB}(x',b)\,dx' \right\} \qquad \text{(IV-16)}$$

Comparing equations (IV-12) and (IV-15), one finds--

$$C_L = \frac{2}{U_o b} \,\overline{\Gamma_B(x)} = \frac{2}{U_o c} \,\overline{\Gamma_A(y)} \qquad \text{(IV-17)}$$

where the averages refer to the spatial coordinates.

Since the lift is simply the surface integral of the pressure distribution, it is found that--

$$\int_o^c \Gamma_B(x')\,dx' = \int_o^b \Gamma_A(y')\,dy'$$

$$= \frac{1}{\rho U_o} \int_o^c \int_o^b \Delta p(x',y')\,dy'\,dx' \qquad \text{(IV-18)}$$

If two contours a distance Δy apart are considered (see Figure 54), the net lift on the enclosed strip can be computed—

$$\Delta L = \int_y^{y+\Delta y} \rho U_0 \, \Gamma_A(y')dy' \qquad (IV-19)$$

and—

$$\Delta L = \int_y^{y+\Delta y} \int_0^c \Delta p(x',y')dx'dy' \qquad (IV-20)$$

One can then deduce—

$$\Gamma_A(y) = \frac{1}{\rho U_0} \int_0^c \Delta p(x',y)dx' = \Gamma_B(c,y) \qquad (IV-21)$$

Similarly, it is also found that—

$$\Gamma_B(x) = \frac{1}{\rho U_0} \int_0^b \Delta p(x,y')dy' \qquad (IV-22)$$

The above relationships (with the exception of equation (IV-21)) are not strictly valid due to the breakdown of the concept of the sheet near the tip. They do, however, provide a good approximation which relates the velocity (circulation) and pressure fields in an integral fashion.

Lastly the crossflow at the trailing edge over the inboard region can be related to the pressure field through equations (IV-6) and (IV-21)—

$$\Delta U_y(c,y) = \frac{1}{\rho U_0} \frac{\partial}{\partial y} \int_0^c \Delta p(x',y)dx' \qquad (IV-23)$$

IV.4. Bound Vorticity in the
Inboard Region

The surface crossflow differential distribution
respresenting the x-component of bound vorticity over
the inboard portion of the wing is presented graphically
in Figures 55-57. Spanwise profiles are shown for 10%
chord intervals along the surface.

Values of the crossflow velocity component have
been rendered non-dimensional through division by the
free stream velocity. The resulting parameter can be
shown to be independent of the free stream value at the
trailing edge, i.e.,

$$\frac{\Delta U_y(c,y)}{U_o} = \frac{c}{2} \frac{dc_1(y)}{dy} \tag{IV-24}$$

This result follows from the equations discussed above.

The parameter, h, from equation (IV-4) has been
adjusted to correspond with the maximum observed value--

$$h = (t + \delta_u + \delta_1)_{max} \tag{IV-25}$$

The experimentally determined value was found to be 0.72
inches or h/c = 0.09.

Examination of the Figures shows that the net
value of the crossflow reverses polarity well inboard
of the tip, but not at the tunnel wall as one would hope.
As indicated in the preceding chapter this is probably
the effect of the tunnel wall boundary layer on the
outer flow. More explicitly, it is the result of the

interaction of the tunnel wall boundary layer with the wall-bound tip vortex. Had the wall boundary layer been negligibly thin one might have expected this vortex to be "suppressed" with respect to the external flow. In this case, however, the tunnel wall boundary layer thickness is appreciable (nearly two inches) so that the complex interaction may well influence the outer flow.

A more comprehensive picture of this portion of the flow field can be obtained from Figure 58 which is a planform map of the crossflow differential distribution. It can be seen that the actual effect of the crossflow direction reversal is to reduce the effective aspect ratio, though in a highly irregular manner.

Experimentally determined values of the differential can be compared with theory through the use of the circulation function and equation (IV-6) which is restated below in more general form--

$$\Delta U_y(x,y) = \frac{\partial}{\partial x} [\Gamma(x,y)] \qquad \text{(IV-26)}$$

In the case of lifting line theory, the elliptic lift distribution gives rise to a trailing edge value of the crossflow differential which is--

$$\Delta U_y(c,y)_{elliptic} = \frac{\Gamma_o (b-y)}{b\sqrt{2by-y^2}} \qquad \text{(IV-27)}$$

If the Schrenk approximation is employed, the corres-
ponding prediction for a rectangular wing becomes--

$$\Delta U_y(c,y)_{Schrenk} = \frac{\Gamma_o(b-y)}{2b\sqrt{2by-y^2}} \qquad (IV-28)$$

exactly half the above value. Other values can also
be predicted provided that the circulation function
is known.

These "predicted" values are compared with
measured data at the trailing edge in Figure 59. Two
predictions are shown for the Schrenk approximation.
The solid line represents the value for a wing having
a twelve inch semi-span which is expected on the basis
of the experimental wing geometry. The other curve is
determined for a wing of 8.5 inch semi-span which
corresponds to the location where the crossflow differ-
ential reverses at the trailing edge. The elliptic
prediction (dashed line) is determined only for the
latter case.

Actual values are shown to lie between those
predicted by the Schrenk and elliptic distributions,
erring by as much as 40%. That the experimental data
generate a curve closely resembling that of the predic-
tors (in shape) is shown in Figure 60. Here the cross-
flow is non-dimensionalized through division by the
value at one-inch inboard of the tip (y/b = .083).

Hence the approximate curve shape is correctly estab-
lished.

The use of the crossflow difference as a basis
of comparison provides a more sensitive indicator as to
the detailed nature of the bound vorticity than the
more commonly employed circulation (or lift) distribu-
tion.

An additional question to be addressed by these
results concerns the nature of the circulation function
and the possibilities of a spatially separable solution.
That is, can one express--

$$\Gamma(x,y) = A(x)\ B(y) \qquad\qquad (IV\text{-}29)$$

Since many analyses deal with the span load distribu-
tion exclusively, one might ask whether it is reason-
able to decouple the chordwise dependence in achieving
such a solution. If this is, in fact, the case, then--

$$\frac{\Delta U_y(x,y)}{\Delta U_y(c,y)} = \frac{A(x)}{A(c)} \qquad\qquad (IV\text{-}30)$$

which is a function of x-only.

Experimentally determined values of this function
are shown in Figure 61 for several different spanwise
locations. The parameter appears to be much more
dependent on "x" than span though its y-dependence is
apparently not negligible on the basis of these results.
Equation (IV-29) might be more appropriately written as--

$$\Gamma(x,y) = A(x,y)\ B(y) \qquad\qquad (IV\text{-}31)$$

IV.5. Vorticity Content in the Tip Region

The presence of large rotational gradients and the complex distribution of concentrated vorticity in the tip region prohibit the application of the simple measurement technique described above. A more comprehensive description of spatial vorticity content was therefore obtained through the use of rectangular contours in the Trefftz plane near the wing tip.

A series of these contours forming a rectangular mesh was constructed about the tip and measurements were made of the crossflow velocity component tangent to the local path direction. Integration of the velocity field about the respective paths then yielded the circulation.

Figures 62-68 show the results of these measurements for the test condition. Data were obtained in chordwise increments of 10% from the leading edge to the trailing edge. The overall contour size was determined by the amount of spanwise distance influenced by the "rolled-up" portion of vorticity as well as the spatial extent of that vorticity. The distribution and sizes of the measurement cells were based on an attempt to minimize the effects of an out-of-plane flow component on the "X"-wire probe. The streamline

reconstruction technique and results discussed in Chapter III were used in making this determination.

A comparison of Figures 62-68 and corresponding Figures 38-43 indicates that the regions of secondary swirl adjacent to the surface do, in fact, exhibit high concentrations of vorticity. Additional traverses in this area indicated that the outer edges of the swirl zones roughly correspond to the boundary of the vorticity bearing regions as one would expect. (A similar correlation was established for the inboard regions of the wing with the additional correspondence between the "vorticity layer" and the boundary layer turbulence envelope.)

The production of vorticity (x-component) is observed to begin almost at the leading edge and predominantly on the lower wing surface. The concentration of vorticity there exceeds that adjacent to the opposing surface from the leading edge downstream to the 40% chord point. From there aft the opposite ratio is observed. Figure 69 depicts this ratio as a function of chordwise location for spanwise regions extending from the tip to one half and one inch inboard, respectively. The ratio, $\Gamma_{upper}/\Gamma_{lower}$, is observed to be independent of the spanwise location forward of the 60% chord location. The deviation of the two curves

downstream of this point is probably due to the "roll-over" of free vorticity onto the upper surface and its interaction with the surface boundary layer. This inter-action is discussed more extensively in a later section.

The shedding of vorticity into the region oppo-site to the side of the tip is also observed to occur close to the leading edge. The significance of the vorticity content in this area is shown in Figure 70 which depicts the percentage of circulation associated with this region compared to the overall wing value as a function of the chordwise location. The amount is observed to increase steadily from the leading edge to the 40% chord point and thereafter remain constant to the trailing edge. This observation does not imply a sudden discontinuance of the shedding process but rather that a kind of equilibrium has been established. That is, the vorticity which is shed into the side region is equal in amount to that rolling over onto the upper surface and out of this region.

A graphic illustration of the comparative amount of shed vorticity is given in Figure 71 which shows the ratio of circulation in the tip region to the local chordwise value for the entire wing $(\Gamma_B(x,o)/\Gamma_B(x,b))$ again as a function of chordwise location. The resulting relation reflects a comparison of shed vorticity to that

being produced over the surface. The curve is seen to be relatively flat, decreasing only slightly toward the trailing edge. This indicates that the amount of vorticity shed into the side region nearly keeps pace with the local production.

IV.6. Effects of Tip-Shed Vorticity

Vorticity shed from the lower wing surface into the region outboard of the tip has been observed to roll up as it moves downstream and spill over onto the upper surface. The movement of this aggregate of vorticity is expected due to the influence of the nominal pressure field near the tip. While it lies adjacent to the tip this vorticity augments the upper and lower surface flows through a "Biot-Savart" kind of influence. In the region where it has rolled over onto the upper surface, however, a more direct viscous interaction with the conventional boundary layer is responsible for local deviations in the expected wing properties.

Early experimentalists discovered that the section lift coefficient near the tip of a wing could deviate markedly from the theoretically predicted value depending on the planform shape of the tip and the wing's orientation. The case of a rectangular wing is illustrated in Robinson, et al.,[51] p. 460, Figure

15 for various aspect ratios. This graph is reproduced

here as Figure 72 and shows a significant increment in

the lift near the wing tip. Pearson[52] was the first

to formulate an empirical correction to theory to account

for this deviation. When the results of these early

pressure measurements are compared with the flow "pic-

ture" established earlier, a possible explanation for

the discrepancy surfaces. The high velocity rotating

flow above the upper surface causes a reduction in the

local pressure coefficient which, in turn, gives rise

to an incremental increase in the value of the section

lift. This hypothesis is supported by measurements of

section pitching moment which predict a more negative

value than expected in this region and a corresponding

chordwise shift in the center of pressure toward the

trailing edge.[52]

Actually, this result may be viewed as some-

thing of a limiting case of the "delta" wing which

experiences leading edge separation. In that case, the

resulting vortex passes over a major portion of the

upper surface and augments the pressure field through-

out (see Thwaites,[49] pp. 511-517). The comparison

would be much closer except for the fact that the tip

thickness distribution controls the rollover location

in conjunction with the wing orientation.

Unlike the case of the delta wing with separated flow, the vorticity which rolls over at low angles of attack is not physically displaced from the upper surface. Delta wing leading edge separation occurs predominantly at high angles of attack and the resulting vortices influence the surface conditions through their induced field. In this case, however, the close proximity of the "free" vorticity and that of the boundary layer results in a complex interaction which is not easily formulated due to the non-neglectable influence of viscosity. It is this interaction which actually prohibits the application of the concept of vortex sheet when modeling this region.

While many investigators have sought to eliminate the "tip singularity" through mathematical manipulation and, in some cases, judicious choice of the tip shape,[33] few have attempted to face the problem on physical grounds and grapple with its restrictions. Recently, numerical analysts[5,32,53] have succeeded in verifying that rollup does, in fact, occur adjacent to the tip. Their results, however, do not illustrate the "rollover" phenomenon since the wing is modeled by an infinitesimally thin sheet of vorticity consisting of a small and finite number of bound filaments. In all cases, the application of the sheet concept is extended

over the entire wing surface including the tip itself.
In these methods, regions of shedding are determined
a priori by the investigator. The results in situ-
ations which simulate actual flows where rollover can
be observed must be viewed with some skepticism.

A primary question, then, concerns the predic-
tion of shedding in the tip region and the likelihood
of rollover given a particular tip shape, specifically
the planform characteristics. If one considers an
"almost"* rectangular wing having possible tip shapes
shown in Figure 73, qualitative statements can be made
regarding the nature of the flow in that region. Figure
73a illustrates a possible situation where, under cer-
tain conditions, shedding will occur over the entire
extent of the tip but rollover will not occur due to
the inability of the pressure gradient to force the
shed filaments over onto the upper surface. In Figure
73b, shedding itself might not exist at the tip due
to the inability of the spanwise pressure gradient to
create a "y"-velocity component large enough. (At
high angles of attack, however, separation may occur
over the tip.) The former case has been numerically
verified by Rehbach[54] for a slightly swept configur-
ation.

---

*The angle, Λ, is kept small enough so as not
to effect the nominal rectangular wing load character-
istics.

If the model of the rectangular slab employed in Chapter III (Figure 46) is recalled, the velocity around the semicircular secondary flow was found to be--

$$U_\theta = \left(\frac{\Delta p}{2\rho}\right)^{1/2} \qquad (IV-32)$$

This implies that the crossflow velocities at the tip on the upper and lower surfaces are given as--

$$U_y(h/2) = - U_y(-h/2) = \sqrt{\frac{\Delta p}{2\rho}}. \qquad (IV-33)$$

Now, one considers the case of a hypothetical, thin slab-wing at negligibly low angle of attack and having spatially uniform upper and lower surface pressures, P_u and P_1, respectively. Then, since

$$L = \int \Delta p \; dS = \Delta p \cdot S = (P_1 - P_u) \cdot S \qquad (IV-34)$$

it is readily observed that

$$U_y(h/2) = - U_y(-h/2) = \frac{U_o}{2} \sqrt{C_L} \qquad (IV-35)$$

which is independent of the slab thickness and overall surface area. For shedding to occur (case "b"), the angle, Λ, must not exceed the following value--

$$\Lambda \geq \tan^{-1} \frac{U_y}{U_o} = \tan^{-1} \frac{\sqrt{C_L}}{2} \qquad (IV-36)$$

Since only small angles have been considered, this becomes--

$$\Lambda \geq \frac{\sqrt{C_L}}{2} \qquad (IV-37)$$

The opposite situation is true for rollover (case "a").
The tip offset angle must be greater than the critical
value (Equation IV-37) for rollover to be prevented.
An additional restriction which surfaces is that of low
to moderate values of angle of attack so that the required
angle, Λ, does not get too large invalidating the
original assumption.

If the restriction on a "uniform" pressure
field is relaxed, then

$$\Lambda_{critical} = \tan^{-1} \frac{1}{U_o} \sqrt{\frac{\Delta p(x,o)}{2\rho}} \qquad \text{(IV-38)}$$

If only case "a" is considered (prediction of shedding)
and rollover is neglected, the pressure field at the
tip can be written as a function of the centerline
pressure. Then--

$$\Lambda_{critical} = \tan^{-1} \frac{1}{U_o} \sqrt{\frac{K(b) \ \Delta p(x,b)}{2\rho}} \qquad \text{(IV-39)}$$

or

$$\Lambda_{critical} = \tan^{-1} \sqrt{\frac{K(b) \ \Delta p(x,b)}{4 \ Q_o}} \qquad \text{(IV-40)}$$

Lastly, the case of an actual airfoil profile
is employed as shown in Figure 74. In this case, it is
readily shown that--

$$U_y(-h/2) \cong - \sqrt{\frac{h(x)}{2\rho} \ \frac{\Delta p(x,o)}{t(x)}} \qquad \text{(IV-41)}$$

where h is the local secondary flow (swirl) diameter
as given in Chapter III. Then,

$$\Lambda_{critical} = \tan^{-1} \sqrt{\frac{h(x)}{t(x)} \; \frac{K(b) \cdot \Lambda p(x,b)}{4 \; Q_o}} \qquad (IV-42)$$

for the case where rollover does not influence the
pressure field.

One can then qualitatively see that, for a more
complex planform like the semi-circular tip shown in
Figure 75, both shedding and rollover can occur to
varying degrees at various locations along the side of
the tip, depending on the airfoil shape and wing orien-
tation.

IV.7. Overall Wing Vorticity
       Distribution

The quantitative descriptions presented in the
preceding sections can be combined to yield the total
distribution of vorticity surrounding the wing. Figure
76 shows the resulting circulation profiles at various
chordwise locations compiled from these data. These
profiles were generated with equation (IV-5).

All vorticity adjacent to the wing is included
in this "running sum" description including the rolled-
up region discussed above. Care must, therefore, be
exercised in attempting to relate these data to the
surface pressure differential in the tip zone. The

absence of detail in this region (in the Figure) is intentional due to the ineffectiveness of the experimental technique to correctly predict the distribution there.

Figure 77 is a replot of the same data but referenced to the local chordwise maximum, $\Gamma_B(x,b)_{max}$. The distinctive similarity in these profiles indicates a corresponding similarity in the various chordwise values of the spanwise pressure gradient. The deviation near the leading edge reflects a corresponding non-uniformity in the pressure differential function but is also due in part to measurement error. Large curvature and radial streamline gradients in this region made it virtually impossible to eliminate flow "out-of-planeness" errors.

Figure 70, referred to in an earlier section, illustrates the comparative influence of various spanwise regions on overall vorticity content. Two sets of data points are employed to display overall wing vorticity development in the chordwise direction, both reflecting different values of the "reference" circulation. In one case the trailing edge value, Γ_o, was employed while in the other the maximum observed value (which occurred at $x/c = 0.80$) was used.

It is of interest that over half of the vorticity directed along the x-axis lies within one inch

(y/b = .083) of the wing. A significant portion also
appears as shed vorticity adjacent to the tip. No
attempt has been made to fit a curve through these
points due to the complex and unknown nature of the
chordwise lift variation, $P(x) \equiv \int_{o}^{b} \Delta p(x,y)dy$. For
comparison, however, the distribution predicted for a
two-dimensional flat plate is also shown. A deriva-
tion of this distribution may be found in Thwaites,[49]
p. 299.

The vorticity content of the various spanwise
segments exhibits a different form if referenced to a
"local" maximum. Figure 78 illustrates this fact with
several representative graphs of $\Gamma_B(x,y)/\Gamma_B(c,y)$ versus
chordwise location for several values of span. The
vorticity content in various regions is observed to be
nearly constant along the chord. This might indicate
that the comparable growth or production of vorticity
does not vary significantly with chordwise position
at least for the inboard reaches of the wing.

The above data can be presented in a more
comprehensive way and one more familiar · to proponents
of the various lifting wing theories. One considers
a situation involving two contours, A_1 and B_2, to the
left of the wing centerline (as shown in Figure 79)
which terminate at points (x_1,y_1) and (x_2,y_2), ·

respectively. Assuming that both contours yield the
same value of the circulation, then the net number of
equal strength vortex filaments passing through A_1
must also pass through B_2. Since Γ_{A_1} and Γ_{B_2} are
equivalent, then

$$\Gamma_{B_1} = \Gamma_{B_2} \tag{IV-43}$$

and the net numbers of filaments intersecting the
capping surfaces of B_1 and B_2 are equal. By connecting
surface points exhibiting equal values of $\Gamma_B(x,y)$,
families of curves are obtained which represent lines
of constant vorticity, or the traditional "bound vor-
tex lines." It must be emphasized that this description
is only valid where the sheet concept can be applied,
i.e., interior to the interactive flow region near the
tip.

Figure 80 is a planform map of the bound vortex
lines developed for the wing at four degrees angle of
attack. The interpretation of the contours is given in non-
dimensional form for more universal applicability as will be
discussed in the following chapter. An apparent dis-
crepancy indicated by the map concerns the inboard
movement of some of the vortex lines near the trailing
edge. This tendency, though not governed by the external
flow while the vorticity is "bound," seems to oppose
the motion at the trailing edge which indicates that the

net crossflow, $U_{y_{upper}} + U_{y_{lower}}$, is outward (-y

direction). The most probable explanation for this

difficulty is simply error in the detailed velocity

measurements. Since the measurement of the circula-

tion profiles is cumulative, i.e., $\Gamma_B(x,y_o)$ is depen-

dent on the flow in the entire region $o < y < y_o$, any small

errors in the velocity measurements are carried over

and magnified through the computation of the circula-

tion. If, in fact, these lines actually do tend

toward the wing center line, possible explanations

would have to include the lower surface separation at

the trailing edge and the influence of the tunnel wall

boundary layer as discussed above.

Another question which arises in light of the

above results is that of an equivalent scheme employing

the "A"-type contours alluded to earlier. Figure 81

depicts such a contour enveloping a wing section.

Measurements were made along the surface

employing these contours (see equation (IV-8)) in an

attempt to reconcile the two methods of measurement.

The paths were selected so that all bound vorticity was

completely enveloped and the vertical path segment near

the trailing edge (x/c = 1.05) was perpendicular to the

free stream. Selection of this wake portion of the

contour was based on considerations discussed in

Thwaites,[49] pp. 192-194, and reviewed briefly in
Section IV.2.

Measurements of the locally parallel component
of the mainflow were made in the inboard region with a
representation sample of the results shown in Figure
82. Graphs of the resulting differential function
have the form shown in Figure 83. Visual inspection
of these curves reveals that a large fraction of the
vorticity resides within one inch of the wing tip.

The largest source of error accompanying these
measurements was that in the velocity data near the
leading edge. The presence of the stagnation point
and uncertainties in flow direction created difficul-
ties in obtaining reliable results in this region.

The chordwise variation in vorticity content
is obtained through the application of equation (IV-14).
The contribution, $I_{AB}(x,y)$, was not measured except aft
of the trailing edge so all profiles must be viewed only
in a comparative light. Figure 84 illustrates this data
when nondimensionalized by local spanwise maximum values.
Again, the predicted two-dimensional flat plate distribu-
tion is presented for comparison. Except for the
curve representing $y = 0.5$ inches ($y/b = .042$), the
similarity in curve shape is remarkable. This evidence
strongly supports the contentions regarding the

similarity in the pressure differential function and
vorticity production made above. Specifically, the
observations of Figures 70 and 84 indicate that--

$$\frac{\Gamma_B(x,y)}{\Gamma_B(x,b)} = F(y) \text{ only} \tag{IV-44}$$

and

$$\frac{\Gamma_A(x,y)}{\Gamma_A(c,y)} = G(x) \text{ only} \tag{IV-45}$$

Expanding the upper relation gives

$$\Gamma_{tip}(x) + \int_{y_o}^{y} \Delta U_y(x,y')dy' = F(y) \{\Gamma_{tip}(x)$$
$$+ \int_{y_o}^{b} \Delta U_y(x,y')dy' \} \tag{IV-46}$$

Differentiation with respect to y indicates--

$$\Delta U_y(x,y) = F'(y) \int_{y_o}^{b} \Delta U_y(x,y')dy' \tag{IV-47}$$

The remaining integral is a function of x only, so
that--

$$\Delta U_y(x,y) = F'(y) R(x) \tag{IV-48}$$

Similar treatment of the second relationship reveals--

$$\Delta U_x(x,y) = G'(x) H(y) \tag{IV-49}$$

In both cases, the flow velocity differentials are
separable functions of the spatial coordinates. It
must be emphasized that these relationships are valid
only where curve similarity is observed, e.g.,

inboard of the tip and downstream of the leading
edge.

These observations provide further support for
the relationship posed by equation (IV-29) over a large
portion of the surface.   )

A comparison of the measurements applied to the
two types of integrals is shown in Figure 85.   The
functions $\Gamma_A(x,b)$ and $\Gamma_B(c,y)$ are shown to be in close
agreement.   Also depicted are the distributions obtained
by DeYoung and Harper[55]--modified lifting line theory,
the Schrenk approximation[56] and an elliptical lift
distribution.   Several data points obtained in early
measurements of the surface pressure differential are
also shown.

The pressure data and circulation measurements
are seen to agree in all but the immediate vicinity
of the tip, as expected.   Only the Schrenk approxima-
tion appears to adequately approximate the correct
behavior of the vorticity distribution.   Again, however,
large errors persist in the tip zone.

CHAPTER V

FLOWFIELD DOWNSTREAM OF THE WING

V.1. Measurements in the Near Wake

In addition to the investigation of the flow
field surrounding the wing, measurements were made in
the "near wake" region to determine its physical pro-
perties.

Velocity field data were obtained to a maximum
of 5 chord lengths downstream of the trailing edge,
specifically, at downstream locations of $x/c = 1.0$
(trailing edge), 2.0, 4.0 and 6.0. The wing angle of
attack was also varied to values of 4, 6 and 8 degrees,
all representing conditions of largely unseparated flow
over the wing surface. The total wind tunnel test
section length was responsible for limiting the maximum
downstream measurement location.

The contour integration techniques discussed
in preceding chapters were employed to obtain the
spatial vorticity distribution in the wake region.
Trefftz plane contours like that of Figure 86 were
employed for the surveys. The z-coordinate levels
(horizontal path elements) were selected to entirely
encompass the identifiable turbulent portions of the

wake, as well as the central vortex core. Hence, all wing generated vorticity was contained within the contour bounds.

Measurements of the wake shape (turbulent edges and mainflow profiles) were also obtained in an effort to identify the physical shape of the vorticity package.

NACA and other experimental data were employed for purposes of comparison, where possible.

V.2. Trailing Edge Vorticity Distribution

Crossflow velocity differential measurements were made at the trailing edge ($x/c = 1.0$) at the three test angles-of-attack. These data were obtained outside of the surface displacement regions but in the quasi-two-dimensional inboard region discussed in preceding chapters. Additional data were obtained which verify the distinctive properties of this region for all values of α employed.

The inboard vorticity distribution is shown in Figure 87. Again, non-dimensionalization of the cross-flow parameter is accomplished with the undisturbed mainflow velocity. The curve shapes show a marked similarity indicating similar local flow characteristics.

This similarity is even more graphically illustrated via the circulation function, as shown in Figure

88. Shown as distributions with respect to spanwise locations, these curves offer the additional feature of including the contribution of the tip increment to the overall vorticity sum. The data strongly support the contention that the wing flow field characteristics are independent of the angle-of-attack, at least over the inboard region. The unseparated nature of the surface flows is probably the key to this relationship.

Care must be exercised in inferring the similarity of the resulting pressure distributions, however, especially in the vicinity of the wingtip. Though an extensive survey of the surface flow was not made at all values of α, reasoning presented in earlier chapters indicates that vortex "spillover" onto the upper surface should occur farther upstream with increasing angles of attack. This would imply a higher value for the tip lift increment (due to interaction with the surface boundary layer) and a probable variation in the section center of pressure.

The inboard flow field, being independent of α, should then be expected to exhibit the appropriately non-dimensionalized characteristics of the test case discussed in preceding chapters. Therefore, the flow "picture" presented in Figure 80 is valid for other values of α for which the inboard flow is unseparated.

Only the interactive tip zone characteristics should
be expected to exhibit local variations.

V.3. Wing Lift Characteristics

Values of the overall wing lift coefficient
were computed from the data described above and compared
with each other as well as other theoretical and experi-
mental data. The calculation employed equation (IV-16)
and circulation data obtained aft of the trailing edge
which will be discussed below.

Since a direct comparison with theory and
other data was desired, the raw experimental data had
to be corrected for various wind tunnel effects. Theo-
retical and empirical corrections for solid blockage
(of both wing and traversing mechanism) and lift effect
were utilized. A complete discussion of these and other
wind tunnel interference effects can be found in Pank-
hurst and Holder,[57] pp. 328-364. The effect of solid
blockage was found to be negligible at the measurement
conditions due largely to the small projected cross-
section at these low angles of attack. The correction
for lift effect, however, was more significant resulting in
an effective increase in angle of attack of approximately
0.5 degrees.

The various curves of wing lift coefficient
versus angle-of-attack are displayed in Figure 89.

Linear curve fits were employed for the experimental
data due to the unseparated nature of the flow in this
case.

Data are presented which illustrate the error
incurred from the use of the "1/r" assumption for the
vortex behavior in the near field (see section III.1).
These measurements, corrected for the approximate load
distribution, predict a lower value for C_L than any of
the theoretical schemes or the contour integral data.

Lifting surface theory, here due to Multhopp,[58]
is observed to predict the lift curve slope with more
accuracy than the lifting line theory as would be
expected.

Numerical results obtained by Rom, et al.,[53]
using the iterative numerical technique discussed in
Chapter I come even closer to the experimental data.
These results combine more "details" of the flow field
behavior than previous investigators have employed.

An empirical relationship attributed to Wood,[59]
seems to provide the closest agreement in this case.
Wood's relation is based largely on an average of a
large array of empirical and experimental results.

V.4. Wing Wake Vorticity
       Distribution

The wing wake, whose detailed shape is discussed
in a later section, can be envisioned as consisting of

a sheet-like structure extending beyond the trailing
edge across the entire span and a core of concentrated
vorticity in the outboard region. The formation of
this core has been discussed in the preceding chapters.

Of interest regarding the rollup process is the
rate of transfer of vorticity from the inboard wake to
the core region, as well as the core's evolution. The
former relationship was investigated for the near wake.
The spanwise distribution of "x"-vorticity is displayed
via the circulation function, with integration from
$y = -\infty$ toward the wing centerline.

Variation of the circulation profiles
downstream for fixed values of α is illustrated in
Figures 90-92. The reference values of circulation,
Γ_o, obtained for the various bounding contours is shown
in Figure 93. Agreement is within experimental expec-
tations. Vorticity generated outboard of the tip (at
the trailing edge) is observed to move toward the
"Betz" value of the spanwise location. A significant
outboard movement of the "sheet" vorticity was not
observed, however. Figure 94 shows more clearly the
chordwise variation of circulation for several span-
wise locations. An increase in this function with the
"x"-cordinate would indicate vorticity transfer toward
the vorticity centroid. No definitive statement about

this trend can be made over the region of investigation. Only at the highest angle of attack (8 degrees) does the expected behavior occur.

Some comparative data obtained by Fage and Simmons[48] using a similar measurement scheme for an aspect ratio 6 rectangular wing is displayed in Figure 90. Their observations appear to fit within the experimental scatter of the present measurements. This result indicates that the rollup process is only weakly dependent on aspect ratio for the entire sheet. This conclusion is consistent with the results of Grow[26] who achieved the same qualitative variation for higher angles of attack.

Figures 95 and 96 show the variation of x-vorticity content with angle-of-attack for fixed downstream locations. T.e correlation between outboard vorticity transfer and increasing angle-of-attack appears to be stronger than with downstream location.

V.5. Shape of the Near Wake

Since the "bound" vorticity adjacent to the wing surface is located within the boundary layer (unseparated displacement region), it is not unreasonable to expect that the shed vorticity downstream should be confined to the resulting wake. Except for the properties of the vortex core this region is

identifiable by the usual characteristics of a high turbulence level and a perceptible velocity defect in the mainflow direction. Both of these properties were studied to identify the wake location corresponding to the vorticity measurements.

Figures 97-99 illustrate the location of the wake edges for the various values of α. The data represent spatial locations where the turbulence indicator, $\sqrt{\overline{w'^2}}/U_o$, dropped below the value 0.002, which is three times the free stream value. Additional data indicating the locations of the maximum x-velocity (U) deficit are superimposed on these Figures.

It is observed that the wake at the wing center line descends more rapidly than at any other location. A marked curling of the inboard wake is also apparent. The vortex core, on the other hand, appears to extend downstream in nearly the free stream direction, positioned slightly above the projected z-location of the trailing edge.

These observations are in qualitative agreement with the results of both Spreiter and Sachs[6] and Chigier and Corsiglia[60] who experimentally investigated the wake shape in this region.

The wake is observed to be thickest in the inboard region with a marked "necking down" toward the

central core. Tight curling near the core is observed
at x/c = 2.0 and to a lesser extent at other down-
stream locations. Diffusion at the wake edges in
this region tends to blur the expected spiral behavior.

Care must be exercised when employing these
results in a comparison with other experiments (actual
flow or numerical) due to the effects of wind tunnel
wall interference. Hackett and Evans[2] investigated the
influence of the proximity of the wall boundaries and
their geometry and noted that "Wall proximity causes
tip vortices to sweep downward less and floor proximity
has an obvious effect on the penetration of the center
of the vortex sheet." Their experimental evidence sub-
stantiates this claim.

If one assumes that all non-core located
vorticity lies along a line representing the wake center
then the preceding description of the vorticity vari-
ation (section V.4) along with the geometry of this
line sufficiently described the wake rollup. As indi-
cated above, however, the wake exhibits a finite
thickness which, in this case, cannot be presumed to
be insignificant. The z-variation of the vorticity
may, in fact, cause some modification in the wake
evolution and rate of rollup. This variation was not
examined in the present study.

V.6. Rate of Rollup; Discussion

The results of the above sections can be combined to give a more graphic picture of the rollup.

The planform location of vortex filaments can be constructed in a manner identical to that described in Chapter IV for the bound filaments. Had this been accomplished one would note only a slight spanwise displacement of the filaments over the region of interest at least ror small angles. This indicates, perhaps, a qualitatively good reason for Prandtl's placement of the free vorticity elements in the lifting line theory.

One glaring conclusion is inescapable from the above result. The wake rollup process is not nearly as marked as one would expect based on the rapid evolution of the core adjacent to the wing surface. Though the near wake shape distorts and some transfer of vorticity into the core takes place, it is near the lifting surface that the most marked evolutive changes take place probably due to its ability to sustain shear.

A number of investigators have attempted to predict the roll-up distance (or time) employing various bases.

Kaden's[61] early work led to the belief that rollup had occurred fully at almost the wing itself.

His basis for the rollup time was the coincidence of
the vortex core with the "Betz" centroid. His analysis,
however, was applied to an open-sided infinite vortex
sheet. A slightly modified analysis by Moore[4] using a
spanwise finite sheet predicted 99% rollup within
3.5 chord lengths of the trailing edge using the same
criterion.

Spreiter and Sachs[6] slightly improved analysis
employing the bound vortex and a semi-inifinite sheet
yielded a value of 4.45 chord lengths for the present
test case. Again the criterion was the same.

In all of the above cases, agreement between the
estimates and the current experiment is poor. Perhaps
the data is in error, but it is more probable that what
is at fault is the rollup criterion. It has been shown
that a vortex "center" does, in fact, coexist with a
sheetlike structure of vorticity extending to the wing
centerline.

A more realistic criterion would seem to be the
requirement of "1/r" behavior of the velocity field,
though this location is difficult to predict.

Another interesting parameter is the non-
dimensional distance between the trailing edge and some
location, 1*, where an infinitesimally weak (no vor-
ticity) fluid element initially at the wing centerline

has revolved around the central core one revo'ution. A simplified analysis employing a fully rolled up potential vortex extended rearward from the tip at the trailing edge gives rise to an upper bound in this case. It can be shown that--

$$l^* = \frac{4\pi^2 b^{*2} U_o}{\Gamma_o c} \qquad (V-1)$$

where b^* is the effective semi-span. For an elliptically loaded wing this can be written--

$$l^* = \frac{2\pi^3 b^{*2}}{C_L c^2} \qquad (V-2)$$

In the present case, for $\alpha = 4$ degrees, the approximate value of this parameter is $l^* = 612$, i.e., 612 chord lengths downstream of the trailing edge.

CHAPTER VI

SUMMARY AND CONCLUSIONS

The following list summarizes the major results
of this investigation and its primary conclusions:

1. The experimental technique employed for the
measurement of the circulation and vorticity distribu-
tions appeared to provide satisfactory data for the flow
conditions utilized.

2. The flow field surrounding the wing could
be separated into various spatial regions each exhibiting
unique properties. This separation facilitated the
local simplification of the flow field from the more
complex general three-dimensional situation.

3. The surface boundary layers were found to
contain all of the wing generated vorticity except in
the immediate proximity of the tip. This verification
lends credence to the application of the vortex sheet
as a replacement model for the actual wing if one
envisions the surface boundary layer and wing thick-
nesses approaching zero.

4. The flow field near the wingtip is observed
to exhibit a high degree of rollup immediately adjacent

to the wing surface similar to that expected in the
wake. The resulting crossflow plane secondary flow
is observed immediately downstream of the leading edge
in the region opposite the side of the tip. Vortex
shedding from the lower wing surface is responsible
for this occurrence.

5. This rolled-up "free" vorticity is seen
to roll over onto the upper surface at a predictable
chordwise location for the simple geometric tip shape
employed.

6. The behavior of the shed vorticity at the
tip can modify the expected surface pressure distribu-
tion and resultantly invalidate the applicability of the
vortex sheet concept due to direct viscous interaction
with the conventional wing boundary layer.

7. Investigation of the inboard bound vorticity
distribution revealed that the bound circulation func-
tion could be expressed approximately as the product
of two separable functions of the spatial coordinates,
x and y.

8. A rolled up vortex with an identifiable
core was observed to emanate from the upper surface at
the trailing edge. This region was found to contain
over 60% of the total wing generated vorticity for the
configuration tested.

9.   The trailing edge vorticity distribution
was found to be independent of the wing angle of attack
for the unseparated conditions studied.   There is good
justification to assume that the _entire_ surface bound
vorticity field exhibits similar characteristics.

10.   The wing lift coefficient is found to vary
nearly linearly with angle-of-attack as expected.
Corrected experimental results are found to be in good
agreement with direct force measurements and various
theoretical and numerical predictions.

11.   A comparison of near surface data and
measurements in the near wake region indicate that
rollup occurs much more violently near the solid surface
than in the boundary-free zone downstream of the wing.

12.   The normalized description of the rollup
process in the near wake region is observed to be nearly
independent of both aspect ratio and angle-of-attack.

13.   The isolated vortex core is observed to
move downstream in nearly the free stream direction
while the inboard wake is displaced downward (opposite
the lift direction).   The largest displacement is
observed to occur near the wing centerline.   A distinc-
tive curling motion is apparent as the wake evolves.

14.   The thickest portion of the wake (z-
direction) occurs downstream of the wing centerline

with a marked necking down observed near the rolled up
core.   A complete examination of the roll up charac-
teristics should include variation in the vorticity
distribution in this direction.

15.   Various estimates of the roll up rate
reviewed in this study are found to err significantly,
predicting a fully rolled up geometry far upstream of
its actual occurrence.   The "x"-oriented vorticity in
the inboard wake region is observed to be ingested into
the core at a slow rate in the near wake region.

BIBLIOGRAPHY

BIBLIOGRAPHY

1. Butter, D. J., and Hancock, G. J. "A Numerical Method for Calculating the Trailing Vortex System behind a Swept Wing at Low Speed," The Aeronautical Journal of the Royal Aeronautical Society, Vol. 75, August, 1971., pp. 564-568.

2. Hackett, J. E., and Evans, M. R. "Vortex Wakes Behind High Lift Wings," Journal of Aircraft, Vol. 8, No. 5, May 1971, pp. 334-340.

3. Bloom, A. M., and Jen, H. "Roll-Up of Aircraft Trailing Vortices using Artificial Viscosity," Journal of Aircraft, Vol. 11, No. 11, November 1974, pp. 714-716.

4. Moore, D. W. "A numerical study of the roll-up of a finite vortex sheet," Journal of Fluid Mechanics, Vol. 63, pt. 2, April 1974, pp. 225-235.

5. Rehbach, par Colmar, "Calcul D'Ecoulements Autour D'Ailes Sans Épaisseur Avec Nappes Tourbillon-naires Évolutives," Recherche Aérospatiale, n° 1973-2 (Mars-Avril), pp. 53-61.

6. Spreiter, J. R., and Sacks, A. H. "The Rolling Up of the Trailing Vortex Sheet and Its Effect on the Downwash Behind Wings," Journal of the Aeronautical Sciences, Vol. 18, No. 1, January 1951, pp. 21-32.

7. Betz, A. "Behavior of Vortex Systems," NACA Technical Memorandum No. 713, Washington, June 1933.

8. Baldwin, B. S., Shaeffer, Y. S., and Chigier, N. A. "Prediction of Far Flow Field in Trailing Vortices," Palo Alto, California, September 11-13, 1972, AIAA 2nd Atmospheric Flight Mechanics Conference, Paper No. 72-989.

9. Sullivan, Roger D. "A Program to Compute the Behavior of a Three-Dimensional Turbulent Vortex," Final Report, Aerospace Research Laboratory TR 74-0009, June 1973.

10. Crow, S. C. "Stability Theory for a Pair of Trailing Vortices," AIAA Journal, Vol. 8, No. 12, December, 1970, pp. 2172-2179.

11. Uberoi, M. S., Chow, C. Y., and Narain, J. P. "Stability of Co-Axial Rotating Jet and Vortex of Different Densities," The Physics of Fluids, Vol. 15, No. 10, October 1972, pp. 1718-1727.

12. Narain, J. P., and Uberoi, M. S. "Trailing Vortex-Pair Instability," The Physics of Fluids, Vol. 16, No. 6, June 1973, pp. 761-768.

13. Tombach, I. "Observations of Atmospheric Effects on the Transport and Decay of Trailing Vortex Wakes," Washington, D.C., January 10-12, 1973, AIAA 11th Aerospace Sciences Meeting, Paper No. 73-110.

14. Dosanjh, D. S., Gasparek, E. P., and Eskinazi, S. "Decay of a Viscous Trailing Vortex," The Aeronautical Quarterly, Vol. 13, May 1962, pp. 167-188.

15. Lezius, D. K. "Water Tank Study of the Decay of Trailing Vortices," AIAA Journal, Vol. 12, No. 8, August 1974, pp. 1065-1071.

16. Nelson, R. C., and McCormick, B. W. "The Dynamic Behavior of an Aircraft Encountering Aircraft Wake Turbulence," Anaheim, California, August 5-9, 1974, AIAA Mechanics and Control of Flight Conference, Paper No. 74-774.

17. Donaldson, C. du P., and Sullivan, R. D. "Decay of an Isolated Vortex," Aircraft Wake Turbulence and Its Detection, Plenum, New York, 1971, pp. 389-411.

18. Brown, C. E. "Aerodynamics of Wake Vortices," AIAA Journal, Vol. 11, No. 4, April 1973, pp. 531-536.

19. Westwater, F. L. "Rolling Up of the Surface of Discontinuity Behind an Aerofoil of Finite Span," ARC R and M No. 1692, August 1935.

20. Yates, J. E. "Calculation of Initial Vortex Roll-Up in Aircraft Wakes," Journal of Aircraft, Vol. 11, No. 7, July 1974, pp. 397-400.

21. Mook, D. T., and Maddox, S. A. "Extension of a Vortex-Lattice Method to Include the Effects of Leading-Edge Separation," Journal of Aircraft, Vol. 11, No. 2, February 1974, pp. 127-128.

22. Chigier, N. A., and Corsiglia, V. R. "Tip Vortices-Velocity Distributions," Washington, D.C., May 1971, 27th Annual National V/STOL Forum of the American Helicopter Society, Preprint No. 522.

23. Mason, W. H., and Marchman, J. F. III. "Far-Field Structure of Aircraft Wake Turbulence," Journal of Aircraft, Vol. 10, No. 2, February 1973, pp. 86-92.

24. Orloff, K. L. and Ciffone, D. L. "Vortex Measurements Behind a Swept Wing Transport Model," Journal of Aircraft, Vol. 11, No. 6, June 1974, pp. 362-364.

25. Muttray, H. "Investigations on the Amount of Downwash behind Rectangular and Elliptic Wings," NACA Technical Memorandum No. 787, February 1936.

26. Grow, T. L. "Effect of a Wing on Its Tip Vortex," Journal of Aircraft, Vol. 6, No. 1, January-February 1969, pp. 37-41.

27. Tombach, I., and Bate, E. R. Jr. "Study of the Motion and Properties of the Vortex Wake of a Light Twin-Engine Aircraft," Final Report, Department of Transportation AV FR 351, DOT-TSC-523, September 1973.

28. Verstyner, H. A., Jr., and Denham, R. E., Jr. "A Flight Investigation of the Trailing Vortices Generated by a Jumbo-Jet Transport," NASA Technical Note TN D-7172, April 1973.

29. von Karmen, T. "Aerodynamics," First Edition, New York: McGraw-Hill, 1963, pp. 48-53.

30. Hoerner, S. Fluid Dynamic Drag, First Edition, Published by Author, Bricktown, New Jersey, 1951, Chapter VII.

31. Rom, J., Zorea, C., and Gordon, R. "On the Calculation of Non-linear Aerodynamic Characteristics and the Near Vortex Wake," Haifa, Israel, August 25-30, 1974, The Ninth Congress of the International Council of the Aeronautical Sciences, Paper No. 74-27.

32. Kandil, O. A., Mook, D. T., and Nayfeh, A. H.
    "Non-linear Prediction of the Aerodynamic Loads
    on Lifting Surfaces," Palo Alto, California,
    June 17-19, 1974, AIAA 7th Fluid and Plasma-
    dynamics Conference, Paper No. 74-503.

33. Jordan, P. F.   "The Parabolic Wing Tip in
    Subsonic Flow," New York, N.Y., January 25-27,
    1971, AIAA 9th Aerospace Sciences Meeting,
    Paper No. 71-10.

34. Freymuth, P.   "Feedback Control Theory for Con-
    stant-Temperature Hot-Wire Anemometers," The
    Review of Scientific Instruments, Vol. 38, No.
    5, May 1967, pp. 677-681.

35. Bank, W.   "Build your own constant temperature
    hot-wire anemometer," Electronic Design News,
    August 1972.

36. King, L. V.   "On the Convection of Heat from Small
    Cylinders in a Stream of Fluid: Determination
    of the Convection Constants of Small Platinum
    Wires, with Applications to Hot-Wire Anemometry,"
    Philosophical Transactions of the Royal Society,
    London, 214A, 1914, pp. 373-432.

37. McMichael, J. M.   "A Study of the Axisymmetric
    Turbulent Wake Generated by Co-Flowing Incom-
    pressible Streams," Ph.D. Thesis, 1971, Aero-
    space Engineering Sciences, University of
    Colorado, Boulder, Colorado.

38. Singh, P. I.   "The Structure and Stability of a
    Vortex," Ph.D. Thesis, 1974, Aerospace Engineer-
    ing Sciences, University of Colorado, Boulder,
    Colorado.

39. Wills, J. A. B.   "The correction of hot-wire
    readings for proximity to a solid boundary,"
    Journal of Fluid Mechanics, Vol. 12, Pt. 3, 1962,
    pp. 388-396.

40. Repik, Ye U., and Ponomarera, V. S.   "The Effect of
    Proximity of Walls in the Readings of a Hot-
    Wire Anemometer in Turbulent Boundary Layers,"
    Heat Transfer--Soviet Research, Vol. 2, No. 4,
    July 1970, pp. 43-49.

41. Francis, M. S., Kennedy, D. A., and Butler, G.
    "The Measurement of Spatial Vorticity Distri-
    butions Using Hot-Wire Anemometry Techniques,"
    Technical Report No. Frank J. Seiler
    Research Laboratory (AFSC), USAF Academy, 1976.

42. Abbott, I. H., and von Duenhoff, A. E. "Theory
    of Wing Sections," 1st edition, New York: Dover,
    1959.

43. Rayleigh, Lord. "On the Stability or Instability
    of Certain Fluid Motions," Proceedings of the
    London Mathematical Society, Vol. 11, 1880,
    pp. 57-70 and Vol. 19, 1887, pp. 67-74.

44. Tollmien, W. "The Production of Turbulence,"
    NACA Technical Memorandum No. 609, 1931.

45. Schlichting, H. "Zur Entstellung der Turbulenz
    bei der Plattenströmmung," Nach. Gesell. d.
    Wiss. z. Göttingen, Math. Phys. Klasse, 1933,
    pp. 181-308.

46. Schubauer, G. B., and Skramstad, H. K. "Laminar
    Boundary Layer Oscillations and Transition on
    a Flat Plate," NACA Technical Report No. 909,
    1943.

47. Karamcheti, K. "Principles of Ideal-Fluid Aero-
    dynamics," 1st edition, New York: Wiley, 1966.

48. Fage, A., and Simmons, B. A. "An Investigation of
    the Air Flow Pattern in the Wake of an Airfoil
    of Finite Span," Philosophical Transactions of
    the Royal Society (London), Ser. A., Vol. 225,
    No. 7, January 1926, pp. 303-330.

49. Thwaites, B. (ed.). "Incompressible Aerodynamics,"
    Oxford: Clarendon, 1960.

50. Bryant, L. W., and Williams, D. H. "An Investiga-
    tion of the Flow of Air Around an Aerofoil of
    Infinite Span," Proceedings of the Royal
    Society (London), Ser. A, Vol. 225, No. 7,
    pp. 199-245.

51. Robinson, R. G., and Herrnstein, W. H. Jr. "Wing-
    Nacelle-Propeller Intereference for Wings of
    Various Spans; Force and Pressure Distribution
    Tests," NACA Technical Report No. 569, 1936.

52. Pearson, H. A. "Empirical Corrections to the Span Load Distribution at the Tip," NACA Technical Note No. 606, 1937.

53. Rom, J., and Zorea, C. "The Calculation of the Lift Distribution and the Near Vortex Wake behind High and Low Aspect Ratio Wings in Subsonic Flow," Scientific Report No. 2, Technion, Israel Institute of Technology, Haifa, AFOSR 71-2145, January 1973.

54. Rehbach, par C. "Étude Numerique de L'Influence de la Forme de L'Extremité d'une Aile sur L'Enroulement de la Nappe Tourbillionnaire," Recherche Aérospatiale, n⁰ 1971-6, November-December, 1971, pp. 367-368.

55. DeYoung, J. and Harper, C. W. "Theoretical Symmetric Span Loading at Subsonic Speeds for Wings having Arbitrary Plan Form," NACA Technical Report No. 921, 1950.

56. Schrenk, O. "A Simple Approximation Method for Obtaining the Spanwise Lift Distribution," NACA Technical Memorandum No. 948, August 19·

57. Pankhurst, R. C., and Holder, D. W. "Wind Tunn Technique," 1st edition, Pitman, London, 195..

58. Multhopp, H. "Methods for Calculating the Lift Distribution of Wings (Subsonic Lifting Surface Theory), A.R.C. R and M No. 2844, January 1950.

59. Wood, K. D. "Aerospace Vehicle Design, Vol. 1, Aircraft Design," 2nd edition, Johnson, Boulder, 1966, p. A66.

60. Chigier, N. A., and Corsiglia, V. R. "Wind Tunnel Studies of Wing Wake Turbulence," Journal of Aircraft, Vol. 9, No. 12, December 1972, pp. 820-825.

61. Kaden, H. "Aufwicklung einer unstabilen Unstetigkeits flache," Ing. Archiv, II Band, 1931, pp. 140-168.

APPENDIX

EFFECT OF LIFT CURVE SLOPE ON THE MAXIMUM
LIFT-DRAG ORIENTATION

The condition for maximum lift-drag ratio is simply--

$$\frac{\partial}{\partial \alpha} \ (L/D) = 0$$

For wings of moderate to high aspect ratio, the conventional relations are

$$C_L = M\alpha$$

$$C_D = K_1 + K_2 \ C_L^2$$

$$= K_1 + K_2 \ M^2 \ \alpha^2$$

Then

$$\alpha_{max \ L/D} = \{\frac{K_1}{K_2 M^2}\}^{1/2}$$

$$= \frac{1}{M} \ \sqrt{\frac{K_1}{K_2}}$$

A <u>small</u> error, ΔM, in the measurement of the lift curve slope results in an error in $\alpha_{max \ L/D}$ of--

$$\Delta \alpha_{max \ L/D} = \frac{\Delta M}{M}$$

FIGURES
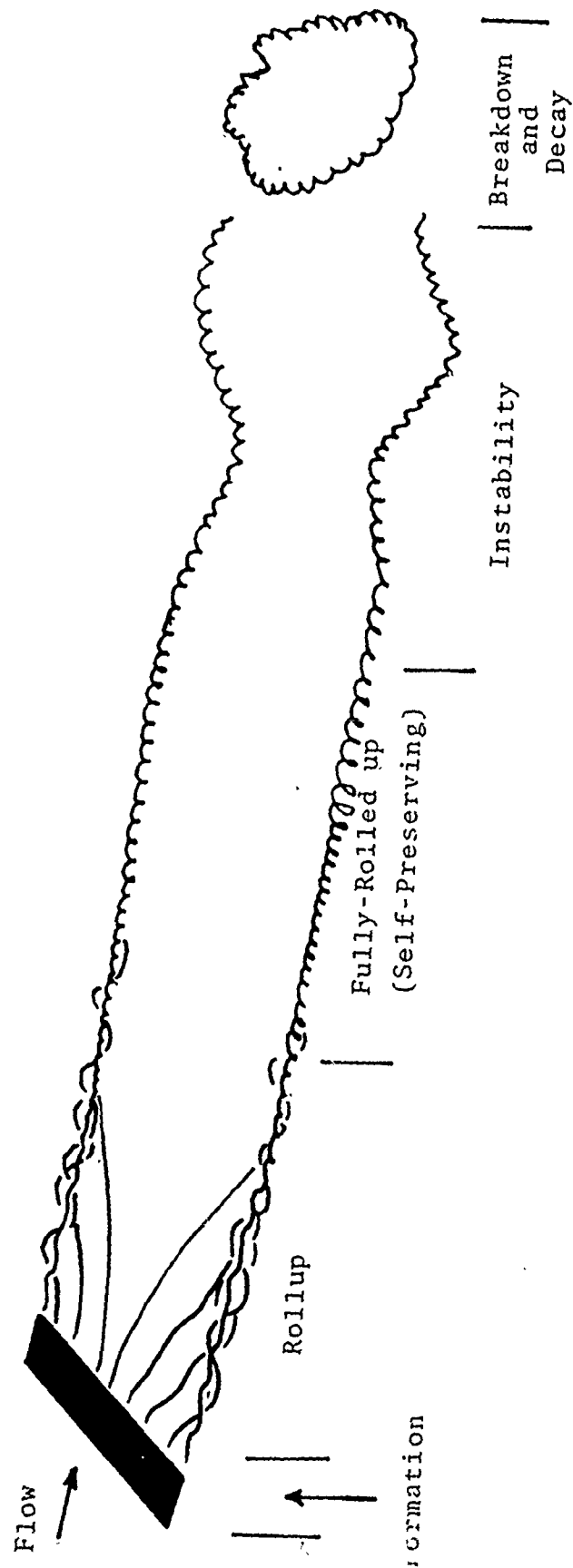
Fig. 1. Stages of Evolution of a Trailing Vortex Pair.
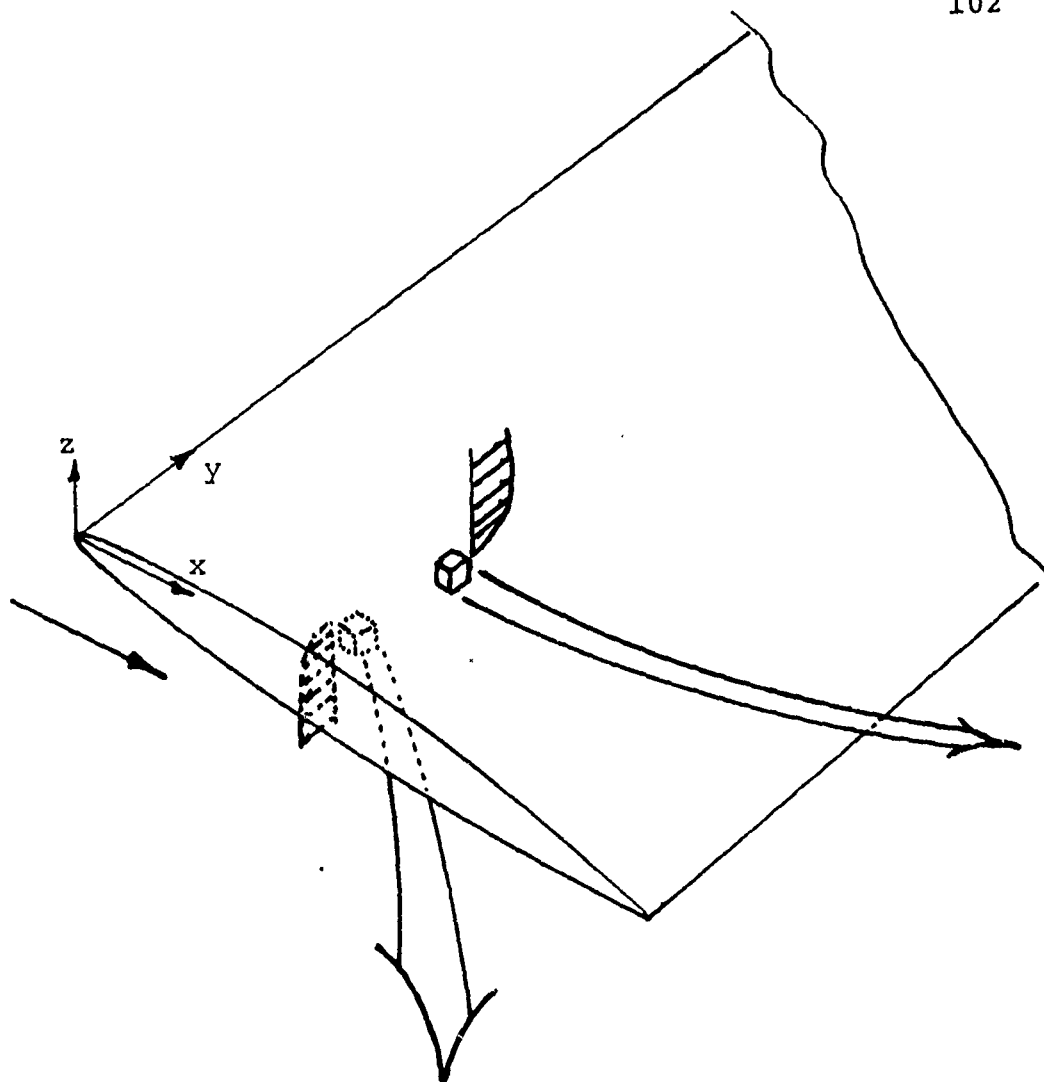
Fig. 2 . Behavior of Fluid Particles Adjacent to
the Upper and Lower Wing.Surfaces.
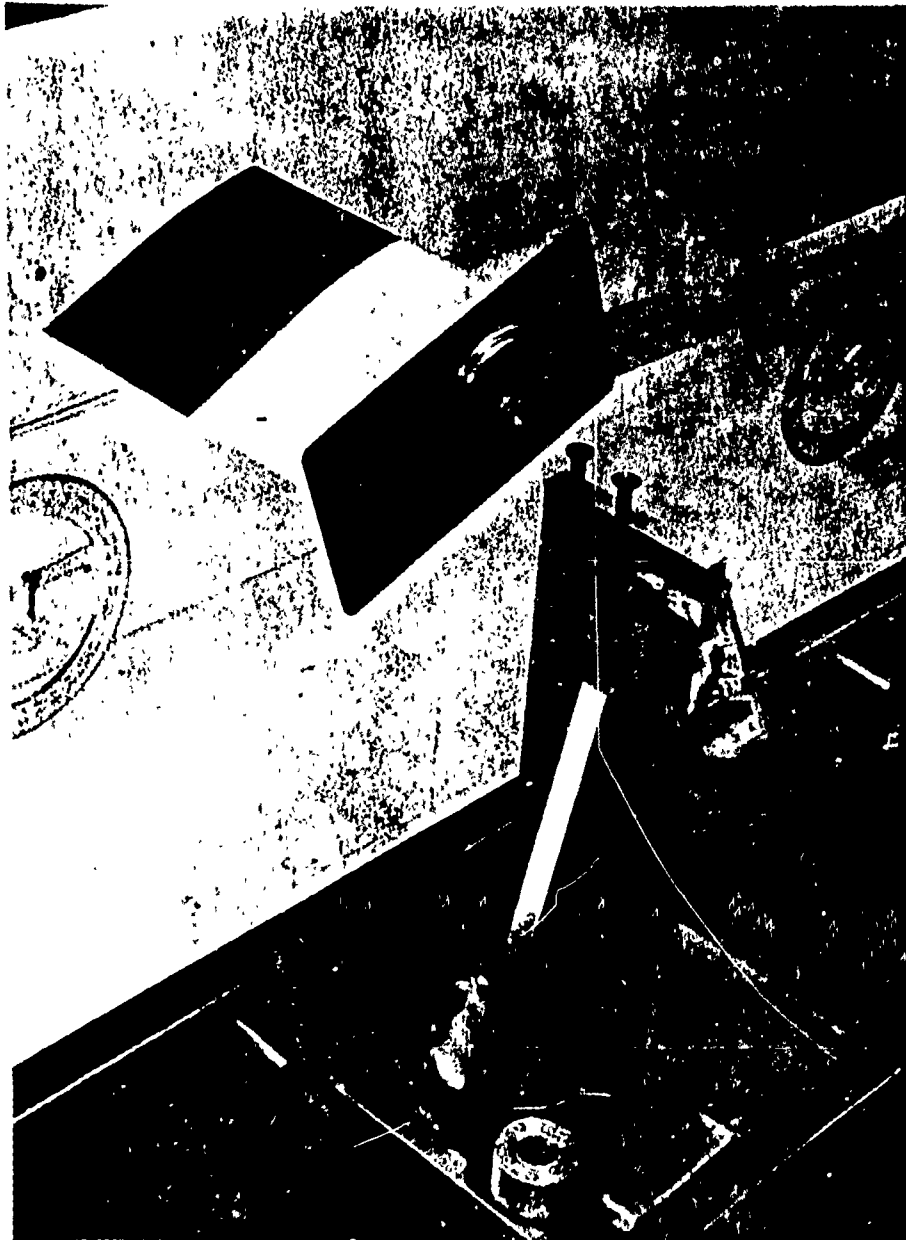
FIG 3   EXPERIMENTAL APPARATUS IN WIND TUNNEL
FACILITY
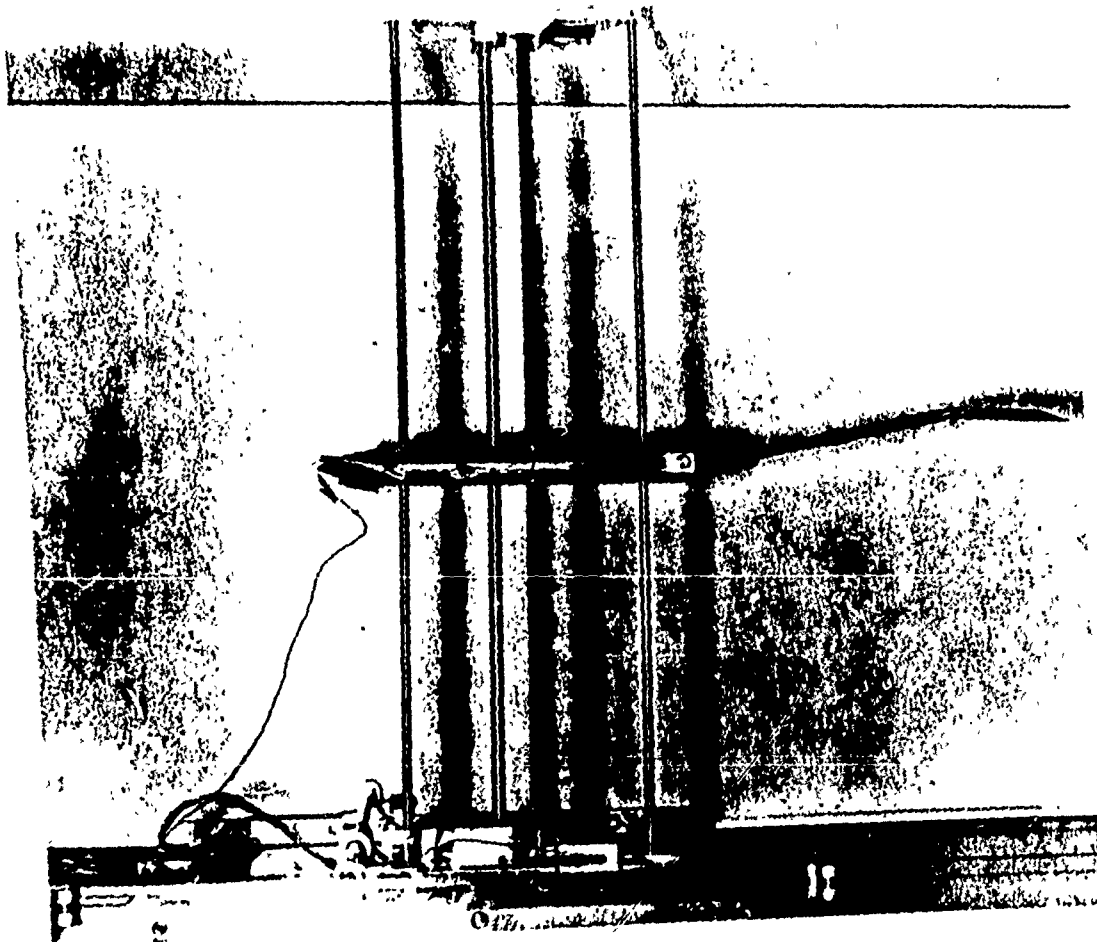
FIG. 4 TEST SECTION TRAVERSING MECHANISM WITH HOT-
WIRE PROBE
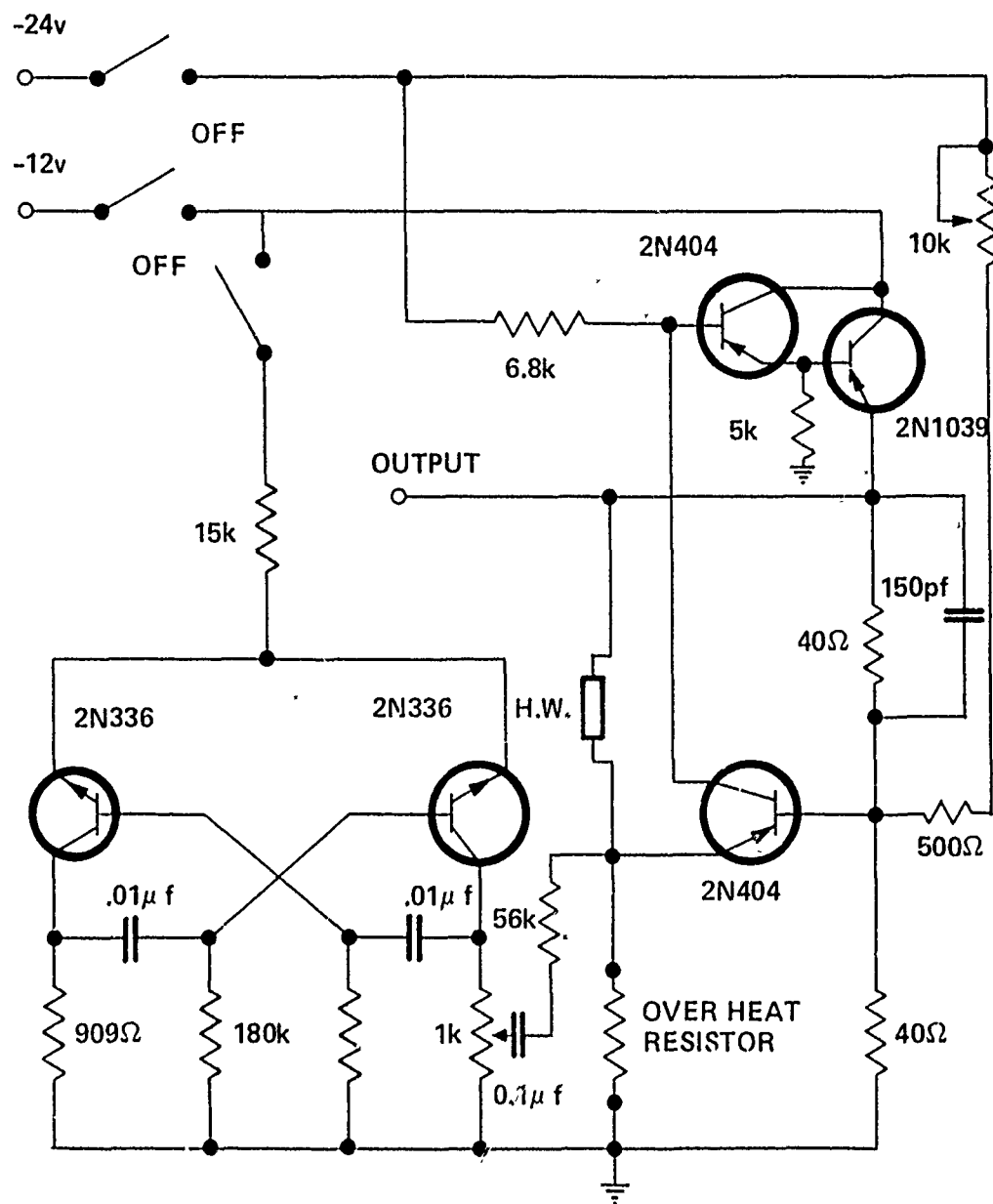
FIG. 5 CONSTANT TEMPERATURE HOT-WIRE ANEMOMETER
AND SQUARE WAVE GENERATOR
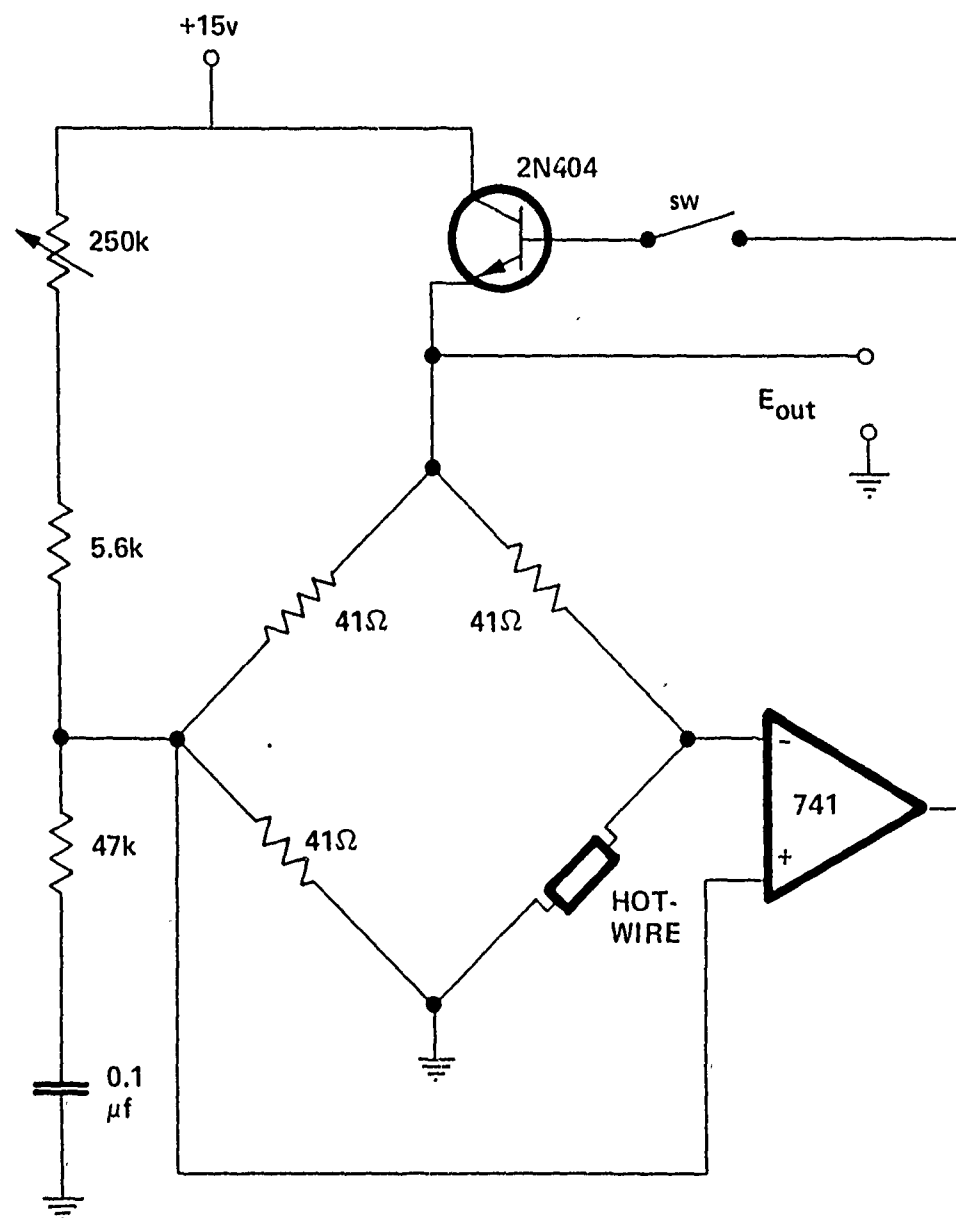
FIG. 6 I.C. HOT-WIRE ANEMOMETER
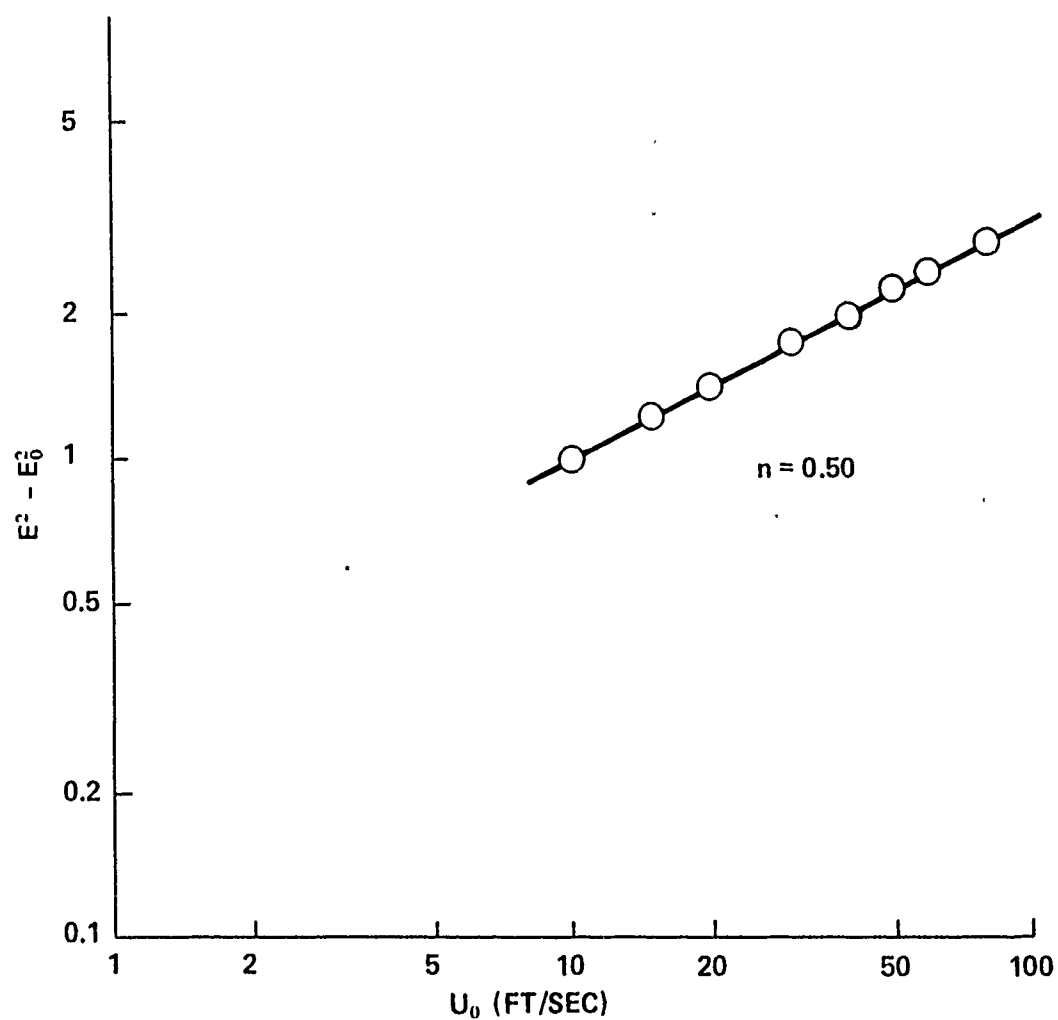
FIG. 7 HOT-WIRE ANEMOMETER VELOCITY
RESPONSE CHARACTERISTIC
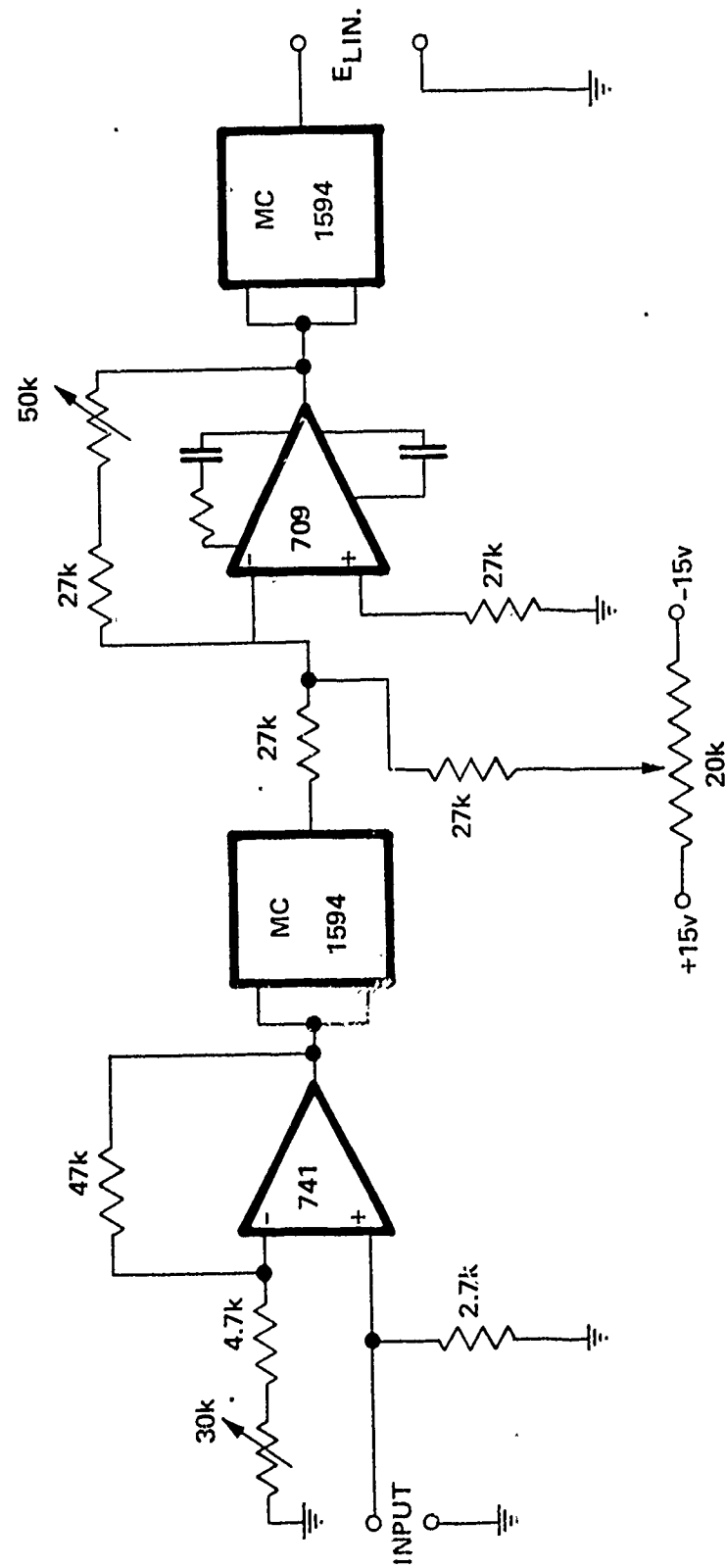
FIG. 8 LINEARIZER CIRCUIT
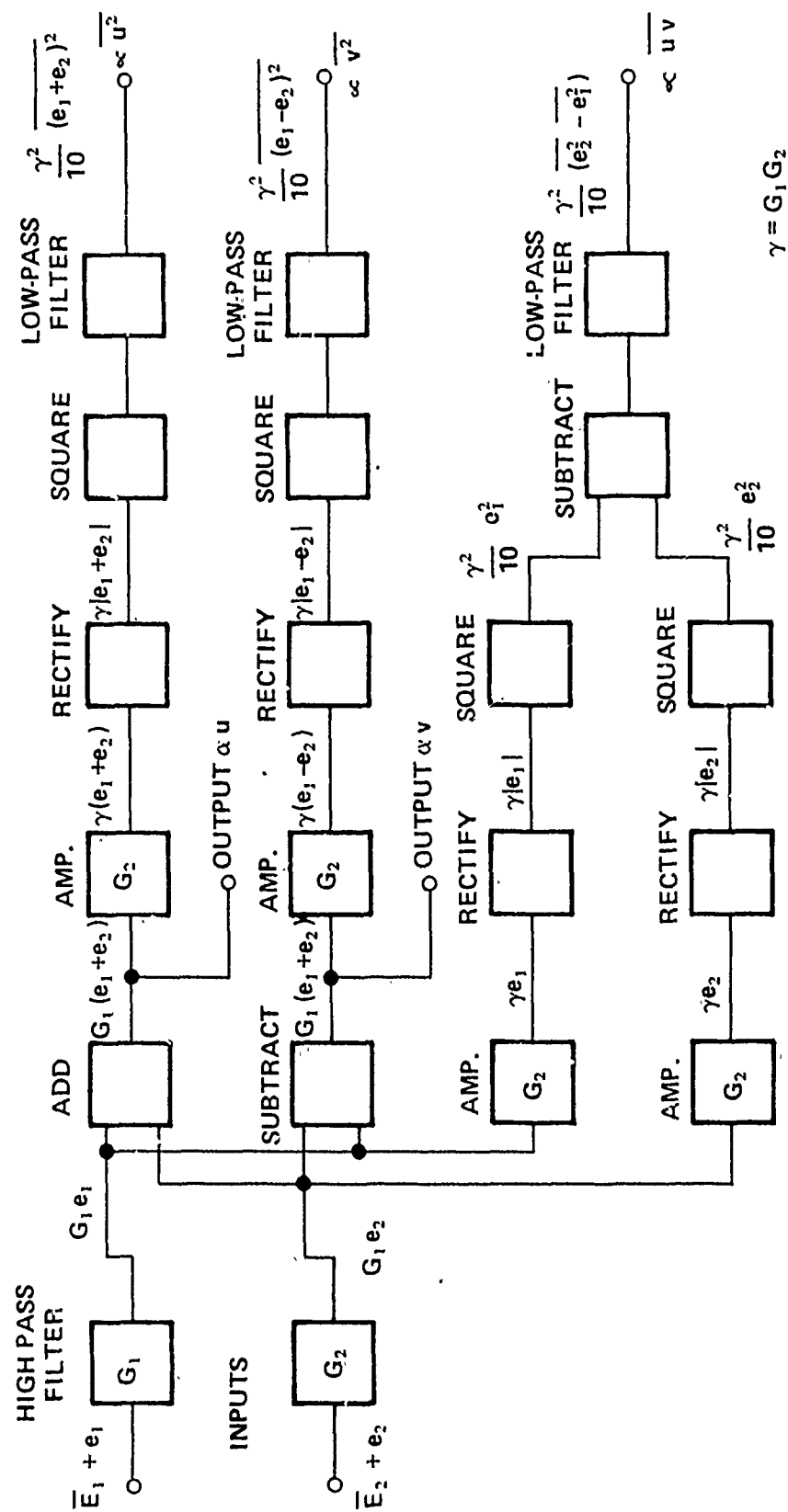
FIG. 9 X-METER A.C. SIGNAL CONDITIONER

(C) LOW-PASS FILTER
0-20μf
46.4k

(F) RECTIFIER
15k
15k
BIAS
+15ν
20k
15k

(B) HIGH-PASS FILTER
15-150k
14.99k
10μf

(E) AMPLIFIER
15k
15k
+15ν
20k
470k
470k
5k
70μf
OUTPUT
TRIM

(A) ADDER $\left(\dfrac{a+b}{2}\right)$
15k
30k
30k
30k
30k

(D) SUBTRACTOR (a − b)
8.2k
8.2k
8.2k
8.2k
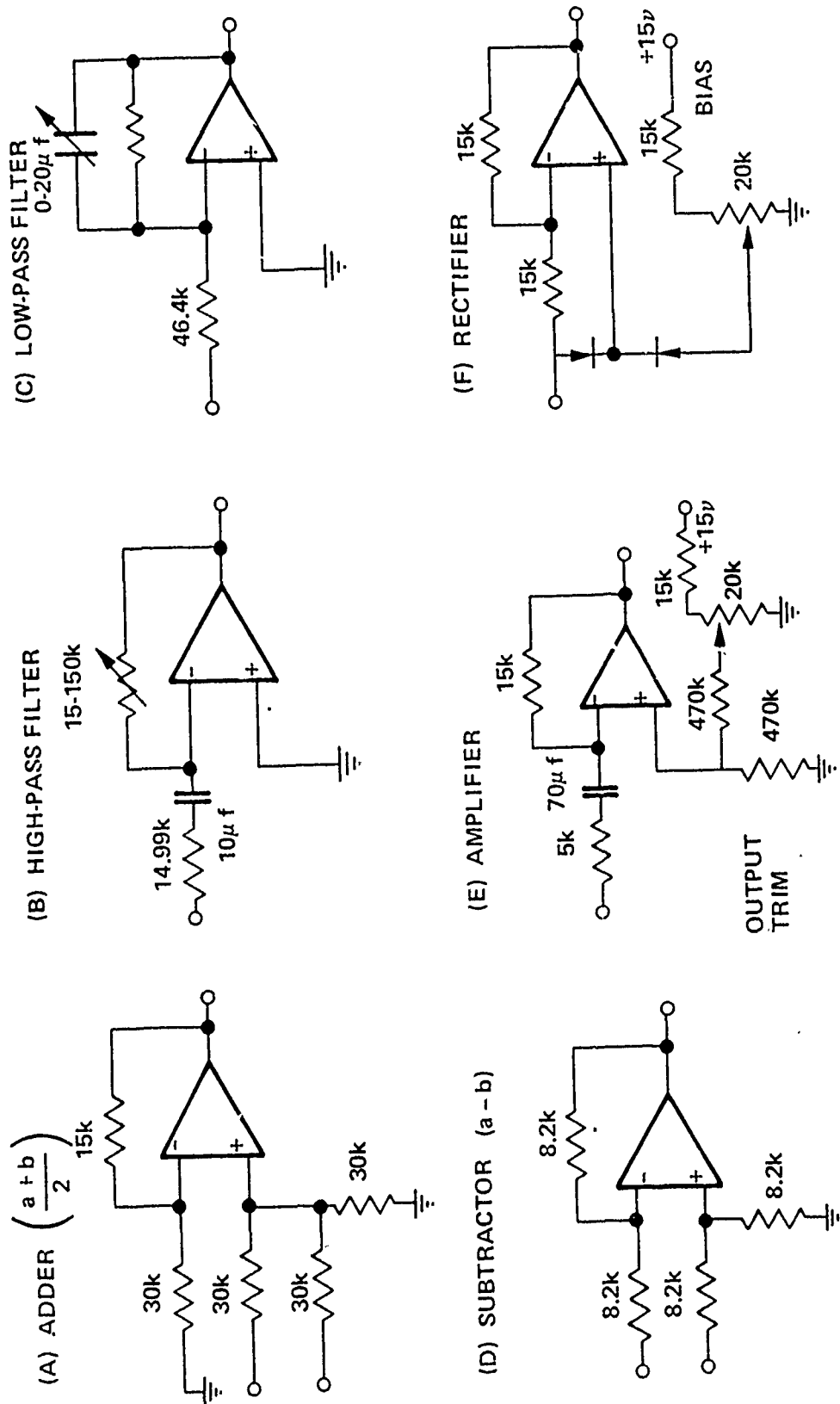
FIG. 10 DETAIL, X-METER CIRCUIT COMPONENTS

"υ" -
JOINT

±20°
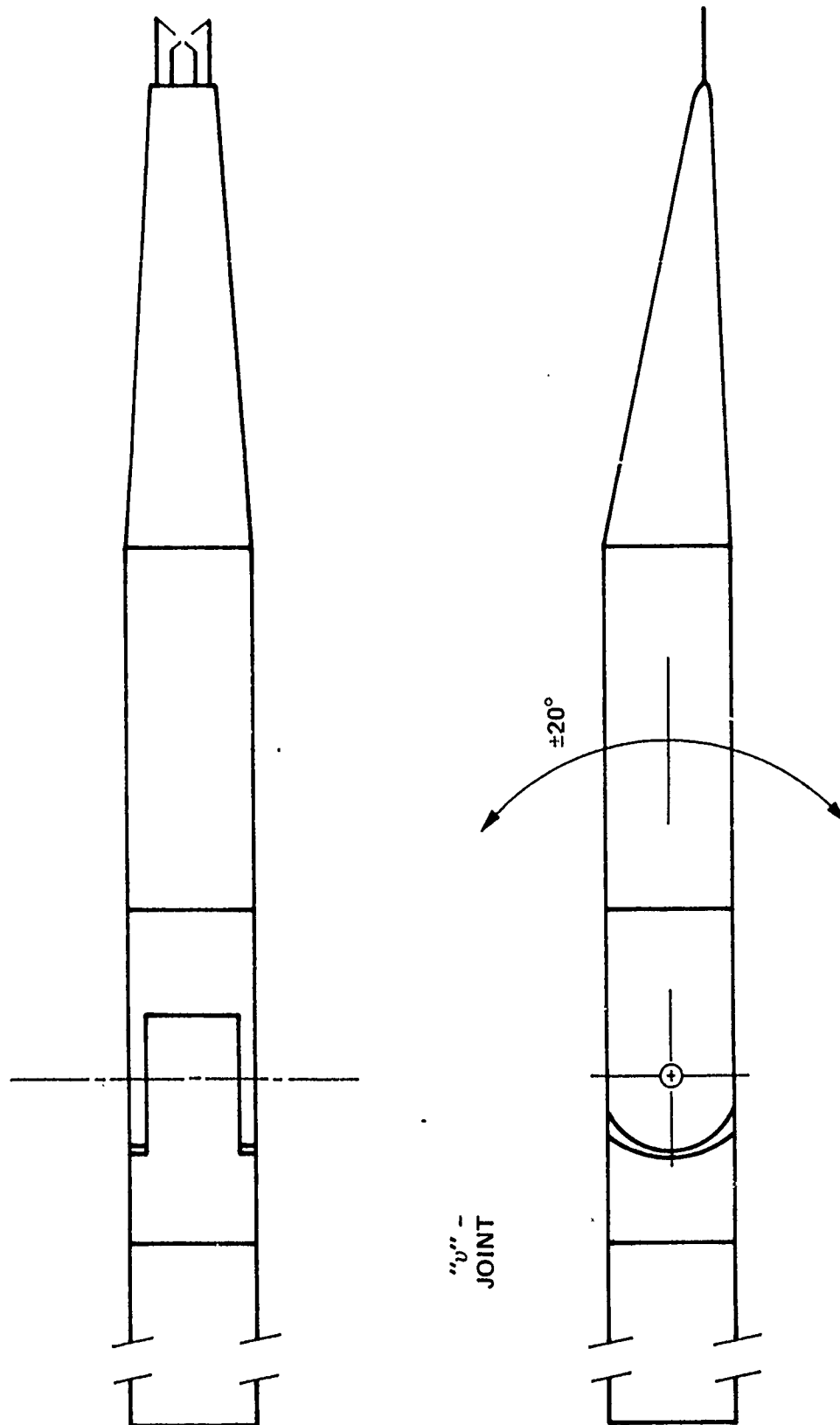
FIG. 11 VARIABLE ANGLE X-WIRE PROBE
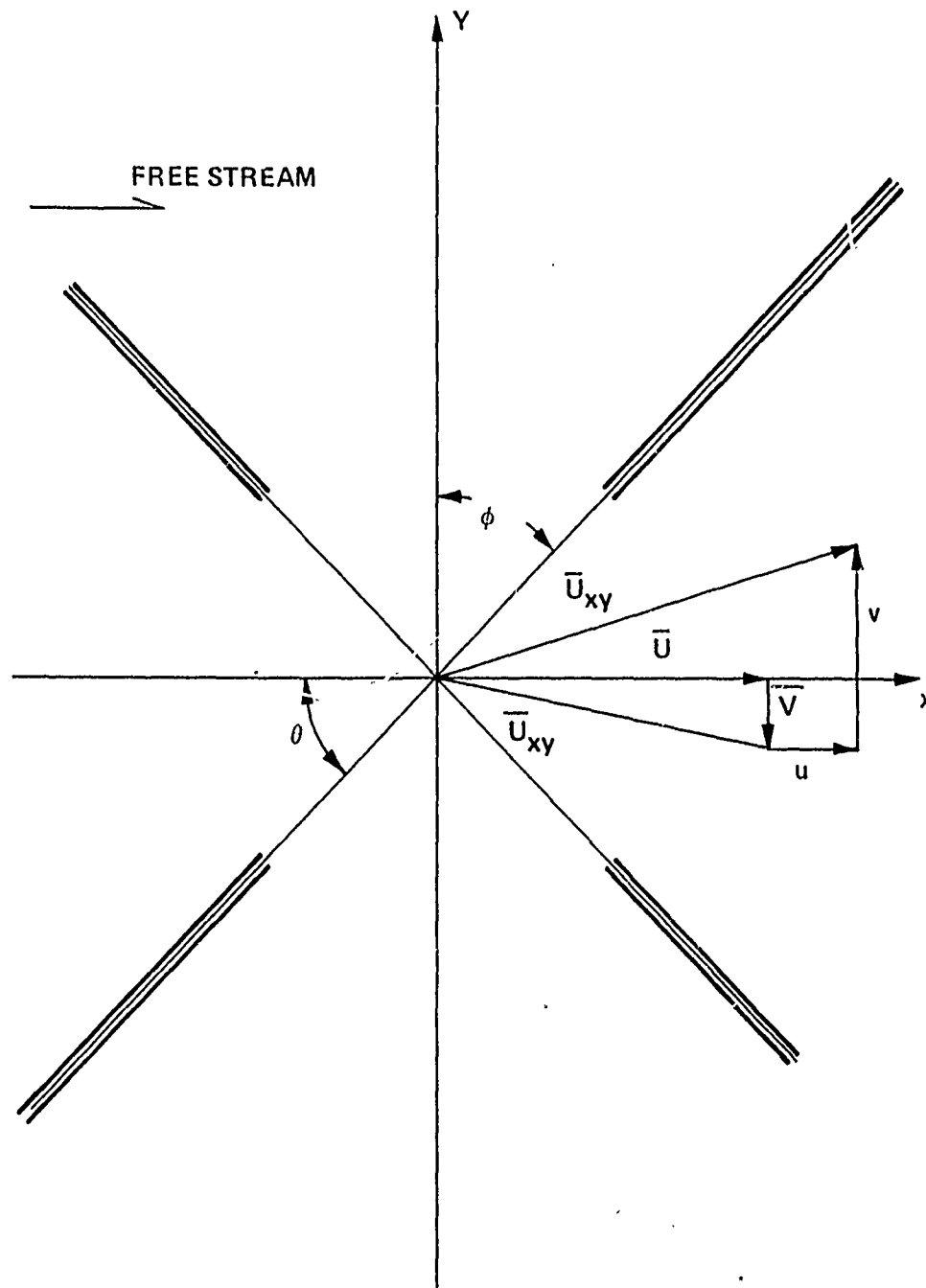
FIG. 12 X-METER GEOMETRY

2004

(23)

* VORTICES

WIND TUNNELS

HOT WIRE ANEMOMETERS

~~ANEMOMETERS~~

WAKE

* FLOW VISUALIZATION

INCOMPRESSIBLE FLOW

LIFTING SURFACES

MODELS   Wind tunnel models

(?) ~~FLOW~~ Fluid/Com

PROBES.

THREE DIMENSIONAL   * TRAILING VORTICES

WINGS

BOUNDARY LAYER

* VORTEX SHEDDING

FLOW FIELDS

OPTICAL EQUIPMENT

(25)

PRANDL BOUND VORTEX FILAMENTS

STREAMLINES

GAERTNER OPTICAL CATHOTOMETERS

New Terms
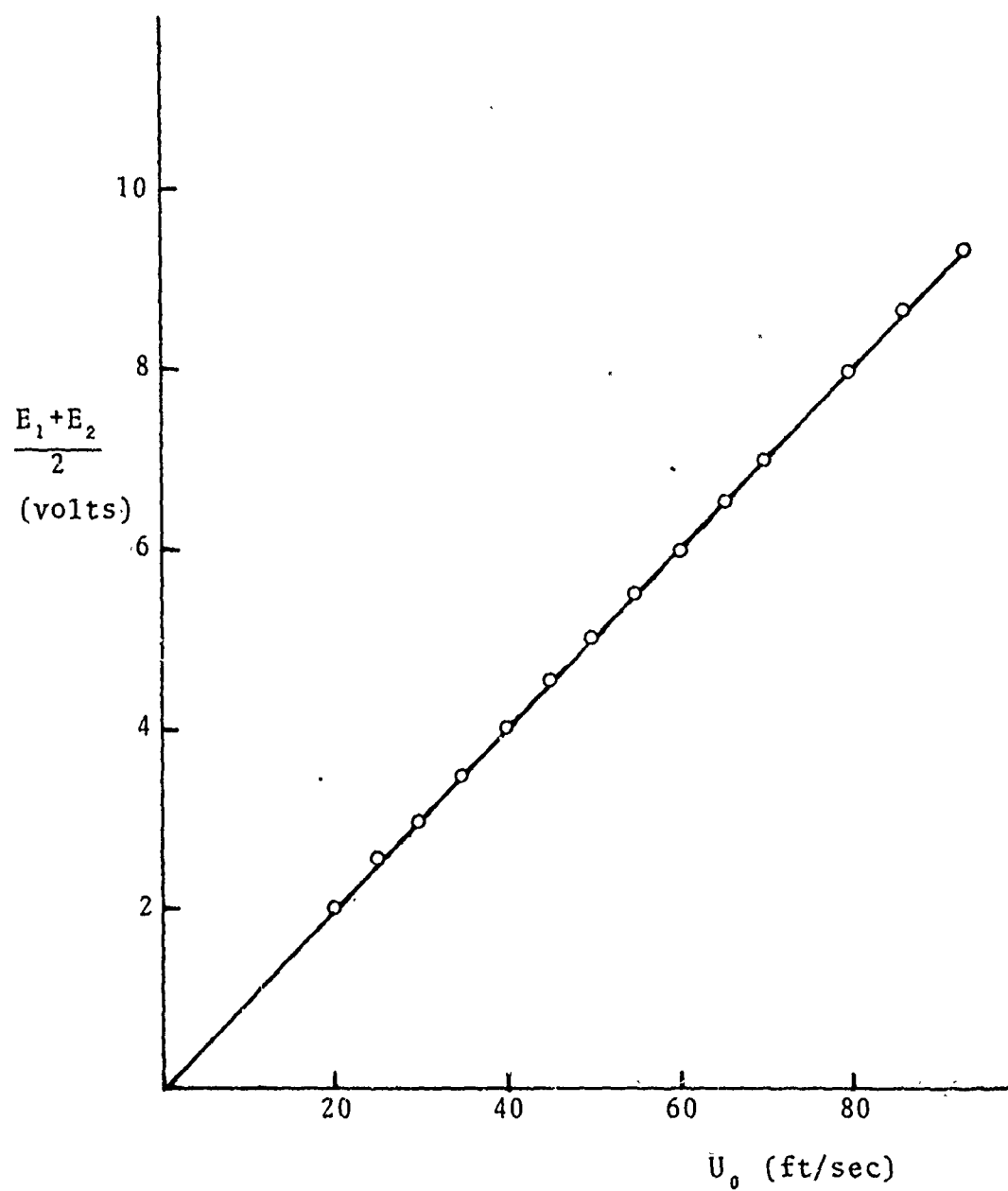
Fig. 13. Linearized Hot-Wire
Response Characteristic.
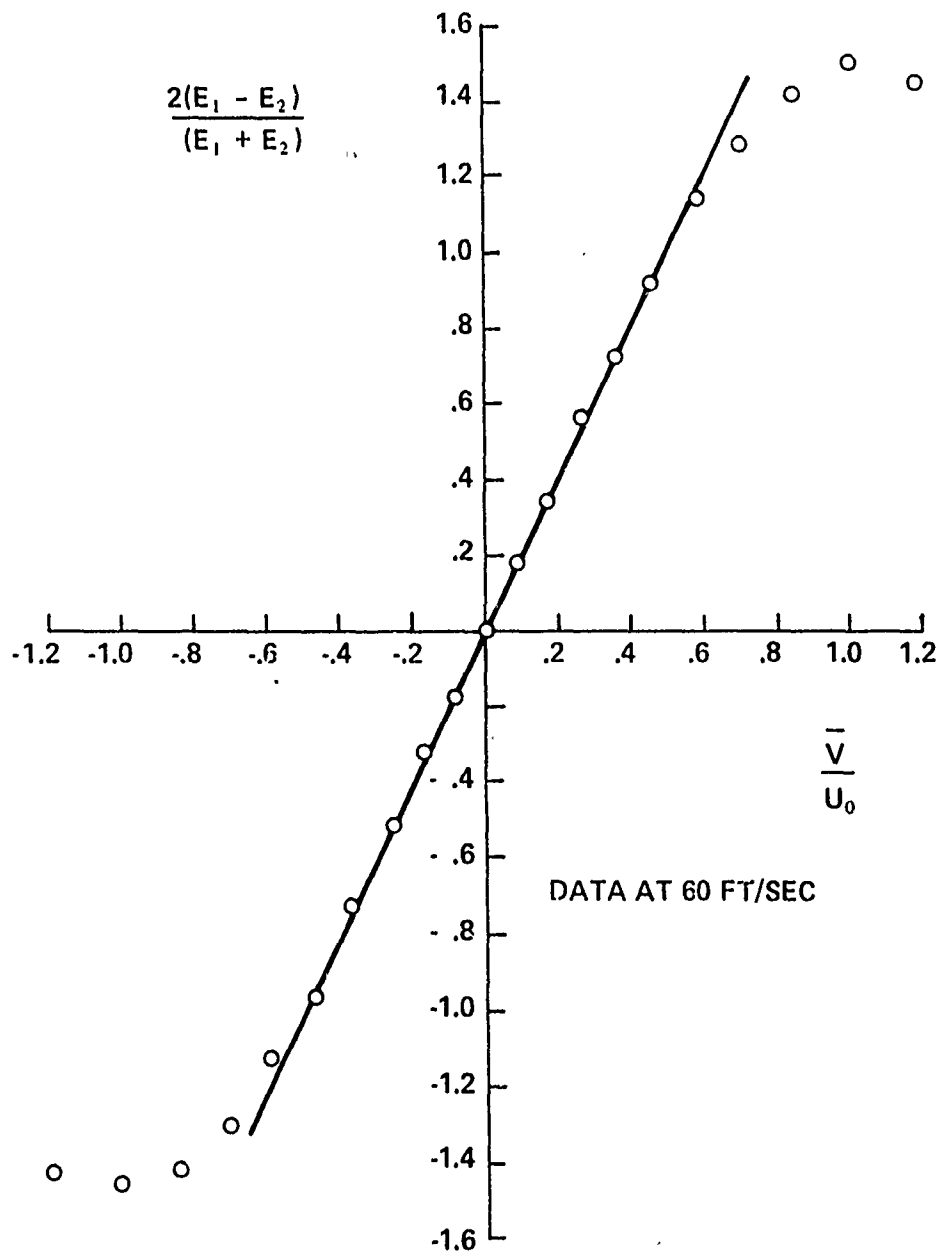
FIG. 14 TRANSVERSE VELOCITY CALIBRATION
X-METER, TYPICAL

Fig. 15. Variation of Lift Coefficient with
Angle of Attack (NACA 64009)

Reynolds No.-
$2.17 \times (10^5)$

C_D

α (Degrees)
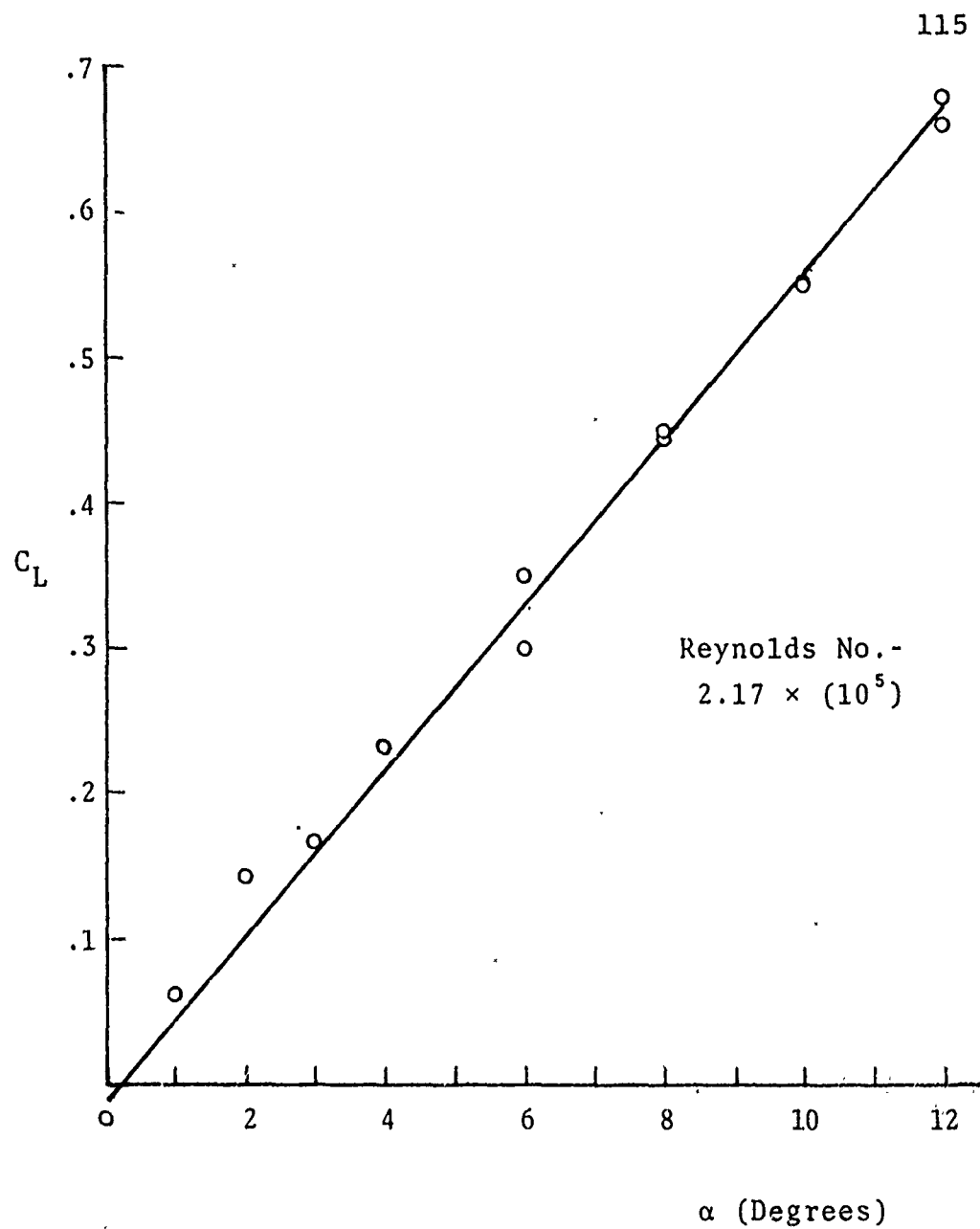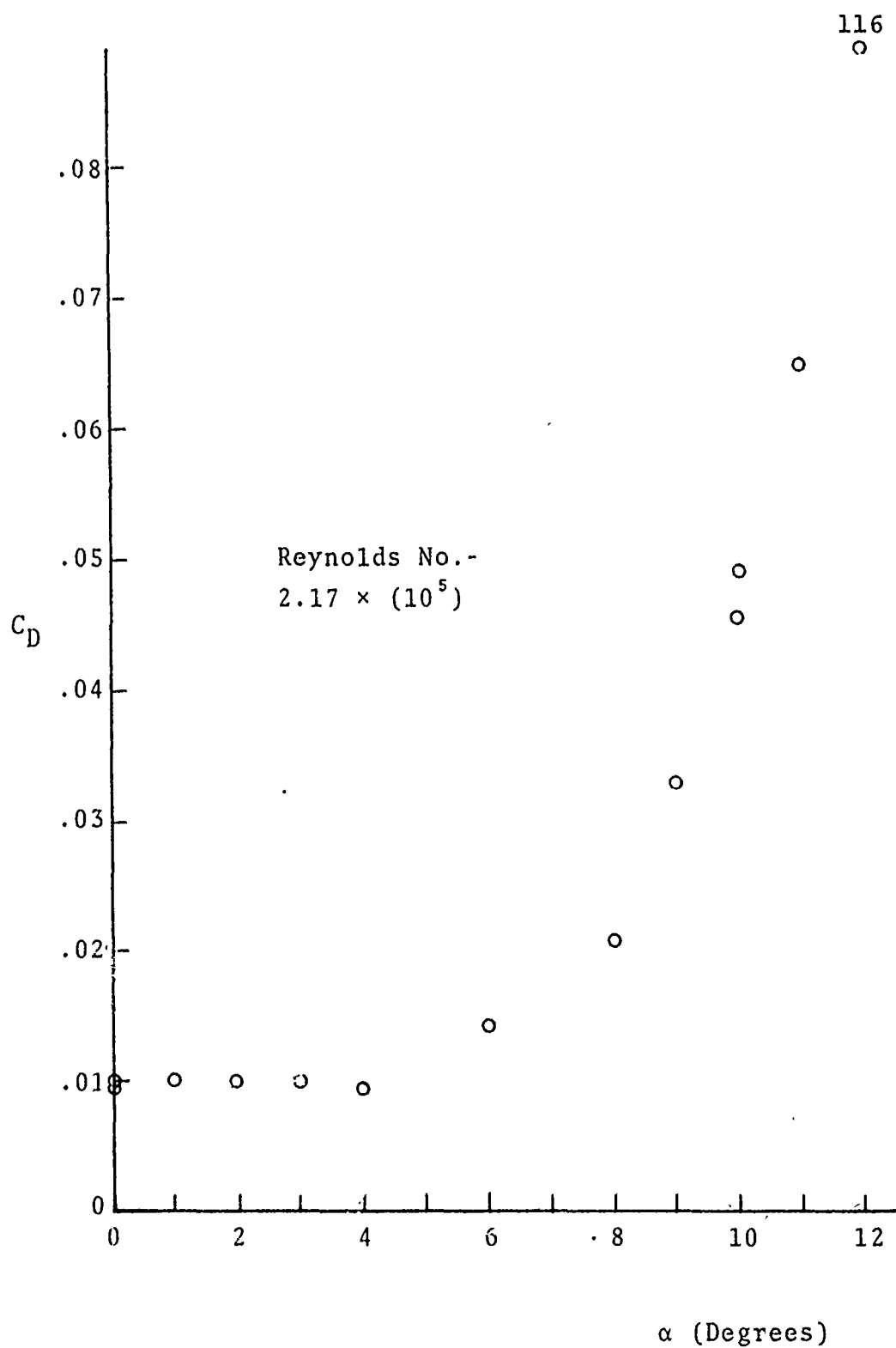
Fig. 16.   Variation of Drag Coefficient with Angle
of Attack (NACA 64009)
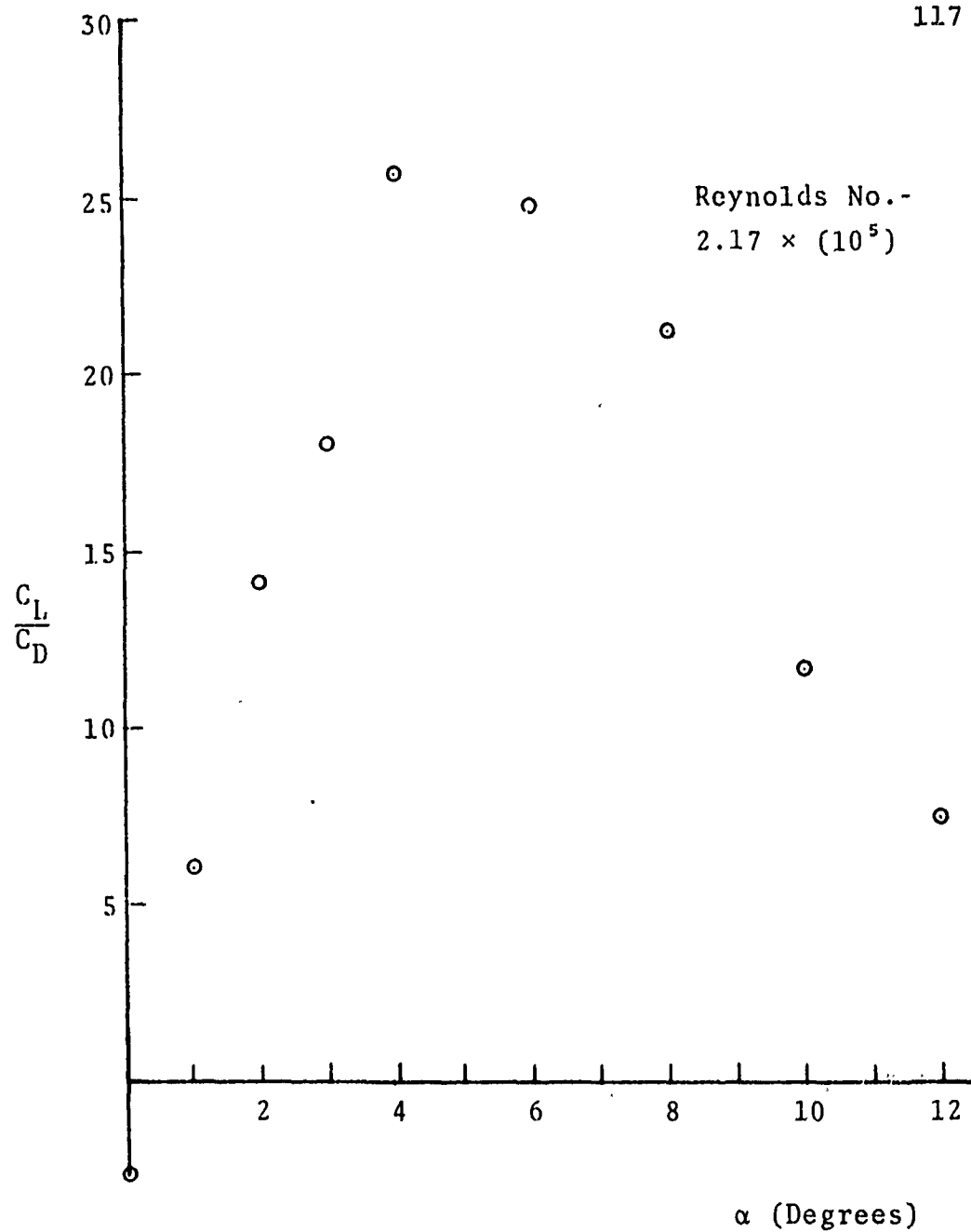
Fig. 17. Variation of Lift-Drag Ratio with Angle of Attack (NACA 64009)
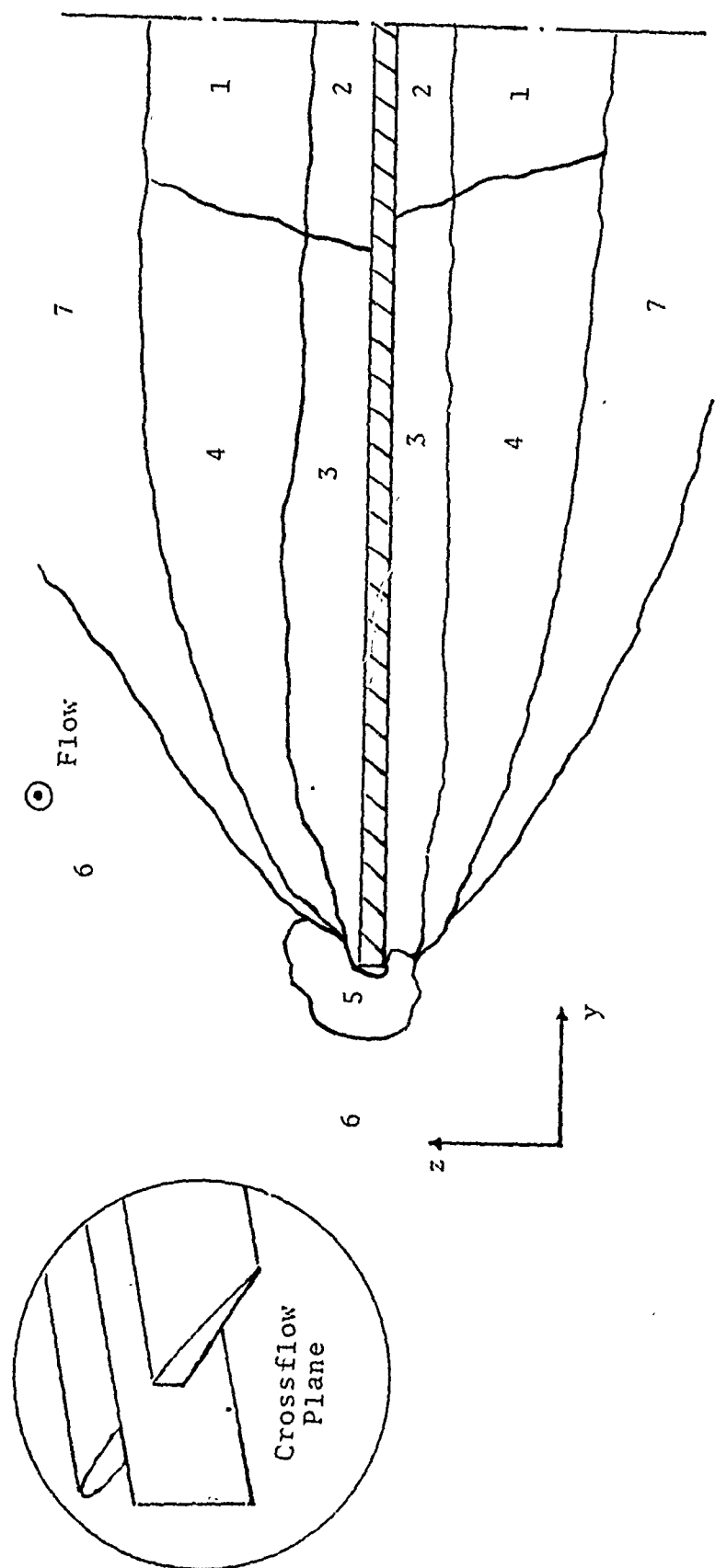
Fig. 18. Flow Regions in the Crossflow Plane
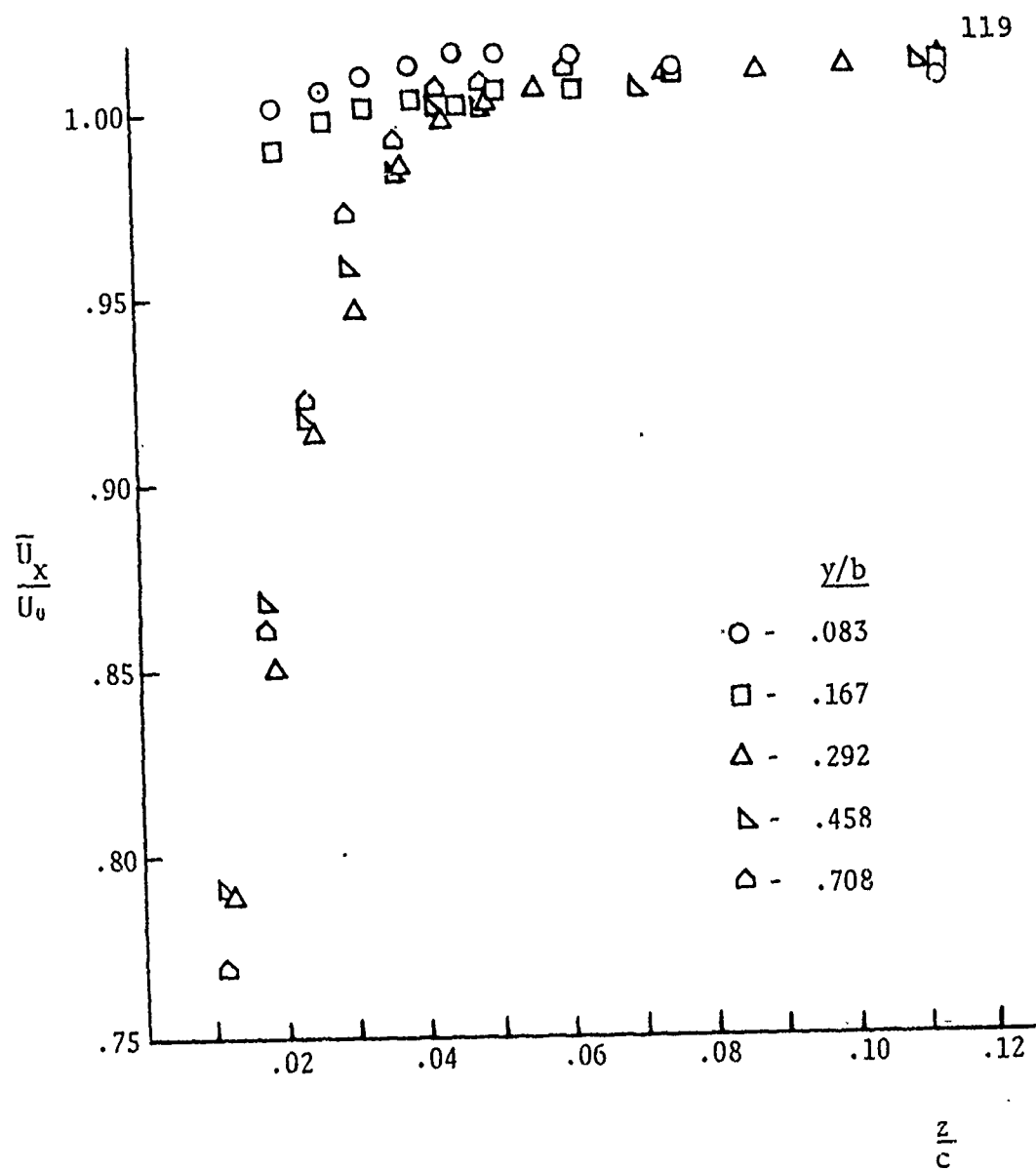
Fig. 19. Mainflow Velocity in the Boundary Layer,
x/c = 0.95
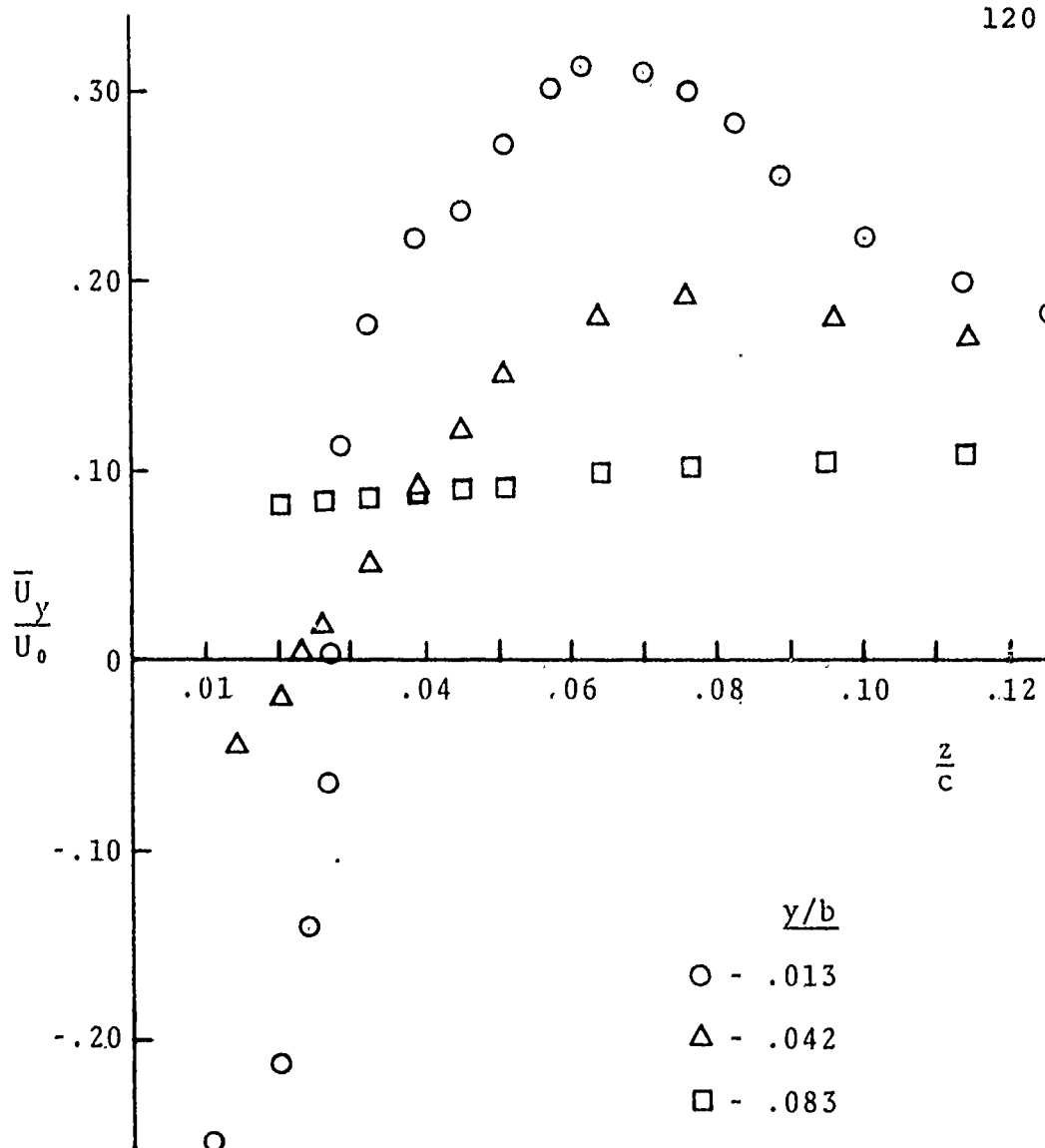
Fig. 20. Crossflow Velocity in the Boundary Layer,
x/c = 0.95
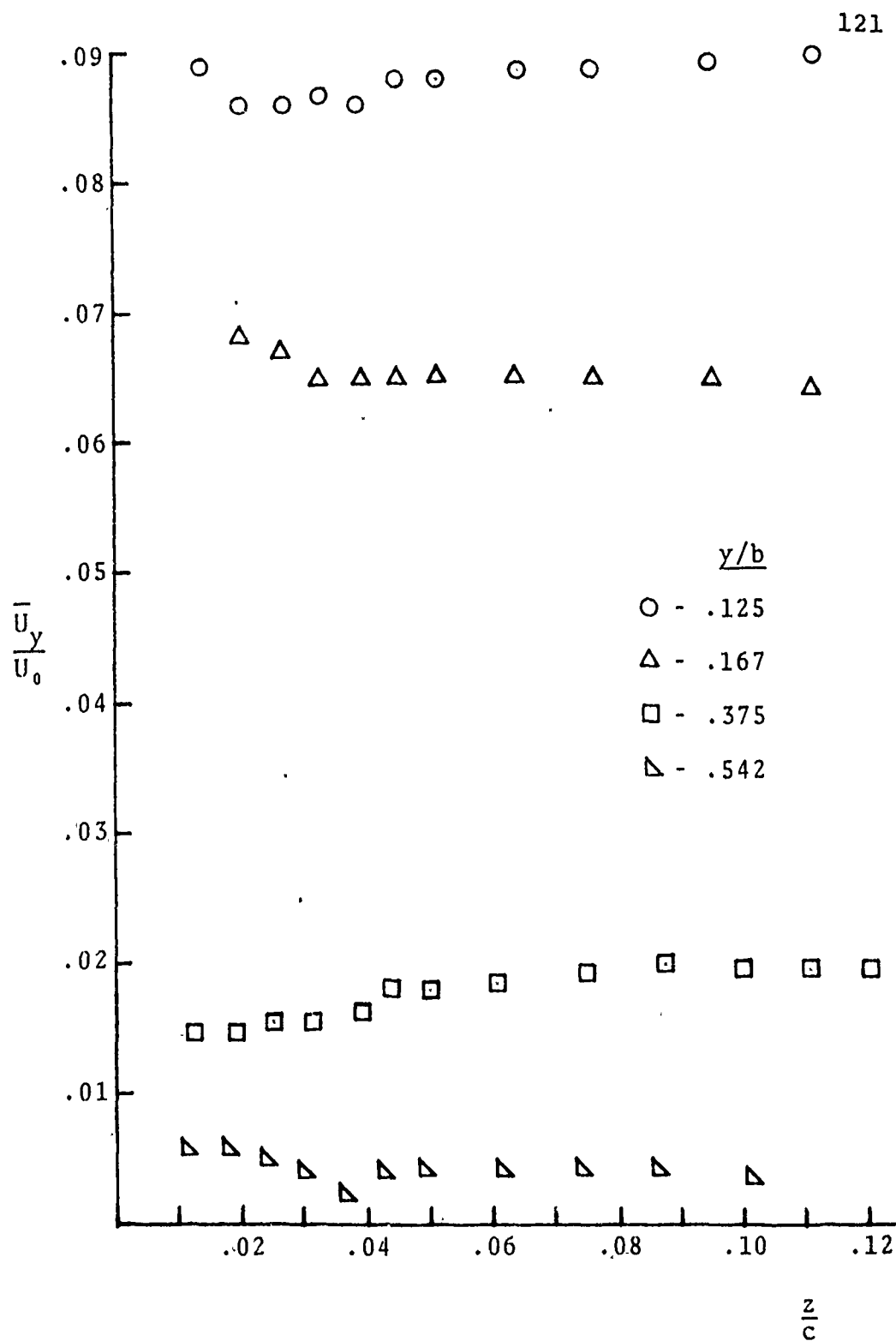
Fig. 21. Crossflow Velocity in the Boundary Layer,
x/c = 0.95
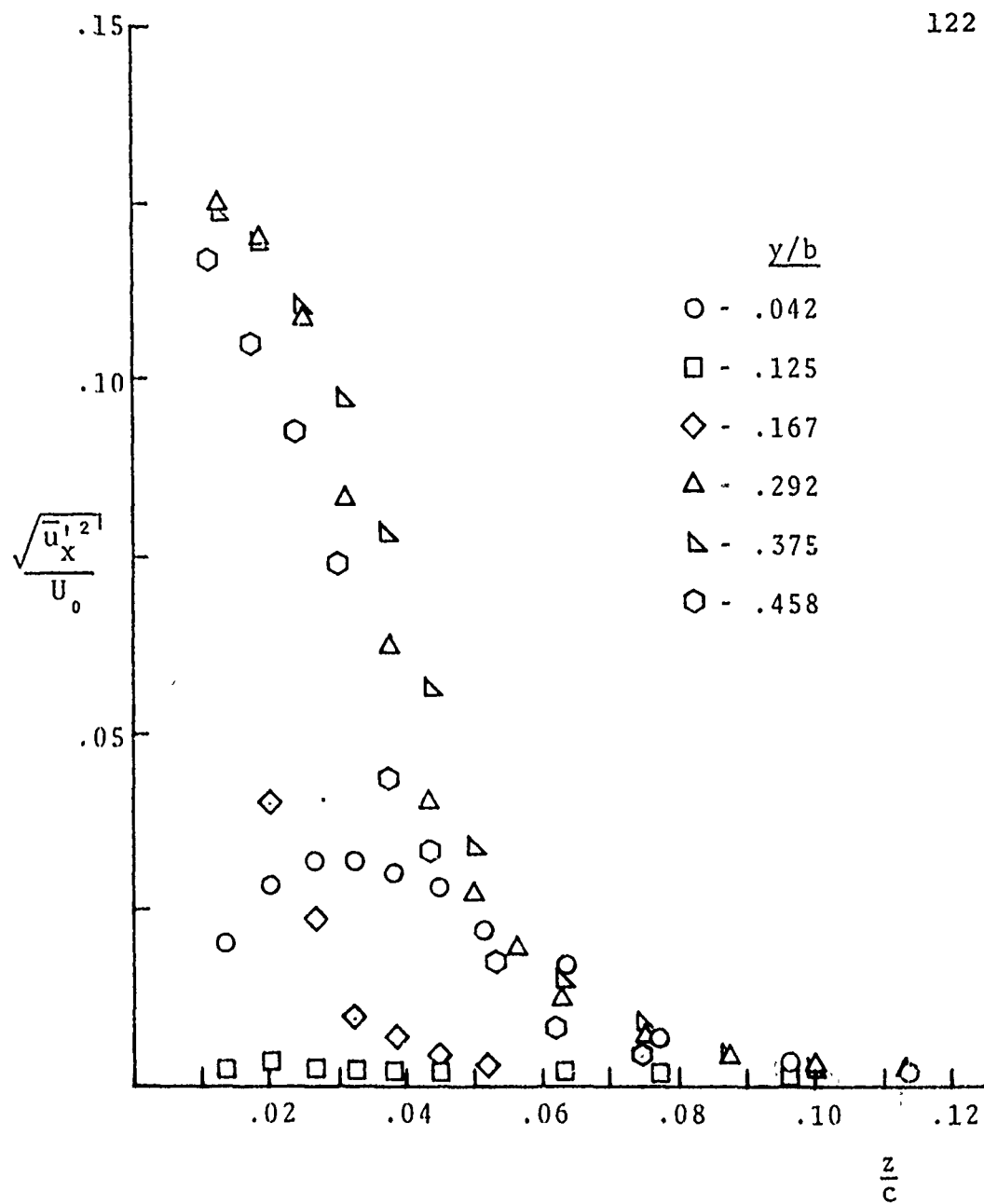
Fig. 22. Intensity of Mainflow Turbulent Component in the Boundary Layer, $x/c = 0.95$
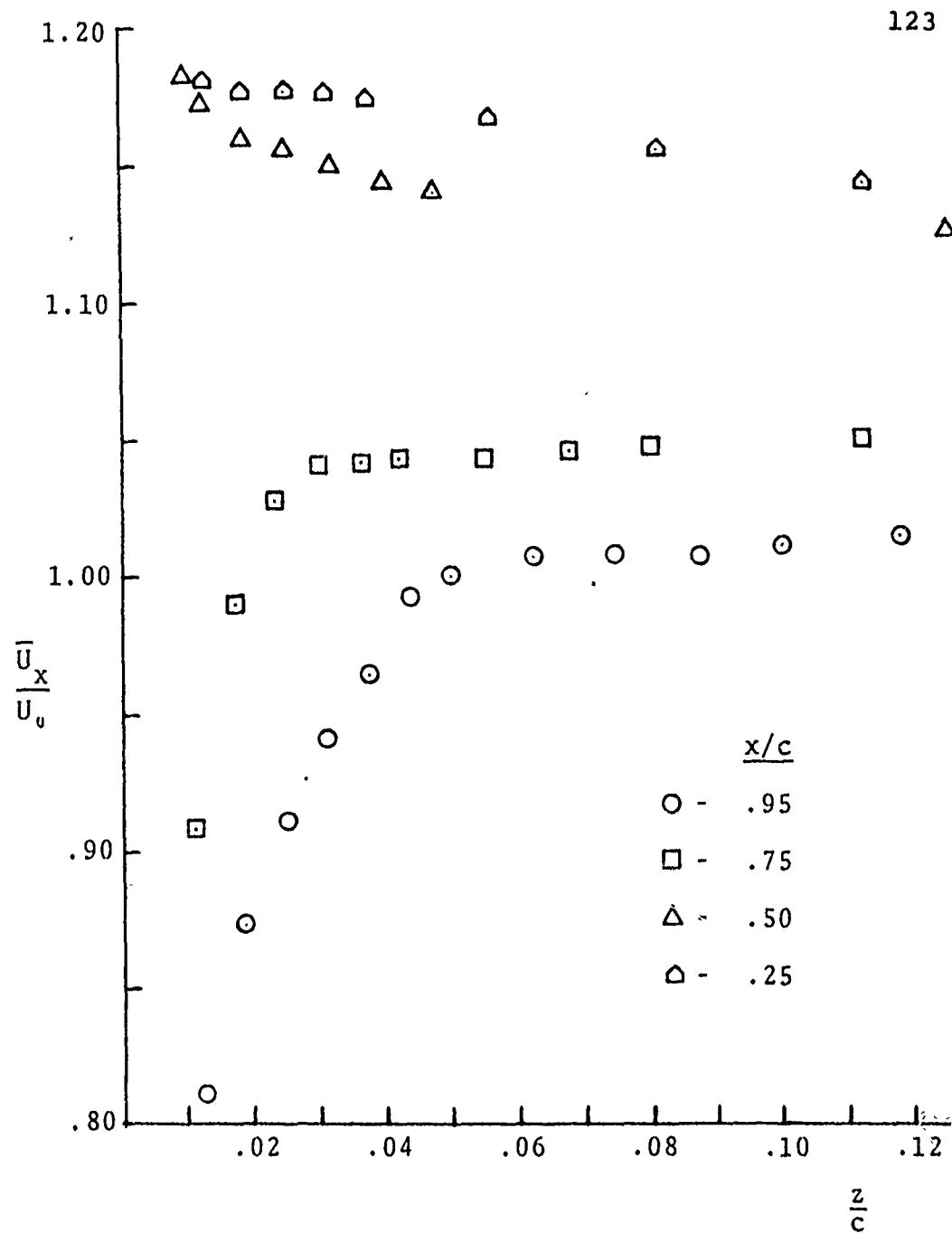
Fig. 23. Mainflow Velocity in the Boundary Layer,
y/b = .375
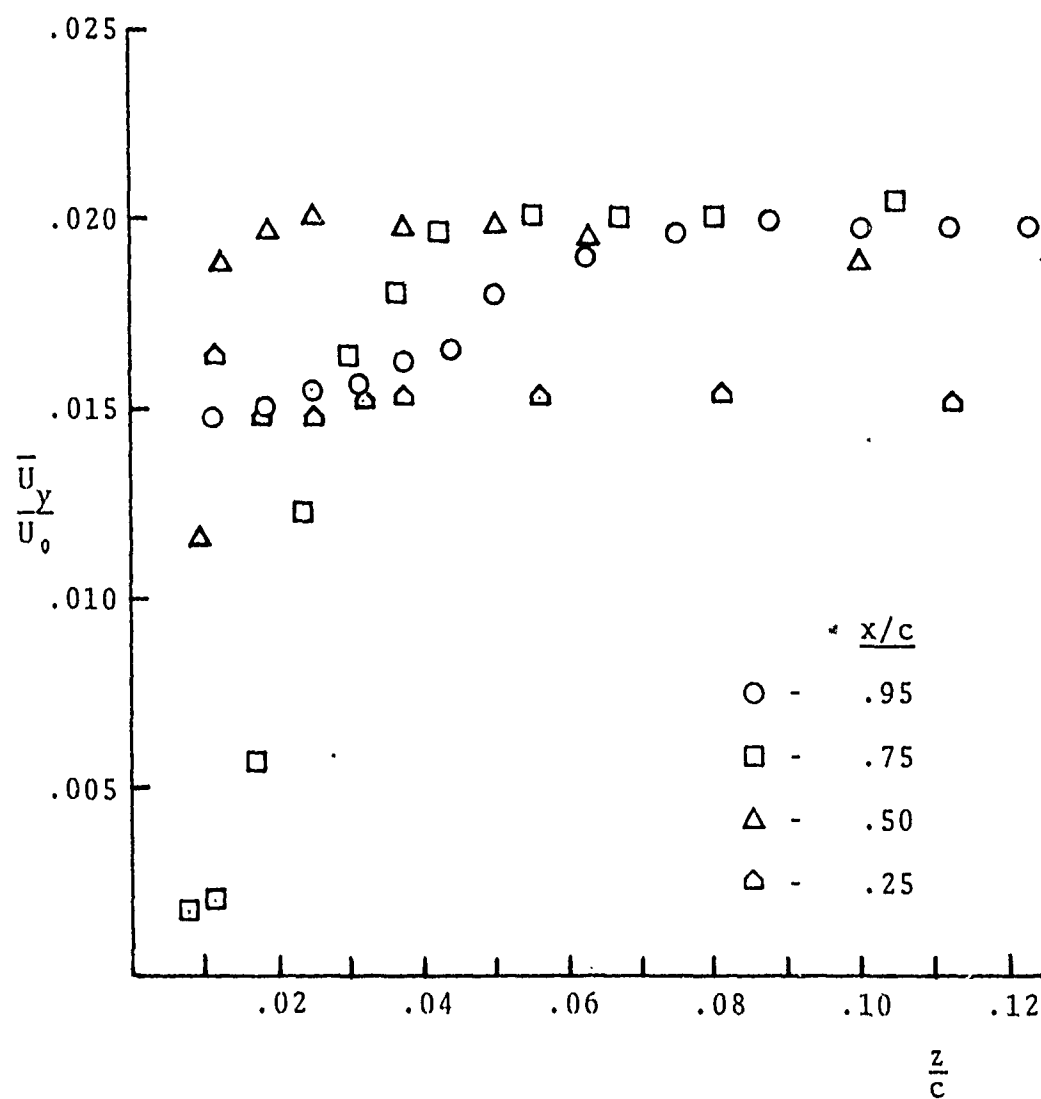
Fig. 24. Crossflow Velocity in the Boundary Layer,
y/b = .375
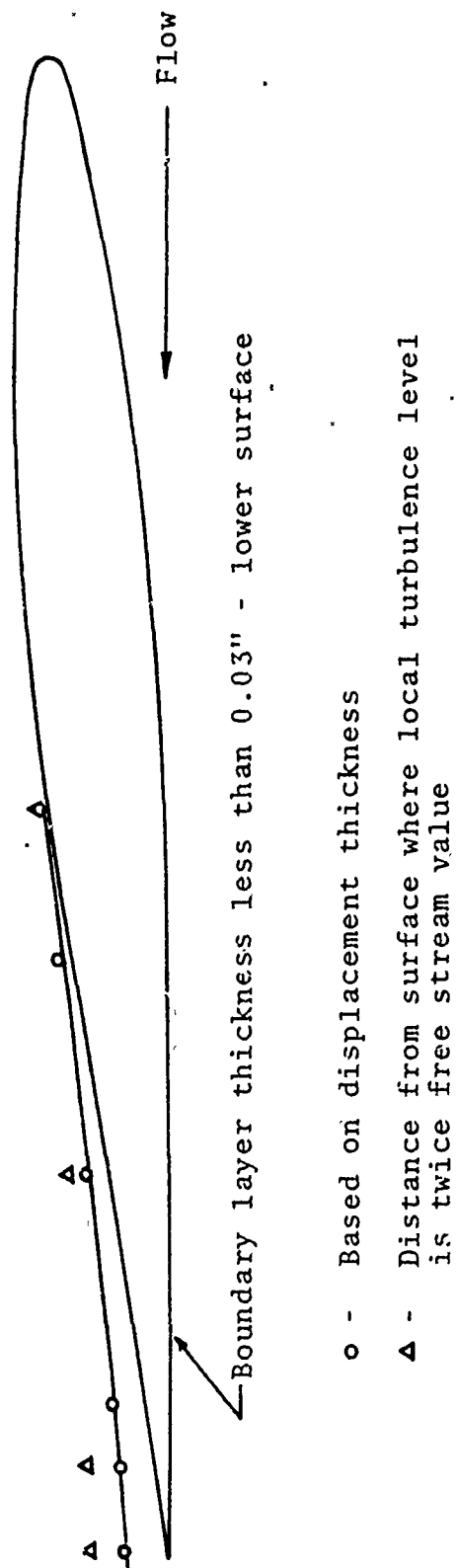
Fig. 25. Chordwise Distribution of Boundary Layer Thickness, Inboard Spanwise Locations

126
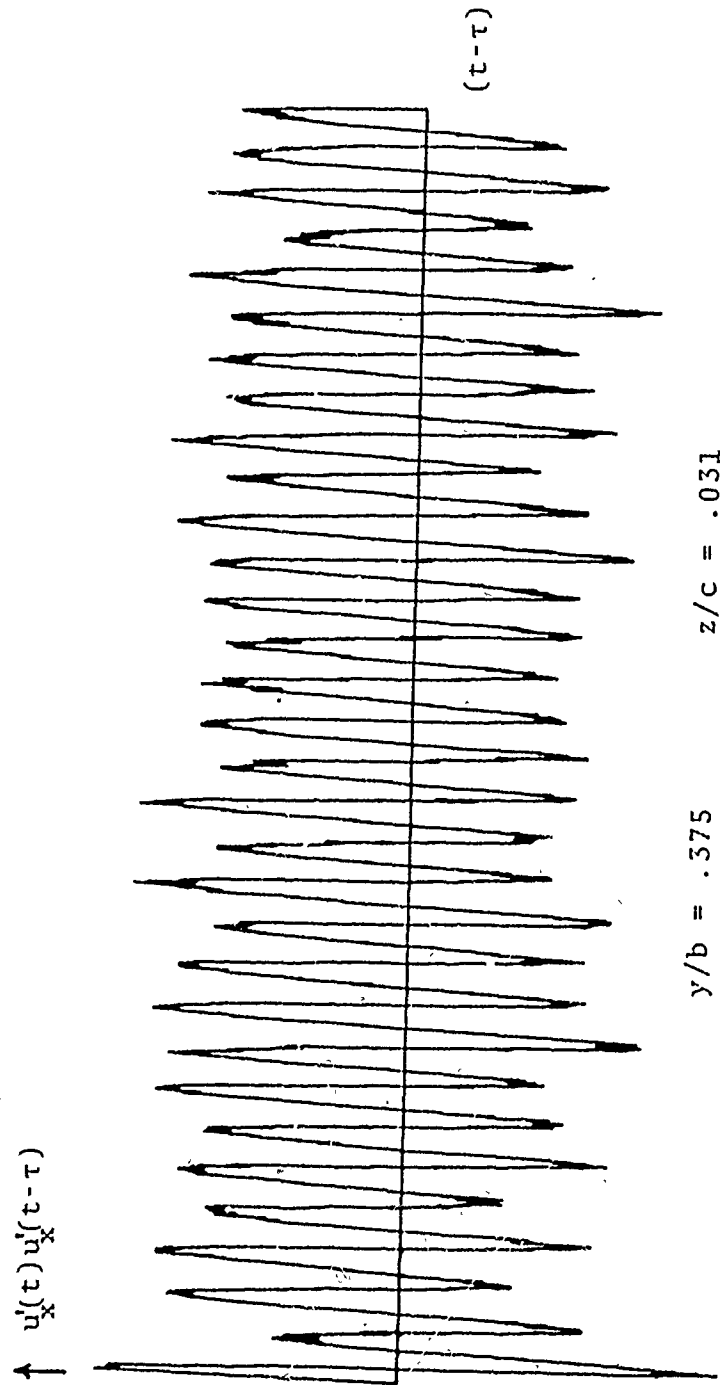
Fig. 26. Autocorrelation function at Outer Edge
of Boundary Layer, $\alpha = 0°$

$y/b = .375$ $z/c = .031$
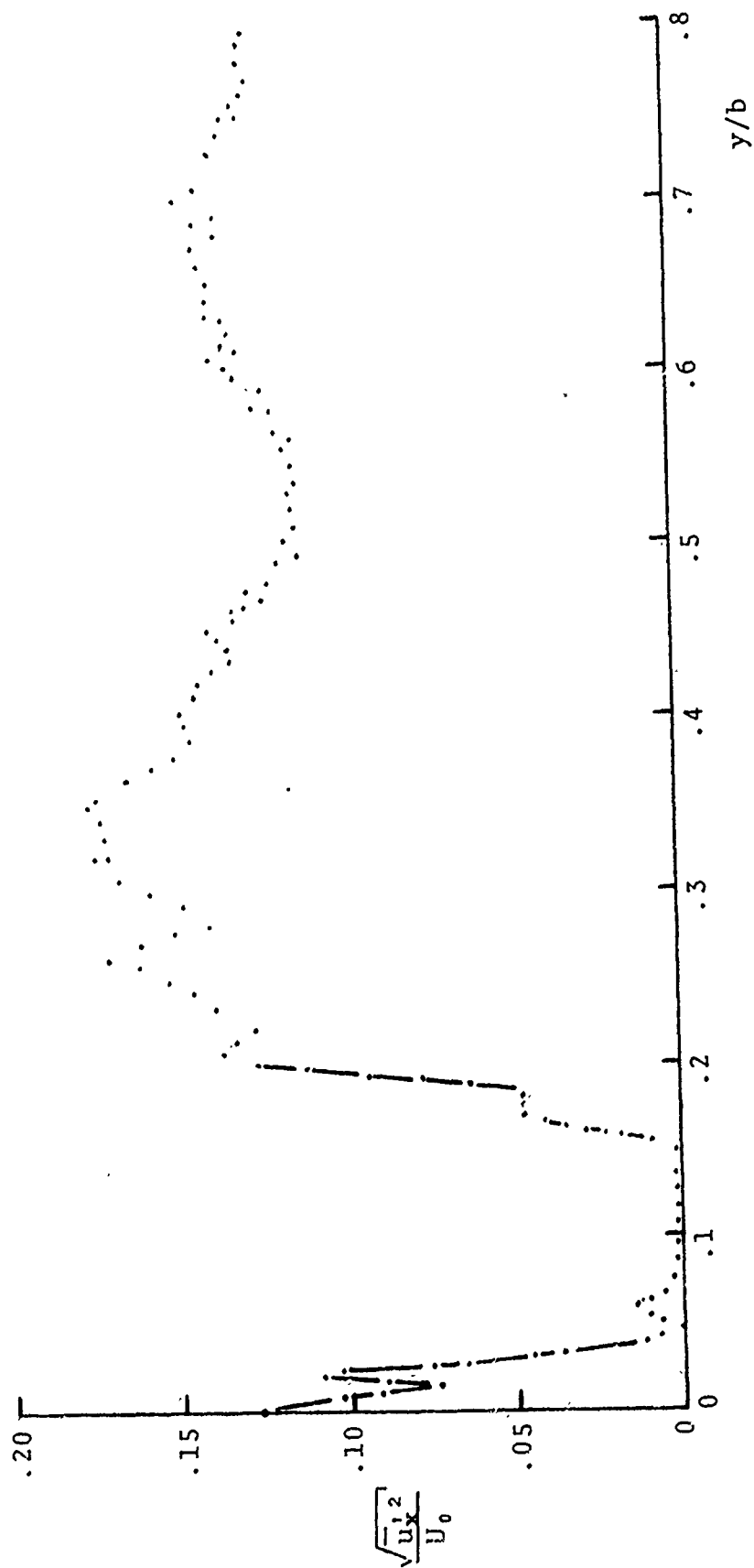
Fig. 27. Spanwise Variation of Turbulence Level in Boundary Layer, x/c = 0.75, z/c = .01, Upper Surface

127
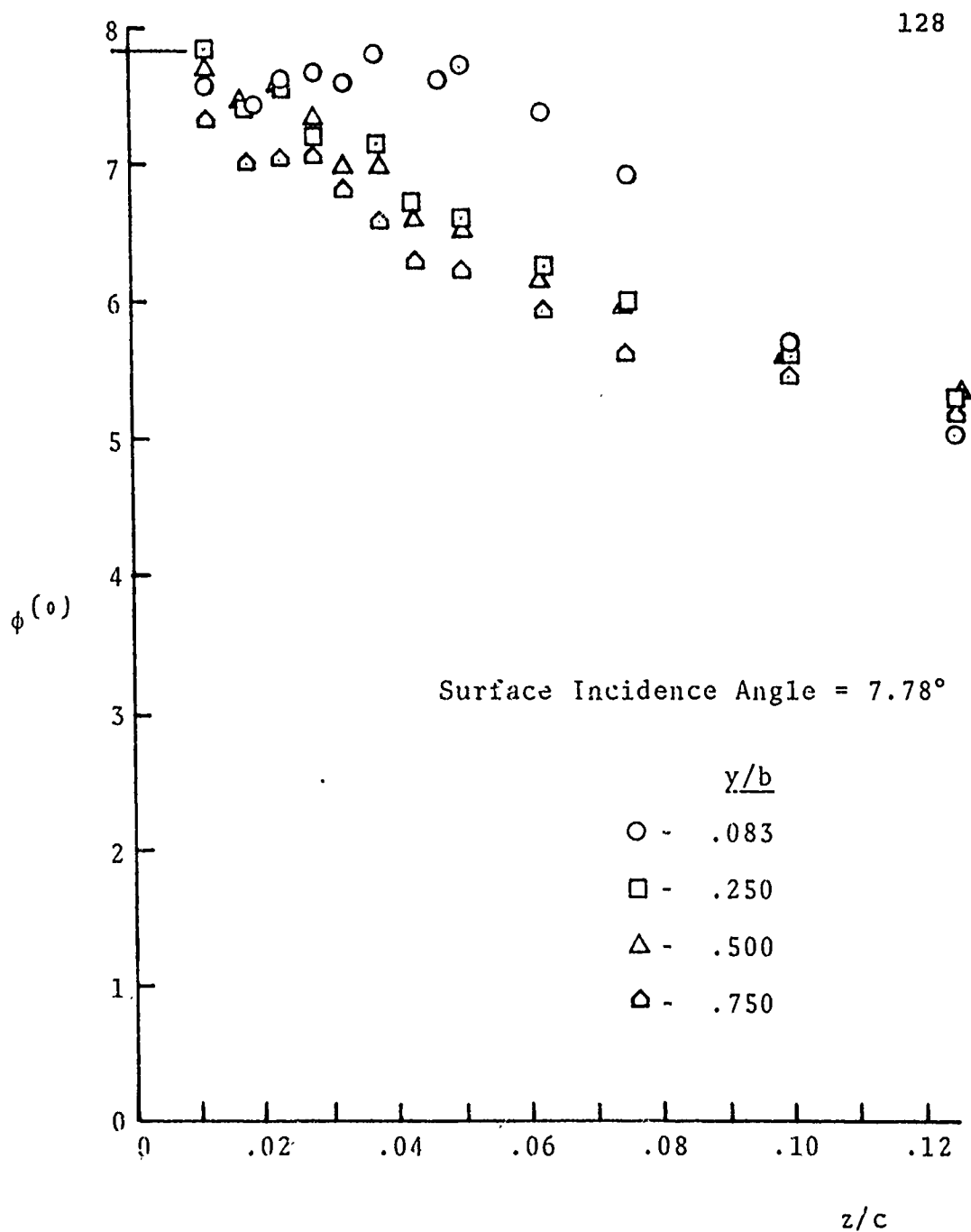
Fig. 28. Downwash Angle Variation with Distance from Upper Surface, x/c = .98
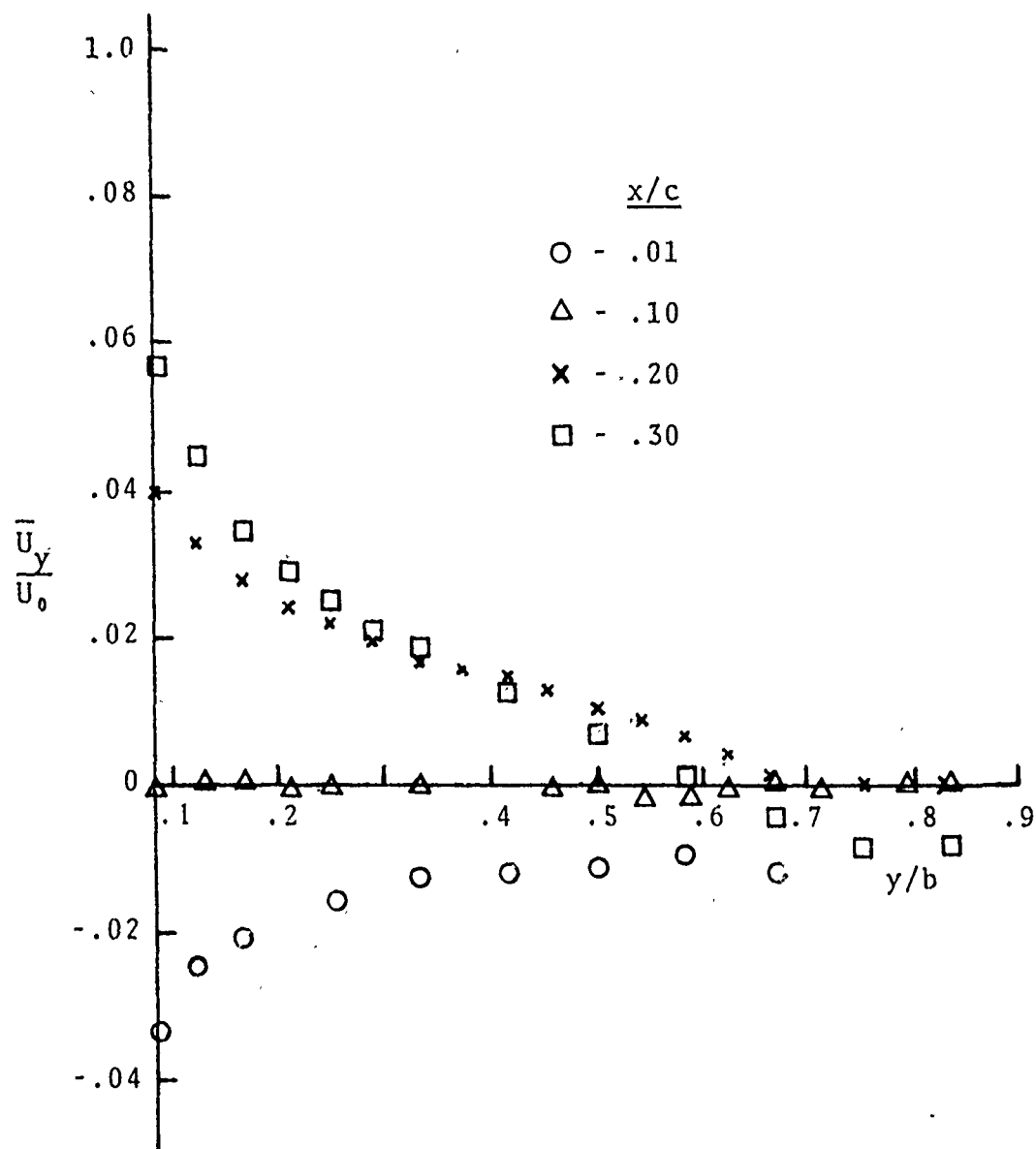
Fig. 29. Crossflow Velocity Variation in the Inboard Region, Upper Surface
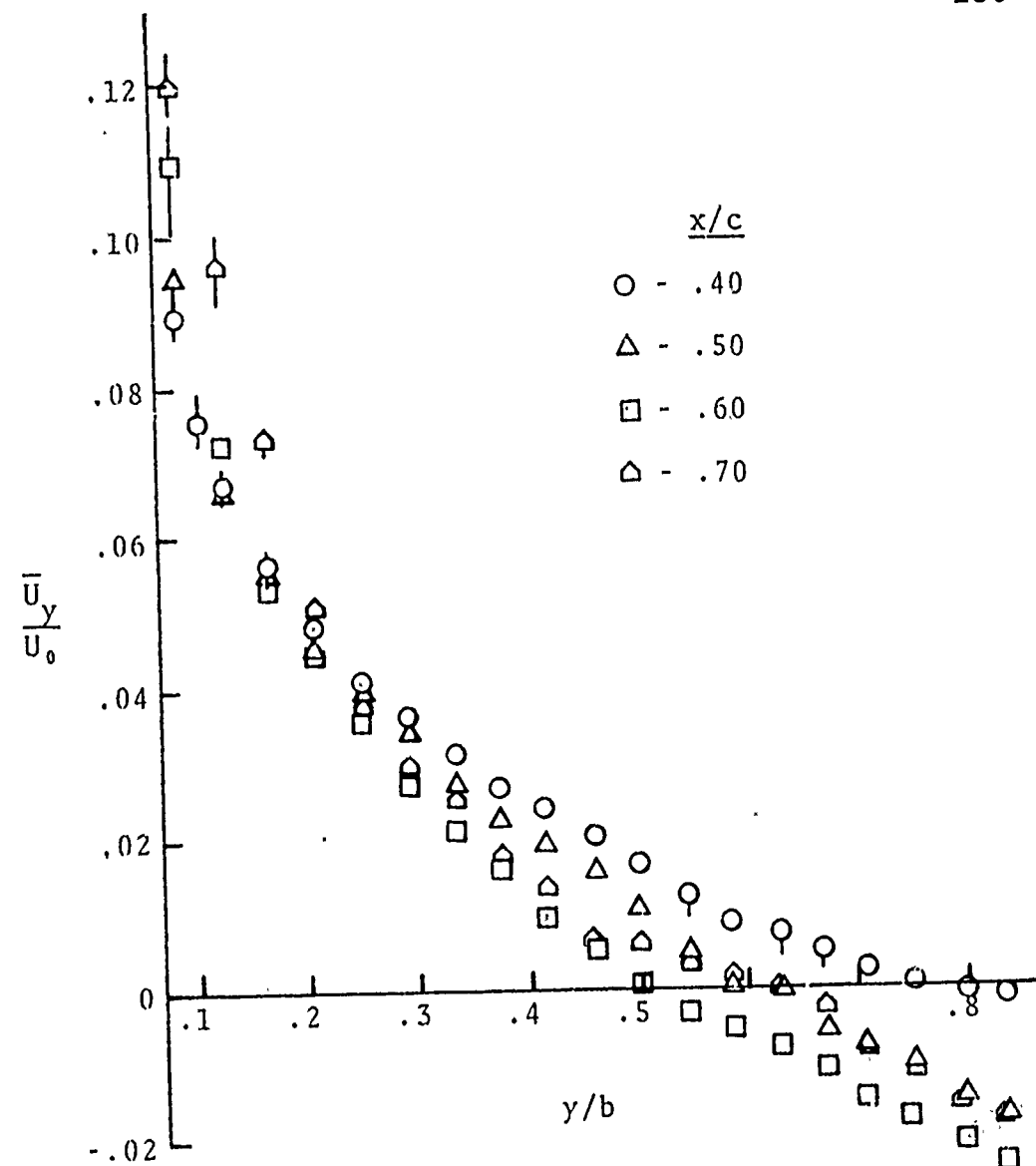
Fig. 30. Crossflow Velocity Variation in the
Inboard Region, Upper Surface
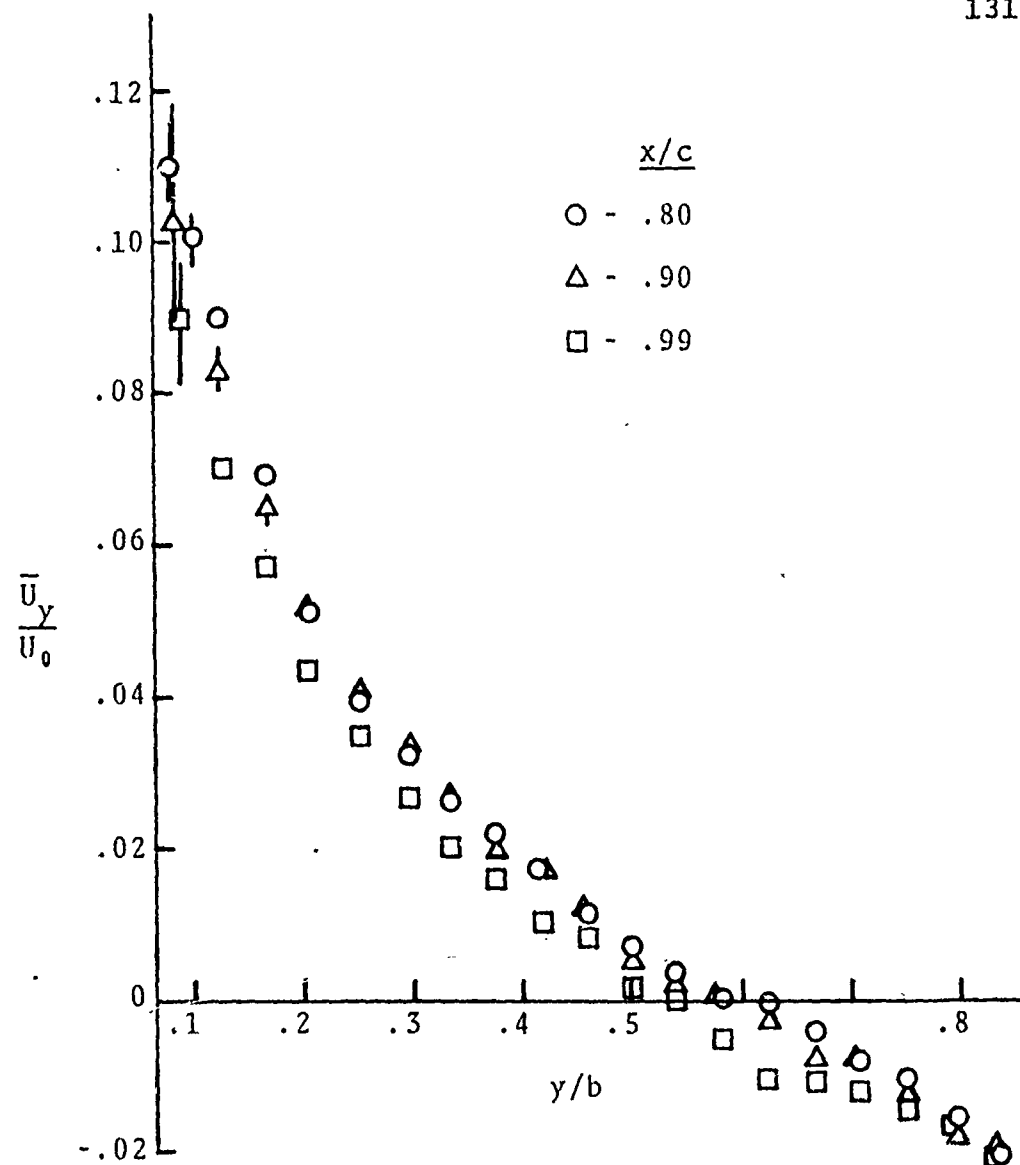
Fig. 31. Crossflow Velocity Variation in the
Inboard Region, Upper Surface
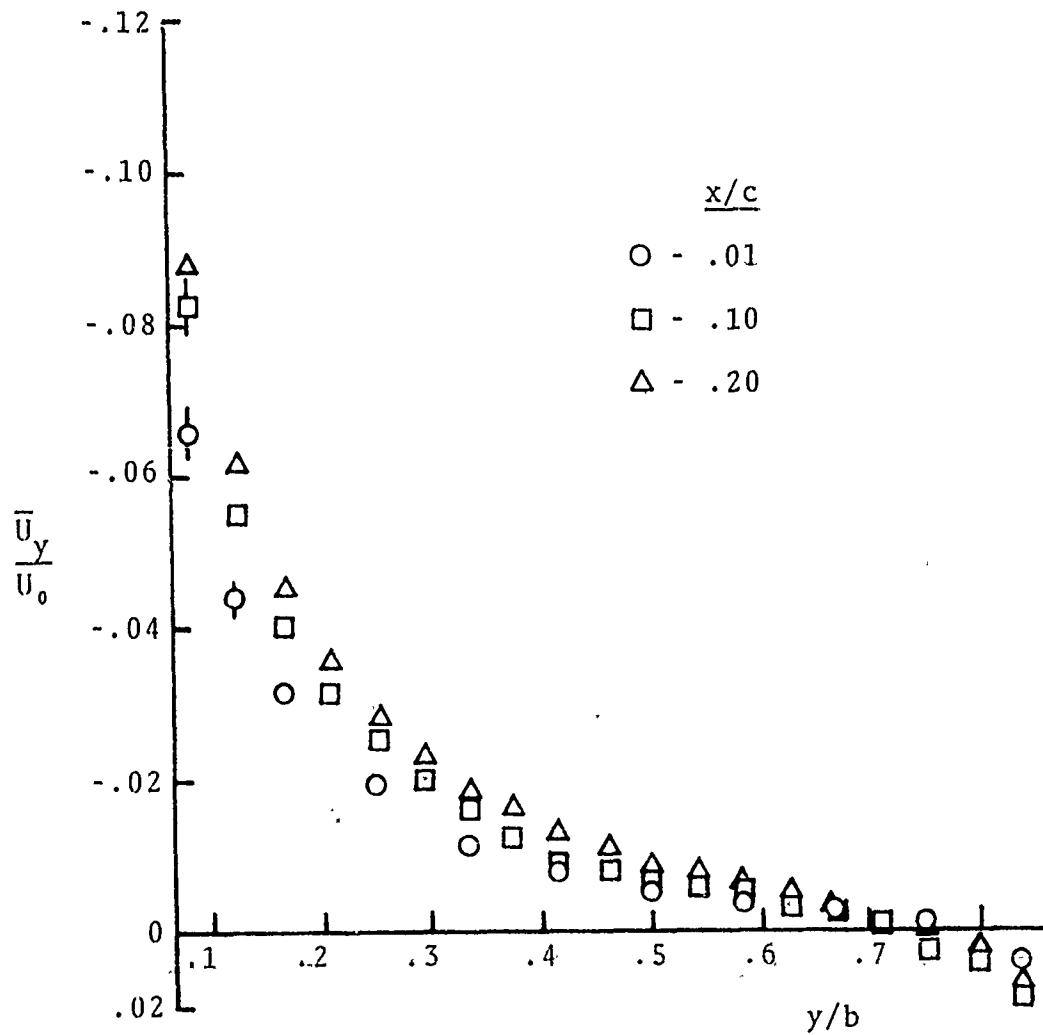
Fig. 32. Crossflow Velocity Variation in the
Inboard Region, Lower Surface
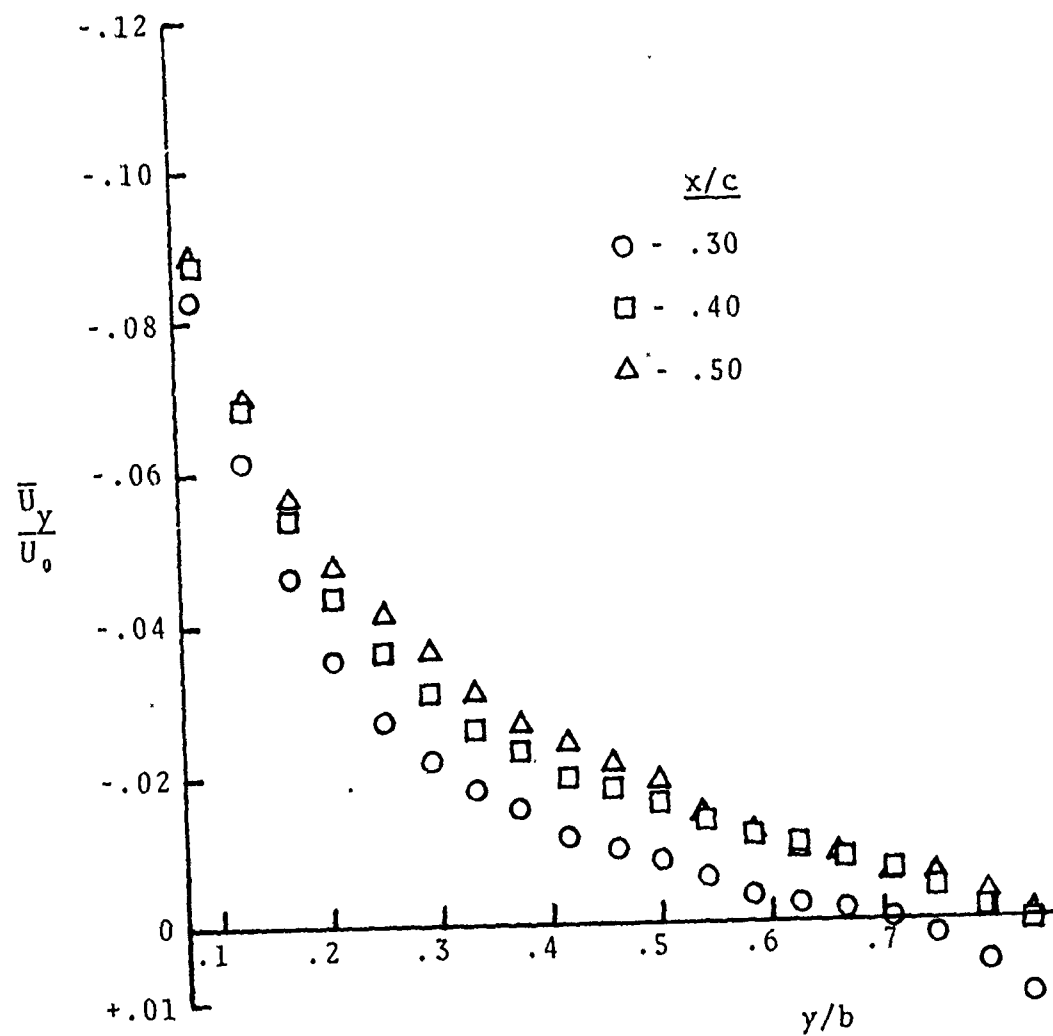
Fig. 33.   Crossflow Velocity Variation in the Inboard Region, Lower Surface
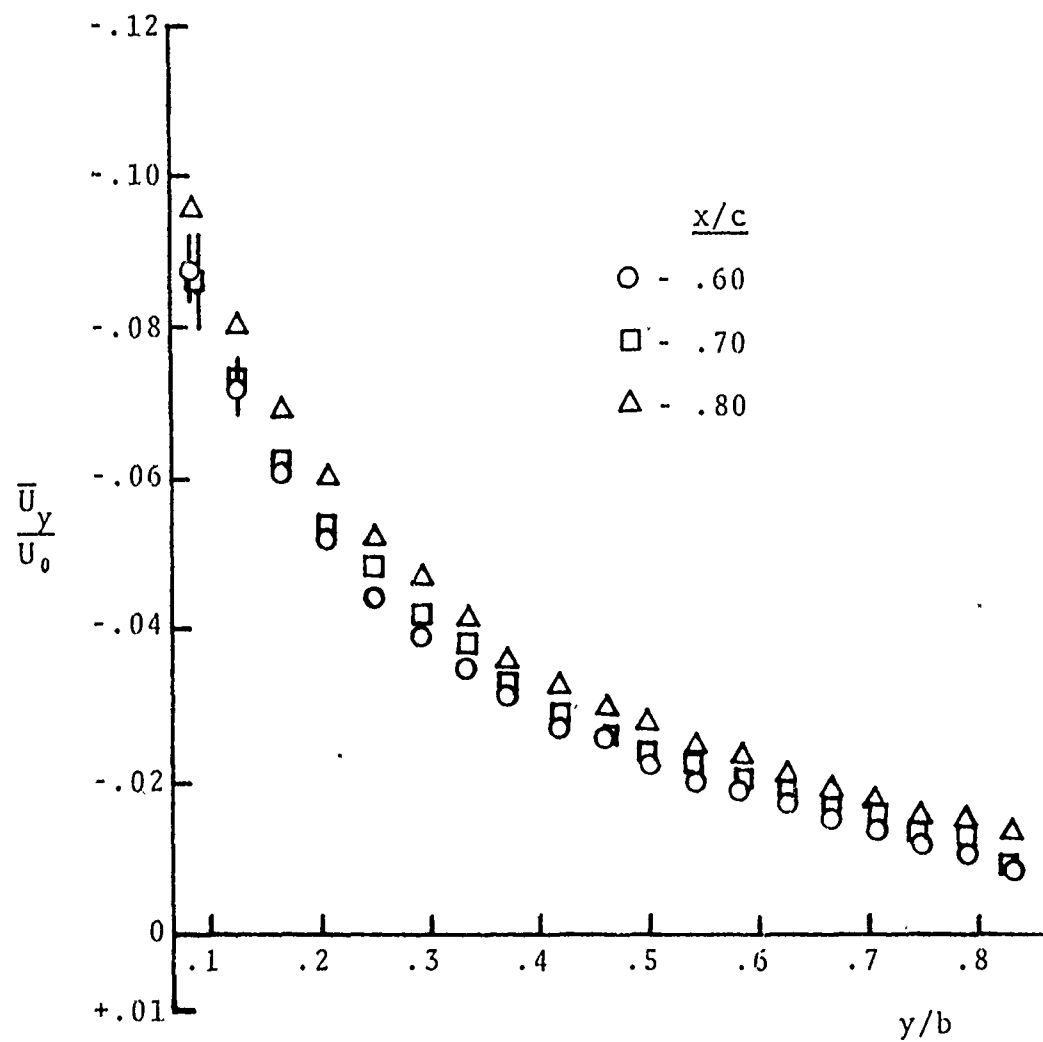
Fig. 34. Crossflow Velocity Variation in the Inboard
Region, Lower Surface
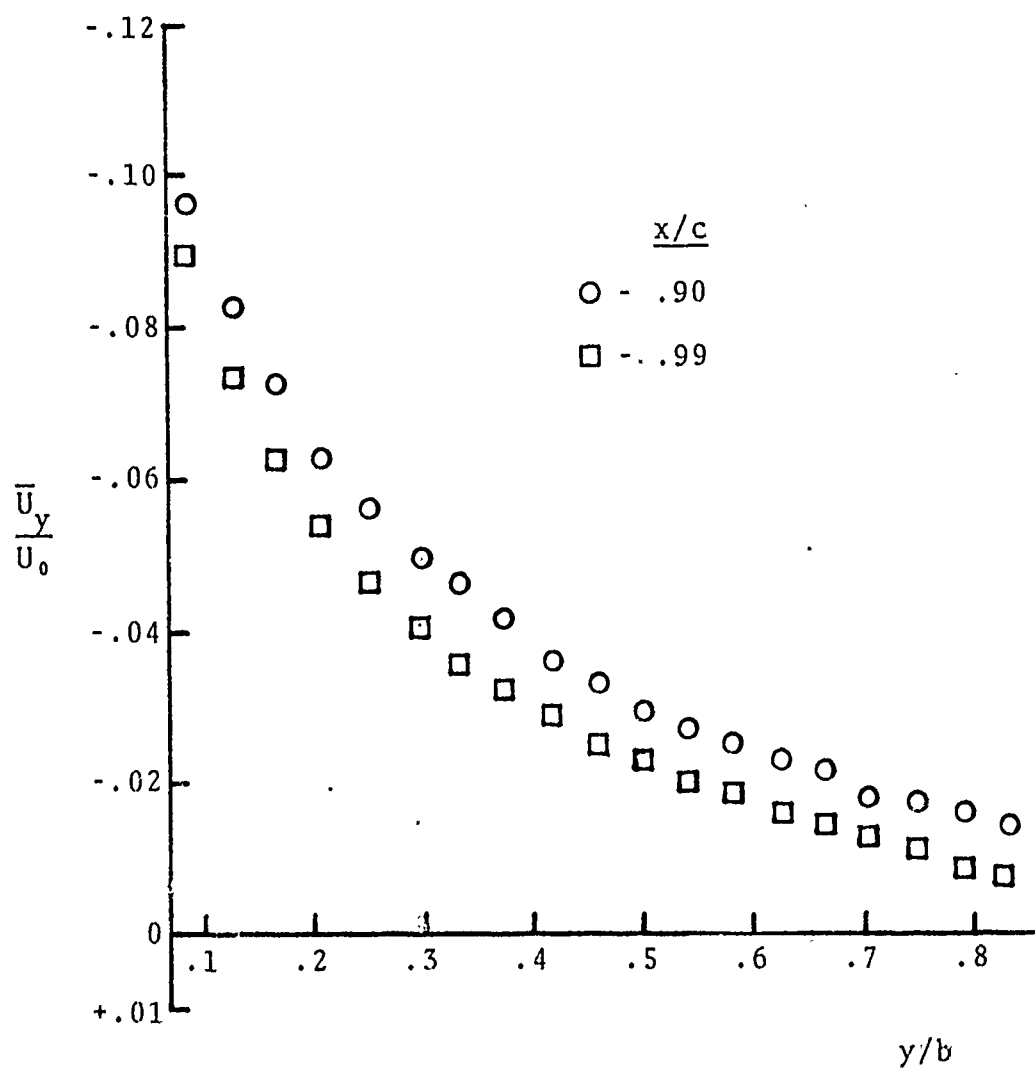
Fig. 35. Crossflow Velocity Variation in the Inboard Region, Lower Surface
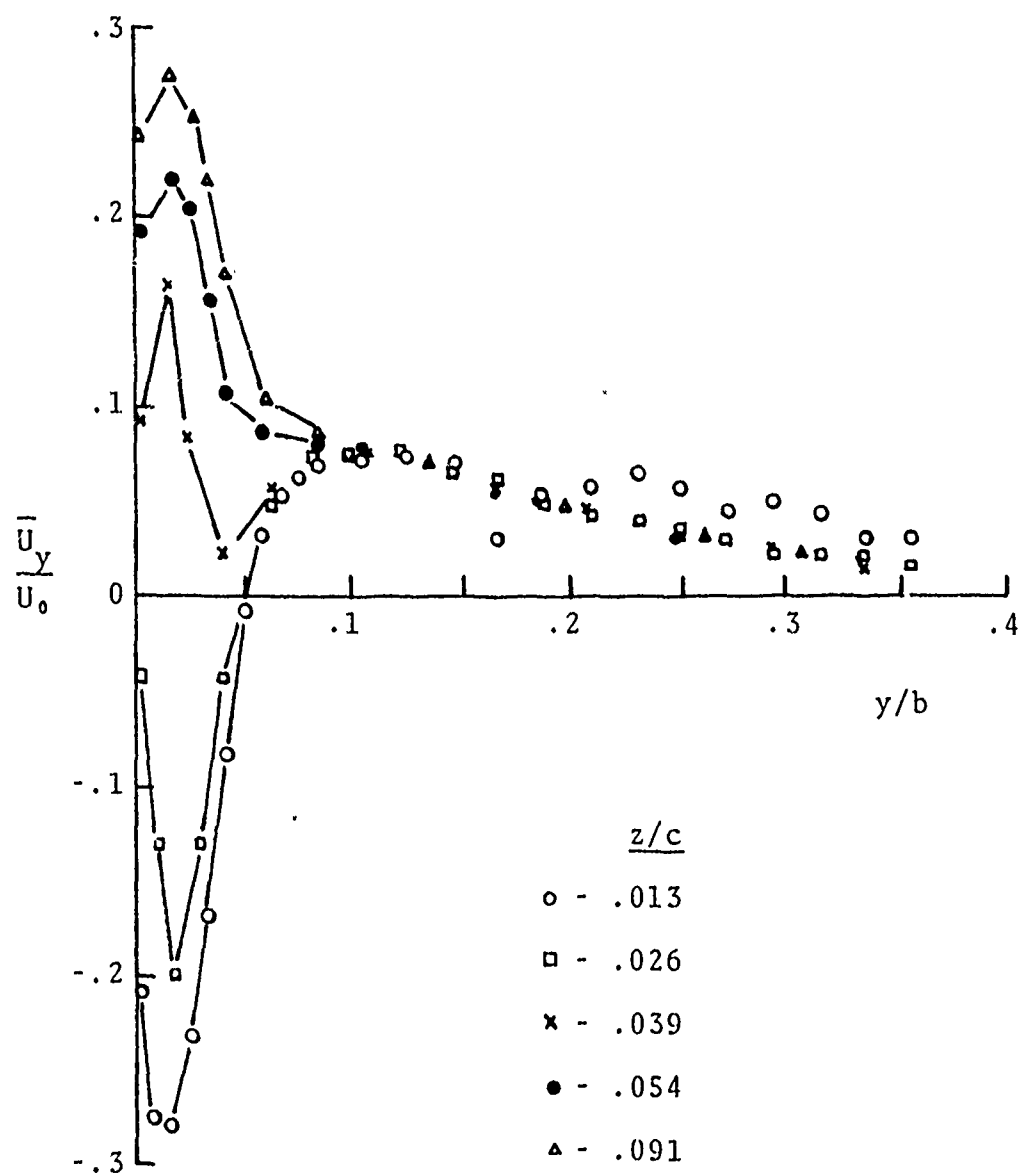
Fig. 36. Crossflow Velocity Variation in the Tip Region,
x/c = 0.98, Upper Surface
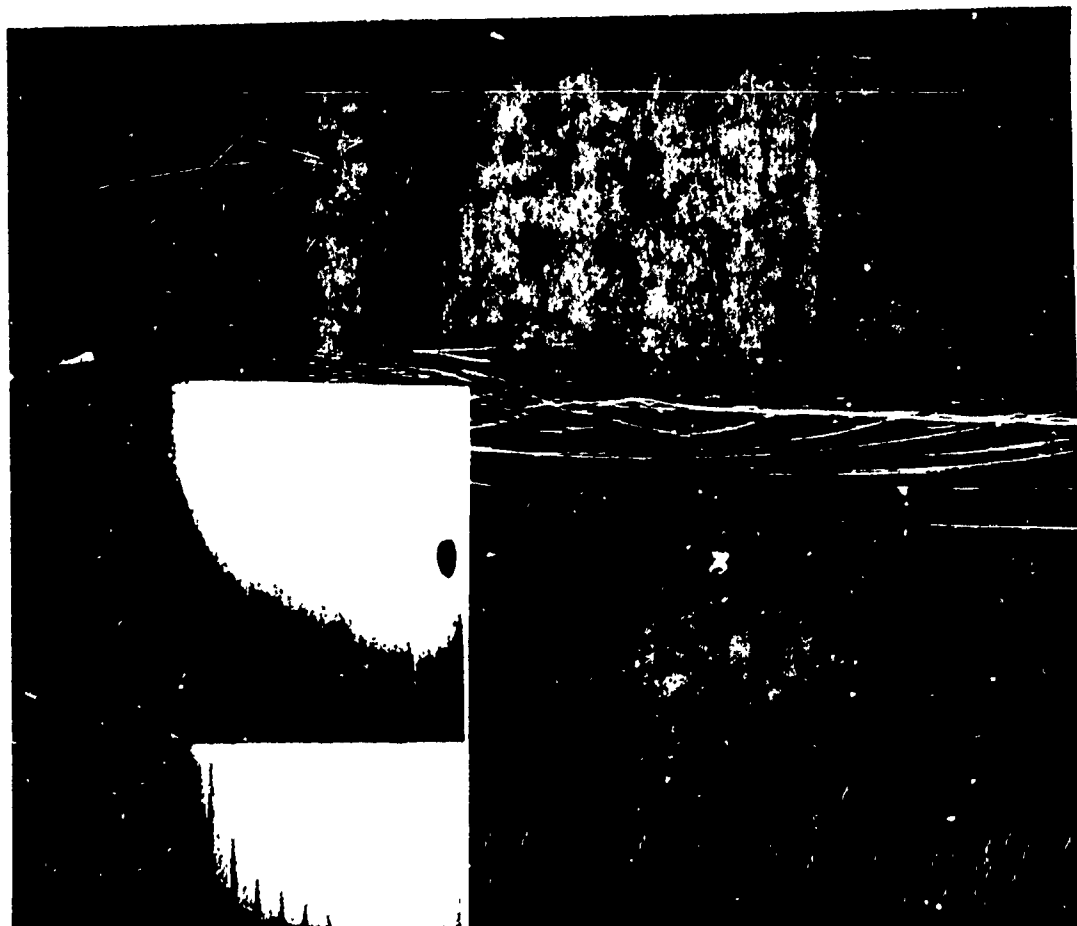
FIG. 37 FLOW FIELD NEAR THE WING TIP, HELIUM BUBBLE
TECHNIQUE, $\alpha = 4°$, $U_o = 60$ ft/sec

⊙ Flow ├──── 1" ────┤
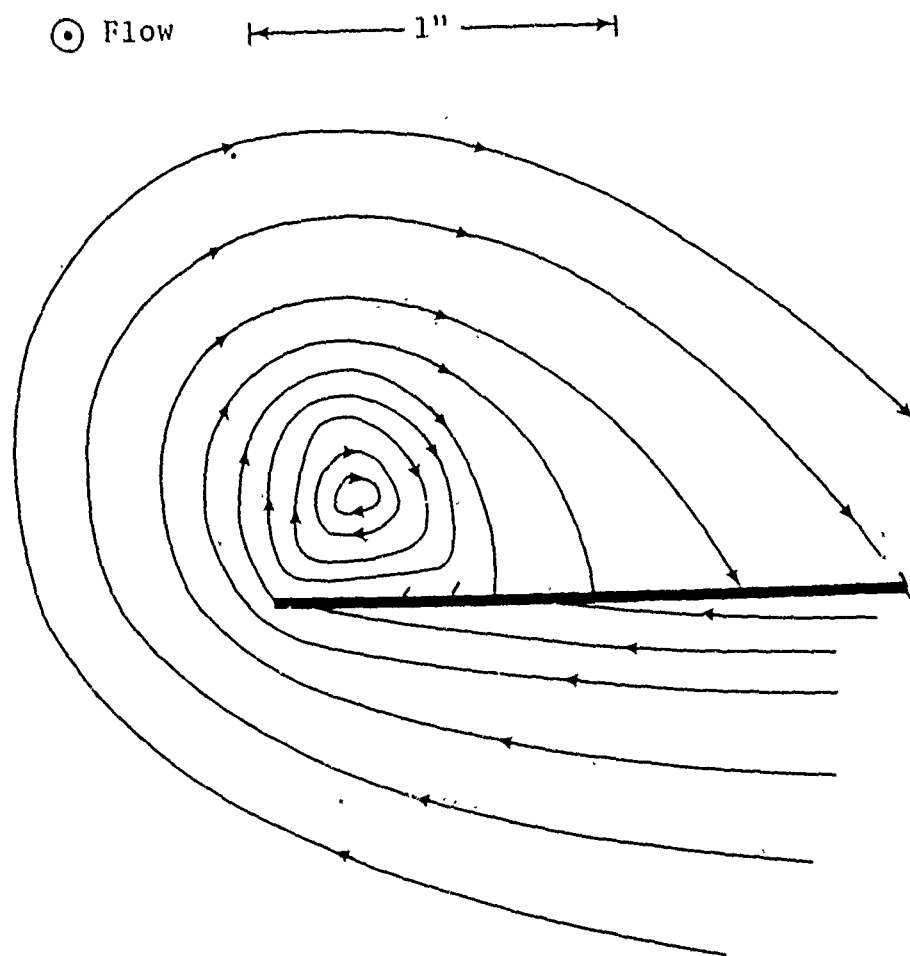
Fig. 38. Sketch of Streamlines in the
Quasi-Trefftz Plane, x/c = .99, α = 4°
Wing Tip Region
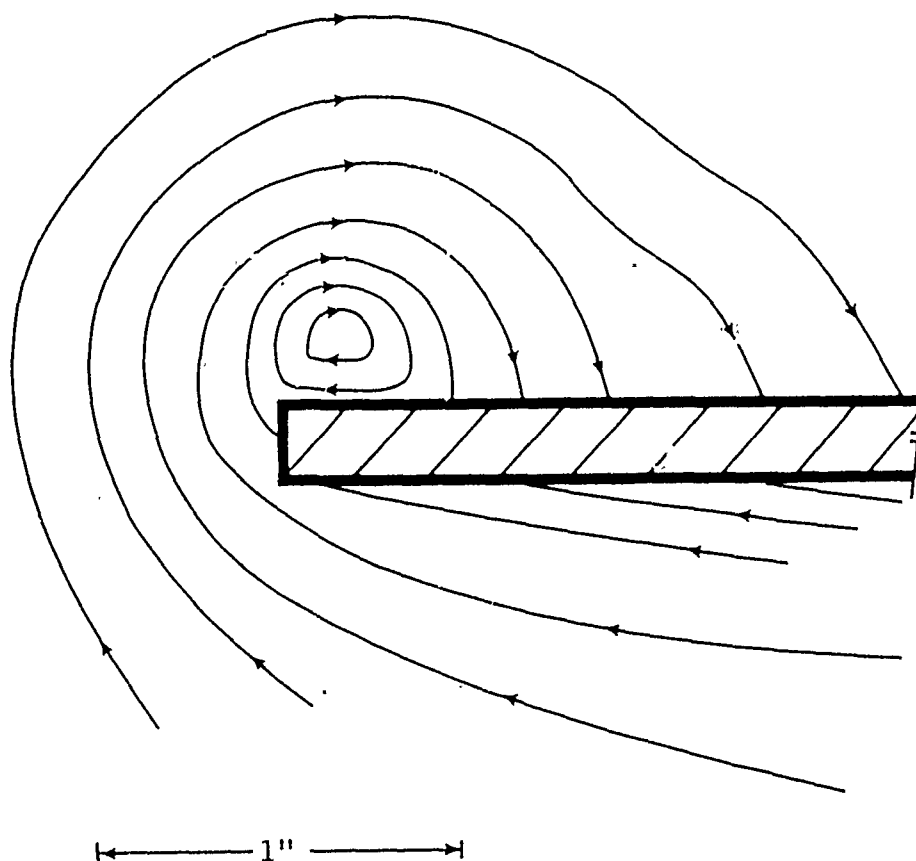
⊙ Flow

Fig. 39. Sketch of Streamlines in the
Quasi-Trefftz Plane, $x/c = .80$, $\alpha = 4°$
Wing Tip Region
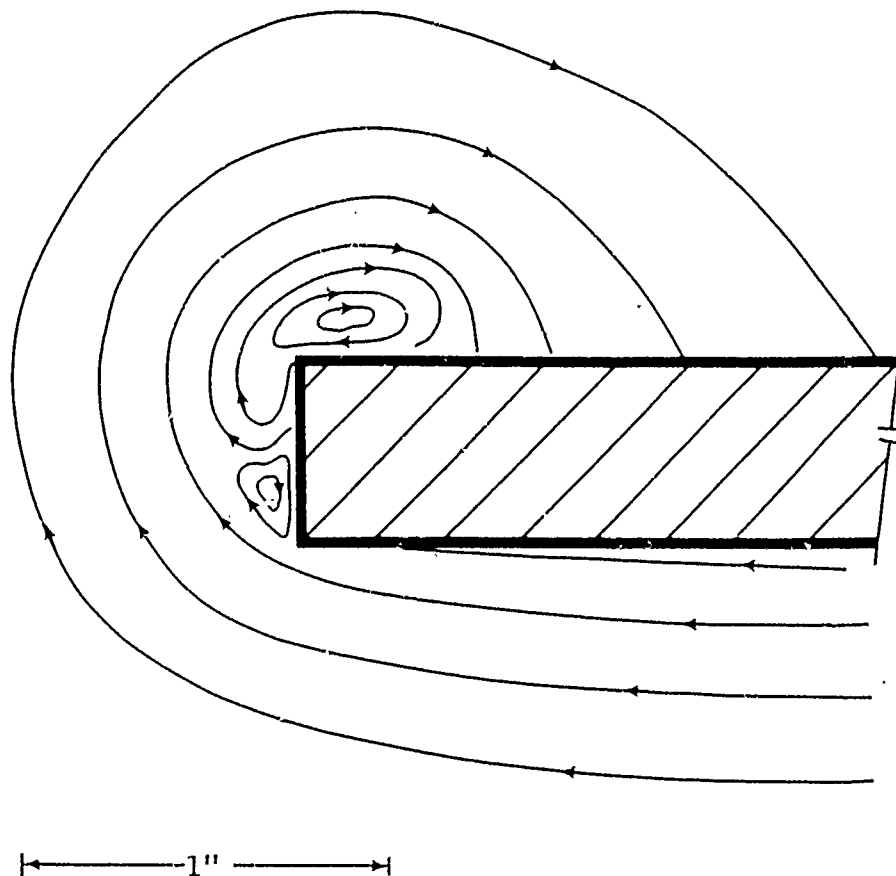
⊙ Flow

Fig. 40. Sketch of Streamlines in the
Quasi-Trefftz Plane, x/c = .60, α = 4°
Wing Tip Region

⊙ Flow

|← 1" →|
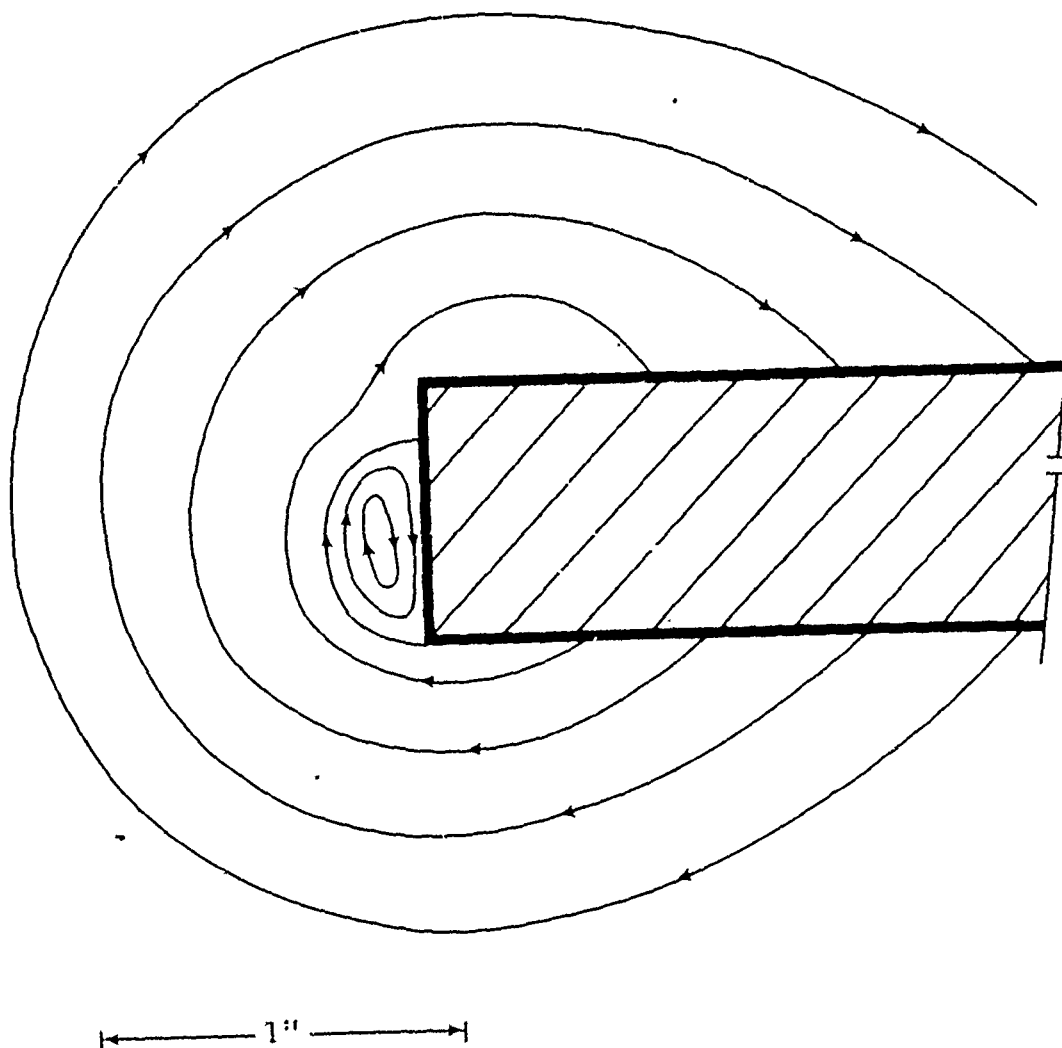
Fig. 41. Sketch of Streamlines in the
Quasi-Trefftz Plane, $x/c = .40$, $\alpha = 4°$
Wing Tip Region
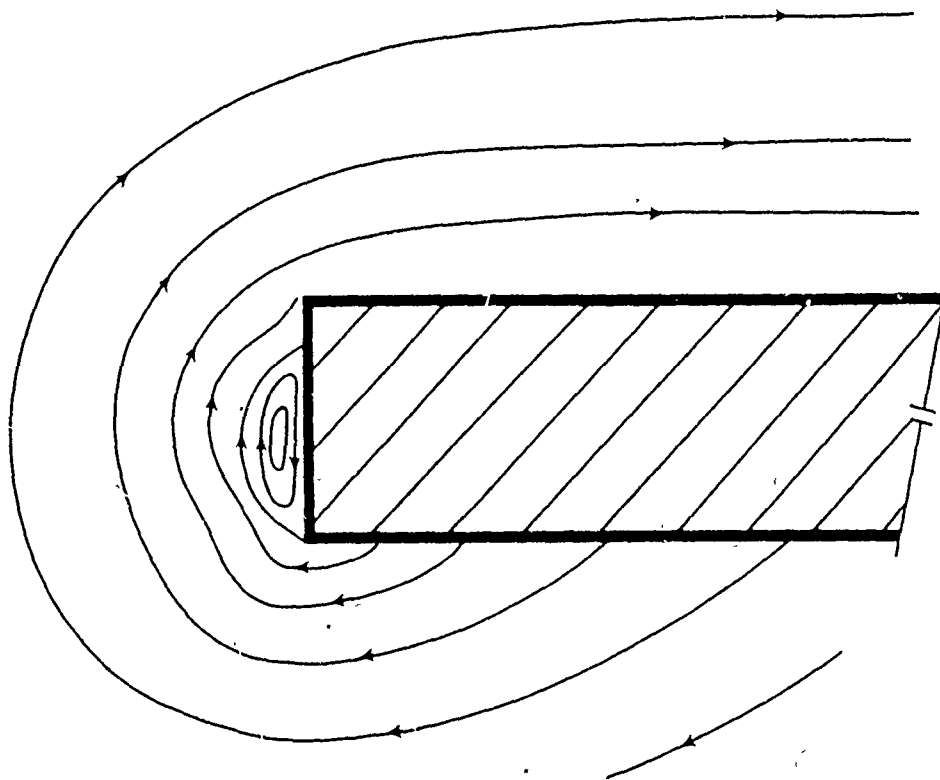
⊙ Flow

|← ——— 1" ——— →|

Fig. 42. Sketch of Streamlines in the
Quasi-Trefftz Plane, x/c = .20, α = 4°
Wing Tip Region
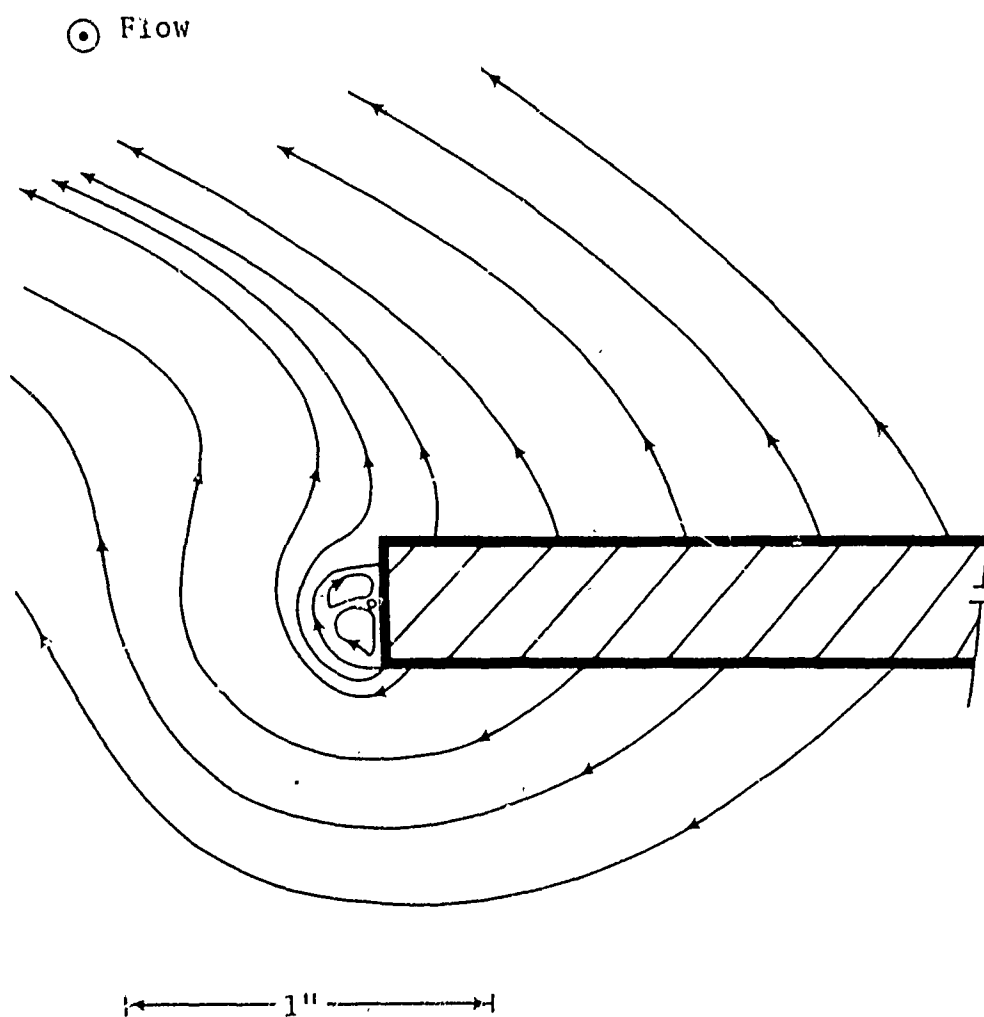
Fig. 43. Sketch of Streamlines in the
Quasi-Trefftz Plane, x/c = .05, α = 4°
Wing Tip Region

$$\frac{x/c}{.10}$$

.20

.30

.40

.50

.60

.70

.80

.90

Upper Wing
Surface
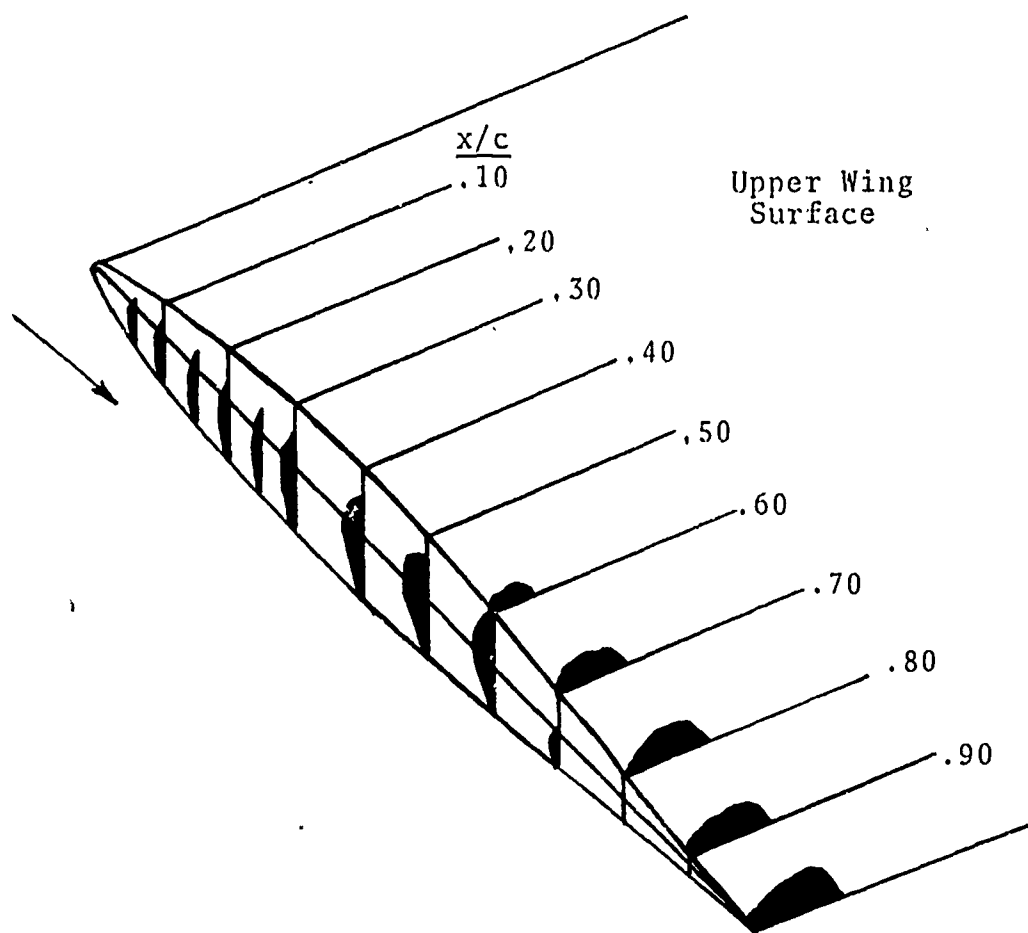
Fig. 44.   Regions of "Reverse Crossflow",
Wing Tip Region, $\alpha = 4°$, $U_0 = 60$ '/sec
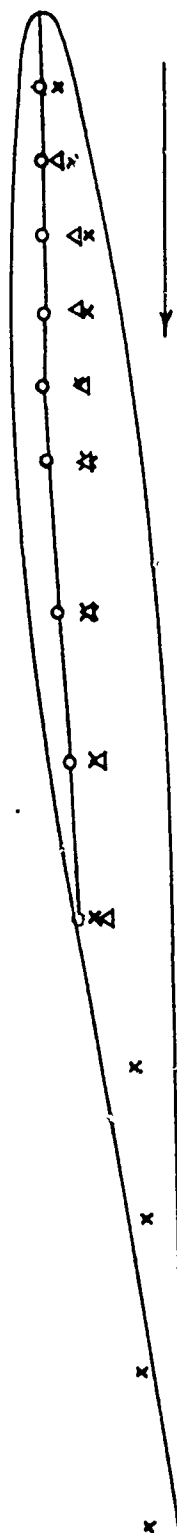
o - Upwash stagnation line

x - Lateral (z) location of maximum upwash

▲ - Lateral (z) location of eddy center, v = w = 0

Fig. 45.   Flow Characteristics Adjacent to the Flat Rectangular
           Wing Tip, α = 4°, U_0 = 60 ▾/sec
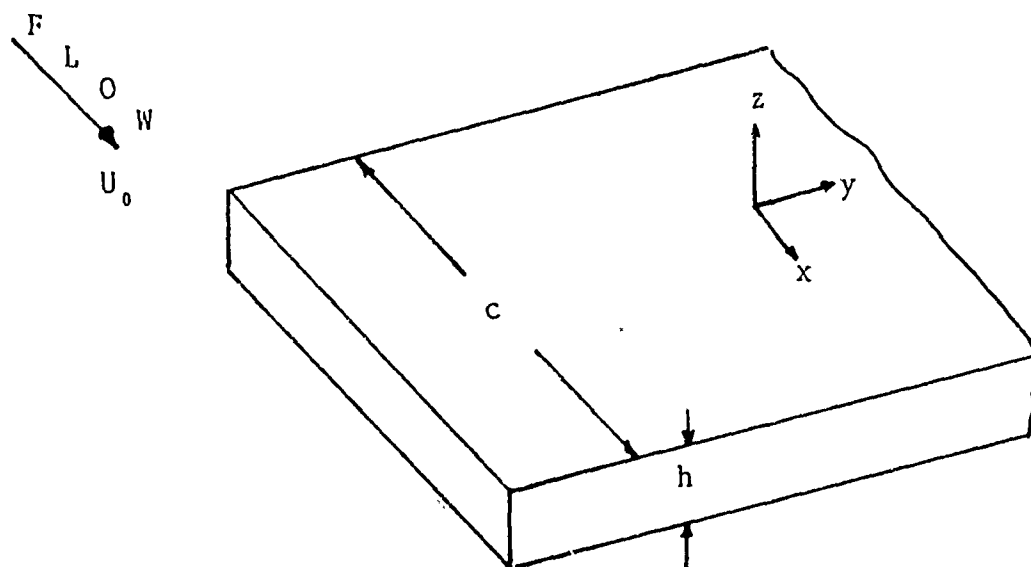
View of cross-section in the Trefftz plane
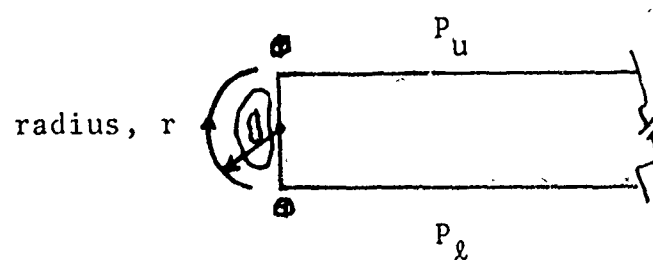
Fig. 46.   Idealized Rectangular "Slab" in
Uniform Flow
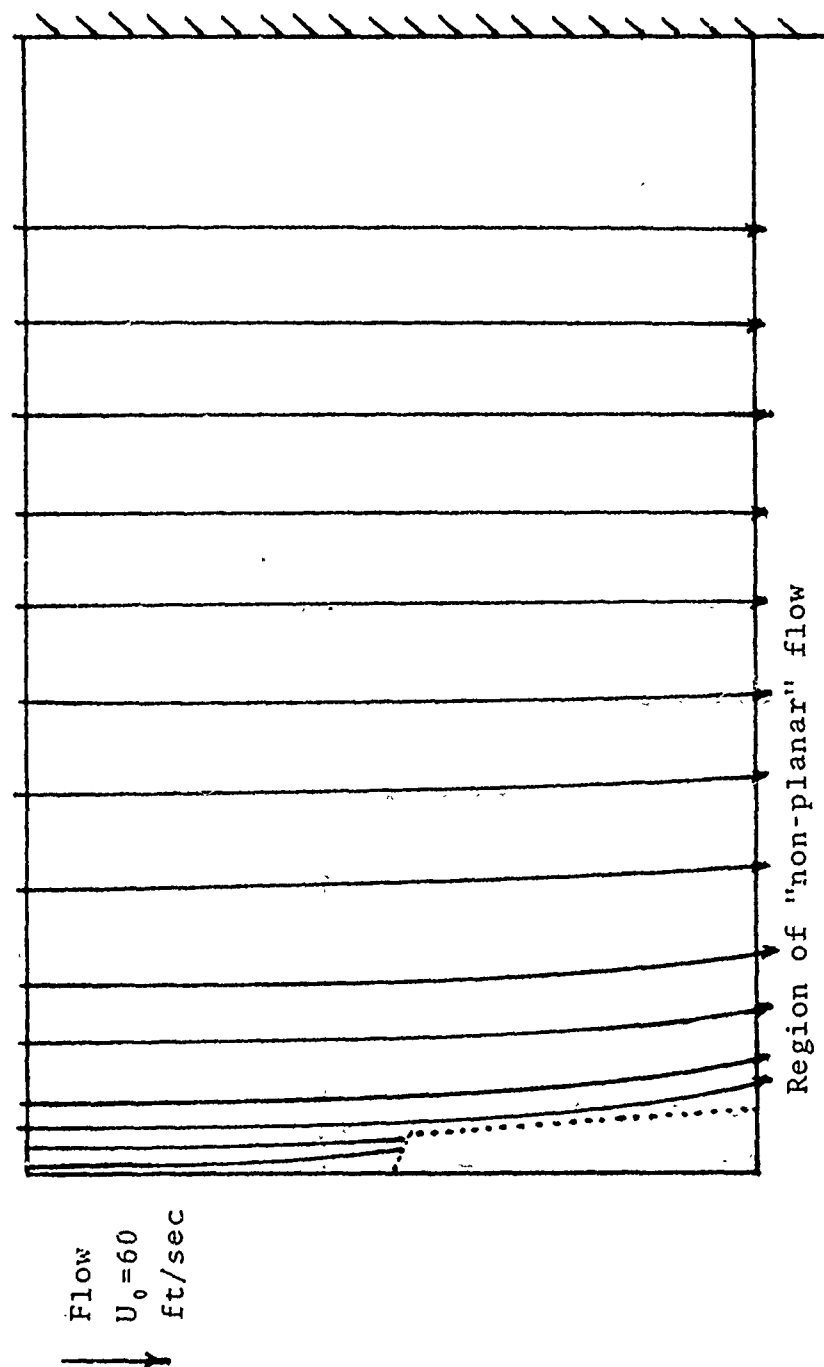
Fig. 47. Streamlines Over Upper Surface, $\alpha = 4°$, (0.1 inches ($z/c = .012$) nominal)

Flow
$U_0 = 60$
ft/sec

0.1 inches, nominal ($z/c = .012$)

0.5 inches, nominal ($z/c = .062$)
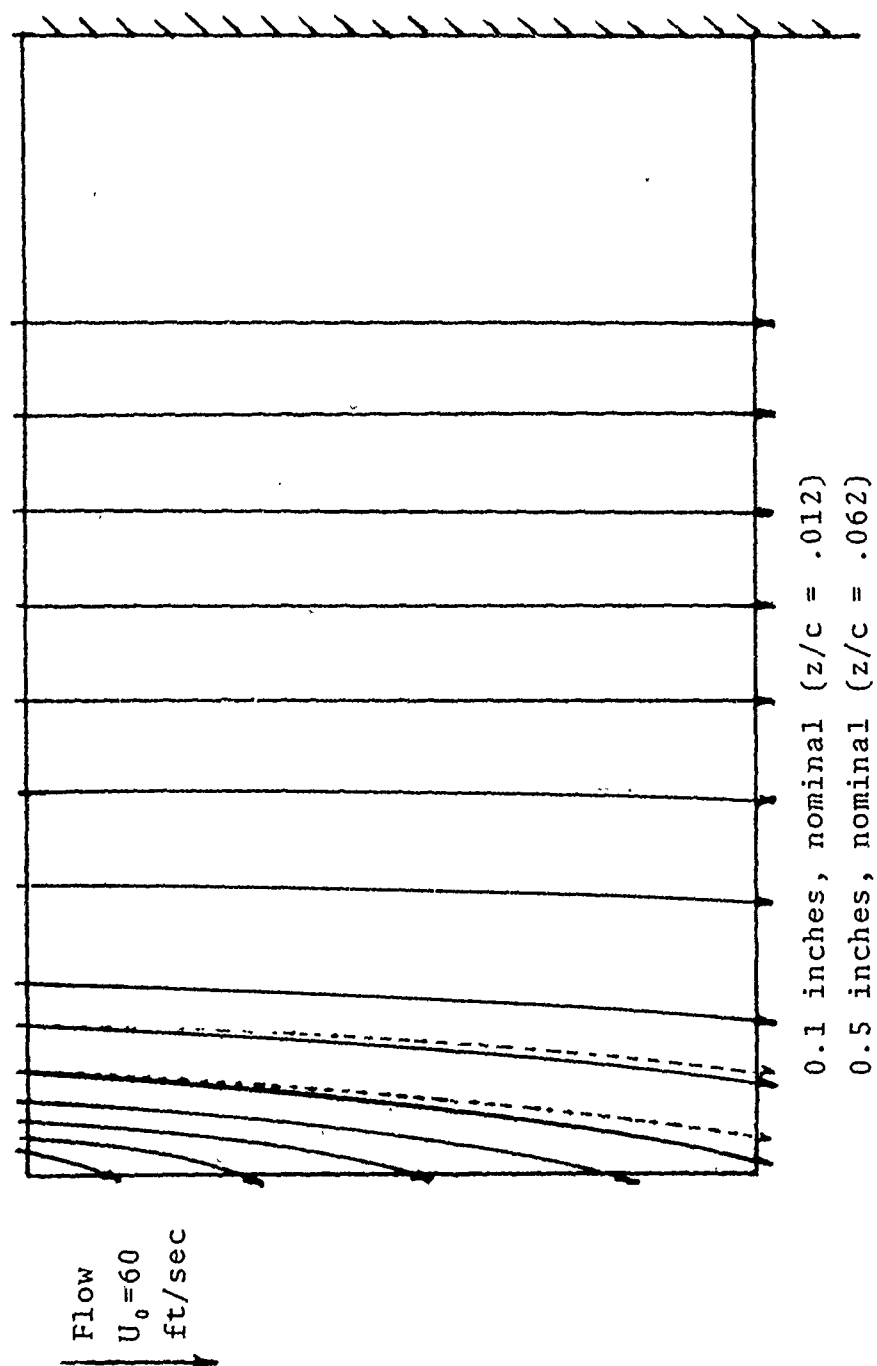
Fig. 48. Streamlines Over Lower Surface, $\alpha = 4°$
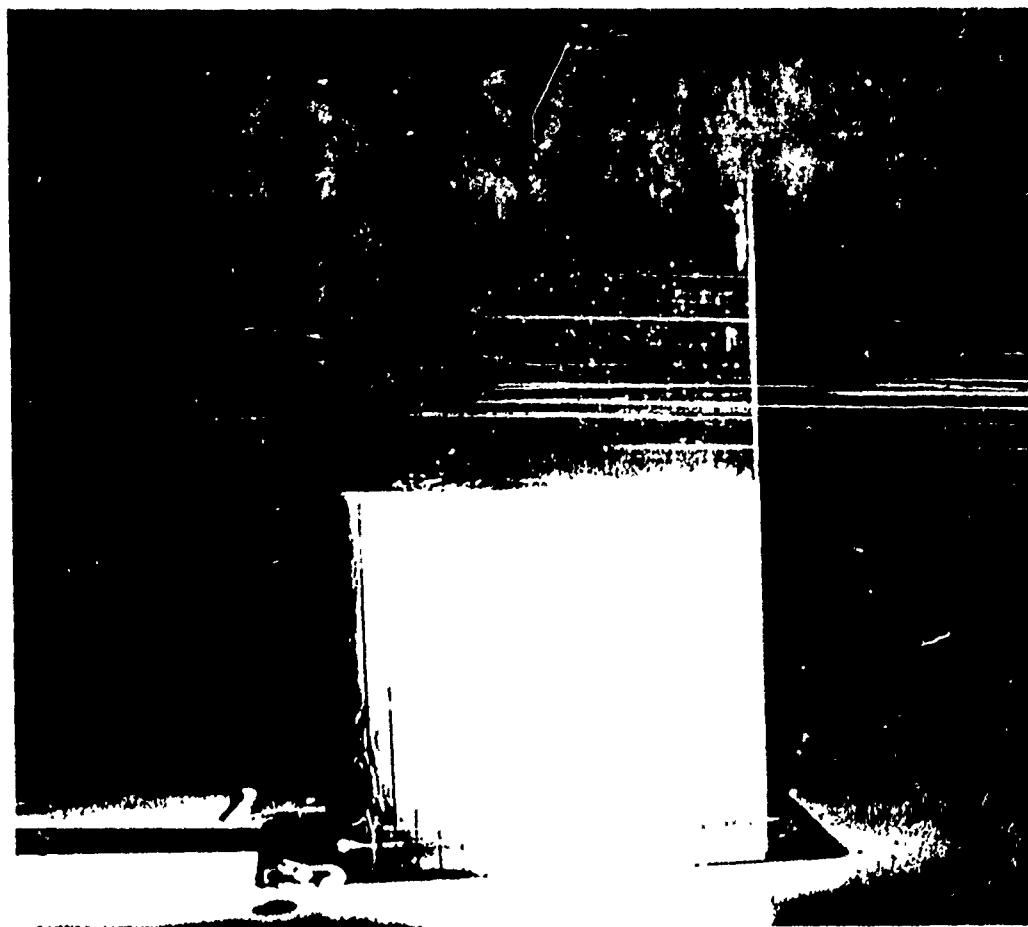
FIG. 49 FLOW OVER THE INBOARD REGION, UPPER SURFACE,
         HELIUM BUBBLE TECHNIQUE, $\alpha = 4°$,
         $U_o = 60$ ft/sec
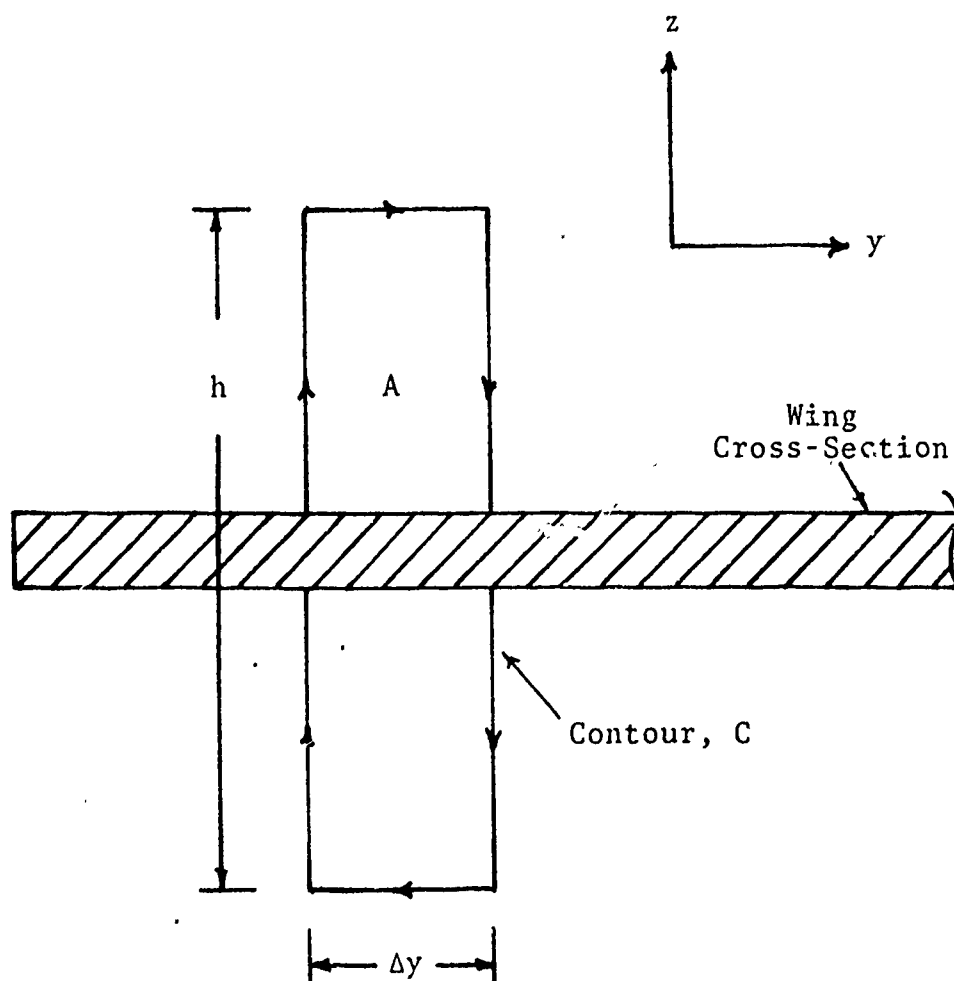
Fig. 50. se of Contour Integration
Adjacent to the Wing Surface
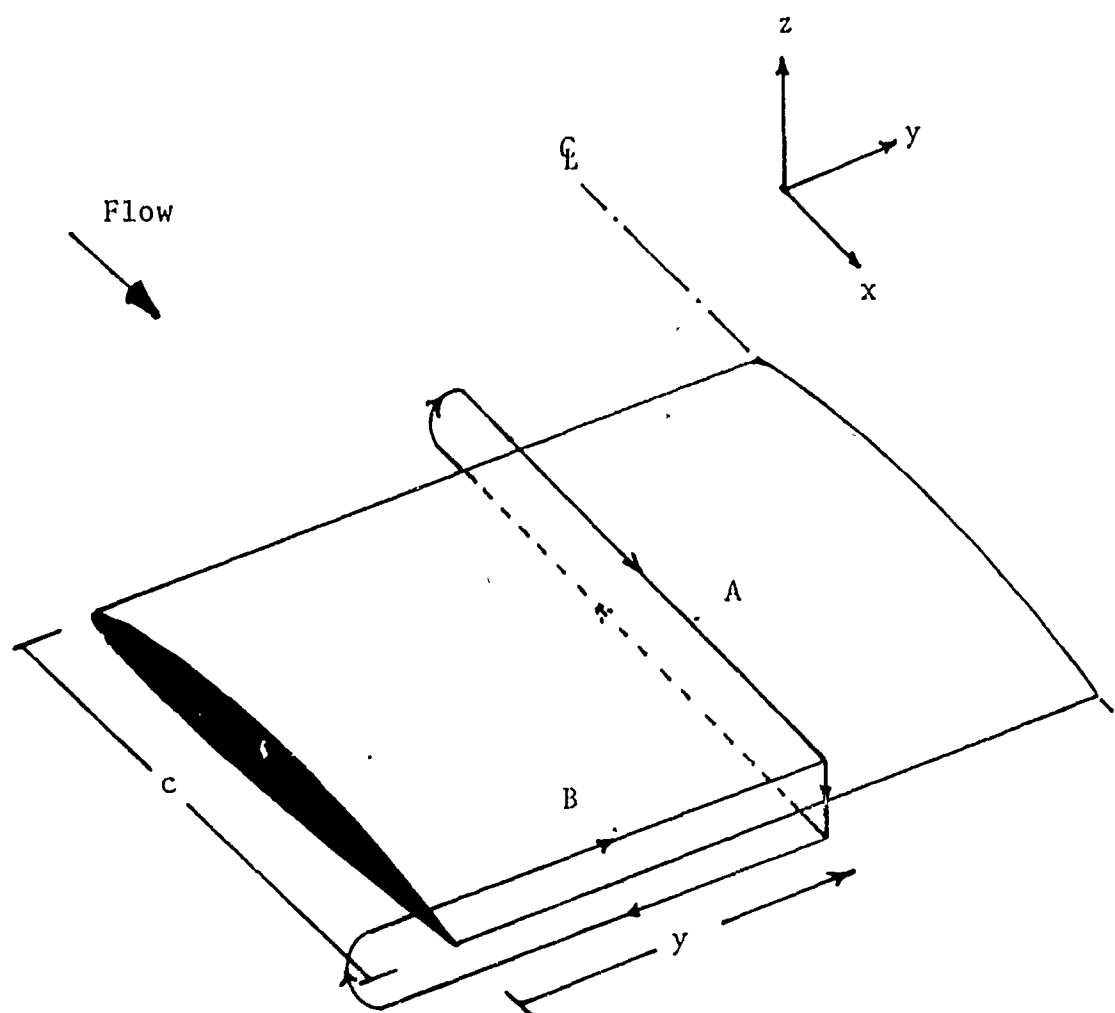
Fig. 51. "A" (xz-plane) and "B" (yz-plane)
Type Contour Integrals Meeting at the
Trailing Edge
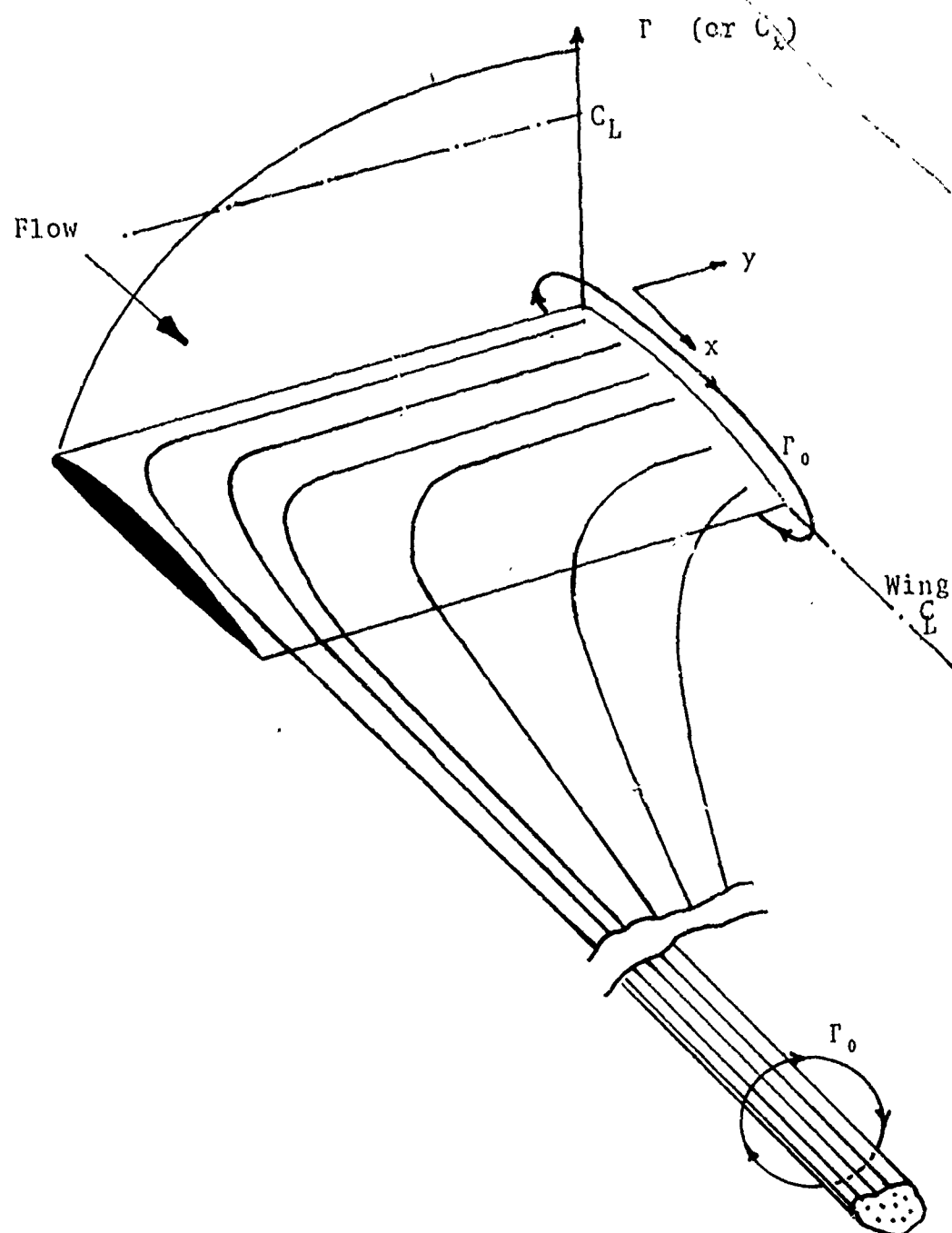
Fig. 52. Bound and Free Vorticity
Associated with the Lifting Wing
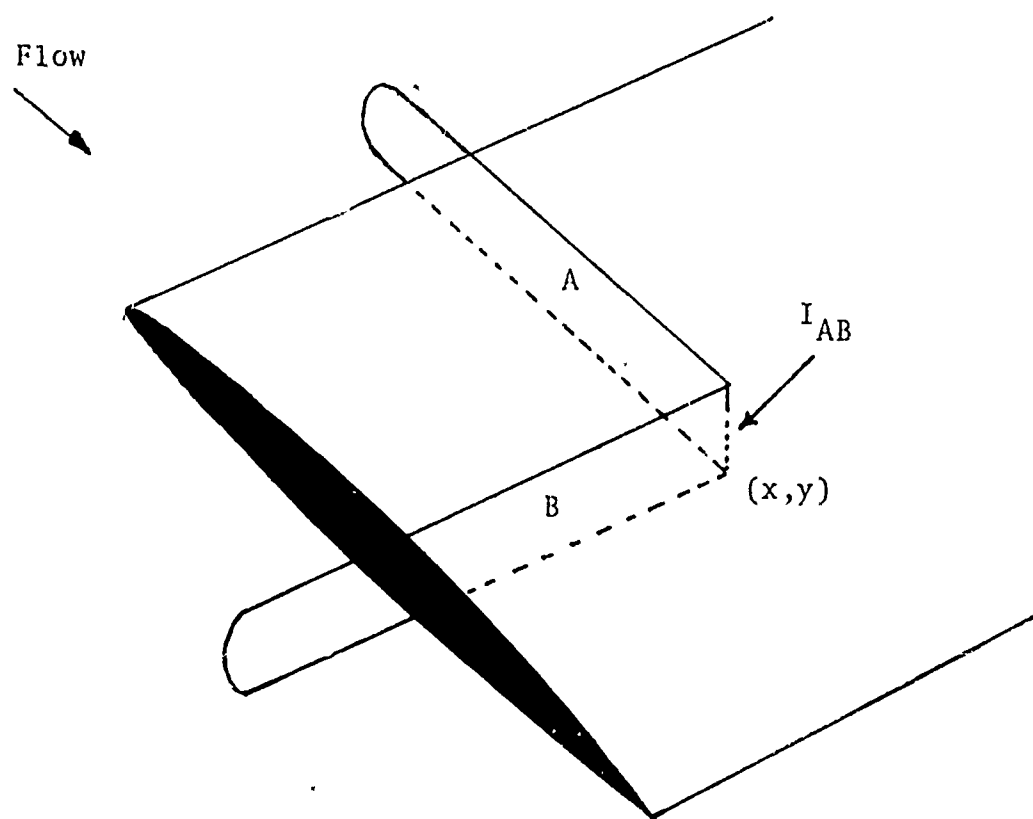
Fig. 53. Pictorial of "A" and "B" - type Integral Paths
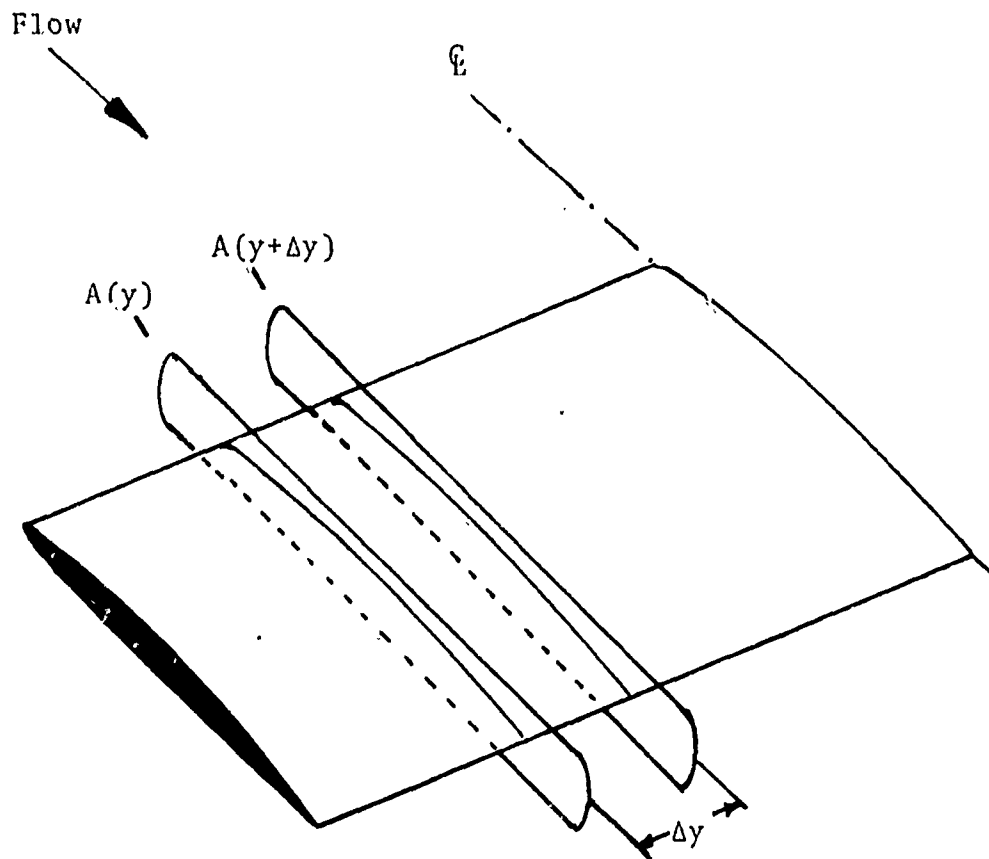
Fig. 54. Chordwise Oriented Strip
of Width, Δy
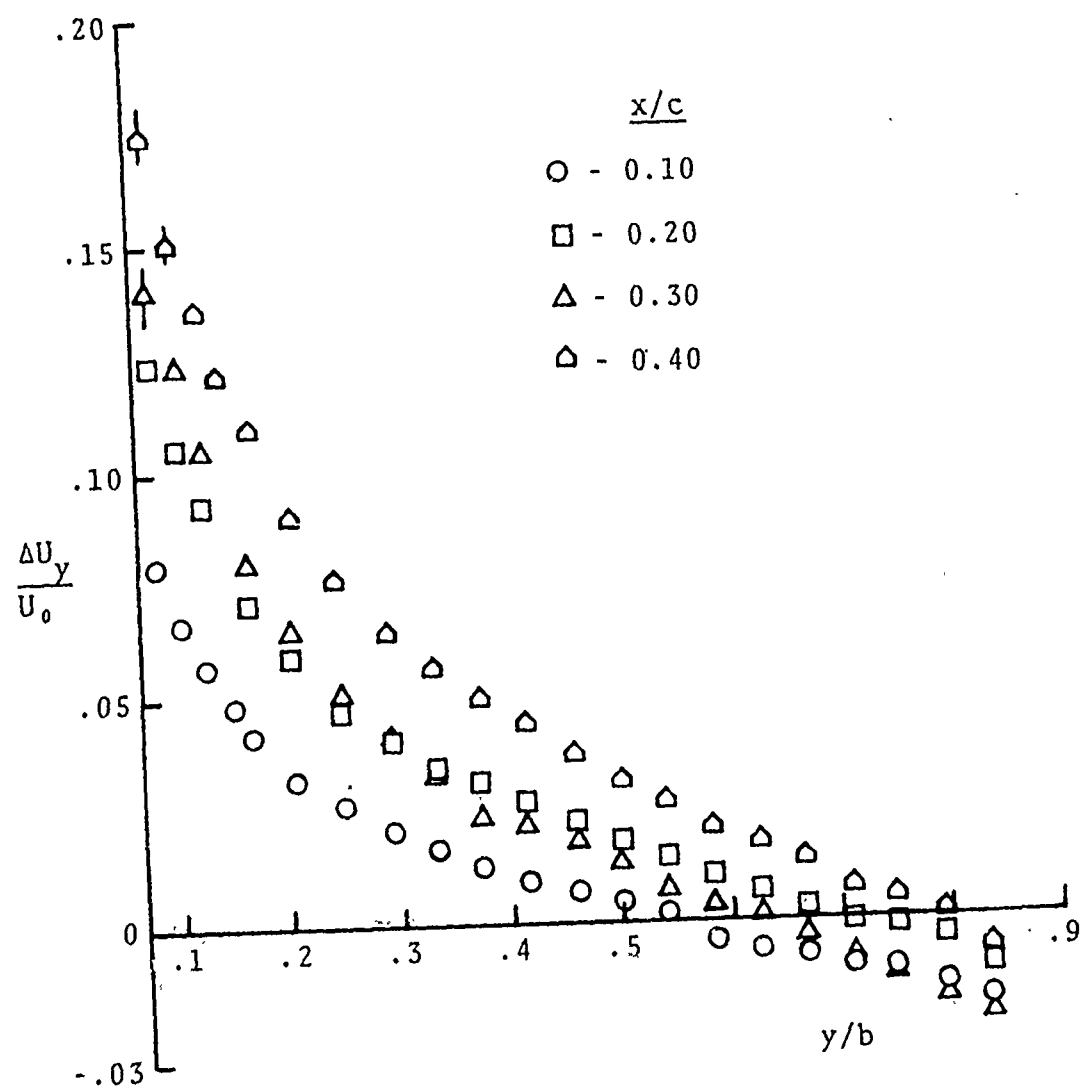
Fig. 55. Crossflow Velocity Differential as a Function of Spanwise Position
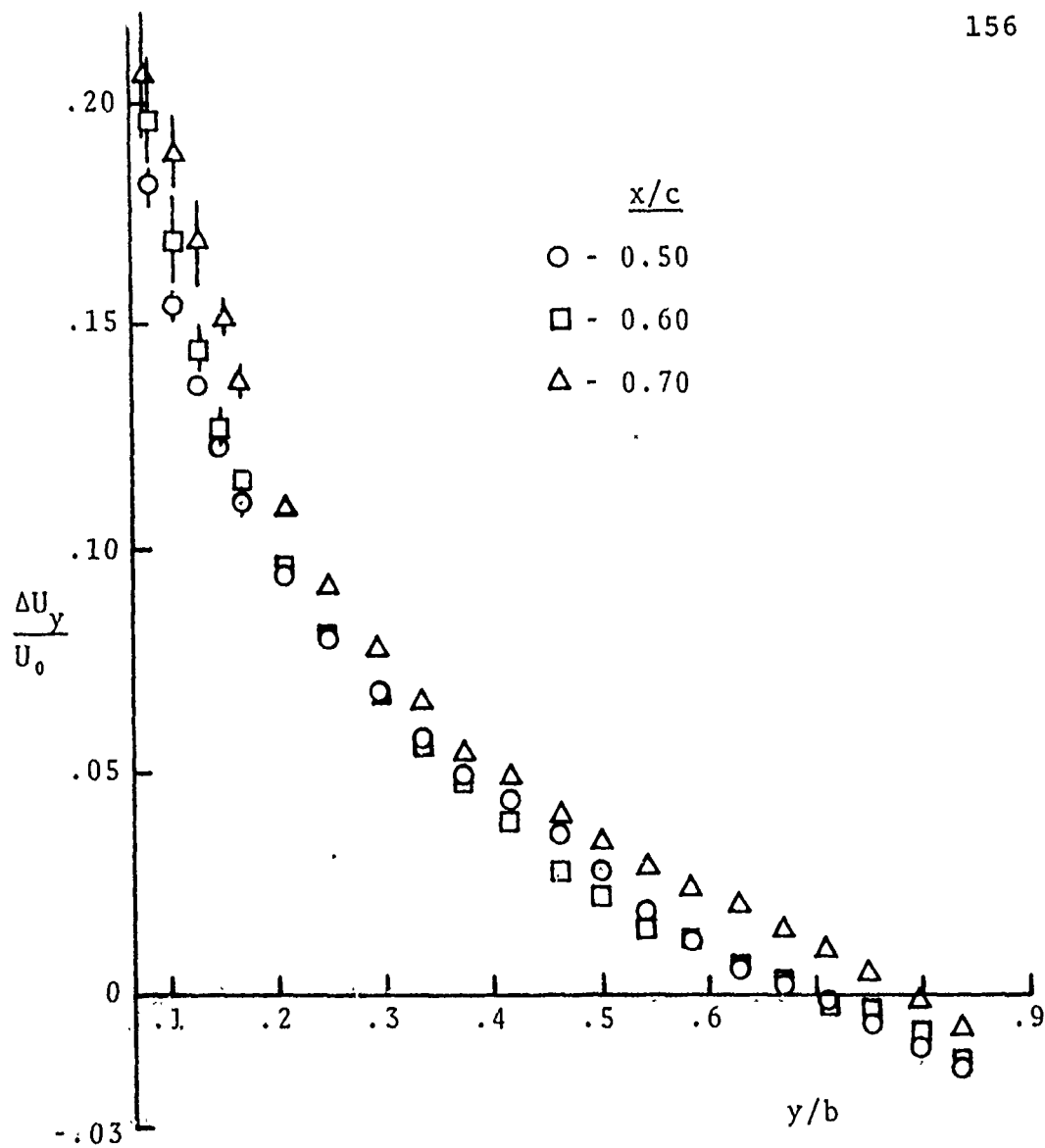
Fig. 56.   Crossflow Velocity Differential as
a Function of Spanwise Position
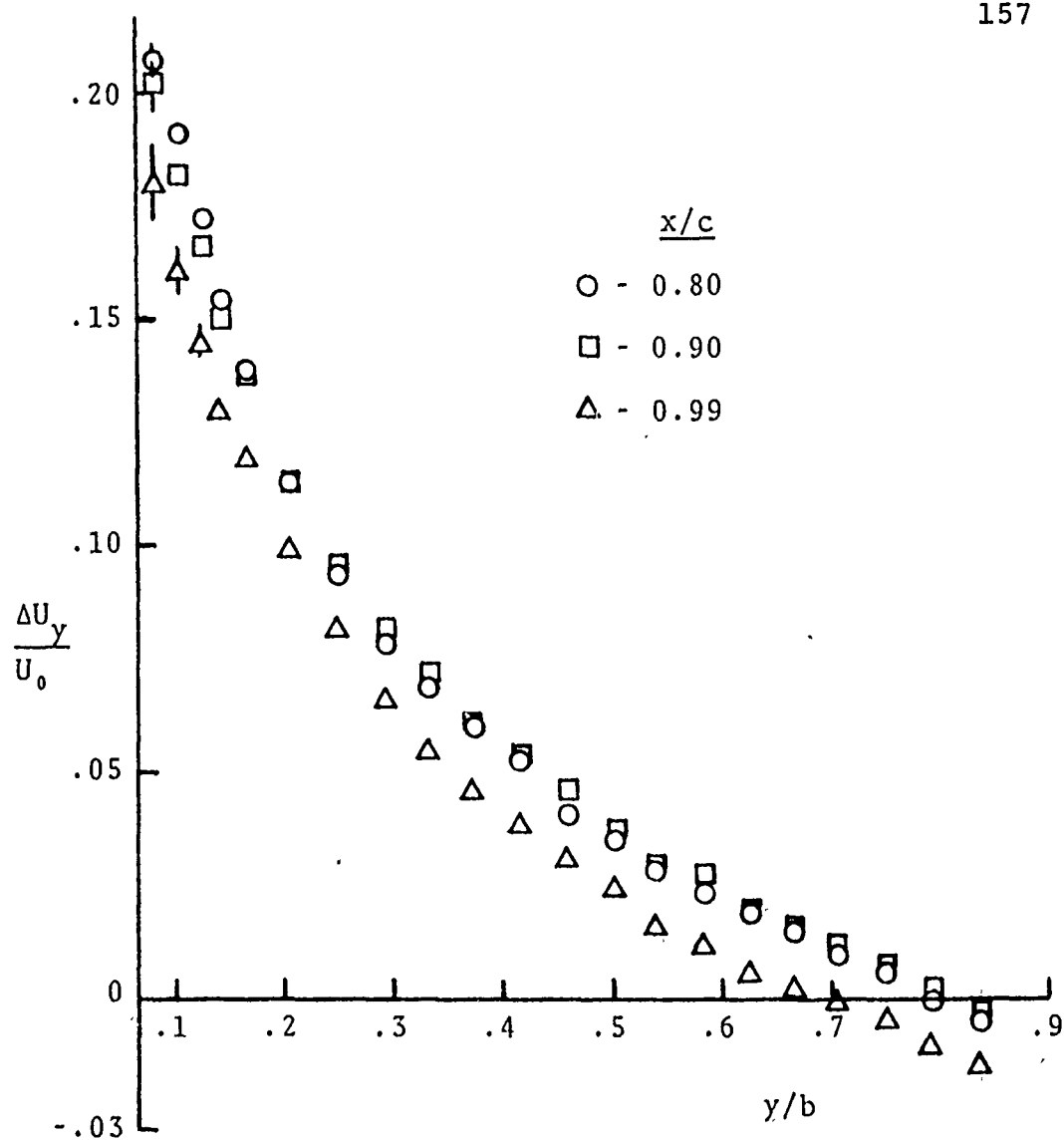
Fig. 57. Crossflow Velocity Differential as
a Function of Spanwise Position
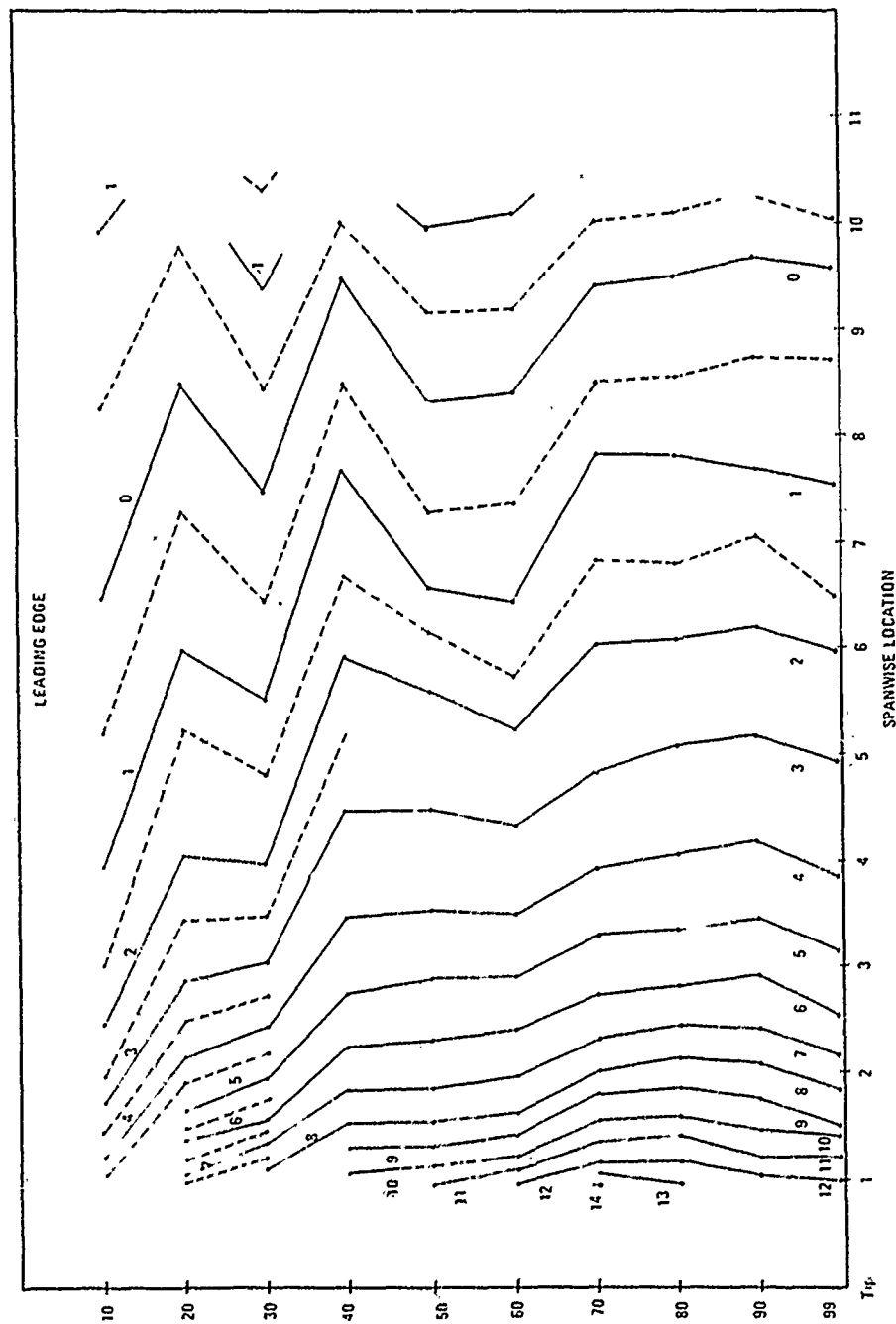
Fig. 58. Crossflow Velocity Differential (ΔU_y) Distribution Over the Planform Surface, (U_o = 60 ft/sec, α = 4 degrees)
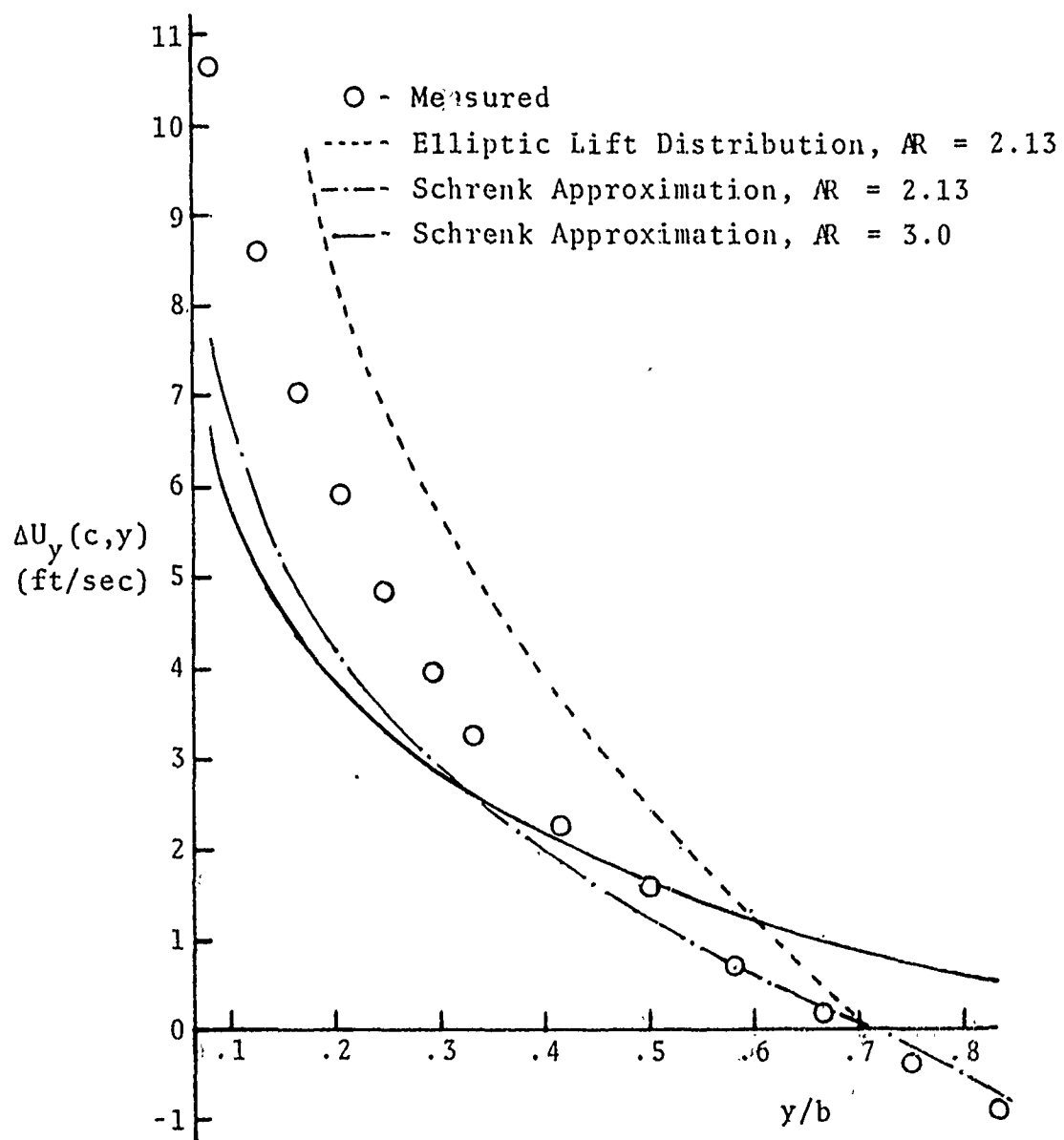
Fig. 59. Comparison of Predicted and Measured Values
of Crossflow Differential Velocity
at the Trailing Edge
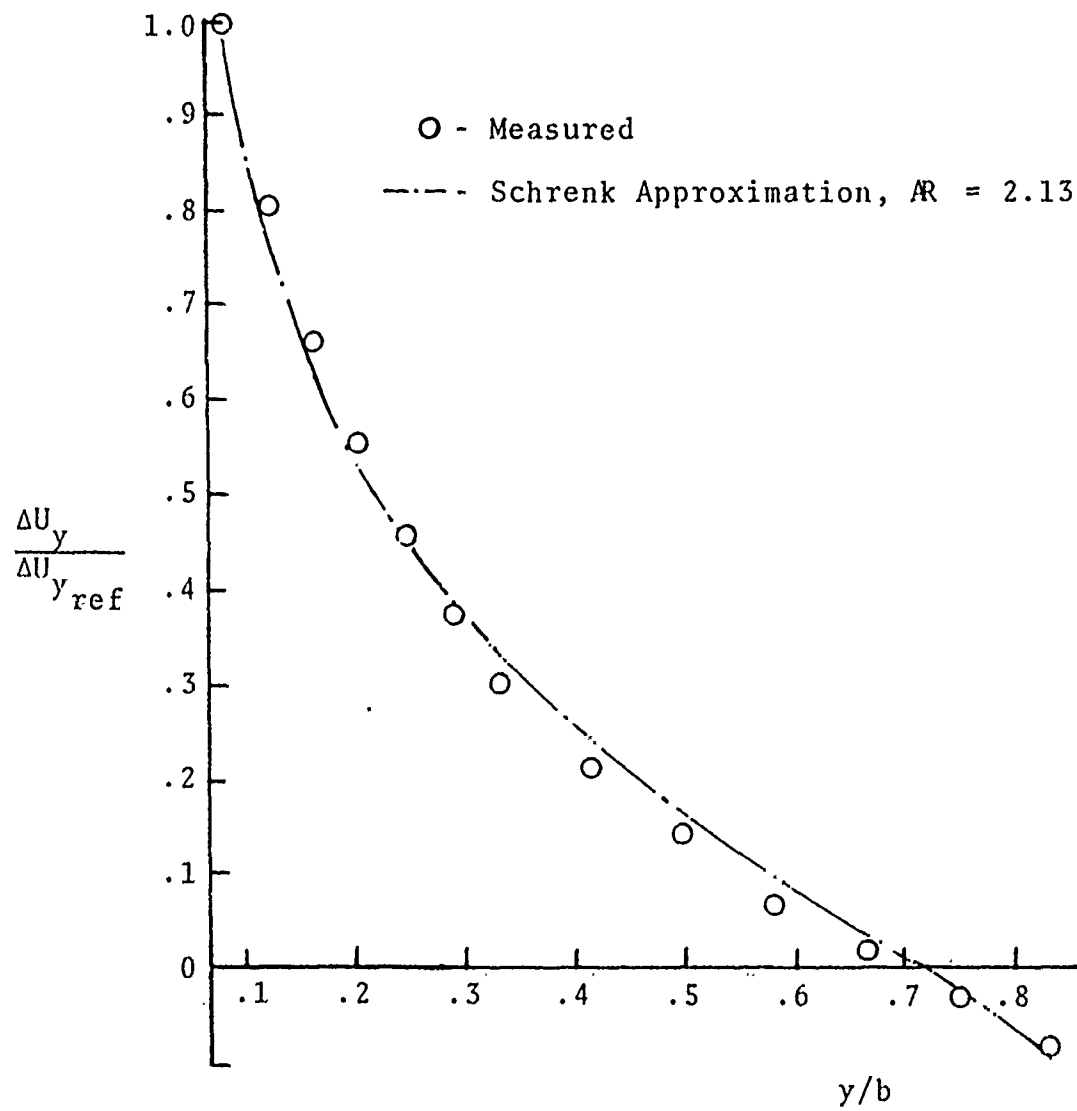
Fig. 60. Comparison of Predicted and Measured
Values of Dimensionless Crossflow Differential
Velocity at the Trailing Edge
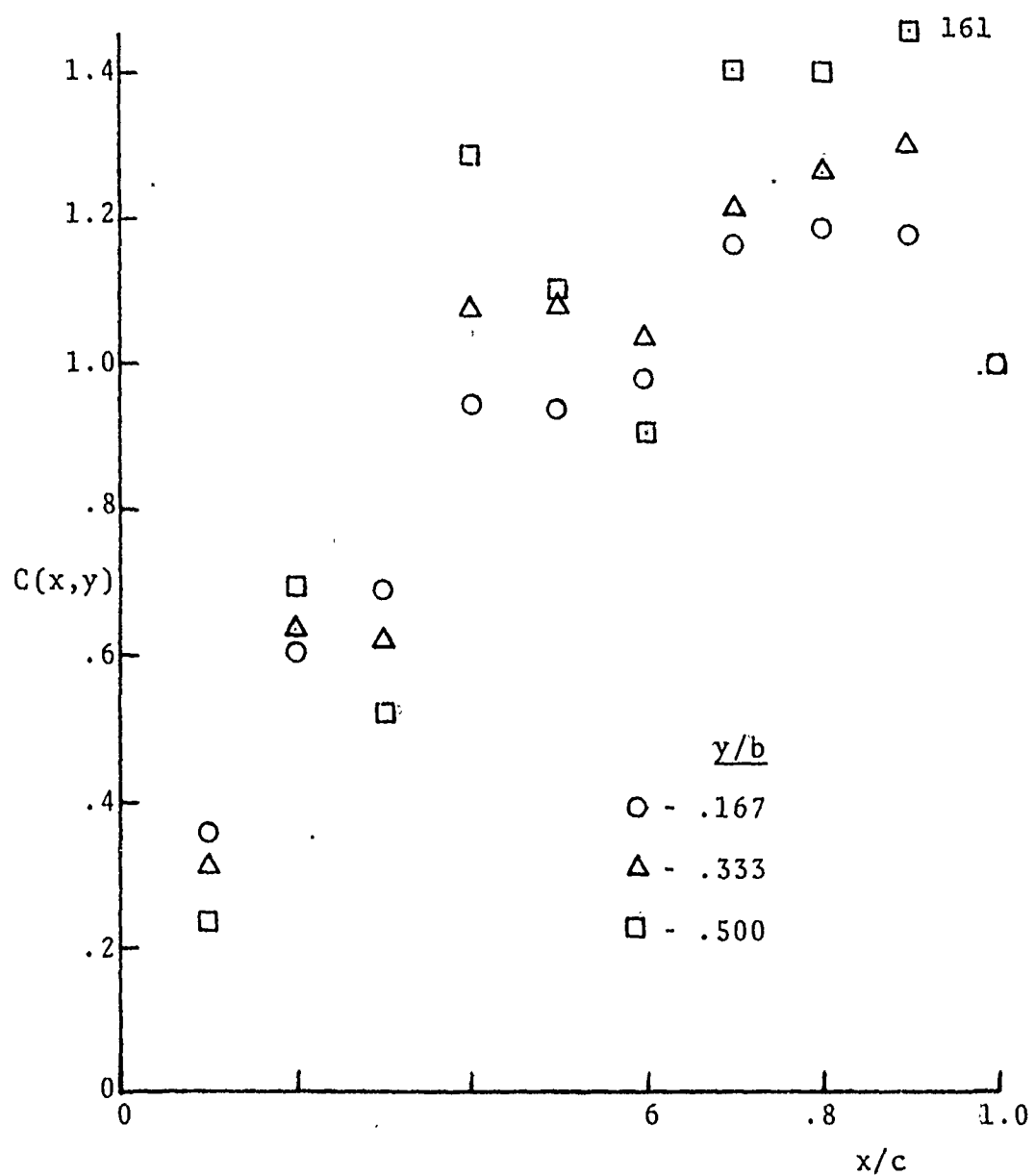
Fig. 61. Uniformity of Dimensionless
Circulation Function

⊙ Flow

1.5 (1.3)	0.9 (0.8)	—	—	—
—	2.5 (2.1)	4.7 (4.0) | 1.5 (1.2)		—
0.4 (0.4)	19.1 (16.3)	26.6 (22.6) | 2.4 (2.0) 8.2 (7.0) | 5.8 (4.9)		9.5 (8.0) 7.6 (6.4)
—	—	0.4 (0.4)	—	0.6 (0.5)
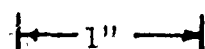
├— 1" —┤ Γ_{tip} = 4.54 ft²/sec

Note: Data in rectangular regions refers to percentage
       of vorticity contained in that region. Upper
       number is referenced to circulation of overall
       tip contour. Lower number (in parentheses) is
       referenced to maximum wing circulation,
       Γ_0 = 5.781 ft²/sec.

Fig. 62. Contour Integrals in the Tip Region,
          Trefftz Plane, x/c = 0.99

⊙ Flow

0.3 (0.2)	-0.5 (-0.4)	—	-0.6 (-0.5)	—
0.3 (0.2)	2.4 (1.7)	0.6 (0.5)	-0.6 (-0.5)	0.4 (0.3)
—	12.0 (8.6)	19.8 (14.2)	0.5 (0.4)	—
-0.3 (-0.2)	21.4 (15.4)	13.6 (9.8) 2.0 (1.4)	4.0 (2.9) 6.0 (4.3)	11.3 (8.1) 8.9 (6.4)
-0.4 (-0.3)	-0.6 (-0.5)	—	—	—
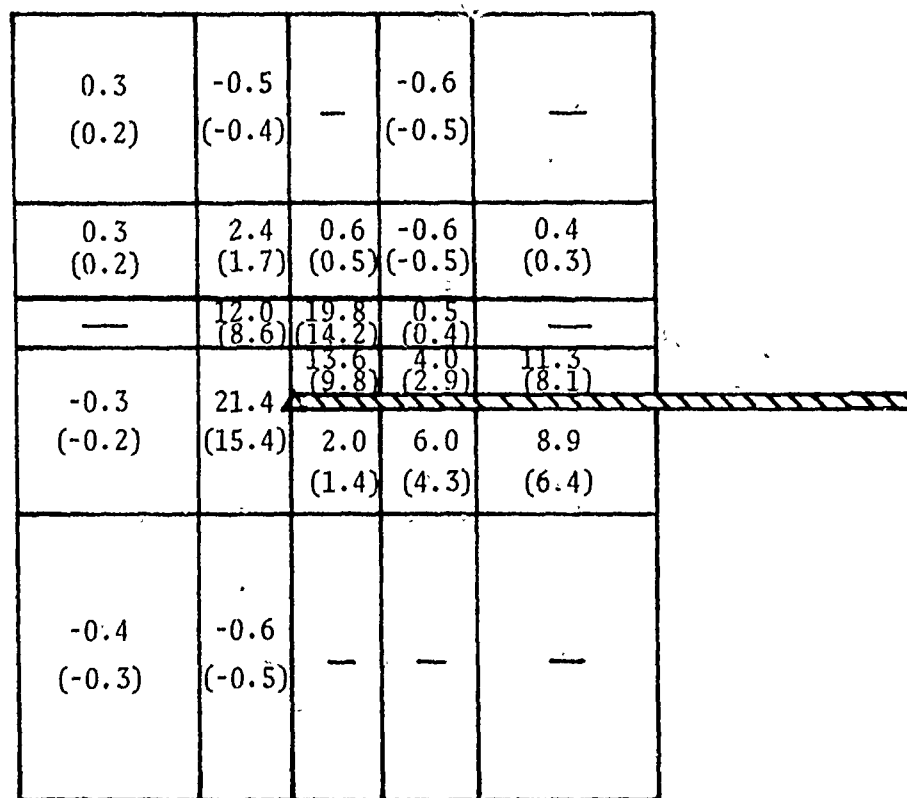
$\longmapsto$ 1" $\longmapsto$ $\Gamma_{tip} = 4.158$ ft^2/sec

Note: Data in rectangular regions refers to percentage of vorticity contained in that region. Upper number is referenced to circulation of overall tip contour. Lower number (in parentheses) is referenced to maximum wing circulation, $\Gamma_0 = 5.781$ ft^2/sec.

Fig. 63. Contour Integral in the Tip Region, Trefftz Plane, x/c = 0.90.

⊙ Flow

1.1 (0.7)	0.7 (0.4)	-0.6 (-0.4)	-0.4 (-0.2)
0.9 (0.4)	2.1 (1.3)	1.1 (0.7)	0.5 (0.3)
		28.8 (17.4)	8.8 (5.3)
1.4 (0.8)	37.8 (22.8)		
		11.1 (6.7)	6.8 (4.1)
0.3 (0.1)	—	—	-0.3 (-0.1)

$\Gamma_{tip} = 3.484$ ft²/sec

(a)   x/c = 0.70

1.0 (0.6)	1.3 (0.7)	-1.5 (-0.9)	-1.0 (-0.6)
-1.0 (-0.6)	7.5 (4.4)	12.7 (7.5)	0.1 (0.1)
		23.9 (14.3)	8.0 (4.8)
-0.4 (-0.2)	29.5 (17.5)		
		12.7 (7.5)	7.3 (4.3)
—	—	—	—

$\Gamma_{tip} = 3.460$ ft²/sec
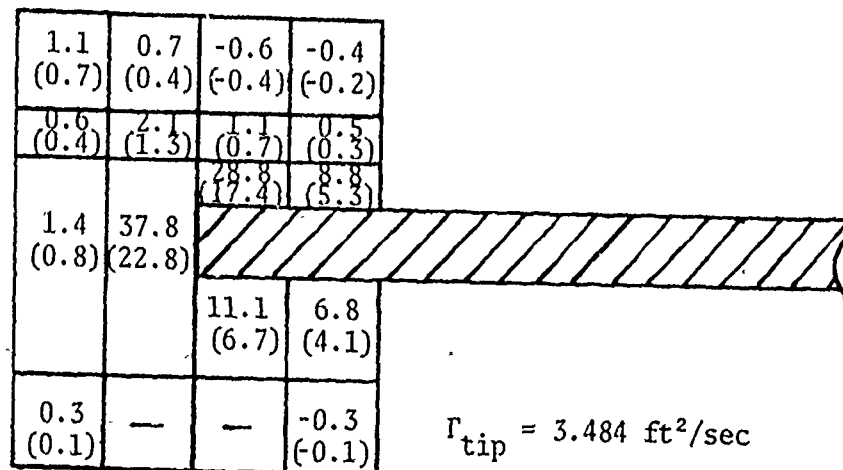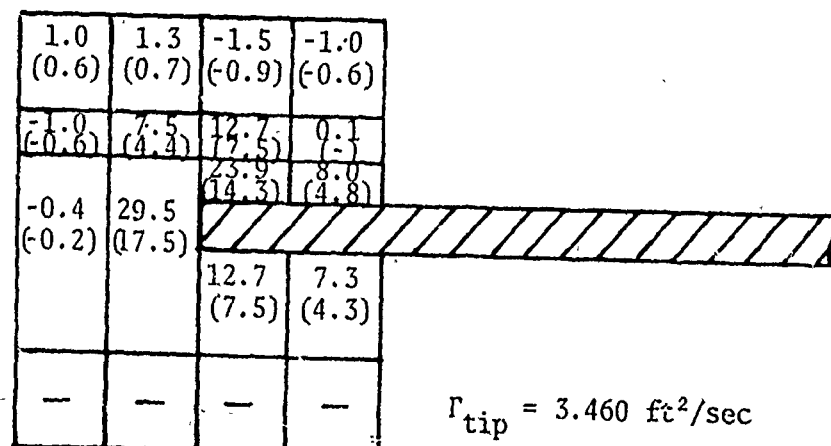
(b)   x/c = 0.80

|← 1" →|

Fig. 64.   Contour Integrals in the Tip Region,
Trefftz Plane

⊙ Flow

—	0.8 (0.4)	—	-0.1 (-)
-0.1 (-)	—	-0.8 (-0.4)	0.4 (0.2)
		22.6 (12.3)	11.2 (6.1)
-0.3 (-0.1)	45.2 (24.5)		
		13.8 (7.5)	7.7 (4.2)
-0.1 (-)	-0.1 (-)	-0.1 (-)	—

Γ_{tip} = 3.14 ft²/sec

(a) x/c = 0.50

—	1.3 (0.7)	-0.1 (-)	0.1 (-)
1.0 (0.6)	1.5 (0.9)	-1.4 (-0.8)	-0.4 (-0.2)
		28.3 (16.6)	11.1 (6.5)
-1.9 (-1.1)	42.8 (25.2)		
		13.5 (7.9)	7.3 (4.3)
-0.4 (-0.2)	-0.4 (-0.2)	0.2 (0.1)	-0.1 (-)

Γ_{tip} = 3.44 ft²/sec
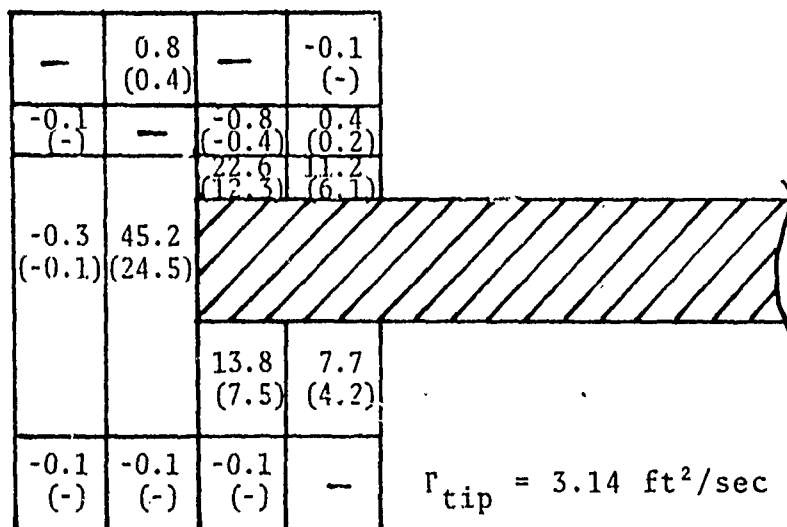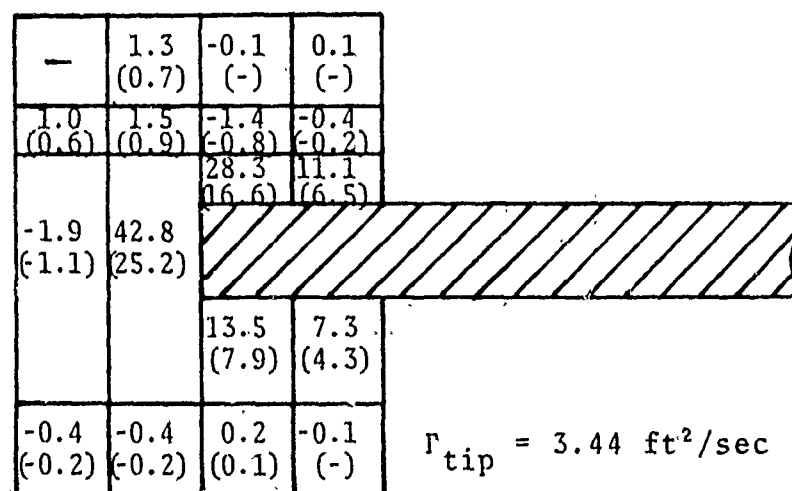
(b) x/c = 0.60

├── 1" ──┤

Fig. 65. Contour Integrals in the Tip Region,
Trefftz Plane

—	—	-0.1 (-)	0.3 (0.1)
		13.6 (6.4)	6.9 (3.2)
0.8 (0.4)	45.2 (21.2)	//////	//////
		22.6 (10.6)	11.5 (5.4)
-0.3 (-0.1)	—	-0.5 (-0.2)	—

$\Gamma_{tip} = 2.705$ ft^2/sec

(a)   x/c = 0.30

0.1 (-)	0.7 (0.4)	0.6 (0.3)	0.1 (-)
—	0.1 (-)	-0.1 (-)	-0.3 (-0.1)
		16.8 (8.6)	9.5 (4.9)
0.3 (0.1)	45.9 (23.6)	//////	//////
		16.9 (8.7)	9.2 (4.7)
-0.1 (-)	0.1 (-)	-0.1 (-)	0.3 (0.1)

$\Gamma_{tip} = 2.97$ ft^2/sec
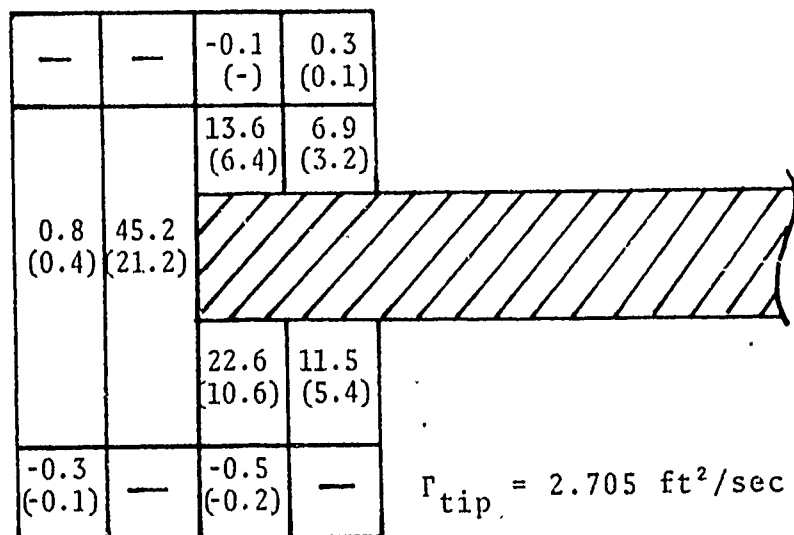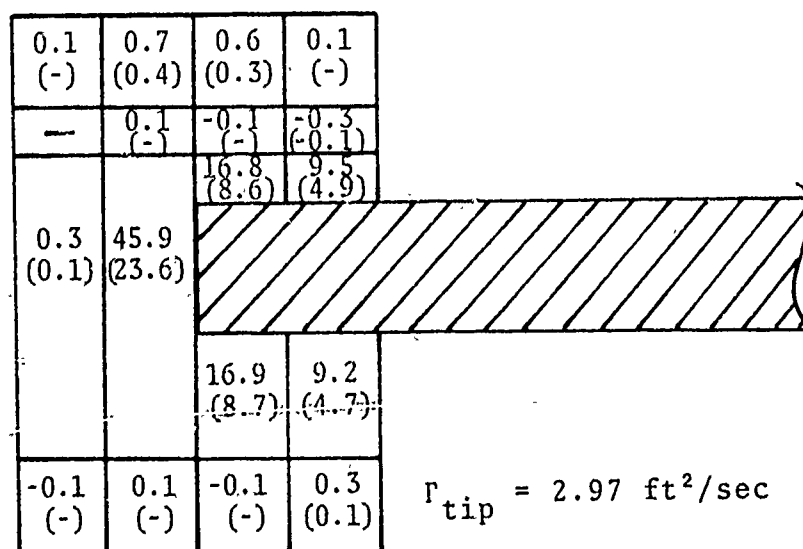
(b)   x/c = 0.40

|← 1" →|

Fig. 66.   Contour Integrals in the Tip Region,
Trefftz Plane

(a)   x/c = 0.10

Γ_{tip} = 1.79 ft²/sec

(b)   x/c = 0.20

Γ_{tip} = 2.26 ft²/sec
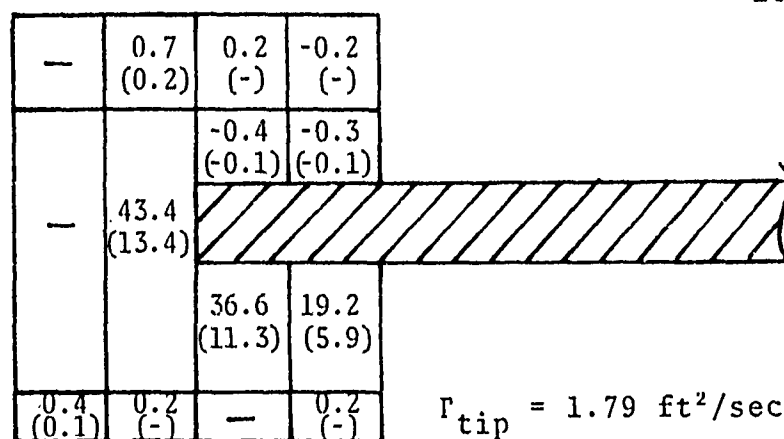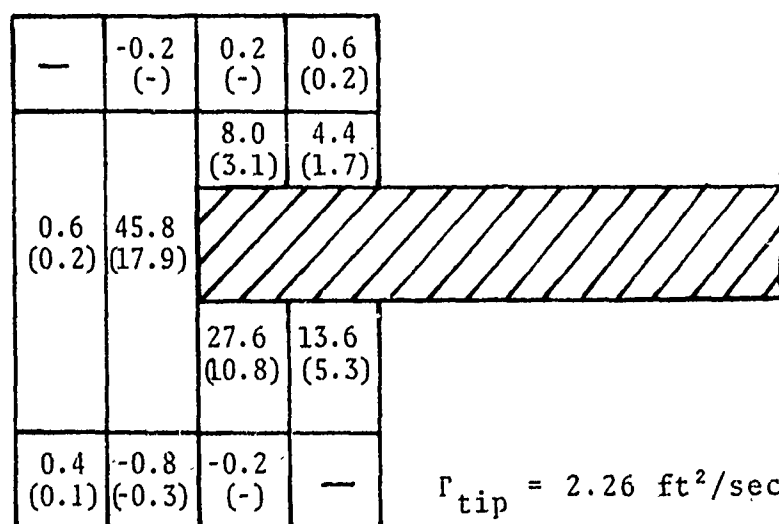
|← 1" →|

Fig. 67.   Contour Integrals in the Tip Region, Trefftz Plane

⊙ Flow

├── 1" ──┤

1.6 (0.2)	-0.5 (-)	1.0 (0.1)	-1.0 (-0.1)
	37.4 (5.2)	-28.9 (-4.0)	-15.0 (-2.1)
—		72.7 (10.1)	32.6 (4.6)
—	—	—	—

$\Gamma_{tip} = 0.807$ ft²/sec
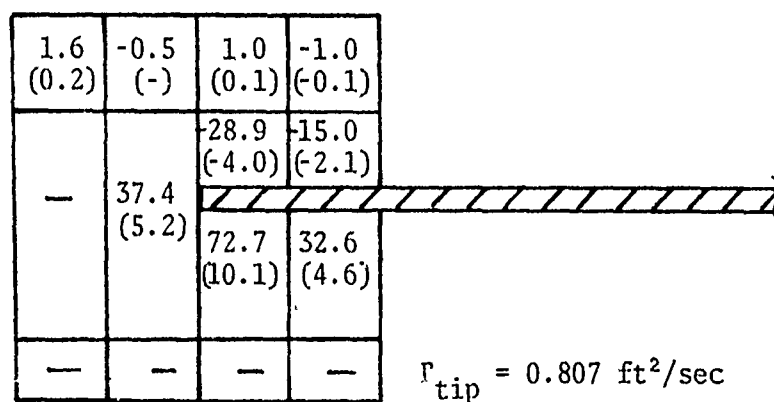
Fig. 68. Contour Integral in the Tip Region,
Trefftz Plane, x/c = 0.01
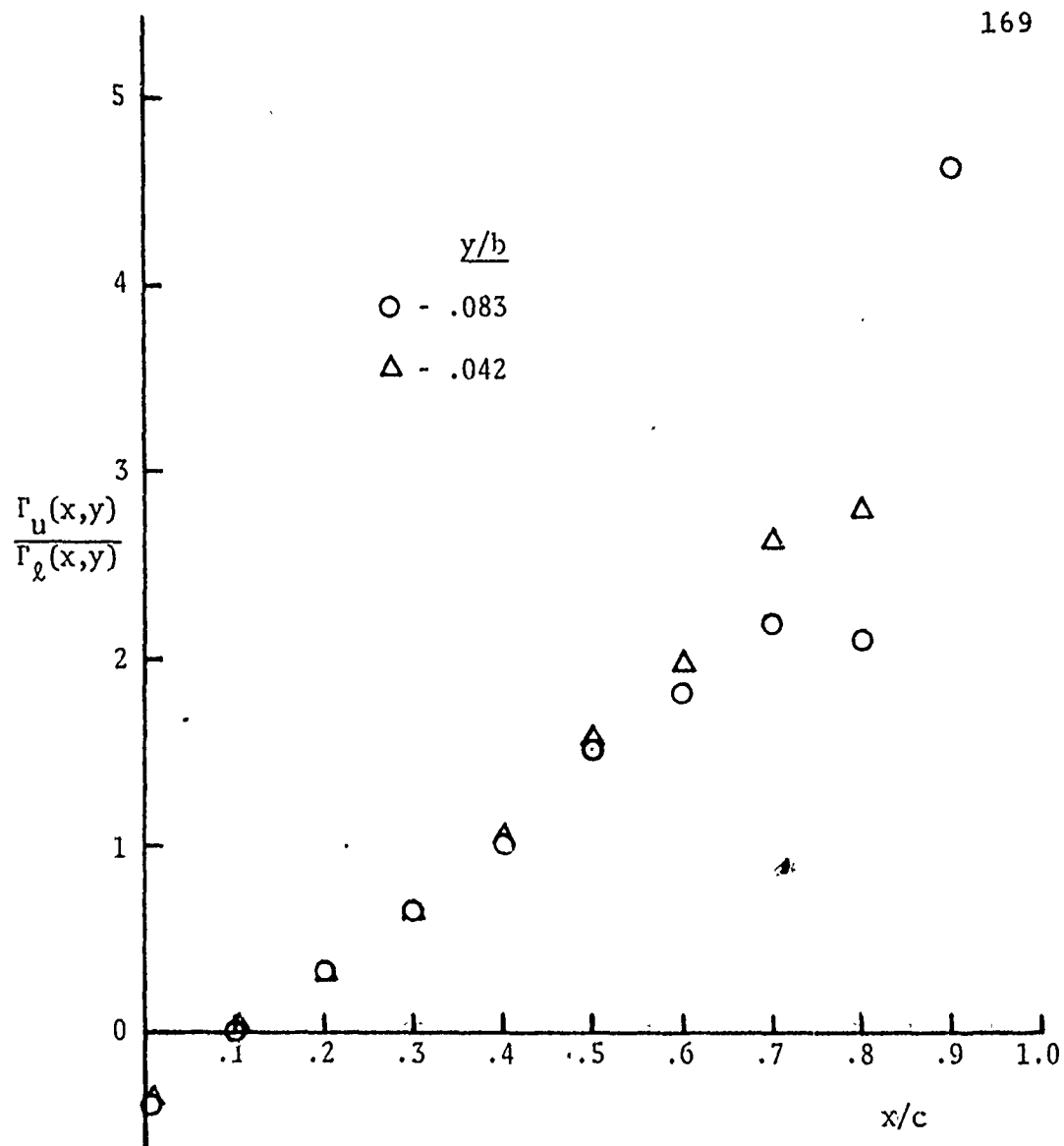
Fig. 69. Ratio of Circulation of Flow on the
Upper Surface to Corresponding Region on
the Lower Surface

Legend
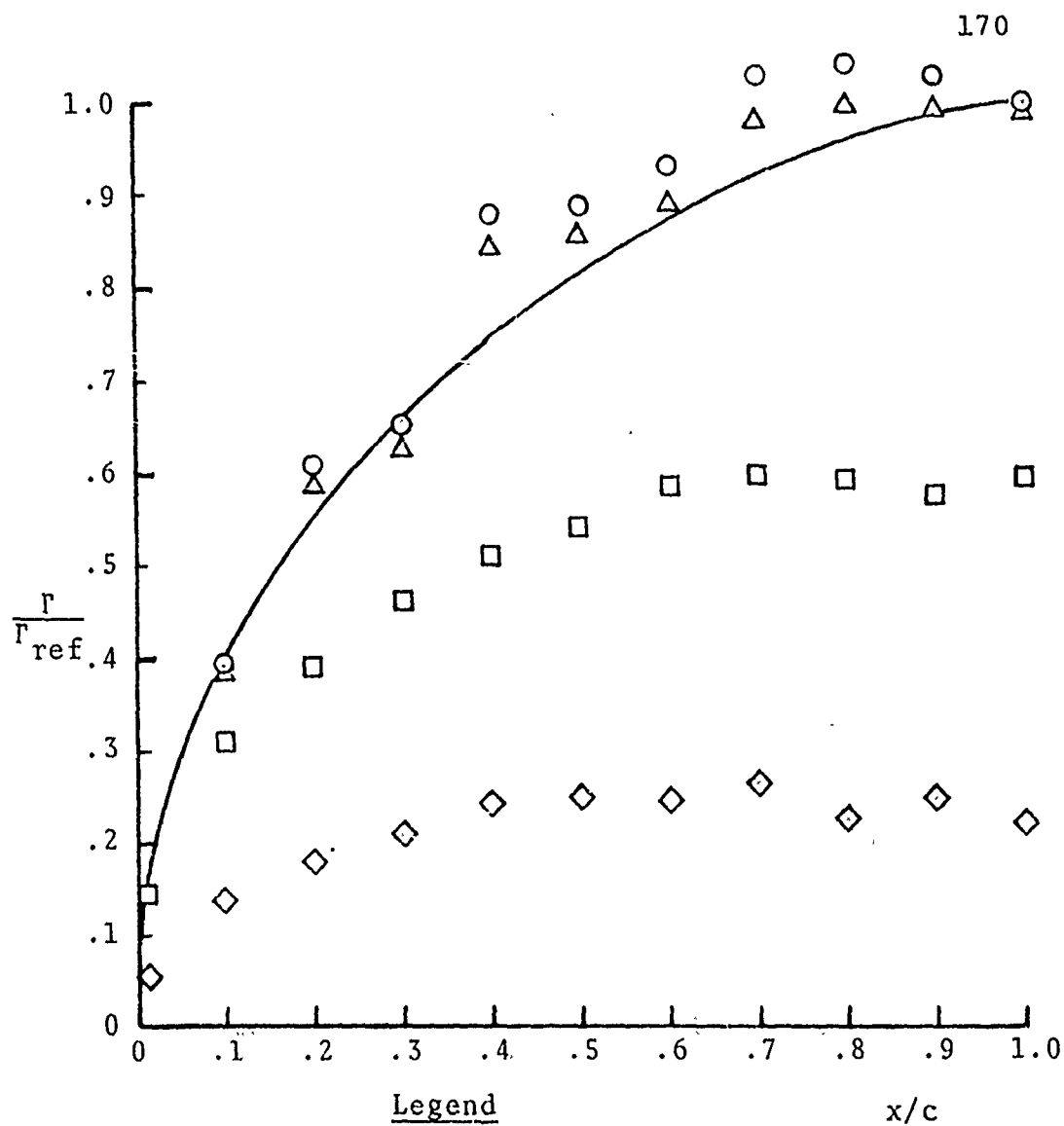
○ - $\Gamma(x, y = 10")$, $\Gamma_{ref} = \Gamma_0$

△ - $\Gamma(x, y = 10")$, $\Gamma_{ref} = \Gamma_{max}(x=c)$

□ - $\Gamma(x, y = 1")$, $\Gamma_{ref} = \Gamma_0$

◇ - $\Gamma(x, y = 0)$, $\Gamma_{ref} = \Gamma_0$

— - Predicted Flat Plate Distribution

Fig. 70. Chordwise Variation of Wing Circulation
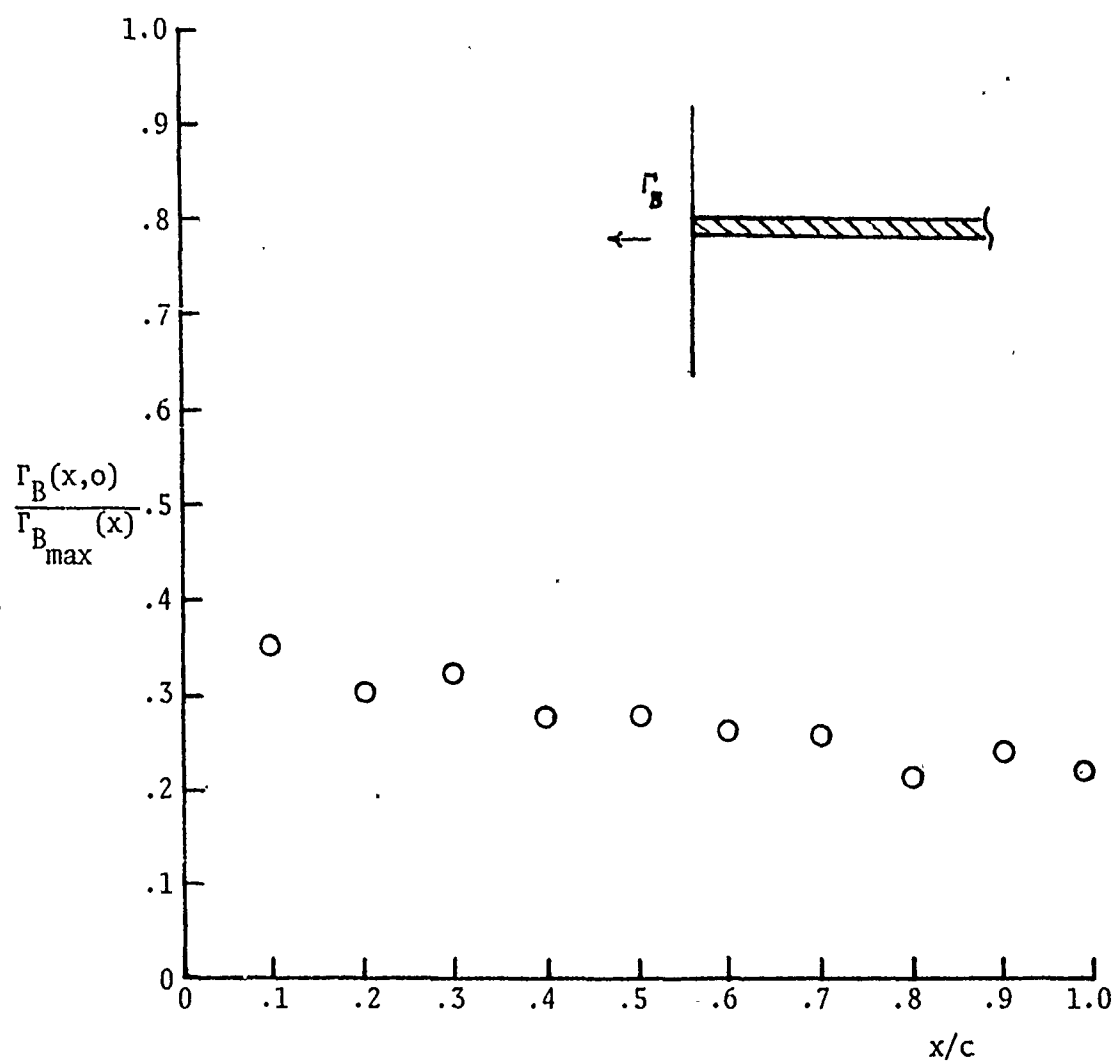
Fig. 71. Circulation of Fluid Outboard of
the Wing Tip as a Function of Chord
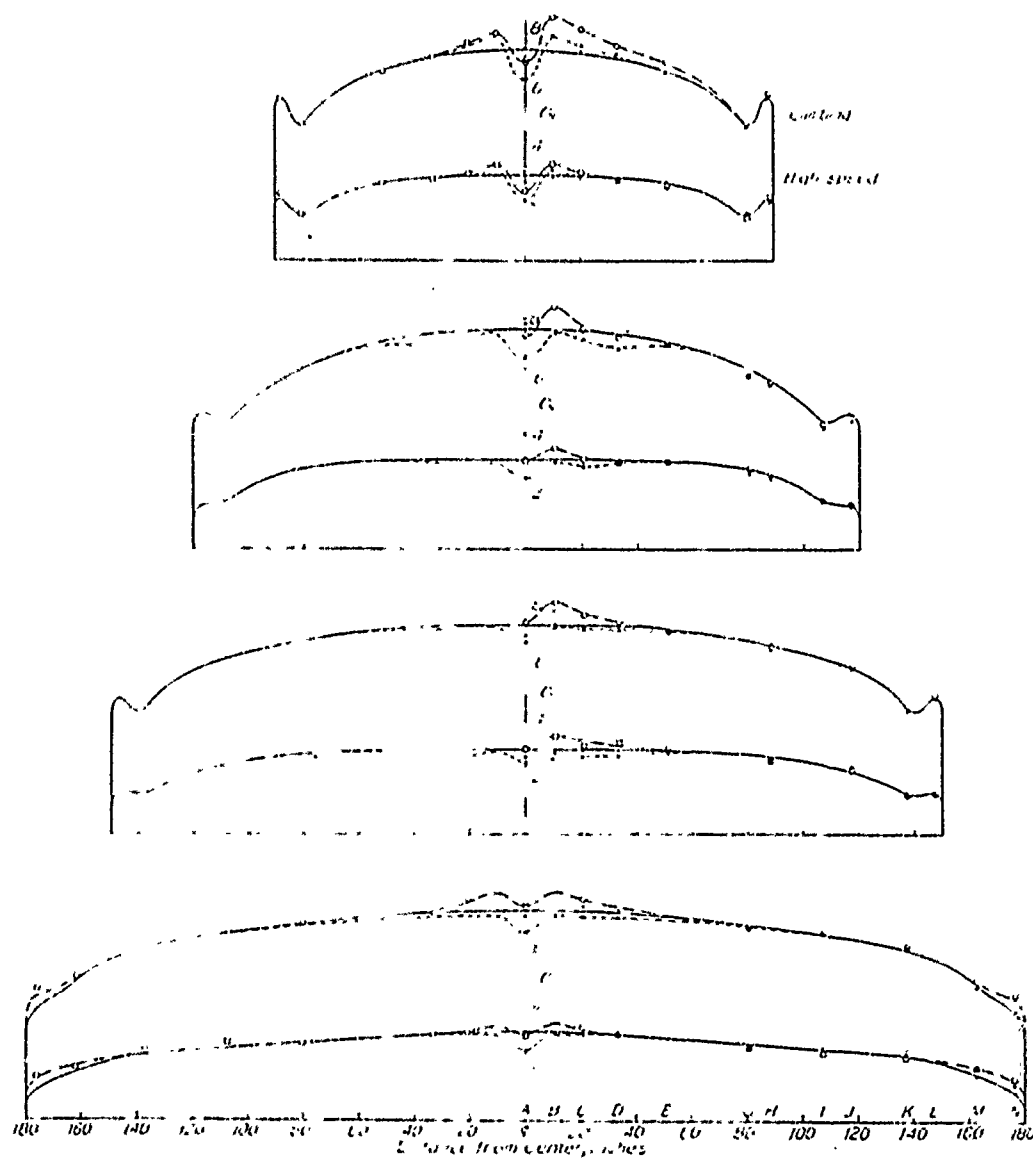
Fig. 72 Span Load Distribution for a Rectangular
Wing (Reference 50)
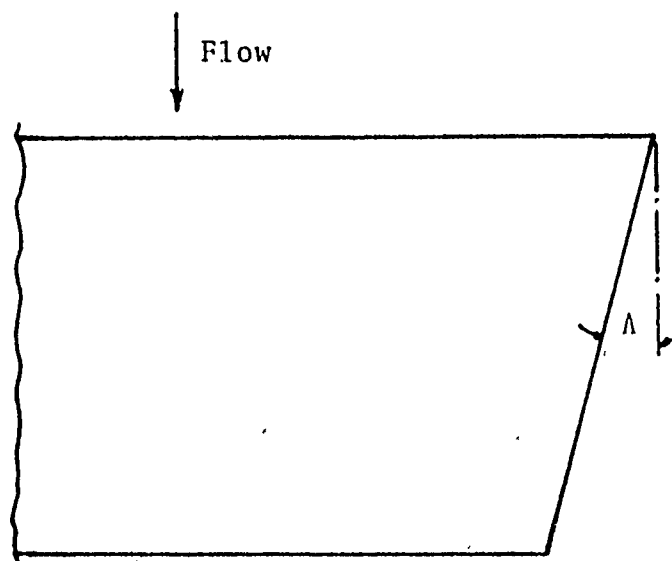
Flow

(a) Negative Sweepback
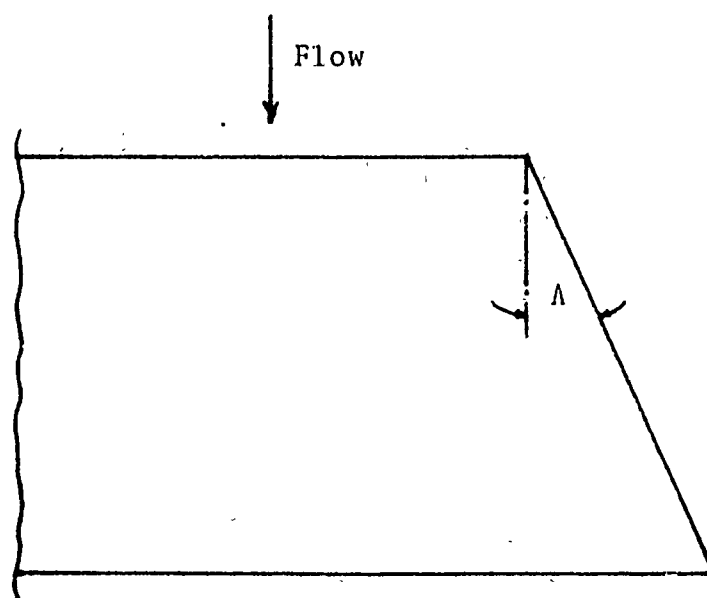
Flow

(b) Positive Sweepback

Fig. 73.   Sweepback at the Wing Tip
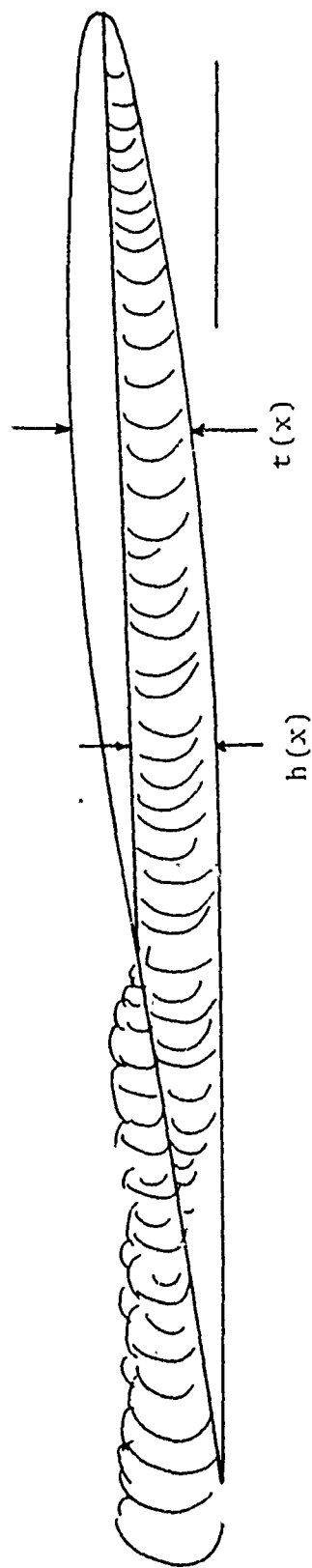
Fig. 74.   Airfoil and Flow "Thickness"
at the Wing Tip

Flow

No Shedding

Some Shedding,
No Rollover

Combined
Shedding
and
Rollover

Shedding Only
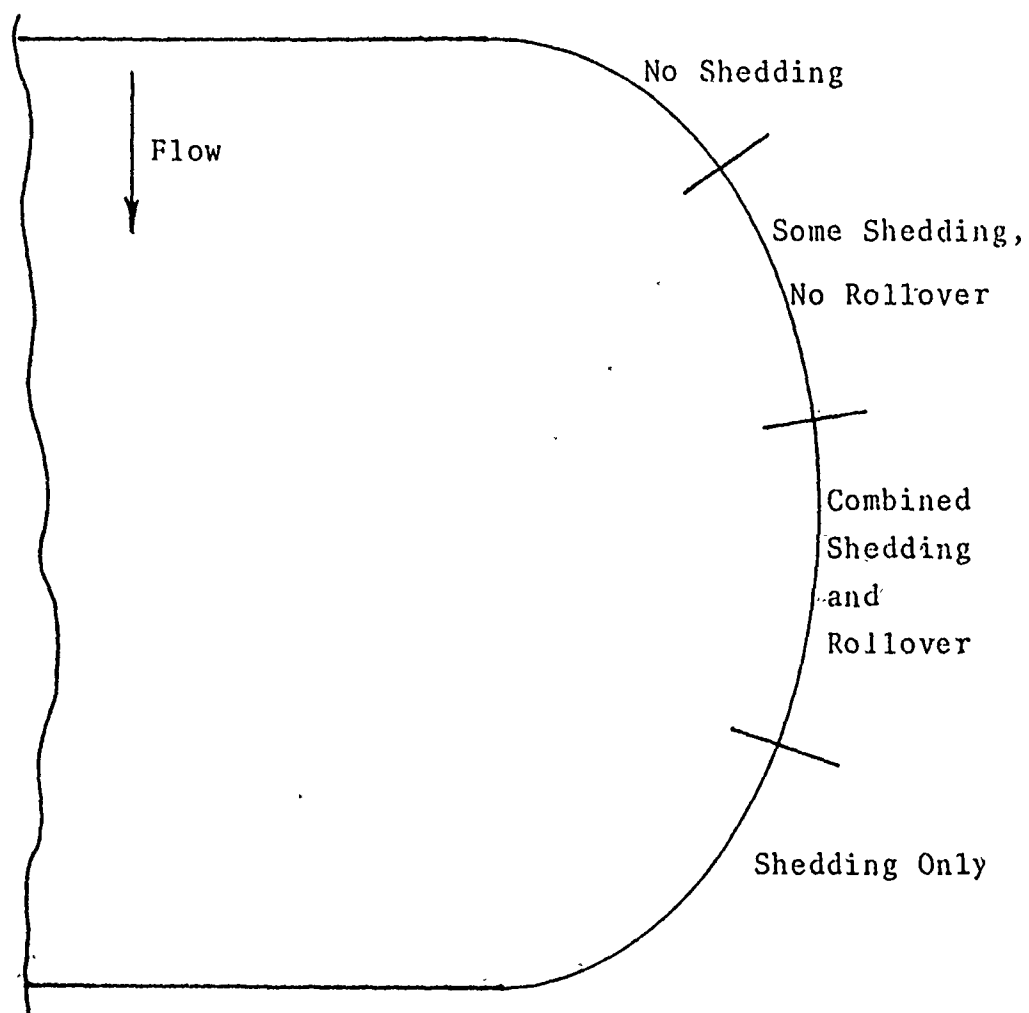
Fig. 75. Behavior of Vorticity Field Near
a Rounded Wing Tip
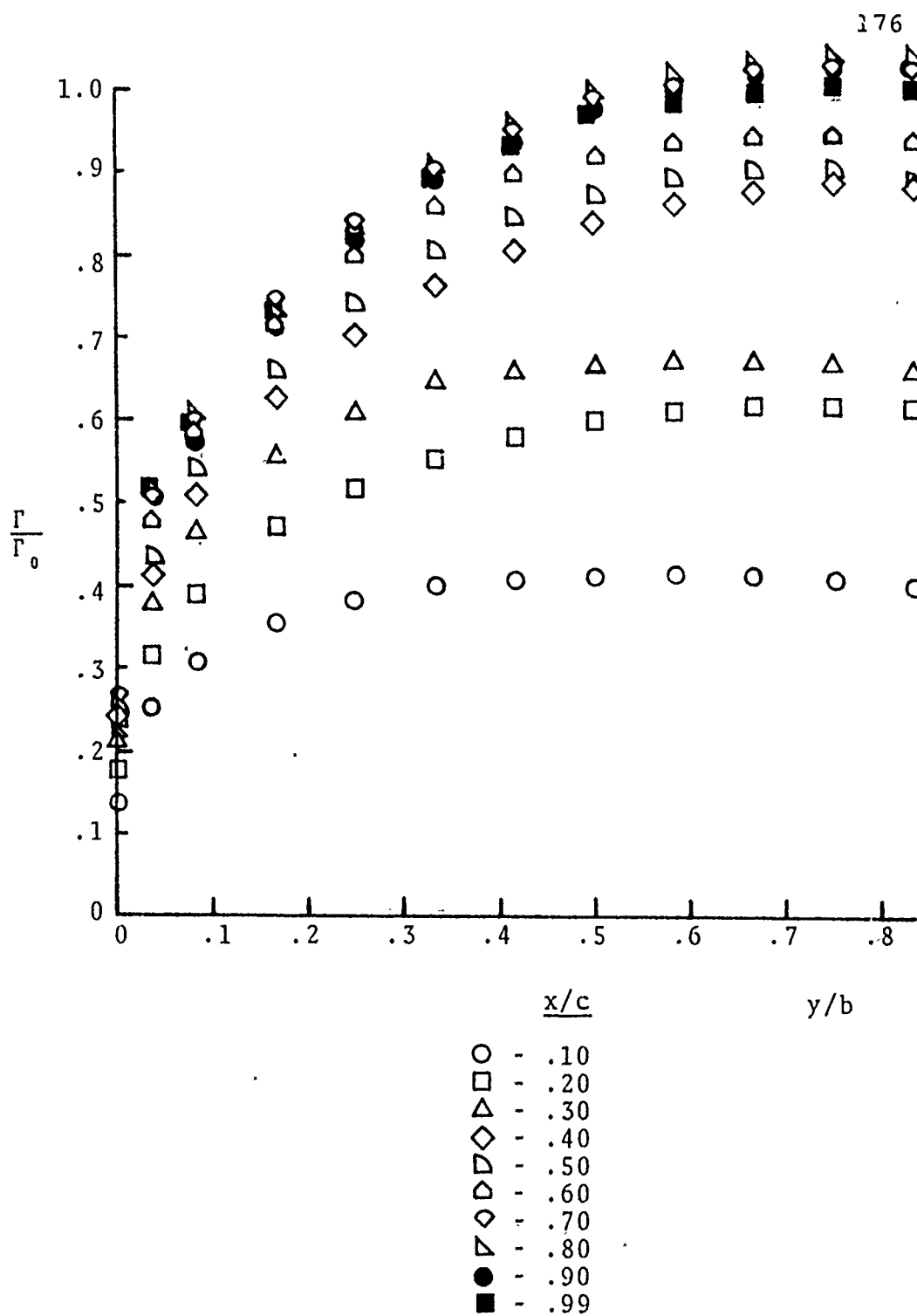
Fig. 76. Spanwise Circulation Profiles as
a Function of Chord, $\Gamma_0 = 5.781$ ft^2/sec
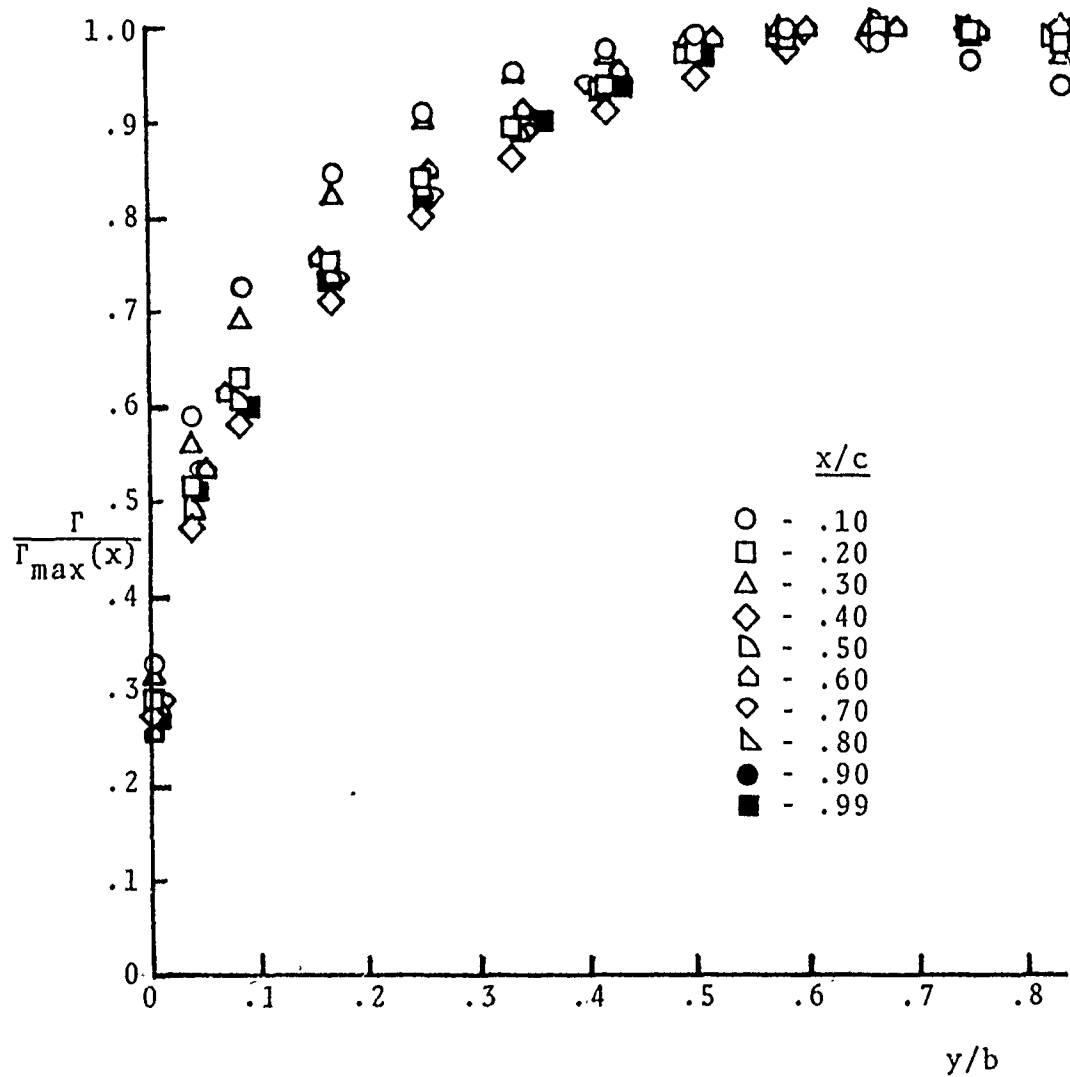
Fig. 77. Spanwise Circulation Profiles (Referenced to Local Maximum Chordwise Circulation)
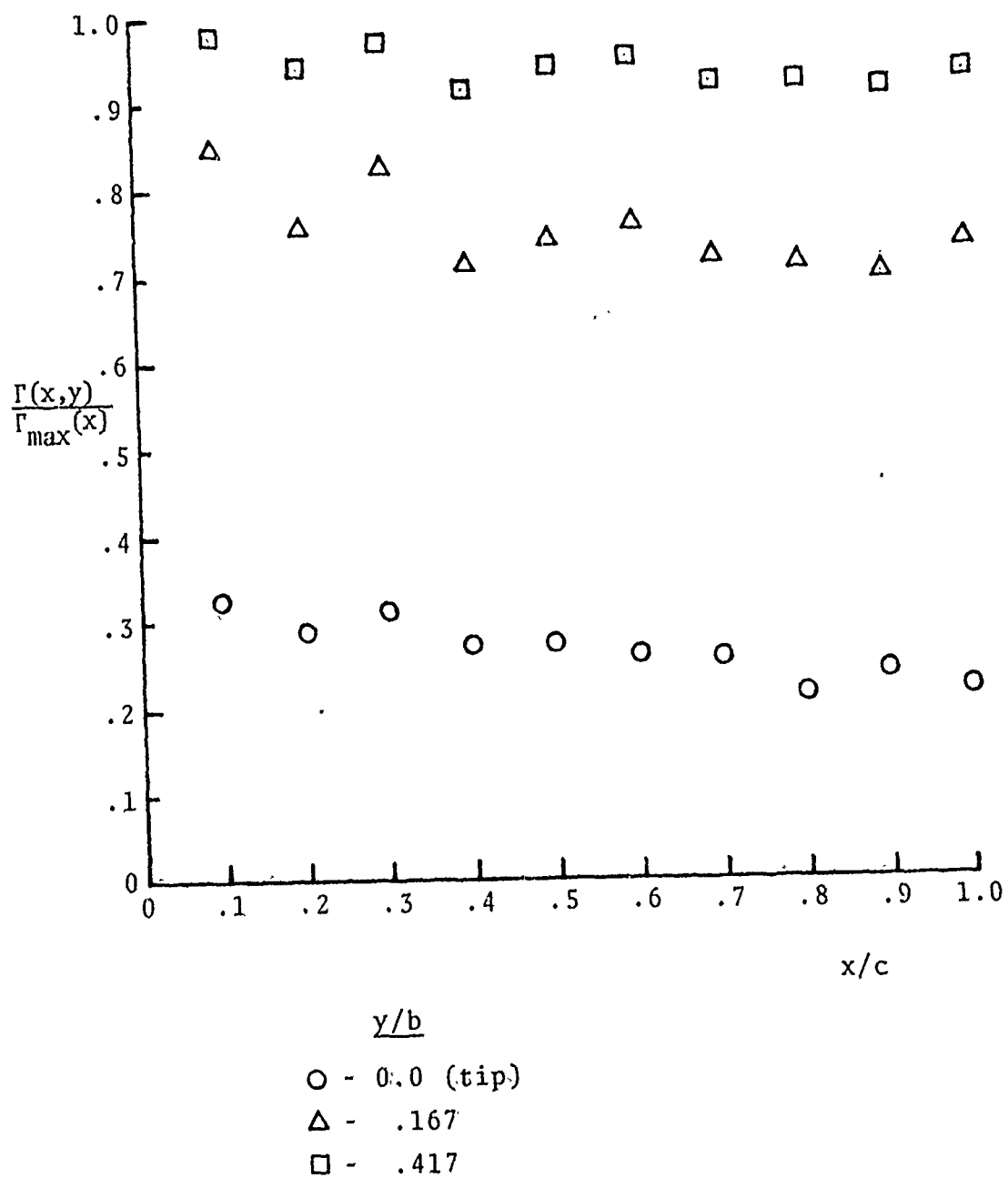
Fig. 78. Chordwise Variation of Circulation Function
(Referenced to Maximum Chordwise Value)
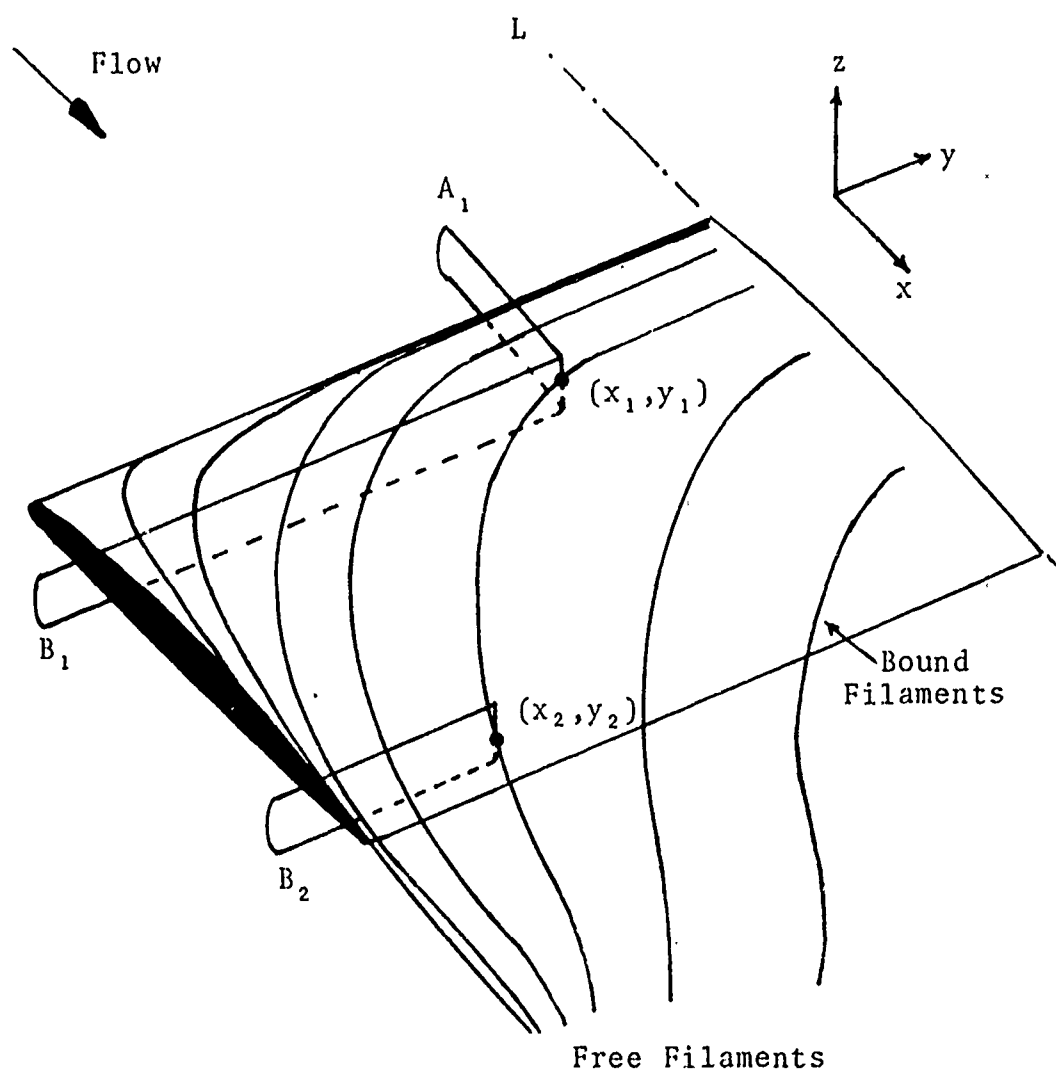
Fig. 79. Contour Integrals and the Bound
Vorticity Distribution
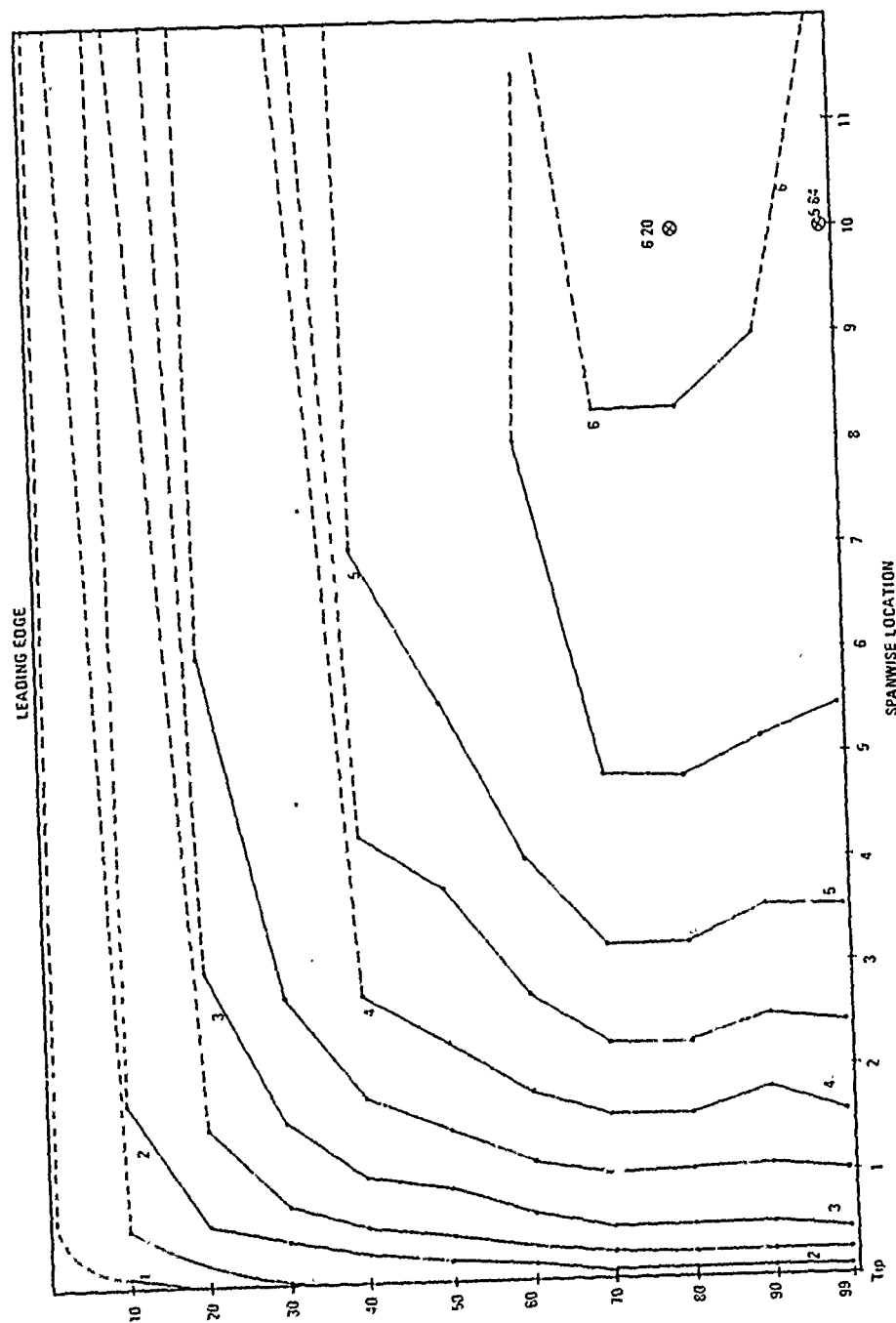
Fig. 80. Bound Vortex Elements Over the Wing Surface
($\alpha = 4°$, $U_o = 60$ ft/sec)

Legend

Line No.	Γ (ft^2/sec)	Γ/Γ_o
1	1	.173
2	2	.342
3	3	.513
4	4	.685
5	5	.857
6	6	1.027
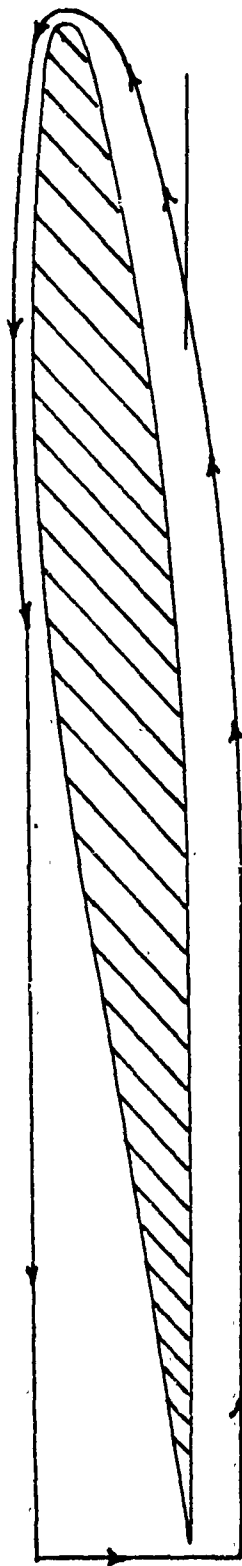
Fig. 81. Contour Description, "A" type Contours,
(to Scale)
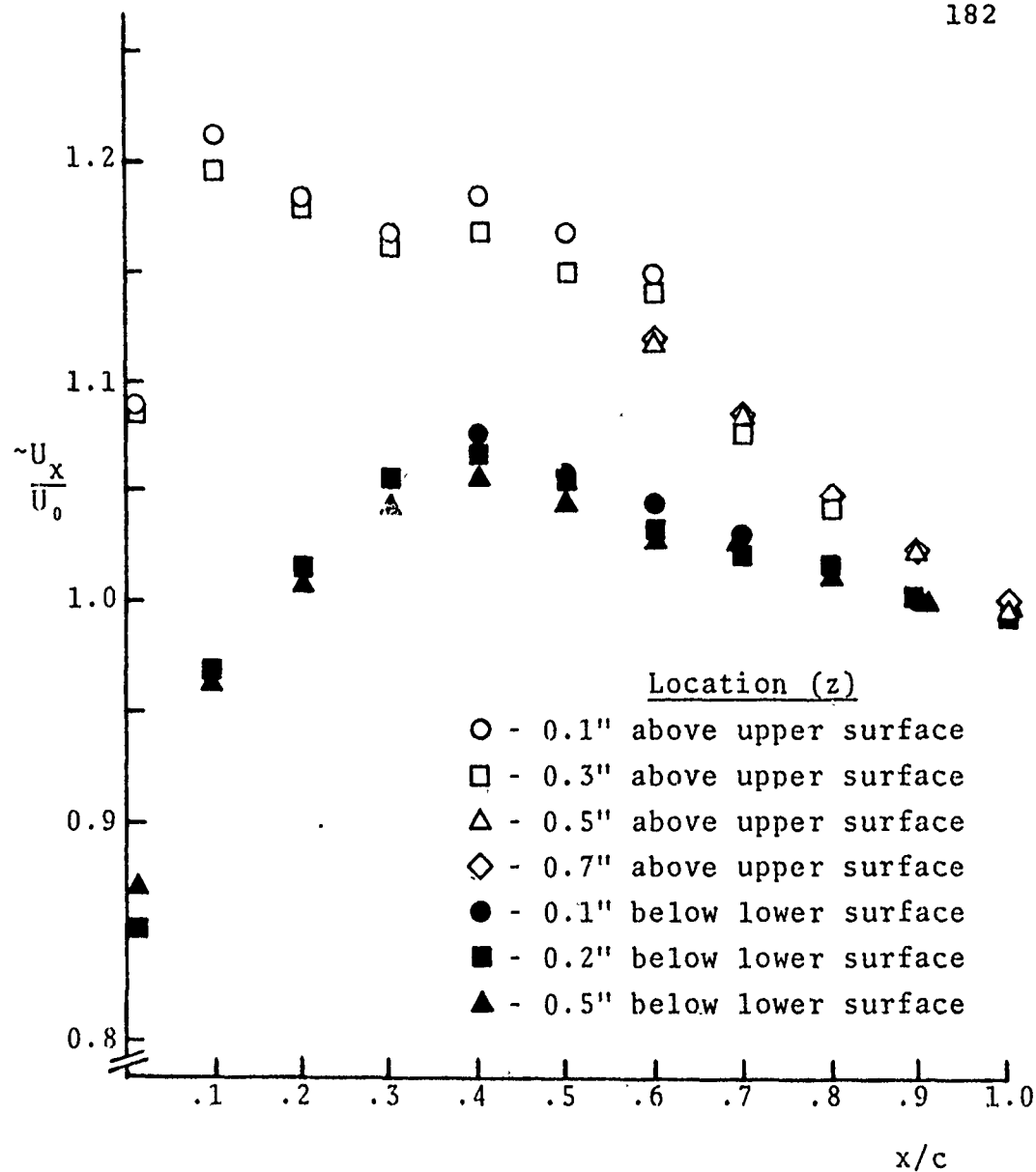
Fig. 82.   Chordwise (x) Component of Velocity
            Adjacent to the Wing Surface,
            Inboard Region, y/b = 0.25
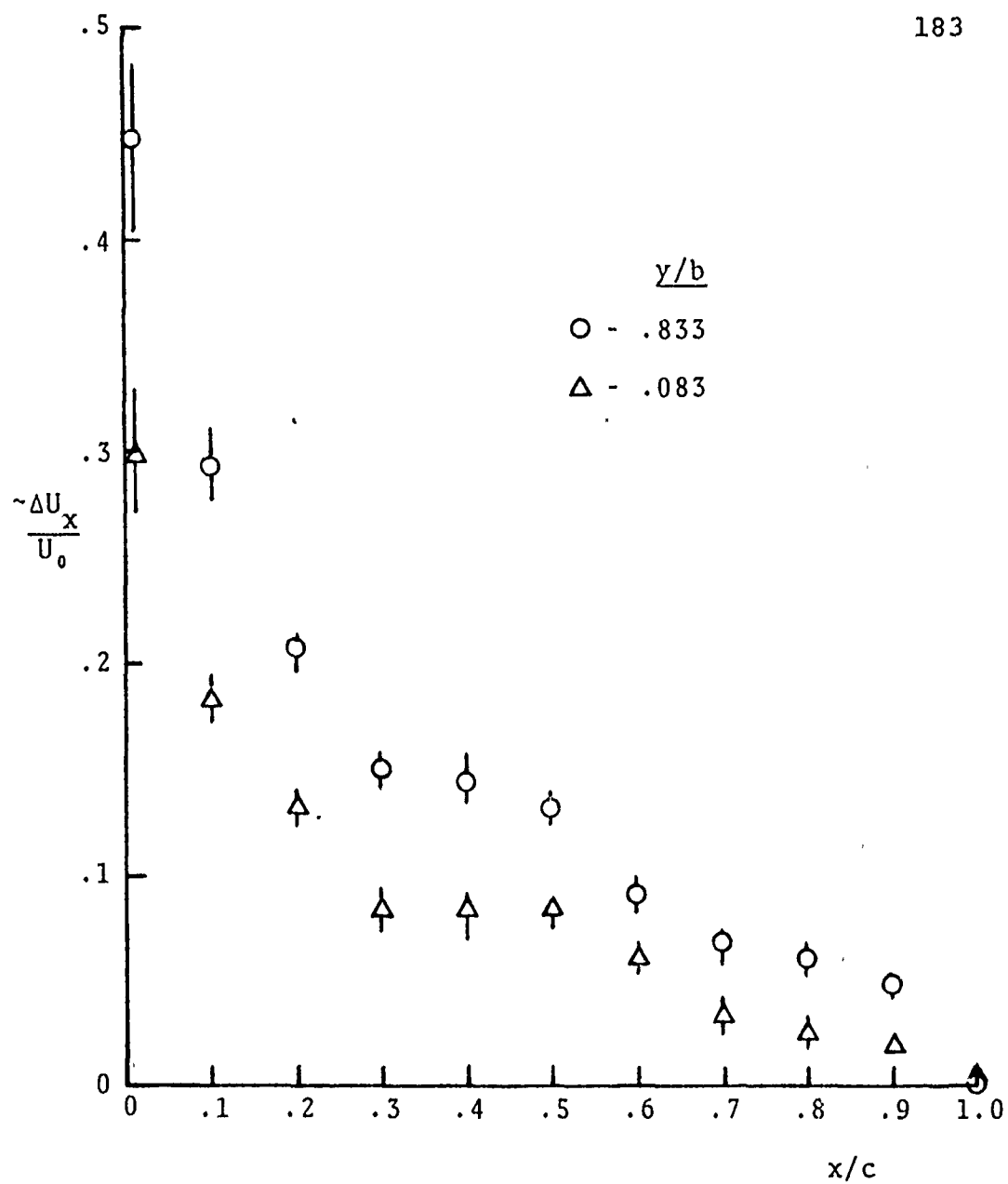
Fig. 83.   Mainflow Differential Velocity as a
Function of Chordwise Location
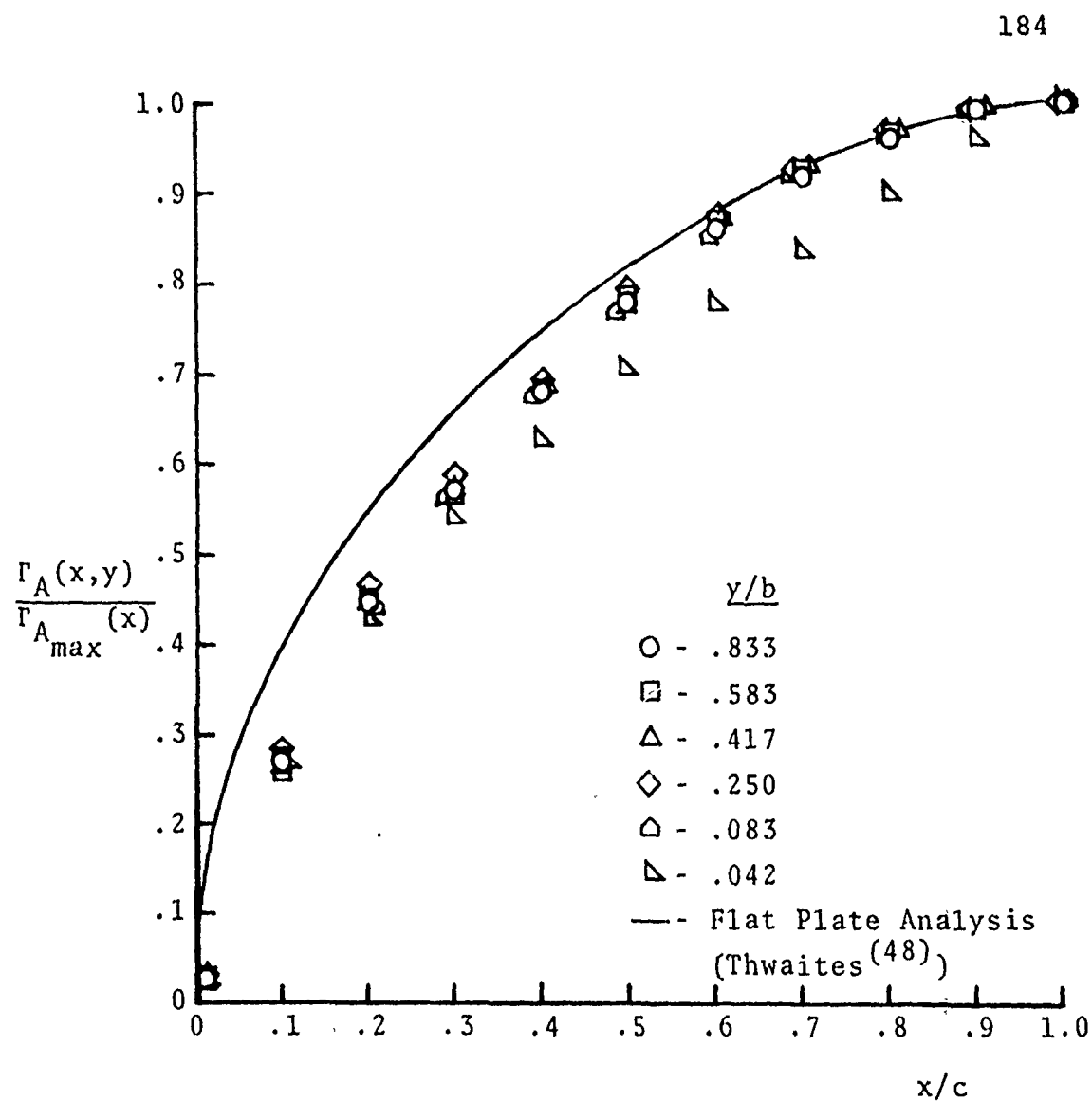
Fig. 84. Chordwise Variation of Circulation Function
as Obtained by "A" - type Contours
(referenced to local spanwise maximum value)
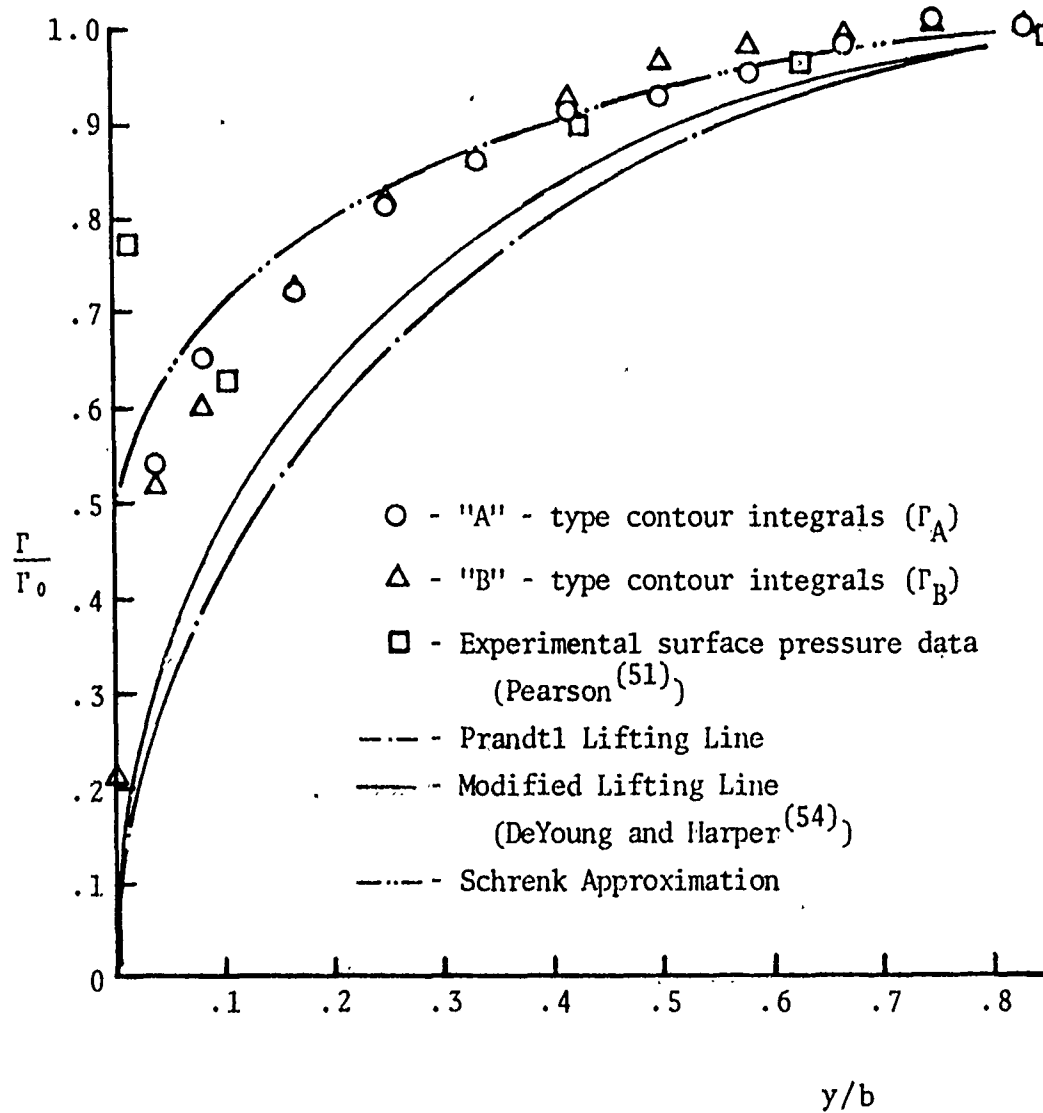
Fig. 85. Spanwise Variation of the Wing Circulation
Function, $\Gamma(c,y)$
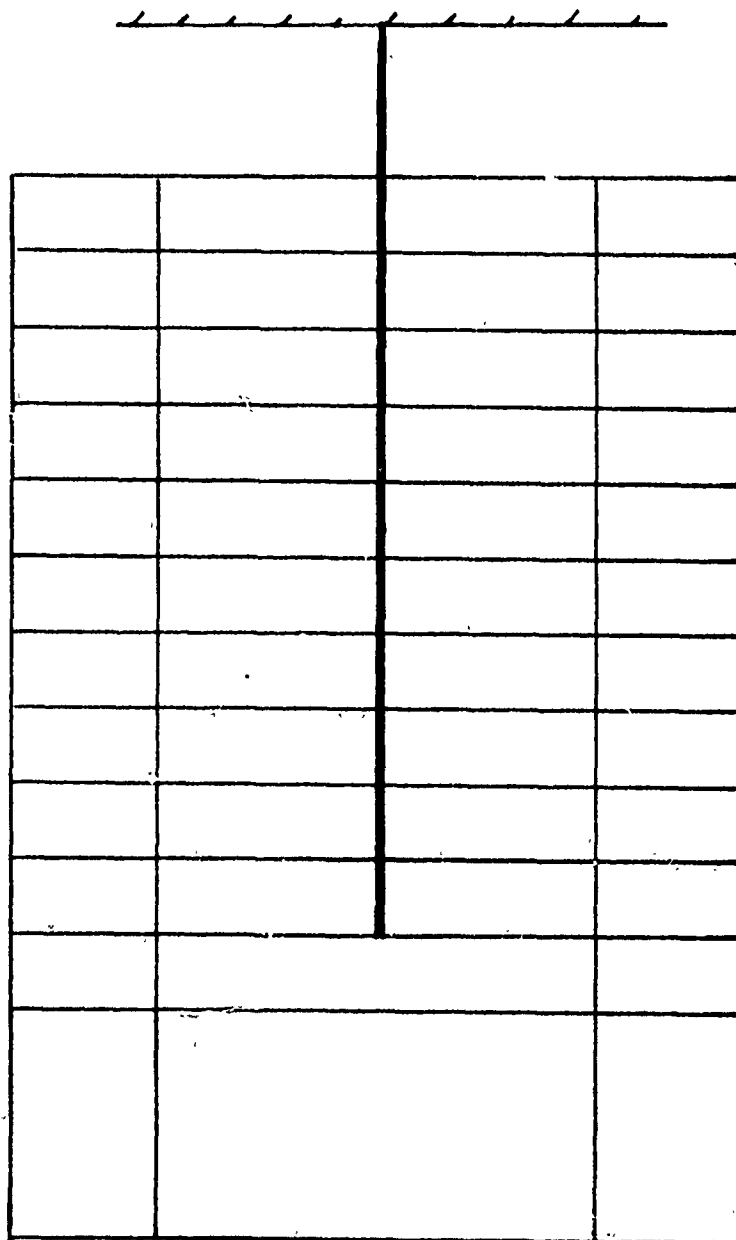
Fig. 86. Schematic of Contour Layout in the Wake Region
(View Looking Upstream)
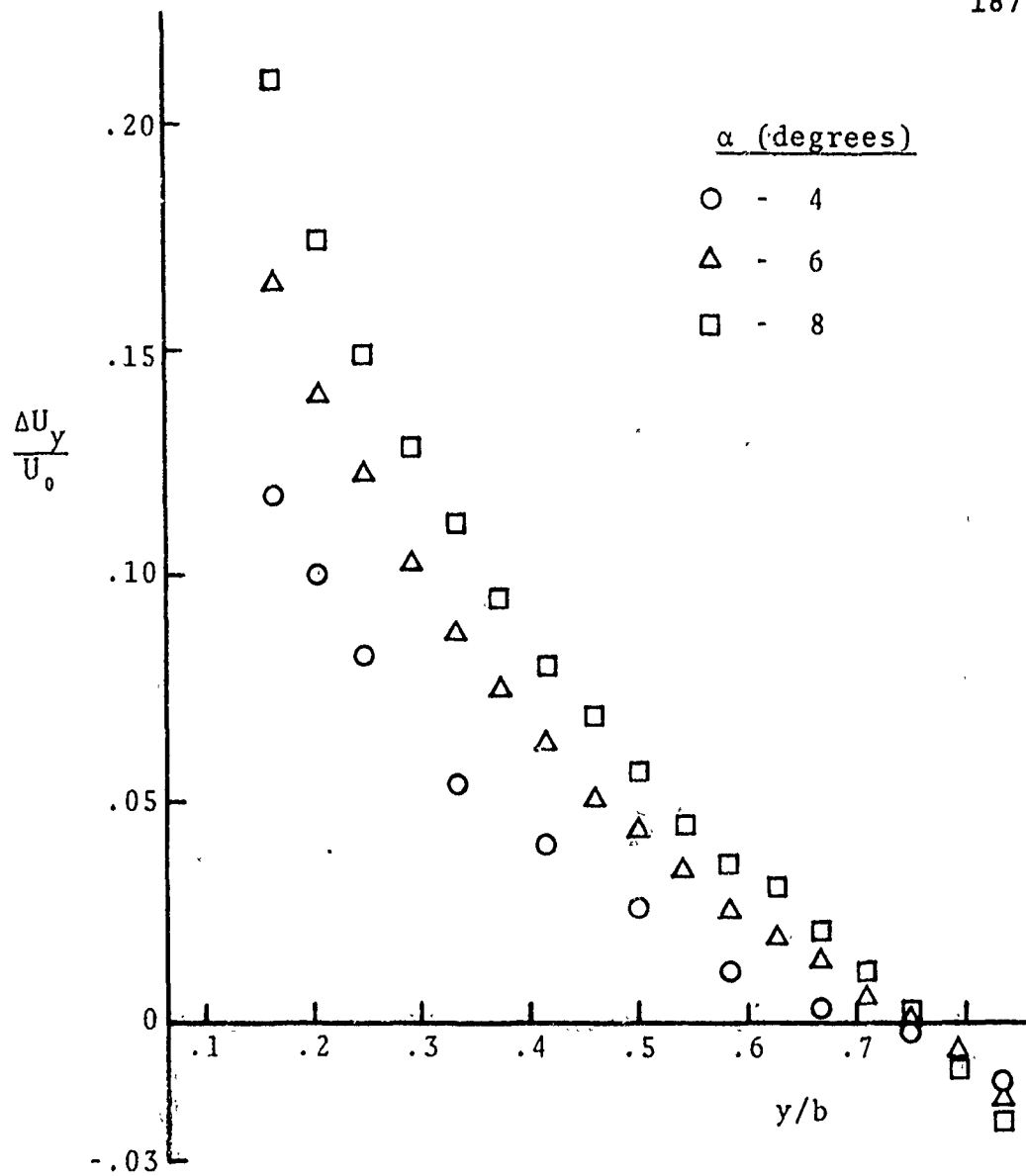
Fig. 87. Vorticity Distribution at the Trailing
Edge Over the Inboard Wing Region
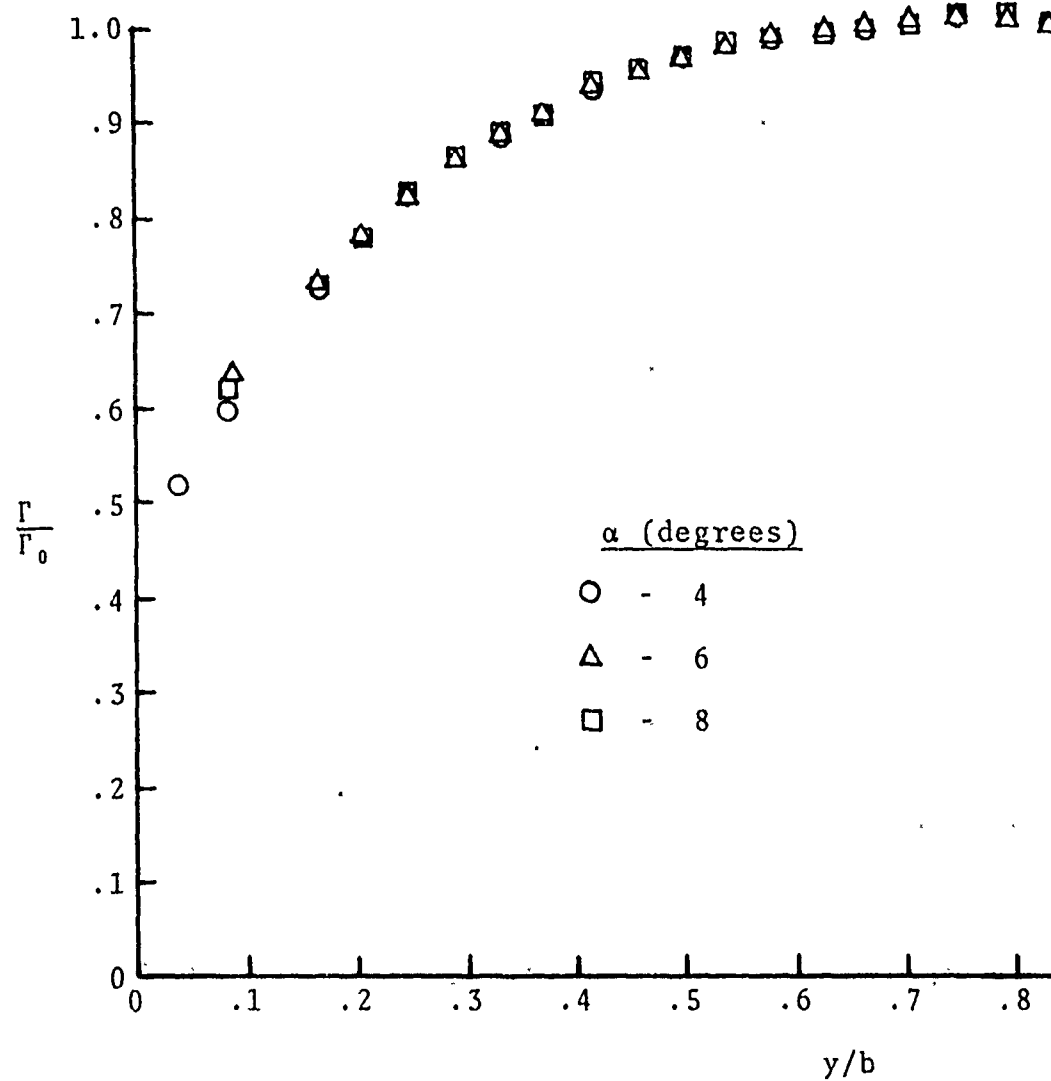
Fig. 88. Circulation Function at the Trailing Edge

C_L

O - Contour Integral (corrected, average value)
△ - Cylindrical Symmetry Assumed (1/r)
—— - Linear fit to contour data and 1/r distribution
- - - - Lifting Line Theory
—·—·— Lifting Surface Theory
—··—··— K.D. Wood Approximation
····□···· Rom's [52] Prediction
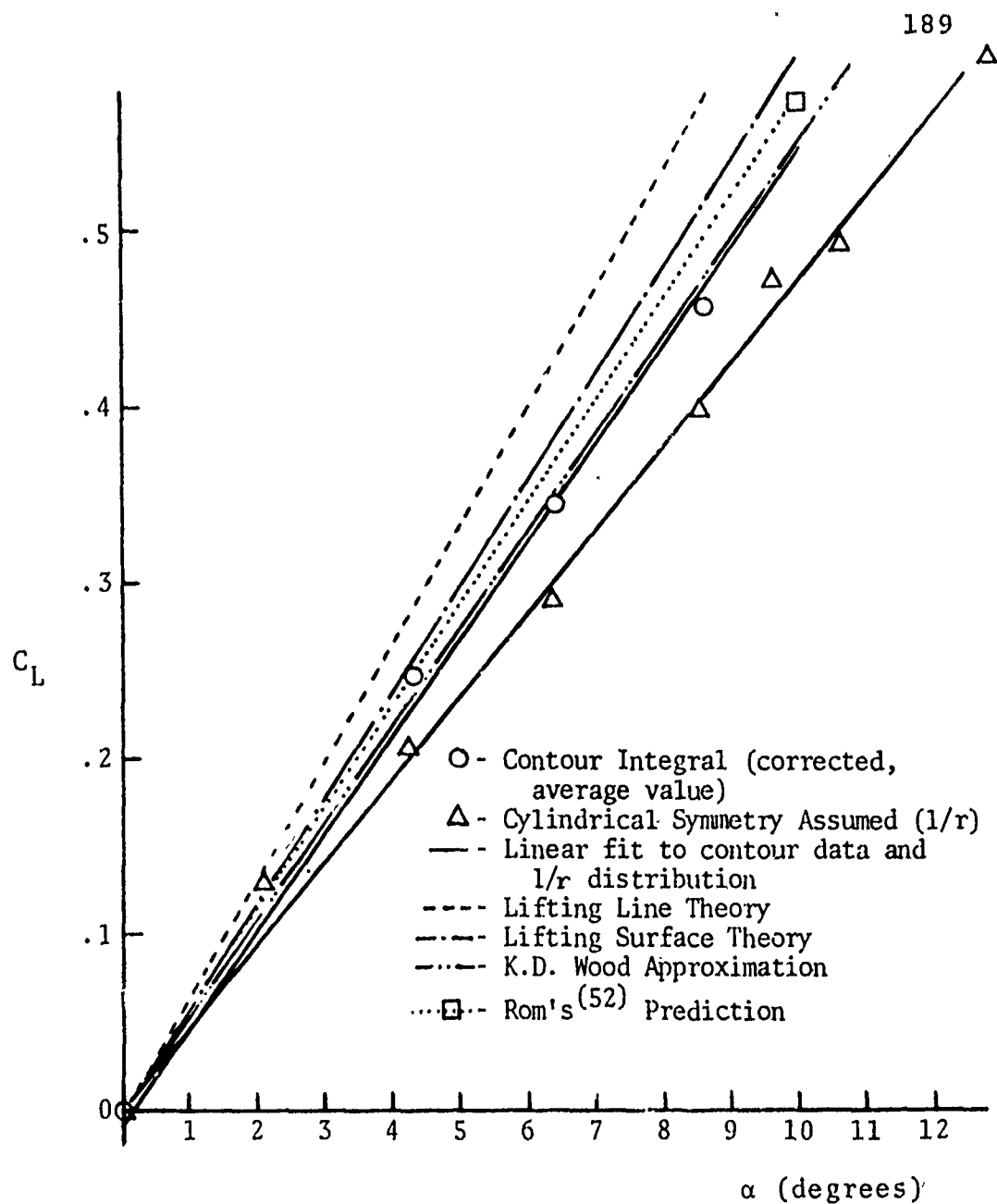
α (degrees)

Fig. 89. Variation of Lift Coefficient with
Angle of Attack - Theory and Experiment
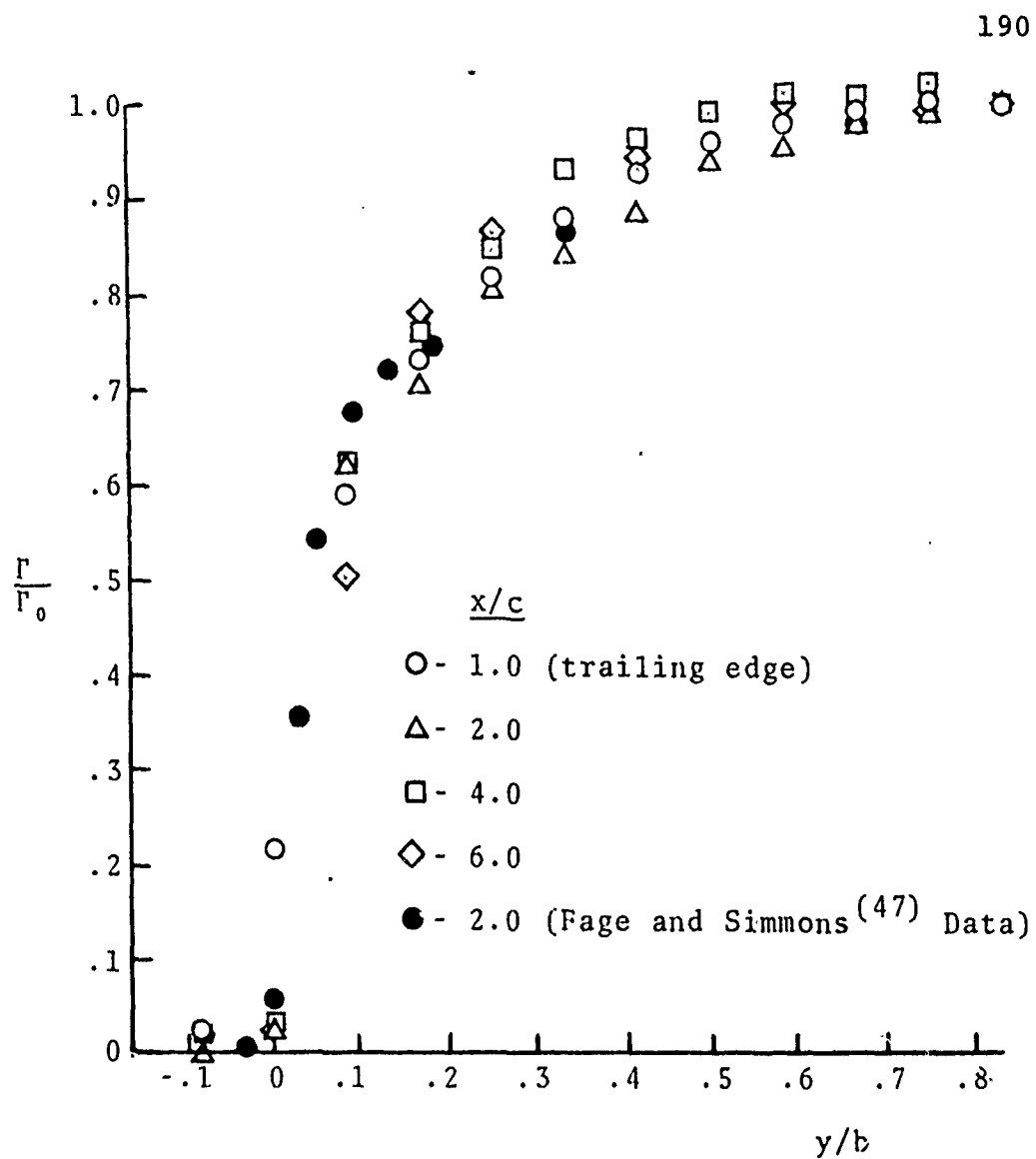
Fig. 90. Non-dimensional Circulation Function at Various
Downstream Locations, α = 4 degrees
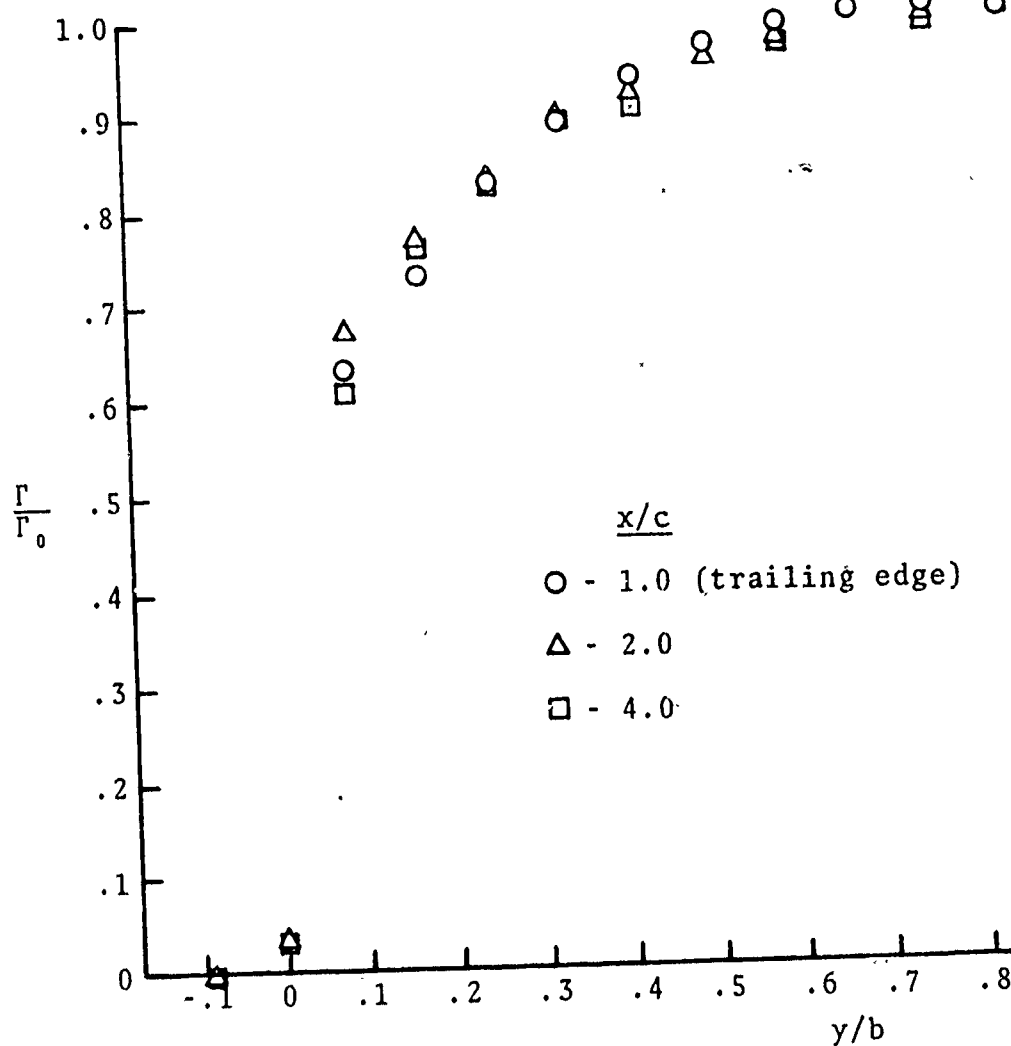
Fig. 91. Non-dimensional Circulation Function at Various Downstream Locations, $\alpha = 6$ degrees
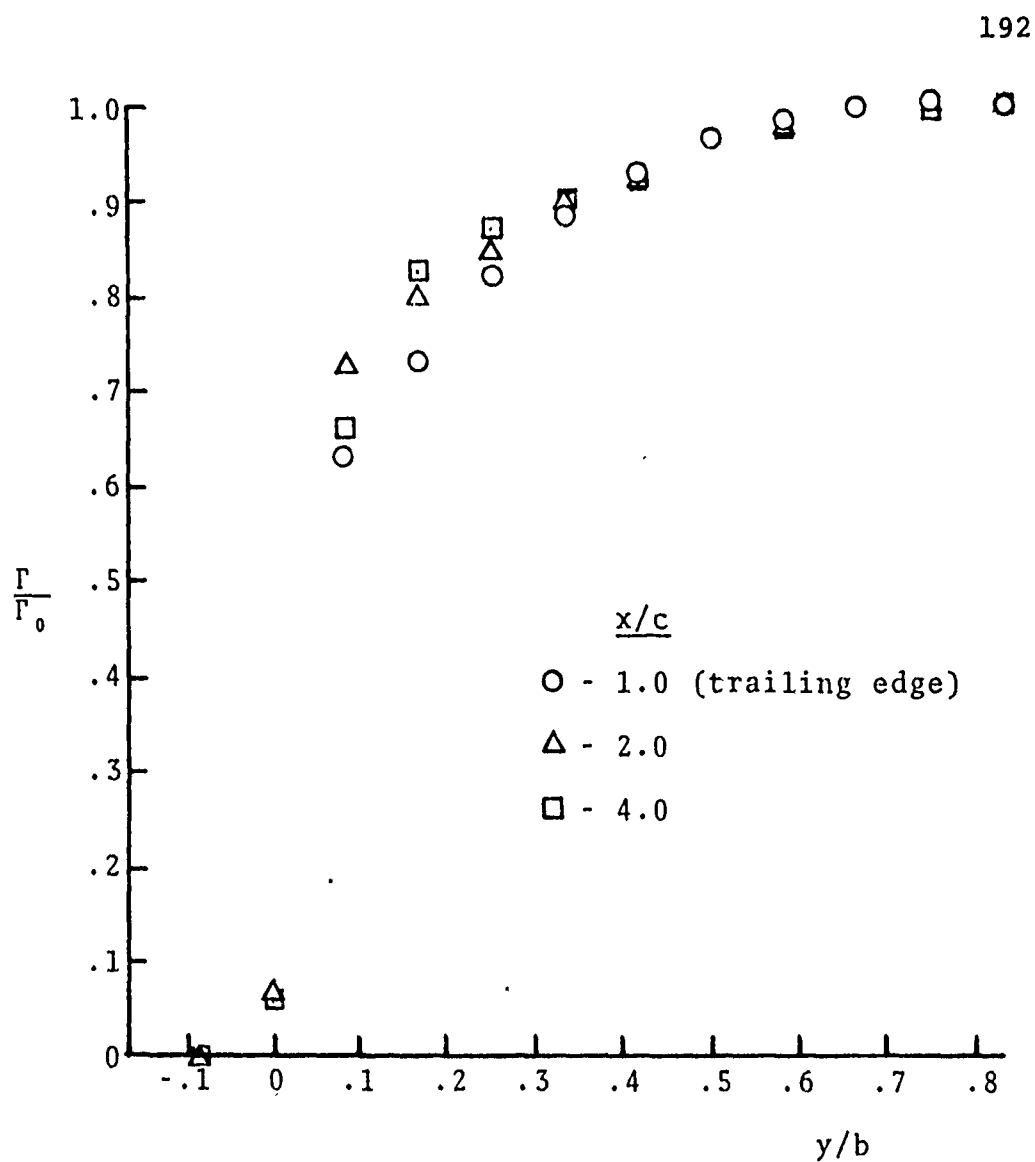
Fig. 92. Non-dimensional Circulation Function at Various Downstream Locations, $\alpha = 8$ degrees
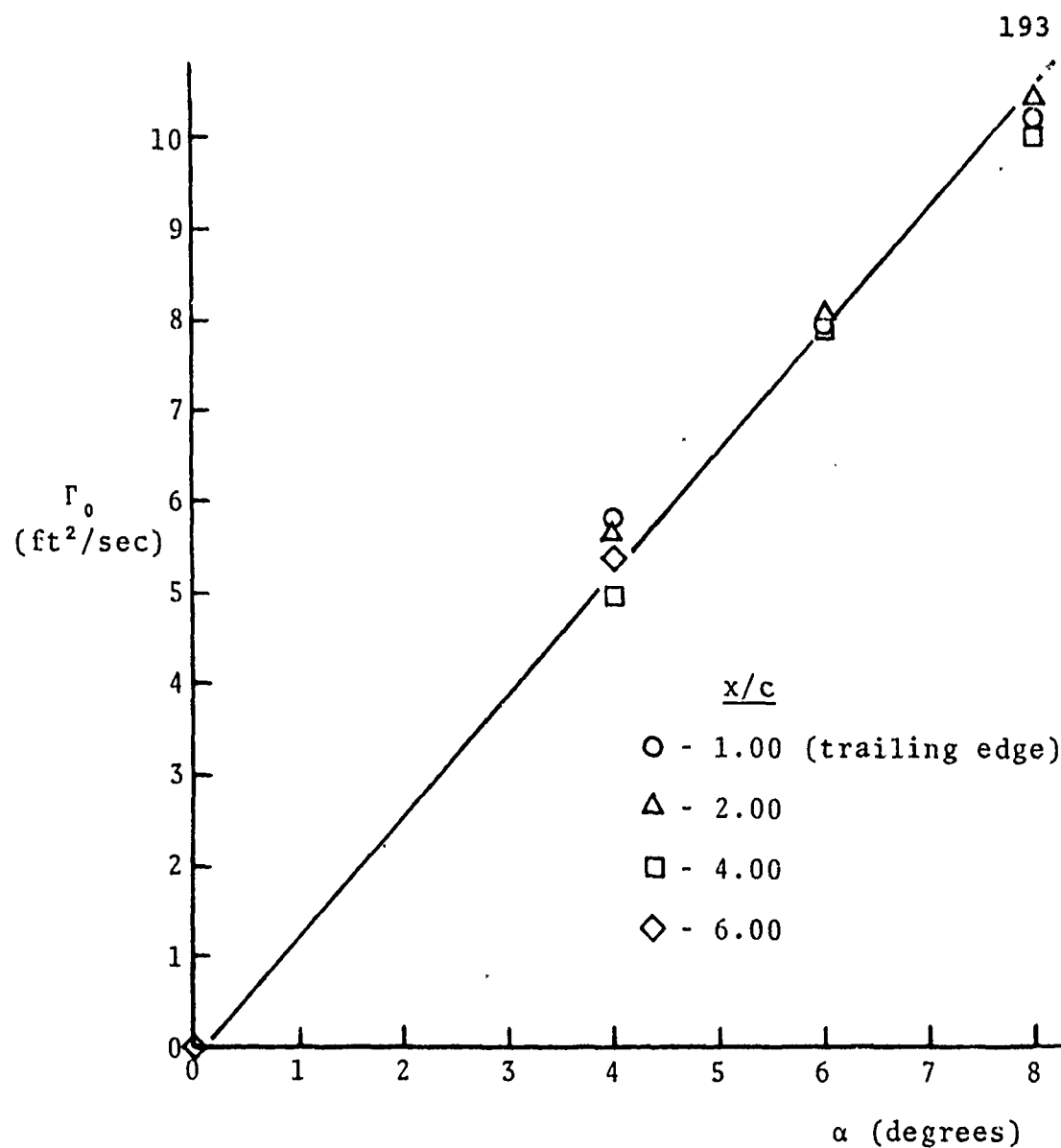
Fig. 93. Variation of Circulation with Angle of
Attack for Various Downstream Locations
(Contour Integrals)
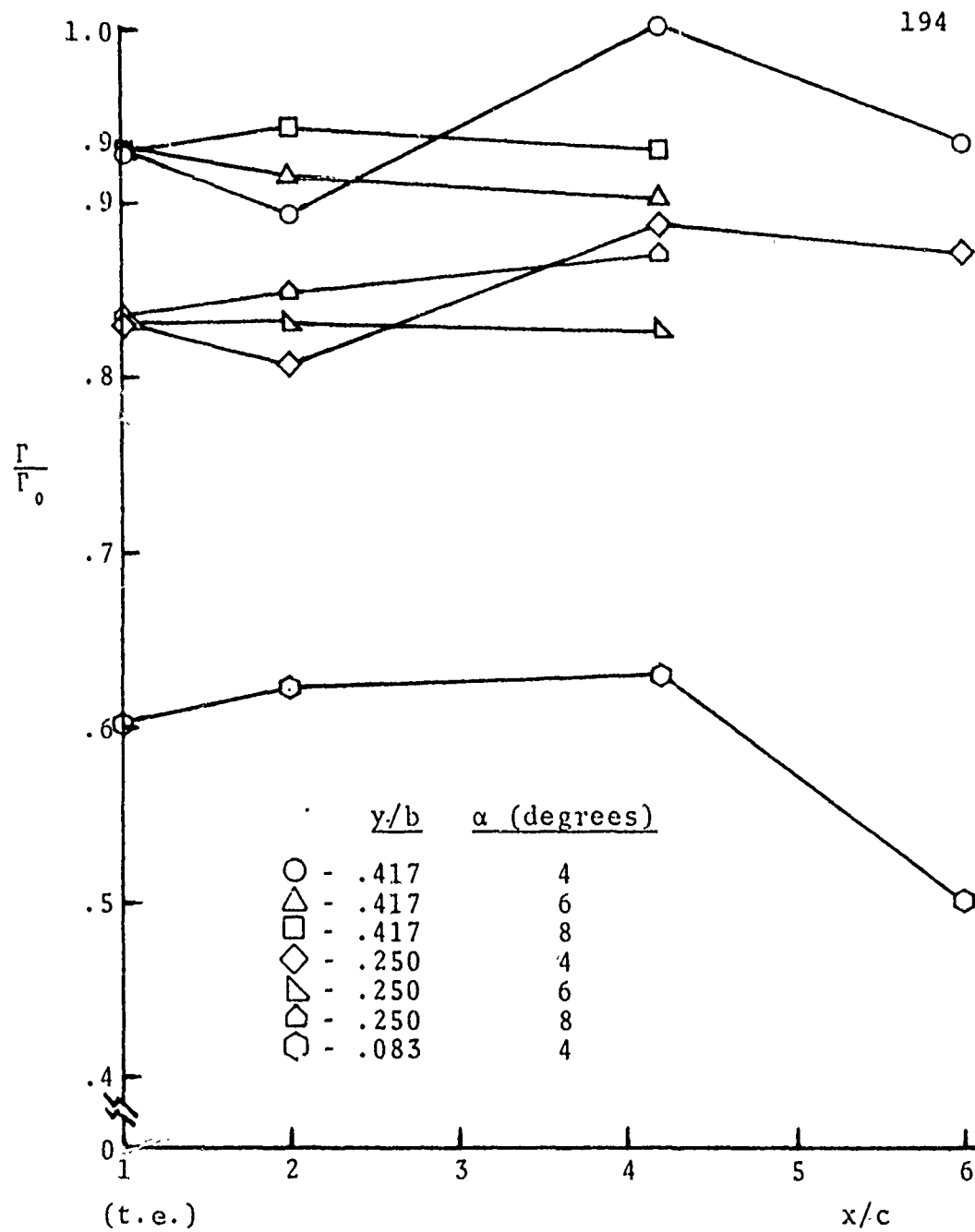
Fig. 94. Variation of Circulation Function
Downstream of the Wing
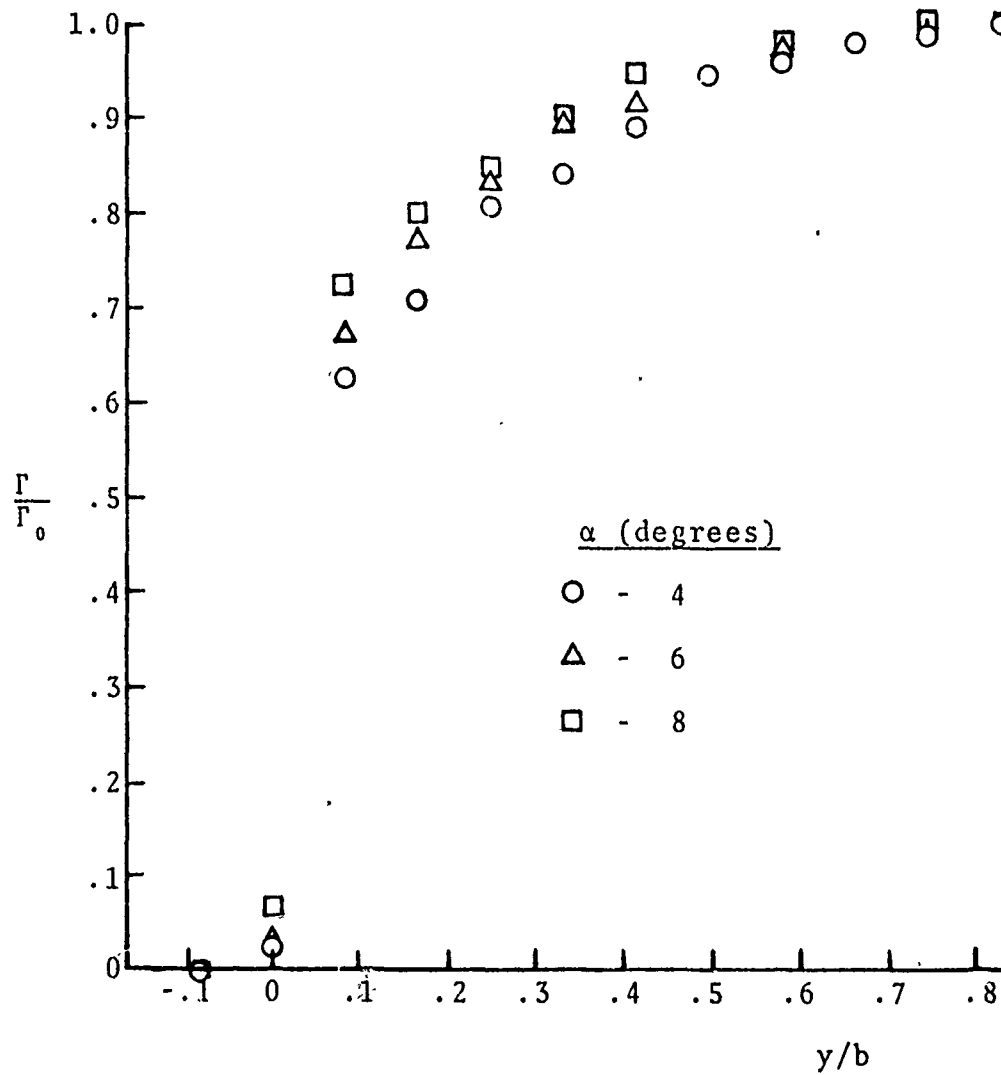
Fig. 95. Non-dimensional Circulation Function at
Various Angles-of-Attack, x/c = 2.00
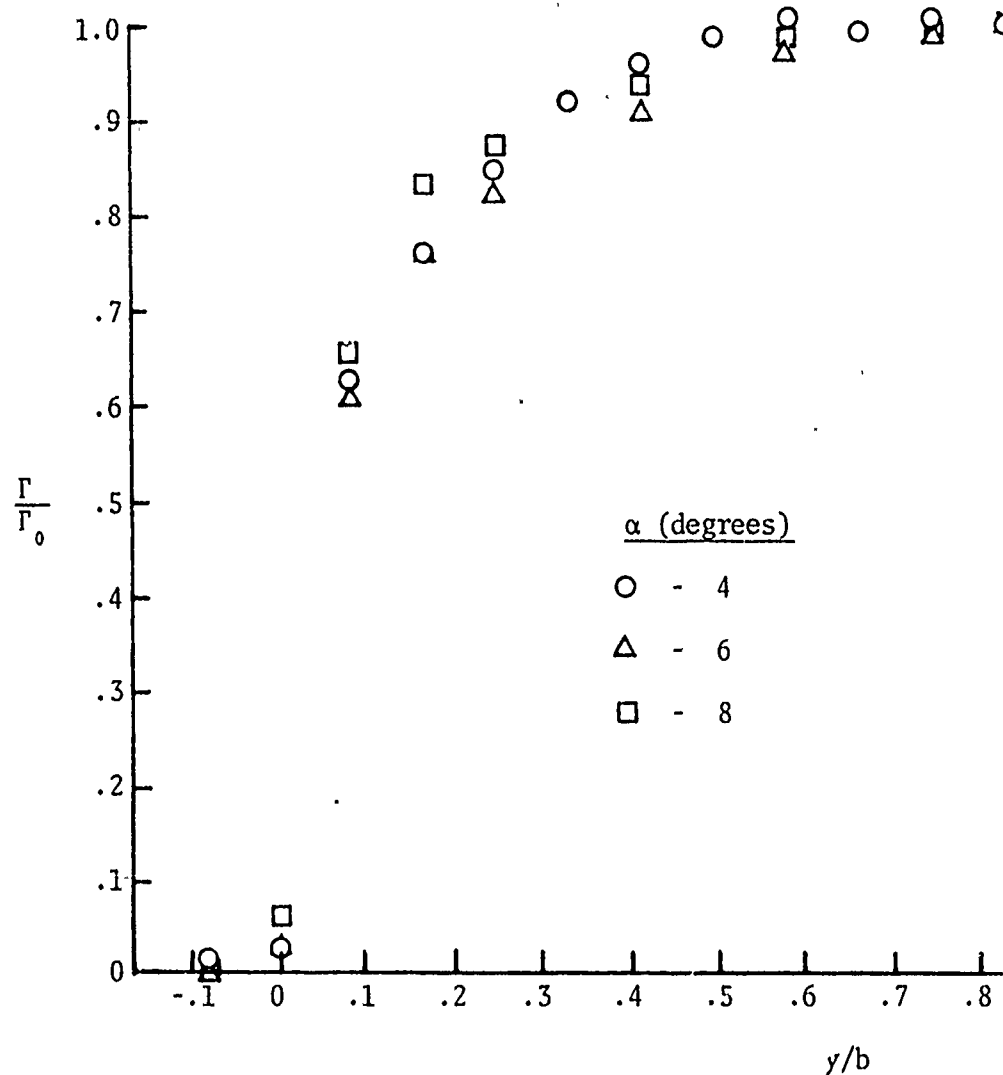
Fig. 96. Non-dimensional Circulation Function at Various Angles-of-Attack, x/c = 4.00

Upper Surface Max. | ⇥.1b⇤ | Trailing Edge

x/c

O - 2, Upper Limit
△ - 2, Lower Limit
□ - 4, Upper Limit
◇ - 4, Lower Limit
△ - 6, Upper Limit
◺ - 6, Lower Limit
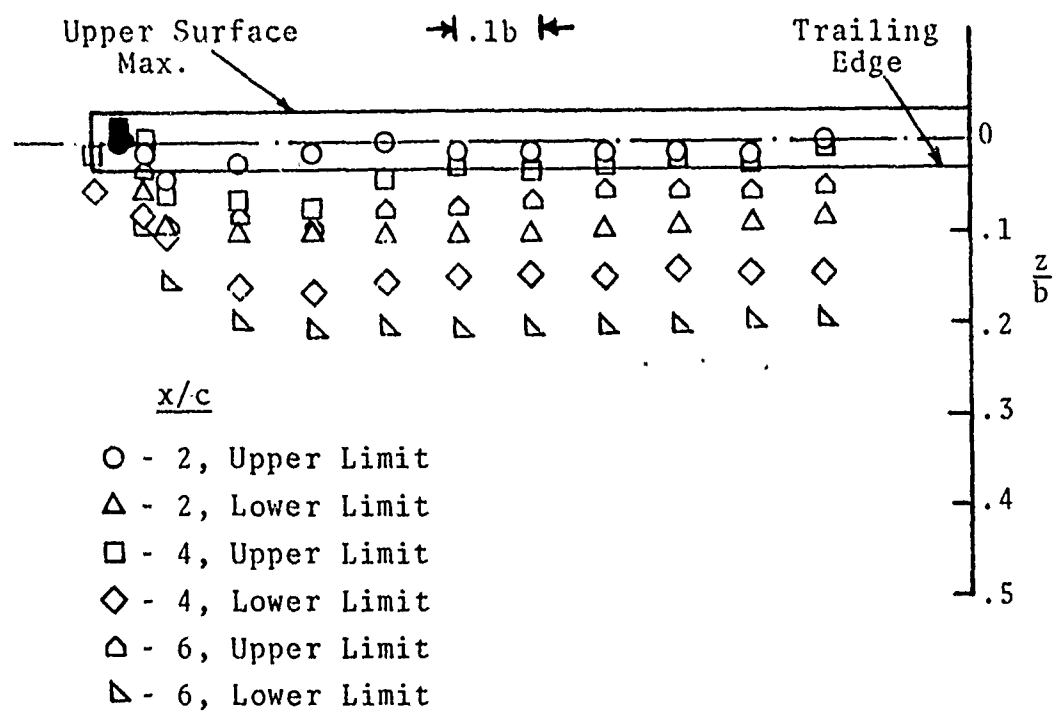
Darkened symbols indicate core center locations

Side View

⊢— 1' —⊣
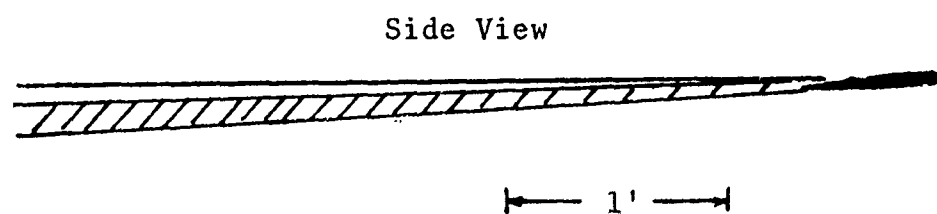
Fig. 97.   Variation of Wake Shape in the Near Field,
$\alpha = 4$ degrees
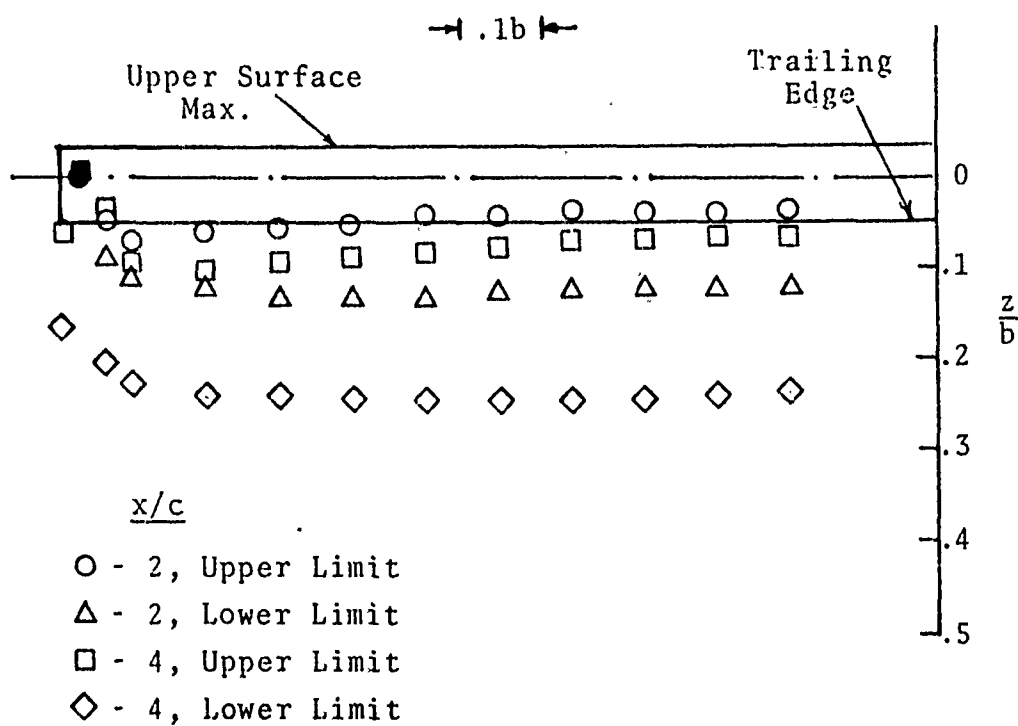
Fig. 98.   Variation of Wake Shape in the Near Field,
$\alpha = 6$ degrees
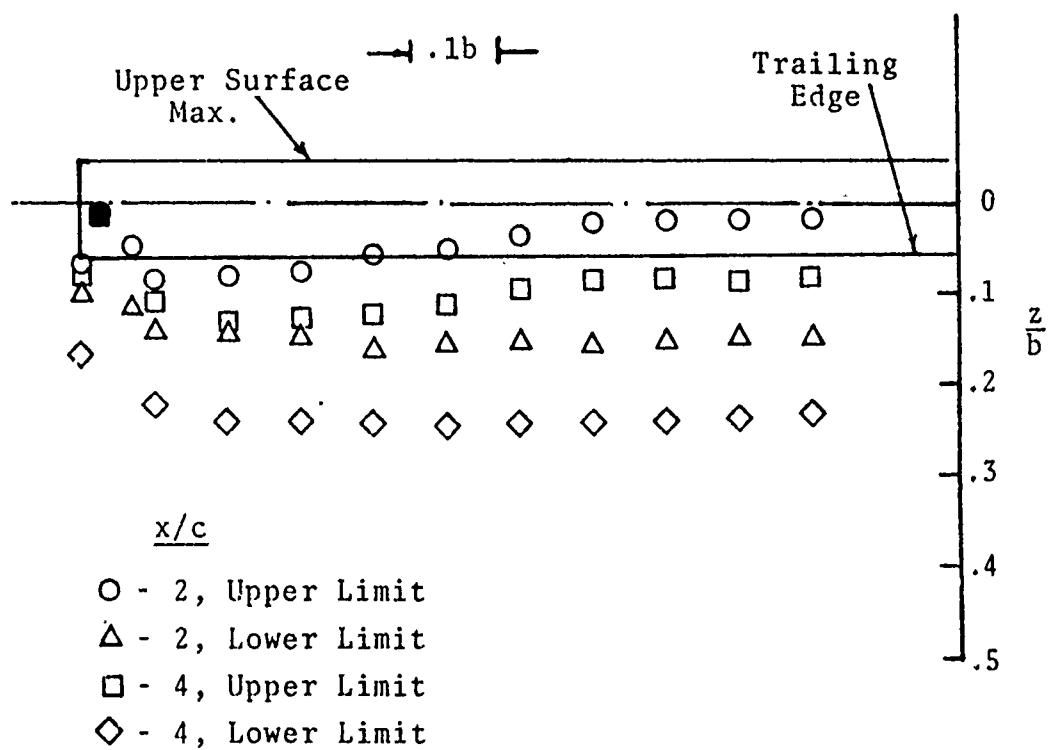
Fig. 99.   Variation of Wake Shape in the Near Field,
α = 8 degrees

ACKNOWLEDGEMENTS